

# Numerical Simulation of Condensation in Transonic Flows

Numerical Simulation of Condensation in Transonic Flows  
F. Put

Cover Image: Condensation cloud over F-18 Hornet of the Swiss Air Force  
Photo taken by Peter Steehouwer (<http://www.steehouwer.com/>)

Thesis University of Twente, Enschede - With ref. - With summary in Dutch.  
ISBN 90-365-1948-9

Copyright ©2003 by F. Put, Enschede, The Netherlands



# **NUMERICAL SIMULATION OF CONDENSATION IN TRANSONIC FLOWS**

## **PROEFSCHRIFT**

ter verkrijging van  
de graad van doctor aan de Universiteit Twente,  
op gezag van de rector magnificus,  
prof.dr. F.A. van Vught,  
volgens besluit van het College voor Promoties  
in het openbaar te verdedigen  
op 19 september 2003 om 16:45 uur.

door

Frits Put

geboren op 2 december 1973  
te Alblasterdam

Dit proefschrift is goedgekeurd door de promotor:  
prof.dr.ir. H.W.M. Hoeijmakers  
en de assistent promotor:  
dr.ir. R. Hagmeijer

*Discovery consists of seeing what everybody has seen  
and thinking what nobody has thought.*

Albert Szent-Györgyi



---

# TABLE OF CONTENTS

---

<b>1</b>	<b>Introduction</b>	<b>1</b>
1.1	Background . . . . .	1
1.2	Condensation in rapidly expanding flows . . . . .	2
1.3	Thesis overview . . . . .	3
<b>2</b>	<b>Physics of condensation</b>	<b>5</b>
2.1	Introduction . . . . .	5
2.2	Condensation . . . . .	6
2.2.1	Condensation during rapid expansion . . . . .	6
2.2.2	Homogeneous nucleation . . . . .	7
2.2.3	Classical nucleation theory . . . . .	9
2.2.4	Droplet growth . . . . .	9
2.3	Governing equations . . . . .	10
2.3.1	Gas-liquid mixtures . . . . .	11
2.3.2	Mass conservation for the mixture . . . . .	13
2.3.3	Description of the liquid phase . . . . .	14
2.3.4	Alternative derivation of Hill's Method of Moments . . . . .	17
2.3.5	Alternative approximate closure using two moment equations . . . . .	18
2.3.6	Equation of state for the mixture . . . . .	19
2.3.7	Resulting set of governing equations . . . . .	21
2.3.8	Speed of sound . . . . .	21
2.3.9	Relation between the liquid mass fraction and the saturation . . . . .	22
2.4	Material properties and constants . . . . .	22
2.4.1	Surface tension . . . . .	23
2.4.2	Liquid density . . . . .	24
2.4.3	Vapour pressure . . . . .	25
2.4.4	Latent heat . . . . .	26
2.4.5	Material properties of the gas phase . . . . .	28
<b>3</b>	<b>Equation of State for Real Gas</b>	<b>29</b>
3.1	Thermodynamics . . . . .	29
3.1.1	Basics . . . . .	29
3.1.2	Discussion . . . . .	31

---

3.2	Classification of gases . . . . .	32
3.2.1	Calorically perfect gas . . . . .	33
3.2.2	Thermally perfect gas . . . . .	33
3.2.3	Real gas . . . . .	33
3.3	EOS of van der Waals . . . . .	34
3.4	Novel real gas EOS . . . . .	35
3.5	Derived quantities of the real gas EOS . . . . .	36
3.5.1	Entropy . . . . .	37
3.5.2	Isobaric and Isochoric Specific Heat . . . . .	38
3.5.3	Total pressure . . . . .	39
3.5.4	Speed of Sound . . . . .	40
3.6	Real-gas EOS for a condensing gas mixture . . . . .	40
<b>4</b>	<b>Numerics</b>	<b>43</b>
4.1	Governing equations in cylindrical coordinates and two dimensions . . . . .	43
4.2	Non-dimensionalisation of the governing equations . . . . .	44
4.3	Numerical Algorithm . . . . .	45
4.4	Finite-volume method . . . . .	45
4.5	Construction of the median dual mesh . . . . .	46
4.6	The convective flux term . . . . .	46
4.6.1	Edge-wise flux computation and distribution . . . . .	46
4.6.2	Flux-vector splitting schemes . . . . .	47
4.6.3	Higher-order fluxes . . . . .	49
4.6.4	Second-order solution reconstruction in a triangle . . . . .	53
4.7	The axi-symmetric source term . . . . .	54
4.8	The condensation source term . . . . .	55
4.9	Time integration . . . . .	55
4.10	Boundary conditions . . . . .	57
4.10.1	Inflow and Outflow Boundaries . . . . .	57
4.10.2	Far-field boundaries . . . . .	62
4.10.3	Solid Walls . . . . .	62
4.11	Solution continuation on subsequent meshes . . . . .	62
<b>5</b>	<b>Validation</b>	<b>65</b>
5.1	NACA 0012 airfoil . . . . .	65
5.1.1	Generation of the unstructured mesh . . . . .	66
5.1.2	Results . . . . .	67
5.2	Parallel-jet nozzle A1 . . . . .	73
5.2.1	Dry flow with shock . . . . .	76
5.2.2	Flow with condensation . . . . .	77
5.2.3	Comparison between fine and coarse mesh wet flow solution . . . . .	80
5.2.4	Comparison with results from literature . . . . .	81
5.2.5	Discussion of the present numerical result . . . . .	83
5.3	Supersonic underexpanded dry jet . . . . .	85
5.3.1	The computational domain . . . . .	87
5.3.2	Boundary conditions . . . . .	87

---

5.3.3	The mesh . . . . .	88
5.3.4	Instabilities occurring in the jet . . . . .	89
5.3.5	Results for pressure ratio 30 . . . . .	90
5.3.6	Results for varying pressure ratio . . . . .	95
<b>6</b>	<b>Condensation of xenon in an underexpanded jet</b>	<b>101</b>
6.1	Introduction . . . . .	101
6.2	Xenon jet without condensation . . . . .	102
6.3	Xenon jet with condensation . . . . .	104
6.4	Influence of maximum liquid fraction on the underexpanded jet . . . . .	107
6.5	Influence of the saturation in the reservoir . . . . .	110
6.6	Conclusion . . . . .	110
<b>7</b>	<b>Condensation in real-gas flows in three dimensions</b>	<b>113</b>
7.1	Hill's method of moments for a multiple component mixture . . . . .	113
7.1.1	Multi-component droplet growth . . . . .	114
7.1.2	Nucleation model . . . . .	116
7.1.3	Closure of Hill's equations . . . . .	116
7.2	Determination of the coefficients of the real-gas EOS . . . . .	116
7.2.1	The weight function . . . . .	119
7.3	3D test-case: The flow of natural gas through a Condi-Cyclone . . . . .	122
7.3.1	Generation of the real-gas EOS parameters . . . . .	123
7.3.2	Flow in the Laval nozzle . . . . .	124
7.3.3	Flow in the vortex generator and deposition section . . . . .	127
<b>8</b>	<b>Concluding remarks</b>	<b>131</b>
	<b>References</b>	<b>133</b>
<b>A</b>	<b>Coordinate transformation</b>	<b>139</b>
A.1	Governing equations in cylindrical coordinates . . . . .	139
A.1.1	Mass conservation equation . . . . .	141
A.1.2	Momentum conservation equation . . . . .	141
A.1.3	Energy conservation equation . . . . .	142
A.1.4	Hill's method of moments . . . . .	142
A.1.5	Axi-symmetric flow without swirl . . . . .	142
<b>B</b>	<b>Mesh-to-mesh interpolation</b>	<b>145</b>
	<b>Summary</b>	<b>151</b>
	<b>Samenvatting</b>	<b>153</b>
	<b>Acknowledgment</b>	<b>155</b>
	<b>Curriculum Vitae</b>	<b>157</b>

---





## 1.1 Background

Perhaps the most familiar and most important substance known to mankind is water. It is present in large quantities in the earth's seas and lakes. Due to the heating of the earth by the sun, the water evaporates and dissolves as a vapour in the air around it, forming a mixture of air and water vapour that forms the earth's troposphere. In the earth's troposphere the temperature decreases with height, about  $6.5\text{ }^{\circ}\text{C}$  per km. Due to the decrease in temperature in an upward motion of the air, or when air strikes along a cold surface, the water vapour condenses on tiny particles like salt, dust and other particles, forming small water droplets. During this phase transition (latent) heat is released which increases the temperature. Depending on the circumstances, these initially small droplets can become large enough to form rain clouds, from which the water droplets then return to the earth under the influence of the earth's gravity field.

The formation of clouds is governed by relatively slow state-changes. During these slow state-changes the air/water mixture is at all times in thermodynamic equilibrium. In technological processes, however, a much more rapid change can occur and condensation takes place at non-equilibrium conditions. The condensation adds heat to the flow, resulting in a complex interaction of the condensation process with the flow. In the picture below, a



FIGURE 1.1:  
*Condensation  
cloud around F-18  
Hornet. U.S. Navy  
photo by Ensign  
John Gay.*

nice example of non-equilibrium condensation in a transonic flow is seen. The water vapour

---

present in the air around the aircraft condenses in the high-speed flow over the jet aircraft (see Campbell and Chambers, [16]).

Another, similar example is the condensation that takes place in the core of tornados (twisters) where the pressure drops to low values. On a somewhat smaller scale we can observe this phenomenon in the strong vortices that are formed at the side edges of extended flaps of transport aircraft during landing. This condensation makes the vortices visible for the passengers. Also, in the early day of high-speed wind-tunnels, condensation in humid air caused an undesired mist-flow in the test section, that in later designs was prevented by drying the air before accelerating and expanding it in the wind tunnel.

In industry, condensation can be an unwanted side-effect, such as is the case for a steam-turbine. The heat released by the condensing water vapour results in performance losses. To prevent or minimize these performance losses, it is important to understand the underlying physics that are relevant in the condensation process. On the other hand, condensation can also be employed in a useful way in industry, for example in the drying of gases and the separation of condensable components from gas mixtures in a Condi-Cyclone.

In a Condi-Cyclone the high-pressure gas or gas mixture is expanded to high speed in a converging-diverging nozzle. This creates a high cooling-rate that results in a high value of the super-saturation. In this non-equilibrium flow, homogeneous nucleation provides a very large number of nuclei, that subsequently grow and exhaust the vapour part of the mixture. In the next step a swirling flow is generated that works as a cyclone for the droplets formed in the nozzle.

A relatively new industrial application in which condensation is an important phenomena is found in Extreme Ultra-Violet (EUV) lithography. In this type of application xenon flows from a reservoir chamber through a nozzle into an ambient environment with relatively low pressure. The jet which is formed in this way is expanding rapidly, causing the xenon to partially condense, resulting in a non-equilibrium mixture of vapour and droplets. A laser is then aimed at the mixture, resulting in the emission of EUV-light.

In the present work, a numerical method is developed that can be used for the numerical simulation of high-speed flows with condensation in complex three-dimensional geometries. The method enables the study of complex physical phenomena in multi-phase dispersed flow, including high-pressure gas dynamics, shock waves and other compressible-flow effects, phase transition and multi-phase flow, and the creation, convection, and transport of vorticity. The method is a finite-volume method for unstructured grids. It has the advantage over a structured-grid method that it can more easily discretize complex geometries, such as highly-swept edges of a vortex generator and solid surfaces intersecting at small angles. In addition, unstructured meshes have the benefit of easy local clustering of nodes in regions with high flow-gradients, which reduces the number of grid points required for a numerical simulation.

## 1.2 Condensation in rapidly expanding flows

During rapid expansion of a condensable gas, for example the flow in a converging-diverging nozzle, the thermodynamic state of the flow may approach the coexistence region between the vapour and liquid phase. When the cooling rate (the time-rate of change of the temperature) in the flow is very high, typically  $10^6 \text{ K/s}$ , the gaseous phase may depart radically from

---

the equilibrium phase distribution. A state of high super-saturation is therefore achieved, indicating the non-equilibrium state of the vapour. Due to the high-cooling rate, the number of small clusters of molecules (nuclei) formed due to statistical fluctuations, far exceeds the number of foreign particles present in the vapour. Therefore the phase-transition is preceded by homogeneous nucleation. When the small clusters exceed some critical size, the clusters are stable and rapidly grow into droplets, growing in size until equilibrium is re-established.

Condensation in flows of gas mixtures at high speed has been investigated by, amongst others, Hill [31], Wegener [67], the group of prof. Schnerr in Germany: Dohrmann [23], Mundinger [46], Adam [3], Heiler [29], Winkler [69], and the group of prof. van Dongen in the Netherlands: Luijten [42], Luijten et al. [44] [45], Prast [52], Lamanna [38], Peeters [50]. Most of their numerical results, however, are restricted to the condensation of water in a non-condensing background or of the condensation of pure water-vapour, all at relatively low pressures.

### 1.3 Thesis overview

In this thesis Computational Fluid Dynamics (CFD) is used as a tool to develop a method to predict high-pressure high-speed flows with condensation expanding to low pressures at low temperatures. The computational method is based on the Euler equations, describing the flow of an inviscid fluid, augmented with Hill's method of moments, describing the condensation process. In this study we assume the flow to be steady. The underlying physics of inviscid flow with condensation is described in chapter 2, together with the governing equations and relations, required to describe quantities such as surface tension, liquid density and equilibrium vapour pressure. In chapter 3 a novel equation of state for real gases is derived, which can be used to describe the relations between thermodynamic properties of a gas mixture at high pressure. The relations are constructed such that they satisfy Maxwell's fundamental thermodynamic relationships.

In chapter 4 the numerical method is presented, which solves the governing equations on an unstructured mesh. Most of the applications in the present study are for two-dimensional or for axi-symmetric flows, for which an unstructured mesh consisting of triangles is employed. In the method for three-dimensional geometries the unstructured mesh consists of tetrahedra. The method is an unstructured-grid finite-volume method employing the AUSM<sup>+</sup> scheme of Liou [41], second-order accurate fluxes, and fractional time-stepping to cope with the strong source terms due to the condensation.

Chapter 5 is dedicated to the validation of the numerical method by comparing numerical results with numerical results available in literature, as well as available experimental results. The test-cases presented are a benchmark 2D test-case for the solution of the Euler equations applied to the transonic flow around a NACA 0012 airfoil, nozzle flows considered experimentally and numerically by the group of prof. Schnerr, and the underexpanded supersonic jet from a reservoir.

Chapter 6 contains results of the computational method for underexpanded xenon-jets with condensation, as designed by the FOM-Institute for Plasma Physics <sup>1</sup> (de Bruijn et al. [14] [15]) for the generation of EUV light. Chapter 7 describes results that were obtained with the 3D method for a condensing multiple-component gas mixture at high pressure as occurs

---

<sup>1</sup><http://www.rijnh.nl/>

in the Condi-Cyclone configurations developed by Twister B.V.<sup>2</sup>. Chapter 8 contains the conclusions of the present study.

<sup>2</sup><http://www.twisterbv.com/>

---

## 2.1 Introduction

A (pure) substance can take three different forms: vapour (gas), liquid and solid. The behavior of a substance can best be described in a three-dimensional graph, see Wisman [70]. Along the axis we place the pressure  $p$ , the volume  $v$  and the temperature  $T$ . In doing so, we obtain Fig. 2.1; marked in this figure are the regions (surfaces) where two phases exist si-

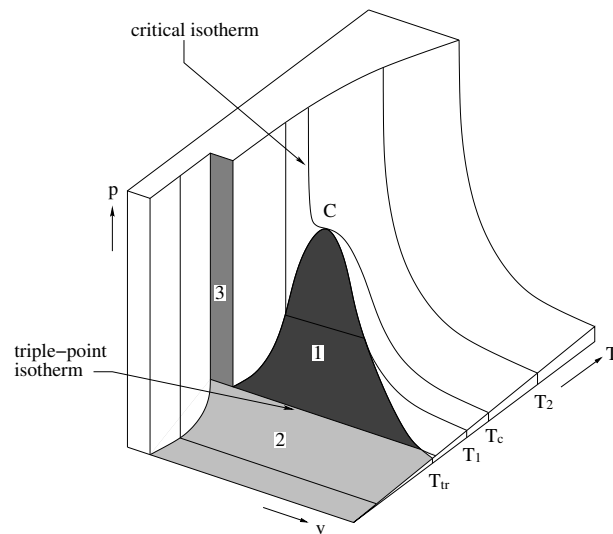


FIGURE 2.1:  $p, v, T$ -diagram of a pure substance (not on scale). 1) liquid+vapour; 2) solid+liquid; 3) solid+vapour. Figure obtained from Wisman [70].

multaneously. Such-like regions are called *coexistence regions*. Two important isotherms are drawn in Fig. 2.1, the *triple-point* isotherm and the *critical* isotherm. The triple-point temperature is the temperature where gas, liquid and solid phase exist simultaneously. Everywhere along the triple-point isotherm there is equilibrium between the three phases, only the relative amounts of the phases are different. A familiar triple-point temperature is that of water,

---

which is 273.15 K. As this temperature can be maintained very accurately and relatively easy, it is used as gauge for the temperature scale.

At higher temperatures, the vapour-liquid coexistence region on the isotherm becomes shorter, as is evident from comparing isotherms  $T_1$  and  $T_{tr}$ . Isotherm  $T_c$  is the last isotherm to have a horizontal point of inflection C. This point C is called the *critical point*; the temperature  $T_c$  the *critical temperature*. For temperatures higher than  $T_c$  there is no observable difference between gas and liquid, although densities can be reached that correspond to liquid densities. At first gases were attempted to liquefy by compression at room temperature [70]. In the 19th century Faraday <sup>1</sup> succeeded in liquefying many gases. However, before the notion of the critical temperature was first recognized by C. Cagniard de la Tour <sup>2</sup> in 1822, further attempts to liquefy gases by compression were doomed to fail. Gases like O<sub>2</sub>, N<sub>2</sub>, H<sub>2</sub> and He were therefore thought to be “permanent gases”. Looking at their critical temperature (table 2.1), this is quite understandable. Nevertheless, by reducing the temperature

gas	O <sub>2</sub>	N <sub>2</sub>	H <sub>2</sub>	He
critical temperature (K)	154.4	126.2	33.3	5.26

TABLE 2.1: Critical temperature of “permanent gases”, obtained from Bird et al. [12]

below the critical temperature, these gases could also be compressed into liquid form. In 1877 Cailletet <sup>3</sup> and Pictet <sup>4</sup> both succeeded in liquefying air (per unit volume, air contains approximately 78.084% N<sub>2</sub> and 20.947% O<sub>2</sub> ). In 1898 Dewar <sup>5</sup> liquefied hydrogen, and in 1908 Kamerlingh Onnes <sup>6</sup> liquefied helium, the last element to change phase from gas to liquid.

## 2.2 Condensation

### 2.2.1 Condensation during rapid expansion

A three dimensional diagram like Fig. 2.1 is useful to consider the matter as a whole, but unsuited for practical use. Then we use two-dimensional diagrams, which are obtained from the three-dimensional diagram by projection onto one of the three bounding surfaces. Projection onto the  $p, T$  surface gives the  $p, T$ -diagram, as is shown in Fig. 2.2. Three phase-curves are present in this graph; the vapour-curve (I), denoting the equilibrium between the gas and liquid phase; the melting-curve (II), denoting the equilibrium between the liquid and solid phase and the sublimation-curve (III), denoting the equilibrium between solid and gas phase.

In a slowly varying flow field the thermodynamic state changes continually from one thermodynamic equilibrium to another thermodynamic equilibrium. However, during rapid expansion of a vapour in, for example, a converging-diverging nozzle, its thermodynamic state can become such that it is far from the equilibrium state, which would be attained during slow

<sup>1</sup>Michael Faraday (Great-Britain)(1791-1867)

<sup>2</sup>Charles Cagniard de la Tour (France)(1777-1859)

<sup>3</sup>Louis Paul Cailletet (France)(1832-1913)

<sup>4</sup>Raoult Pierre Pictet (Switzerland)(1846-1929)

<sup>5</sup>Sir James Dewar (Great-Britain)(1842-1923)

<sup>6</sup>Heike Kamerlingh Onnes (the Netherlands)(1853-1926) Nobel price 1913

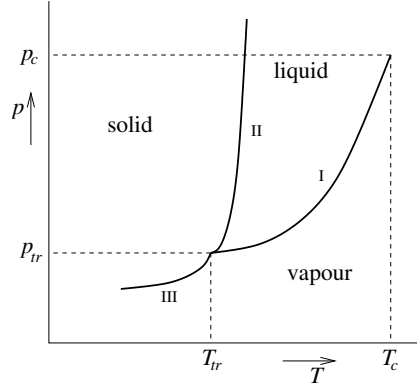


FIGURE 2.2:  $p, T$ -diagram with the phase-curves between the phases. I) vapour-curve ( $p_{v,eq}(T)$ ); II) melting-curve; III) sublimation-curve. Figure obtained from Wisman [70].

expansion. In such case the characteristic time-scale for condensation (i.e. the time needed to form droplets) is larger than the characteristic time-scale of the expansion. The condensation is said to take place under non-equilibrium conditions, where the extent of non-equilibrium is usually expressed in terms of the saturation ratio  $\Phi$ , defined as the ratio of the actual vapour pressure  $p_v$  to the equilibrium vapour pressure  $p_{v,eq}(T)$ :

$$\Phi = \frac{p_v}{p_{v,eq}(T)}, \quad (2.1)$$

and in case  $\Phi > 1$ , it is called the super saturation ratio. The first stage of condensation is called nucleation, and embodies the condensation of vapour molecules on foreign bodies, such as dust particles or other liquid or solid objects (heterogeneous nucleation), or the spontaneous formation of vapour clusters (homogeneous nucleation). In case of rapid expansion, the number of nuclei formed in homogeneous nucleation far exceeds the number of particles involved in heterogeneous nucleation, so that the onset of condensation is solely described by *homogeneous nucleation*. The condition of non-equilibrium persists until the vapour is sufficiently super-saturated to reduce the nucleation barrier at which point nucleation begins. The second stage of condensation is called droplet-growth, the condensation of vapour molecules on stable vapour clusters. During this stage of condensation thermodynamic equilibrium is quickly re-established and prevails thereafter. Due to the formation (latent) heat and the transfer of this heat between the clusters and the vapour there is a heat effect of the condensation imposed on the gas flow. This increases the pressure and the temperature of the gas-liquid mixture. Also, the heat addition decreases the Mach number in case the flow is supersonic, and increases the Mach number in case the flow is subsonic. The increase in temperature resulting from condensation also has the effect of slowing the growth-rate of the droplets which limits their size.

### 2.2.2 Homogeneous nucleation

Homogeneous nucleation involves the formation of meta-stable clusters, from a population of vapour molecules in a super-saturated state, which are big enough to act as condensation

nuclei. The formation of nuclei is the first step towards the formation of liquid droplets. The driving potential behind any nucleation theory is the super-saturation ratio, given by Eq. (2.1).

The free energy of formation of a cluster containing  $n$  molecules can be expressed, on thermodynamic principles, see Luijten [42], as the sum of two terms

$$\Delta G_n = \sigma a_0 n^{2/3} - n k_B T \ln(\Phi), \quad (2.2)$$

where  $k_B$  is the Boltzmann constant, the number that relates the average energy of a molecule to its absolute temperature ( $k_B = 1.38066 \times 10^{-23}$  J/K),  $\sigma$  the surface tension of a flat liquid surface, and  $a_0$  is a molecular surface area, defined as

$$a_0 = (36\pi)^{1/3} (v_l)^{2/3}, \quad (2.3)$$

with  $v_l$  [m<sup>3</sup>/cluster] the liquid molecular volume. The first term in Eq. (2.2) represents the increase in free energy due to the formation of the interface between the two phases, and the second term represents the decrease in free energy due to the formation of the liquid bulk phase. As we can see, for  $\Phi < 1$ ,  $\Delta G_n$  increases monotonically with  $n$ , thus lowering the probability of phase transition to zero. If  $\Phi > 1$  on the other hand, there will always be a value of  $n$  for which it is energetically favorable to initiate the phase transition. This critical cluster value  $n^*$  is found by setting  $(\partial \Delta G_n / \partial n)_{n^*} = 0$ , resulting in

$$n^* = \left( \frac{2\theta}{3 \ln(\Phi)} \right)^3, \quad (2.4)$$

where  $\theta$  is the dimensionless surface tension, defined by

$$\theta = \frac{\sigma a_0}{k_B T}. \quad (2.5)$$

The free energy of formation  $\Delta G_n$  of a cluster as a function of the number of molecules  $n$  in that cluster (for  $\Phi > 1$ ) is sketched in Fig. 2.3.

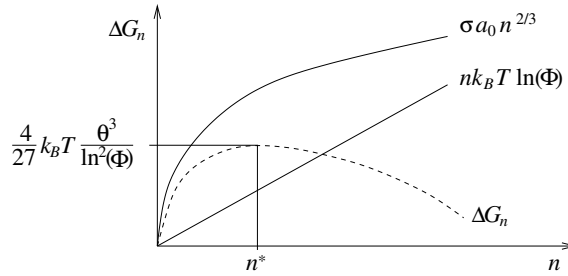


FIGURE 2.3: Free energy of formation of a cluster containing  $n$  molecules in case  $\Phi > 1$ .

Using the definitions of both  $a_0$  and  $\theta$  and using  $n^* v_l = \frac{4}{3} \pi r^{*3}$  we obtain the *Kelvin relation*:

$$r^* = \frac{2\sigma}{\varrho_l R_v T \ln(\Phi)}, \quad (2.6)$$



with  $R_v$  the specific gas constant of the vapour and  $\varrho_l$  the condensate density. The Kelvin relation gives an expression for the critical radius, the smallest radius of a meta-stable cluster of vapour molecules in a super-saturated state, which is in stable equilibrium with its surroundings. Only droplets which have reached the critical radius will be able to grow further. Smaller droplets are unstable and will disintegrate. Note that the following relations were used in deriving the Kelvin relation:  $v_l = \frac{\mathcal{M}}{N_A \varrho_l}$  with  $\mathcal{M}$  the molar mass; the specific gas constant follows from  $R = \frac{\mathcal{R}}{\mathcal{M}}$ ; the universal gas-constant is given by  $\mathcal{R} = k_B N_A = 8314.51$  J/(kg·mol·K), where  $N_A$  is the number of vapour atoms in a mole (Avogadro's number, which for a kg-mole is  $6.02 \times 10^{26}$ , see Bird et al. [12]).

### 2.2.3 Classical nucleation theory

According to the *Classical Nucleation Theory*, which has been widely applied to the study of transonic condensing flows, the nucleation rate  $J$  [number of nuclei / (m<sup>3</sup>·s)] takes the form

$$J = K e^{\frac{-\Delta G_{n^*}}{k_B T}}, \quad (2.7)$$

where  $\Delta G_{n^*}$  is the free energy of formation of a cluster with critical radius

$$\Delta G_{n^*} = \frac{4}{3} \pi r^{*2} \sigma, \quad (2.8)$$

and  $K$  is a constant. The nucleation models presented here are the *Classical Nucleation Theory* (CNT) and the *Internally Consistent Classical Theory* (ICCT), given by:

$$J_{\text{CNT}} = \frac{\rho_v^2}{\varrho_l} \sqrt{\frac{2\sigma}{\pi m^3}} e^{-\frac{4}{27} \frac{\theta^3}{\ln^2(\Phi)}}, \quad (2.9)$$

$$J_{\text{ICCT}} = \frac{1}{\Phi} J_{\text{CNT}} e^{\theta}, \quad (2.10)$$

respectively, where  $\rho_v$  is the vapour density and  $m$  the mass of a vapour molecule. The ICCT model thus differs essentially from the CNT model, by the presence of the factor  $1/\Phi$ , and the exponential factor  $e^{\theta}$ . Both nucleation models are described and discussed in Luijten [42] and Lamanna [38]. In short, the performance of a certain nucleation model strongly depends on the vapour and on the temperature range within which nucleation takes place. It is also very difficult if not impossible to determine the surface tension of a super-cooled liquid (with temperature below the freezing point), and since the nucleation rate depends exponentially on the third power of the surface tension, this makes the assessment of the quality of nucleation models very questionable. Therefore, no sound justification for preferring the ICCT to the CNT model can be given, also since comparison with experiments shows that both models predict the nucleation rate not very accurately, and an empirical correction factor  $\xi$  has to be applied for both models, e.g.  $J_{\text{CNT}}^{\xi} = \xi J_{\text{CNT}}$ , to compensate for the wrong prediction. Experimental validation (if available) of nucleation theory will then indicate the value for the empirical correction factor that leads to satisfactory prediction of the nucleation rate.

### 2.2.4 Droplet growth

Droplet growth is described by the droplet growth rate,  $\dot{r}$ , and involves the net flux of mass towards the droplet and the net flux of energy away from the droplet. This process depends to

a large extent on the Knudsen number  $Kn$ . The latter is defined as the ratio of the mean free path of vapour molecules to the diameter of the droplet,  $Kn = l/(2r_d)$ , where the mean free path is given by  $l = 2\mu\sqrt{RT}/p$ , with  $\mu$  the dynamic viscosity of the gas-phase. For small  $Kn$ , i.e. relatively large droplets, the growth is governed by diffusion; for large  $Kn$ , i.e. small droplets, the growth is controlled by the kinetic process of impingement of vapour molecules onto the droplet.

The droplet-growth model described here is the well-known Hertz-Knudsen growth law for small droplets, see Hill [31], valid for  $Kn > 2$ .

### Hertz-Knudsen droplet growth model

The Hertz-Knudsen growth law is based on a balance between condensation of vapour molecules on the droplet, and evaporation of vapour molecules from the droplet:

$$\dot{r} = \frac{\alpha}{\varrho_l} \left( \frac{p_v}{\sqrt{2\pi R_v T}} - \frac{p_{v,r}}{\sqrt{2\pi R_v T_d}} \right), \quad (2.11)$$

where  $T_d$  is the droplet temperature,  $\alpha$  an accommodation coefficient usually taken equal to 1.0, and  $p_{v,r}$  is the partial super-saturated vapour pressure above a curved surface with radius of curvature  $r$ ,

$$p_{v,r} = p_{v,eq} e^{\frac{2\sigma}{r\varrho_l R_v T_d}}, \quad (2.12)$$

where  $r$  is the droplet radius. In the current work it is assumed that the temperature of the droplets is equal to that of the surrounding gas,  $T_d = T$ . The validity of this assumption depends to a large extent on the latent heat (heat of formation) of the vapour. For water, this assumption can be rather crude, especially in rapid expanding flows, in which droplets grow fast and have little time to conduct their heat to the surrounding gas. A way to account for the difference between the temperature of the droplet and the surrounding gas is given in Lamanna [38].

For xenon, which has a latent heat which is about 32 times smaller than that of water, the assumption of equal droplet and gas temperature is relatively sound.

## 2.3 Governing equations

The Euler equations, augmented with Hill's Method of Moments, have been successfully applied to numerically simulate rapidly expanding condensing flows, among others Munding [46], Adam [3], Prast [52], Lamanna [38]. Comparison between numerical solutions and results of experiments for these types of flow show that viscous effects are negligible and do not need to be included in the governing equations.

In the flow of highly underexpanded jets, viscous effects play an important role in that they control the dynamics of the Kelvin-Helmholtz instability of the contact surface (edge of the plume) and of the slip surface downstream of the Mach disk, see Prudhomme and Haj-Hariri [53]. In the numerical solution of the Euler equations the Kelvin Helmholtz instability and subsequent roll-up is governed by numerical effects. Solving the Navier-Stokes equations instead of the Euler equations, however, leads to several complications. At solid walls, the flow is no longer allowed to slip, as is the case for the Euler equations, but will

---

have zero velocity. This will introduce boundary layers, which will make the computational method much more elaborate since a large number of control volumes is needed to resolve the boundary layer accurately. Furthermore, depending on the flow characteristics, boundary layers can change from laminar to turbulent, which is not only a very complex process, but, with the computational resources at hand, it is also not feasible to resolve all the turbulent length scales.

Since the region downstream of the Mach disk, where viscous effects do play an important role, is not of interest for the current research, in the present study the Euler equations are used to describe the flow of an underexpanded jet.

For the flow of a gas of fixed composition, the Euler equations can be written in vector differential form using index notation:

$$\frac{\partial \mathbf{U}}{\partial t} + \frac{\partial}{\partial x_j} \{\mathbf{F}_j(\mathbf{U})\} = 0, \quad (2.13)$$

where  $\mathbf{U}$  denotes the vector of conservative variables:

$$(\mathbf{U})^T = (\rho, \rho u_1, \rho u_2, \rho u_3, \rho e_t)^T, \quad (2.14)$$

and  $\mathbf{F}$  denotes the vector of the convective fluxes:

$$(\mathbf{F}_j(\mathbf{U}))^T = (F_j^{(1)}, F_j^{(2)}, F_j^{(3)}, F_j^{(4)}, F_j^{(5)})^T, \quad (2.15)$$

with

$$\begin{aligned} F_j^{(1)}(\mathbf{U}) &= \rho u_j, \\ F_j^{(i+1)}(\mathbf{U}) &= \rho u_i u_j + \delta_{ij} p, \quad i = 1, 2, 3 \\ F_j^{(5)}(\mathbf{U}) &= \rho u_j h_t. \end{aligned} \quad (2.16)$$

The specific total energy  $e_t$  is the sum of the specific internal energy  $e$  and the specific kinetic energy  $\frac{1}{2} u_i u_i$ :

$$e_t = e + \frac{1}{2} u_i u_i. \quad (2.17)$$

The specific total enthalpy  $h_t$  is given by:

$$h_t = e_t + p/\rho. \quad (2.18)$$

The Euler equations have to be supplemented by the equations of state, which relate all the thermodynamic quantities to two independent thermodynamical quantities, e.g.  $p = p(\rho, T)$  and  $e = e(\rho, T)$ .

### 2.3.1 Gas-liquid mixtures

Consider an infinitesimally small volume  $V$  large enough to contain a considerable number of droplets. The total mass  $M$  in  $V$  of a mixture consisting of an inert gas and a vapour (e.g. an air/water mixture), where inert means that this gas is assumed not to condensate, is given by the sum of the mass of the inert gas  $M_a$ , the mass of the vapour  $M_v$  and the mass of the condensate  $M_l$

---

$$M = M_a + M_v + M_l, \quad (2.19)$$

where the sum of the mass of the vapour and the mass of the condensate is constant and equal to  $M_{v0}$ ,

$$M_{v0} = M_v + M_l. \quad (2.20)$$

The ratio between the mass of the liquid phase and the total mass is called the liquid mass fraction  $g$

$$g \equiv \frac{M_l}{M}, \quad 0 \leq g \leq g_{max}. \quad (2.21)$$

The maximum value of the liquid mass fraction is reached when all vapour is condensed,

$$g_{max} = \frac{M_{v0}}{M}. \quad (2.22)$$

The density of the mixture in the control volume  $V$  is defined by

$$\rho \equiv \frac{M}{V}, \quad (2.23)$$

so that the density of the inert gas and the vapour follow as

$$\rho_a = \frac{M_a}{V} = (1 - g_{max})\rho, \quad (2.24-a)$$

$$\rho_v = \frac{M_v}{V} = (g_{max} - g)\rho. \quad (2.24-b)$$

In the same way we find an expression for the density of the liquid  $\rho_l$  (note that this is *not* the condensate density  $\varrho_l$ , which is a material property)

$$\rho_l = \frac{M_l}{V} = g\rho. \quad (2.25)$$

With Eqs. (2.24-b) and (2.25) we can express the maximum liquid mass fraction given by Eq. (2.22) as

$$g_{max} = \frac{\rho_{v0}}{\rho}, \quad (2.26)$$

with  $\rho_{v0}$  the sum of the density  $\rho_v$  of the vapour and the density  $\rho_l$  of the liquid,

$$\rho_{v0} = \rho_v + \rho_l. \quad (2.27)$$


---

### 2.3.2 Mass conservation for the mixture

The mass conservation equation, which is the first equation in (2.13), is applied to each component separately. With  $\vec{u}$  the velocity of the inert gas and the vapour, we have

$$\frac{\partial \rho_a}{\partial t} + \frac{\partial}{\partial x_j} (\rho_a u_j) = 0, \quad (2.28)$$

$$\frac{\partial \rho_{v0}}{\partial t} + \frac{\partial}{\partial x_j} (\rho_{v0} u_j) = 0. \quad (2.29)$$

Note that Eqs. (2.28) and (2.29) are only valid if both the vapour and the liquid are transported with  $\vec{u}$ , i.e. we assume that there is *no slip* between the gas/vapour- and the liquid-phase. By substituting Eq. (2.26) in Eq. (2.29), the mass conservation equation for the vapour and the liquid can be written in the following way:

$$\frac{\partial}{\partial t} (\rho g_{max}) + \frac{\partial}{\partial x_j} (\rho g_{max} u_j) = 0. \quad (2.30)$$

Rearranging terms, Eq. (2.30) can be written as

$$g_{max} \left\{ \frac{\partial \rho}{\partial t} + \frac{\partial}{\partial x_j} (\rho u_j) \right\} + \rho \left\{ \frac{\partial}{\partial t} (g_{max}) + u_j \frac{\partial}{\partial x_j} (g_{max}) \right\} = 0. \quad (2.31)$$

The first term between brackets represents the mass conservation equation of the mixture, and is therefore equal to zero. Since  $\rho \neq 0$  we also have

$$\frac{\partial}{\partial t} (g_{max}) + u_j \frac{\partial}{\partial x_j} (g_{max}) = 0, \quad (2.32)$$

which can be written as

$$\frac{D}{Dt} (g_{max}) = 0. \quad (2.33)$$

Hence,  $g_{max}$  is constant along path-lines. From (2.33) we can derive an important conclusion: if  $g_{max}$  is uniform at inflow boundaries, then  $g_{max}$  is uniform over the flow domain, and can thus be regarded as a global constant.

By substituting Eq. (2.27) in Eq. (2.29), the mass conservation equation for the vapour and the liquid can also be written in the following way

$$\frac{\partial \rho_v}{\partial t} + \frac{\partial}{\partial x_j} (\rho_v u_j) + \frac{\partial \rho_l}{\partial t} + \frac{\partial}{\partial x_j} (\rho_l u_j) = 0, \quad (2.34)$$

or, with Eq. (2.25),

$$\frac{\partial \rho g}{\partial t} + \frac{\partial}{\partial x_j} (\rho g u_j) = b, \quad (2.35-a)$$

$$\frac{\partial \rho_v}{\partial t} + \frac{\partial}{\partial x_j} (\rho_v u_j) = -b, \quad (2.35-b)$$


---

where  $b$  represents a phase-transition source term. The mass conservation equation for the vapour, Eq. (2.35-b), can be replaced by Eq. (2.24-b).

The set of mass conservation equations for the mixture is now

$$\begin{cases} \frac{\partial \rho}{\partial t} + \frac{\partial}{\partial x_j}(\rho u_j) = 0, \\ \frac{\partial \rho g}{\partial t} + \frac{\partial}{\partial x_j}(\rho g u_j) = b. \end{cases}$$

The set of equations consists of the mass conservation equation for the mixture and a conservation equation for the liquid mass fraction. However, the right-hand side,  $b$ , representing a phase-transition source term, is as yet unknown. A set of equations describing the condensation process, including Eq. (2.35-a), is derived in the next section.

### 2.3.3 Description of the liquid phase

The General Dynamic Equation (GDE) describes, in absence of coagulation and segregation, the conservation of droplets in phase-space  $(\vec{x}, r)$ , where  $r$  is the radius of a droplet. The GDE reads, see e.g. Seinfeld [59], or Williams & Loyalka [68]:

$$\frac{\partial f}{\partial t} + \frac{\partial}{\partial r}(\dot{r}f) + \frac{\partial}{\partial x_j}(f u_j) = \delta(r - r^*)J, \quad (2.36)$$

where  $\delta$  is the Dirac delta function,  $J$  is the nucleation rate, and  $f$  is the distribution function, defined as the radial derivative of the droplet number density  $n(r, \vec{x}, t)$ ; the number of droplets with radius smaller than  $r$ , per unit volume:

$$f(r, \vec{x}, t) \equiv \frac{\partial n(r, \vec{x}, t)}{\partial r}, \quad (2.37)$$

so that

$$n(r, \vec{x}, t) = \int_0^r f(r, \vec{x}, t) dr. \quad (2.38)$$

For notation shortness, the independent variables in  $f$  and  $r$  are omitted hereafter.

Integrating the product of  $r^k$  and the GDE over  $r$  gives:

$$\frac{\partial}{\partial t} \int_0^\infty r^k f dr + \int_0^\infty r^k \frac{\partial}{\partial r}(\dot{r}f) dr + \frac{\partial}{\partial x_j} \left( \int_0^\infty r^k f dr u_j \right) = \int_0^\infty r^k \delta(r - r^*) dr J. \quad (2.39)$$

By introducing the  $k$ -th moment of the distribution function

$$\mu_k \equiv \int_0^\infty r^k f dr, \quad k = 0, 1, \dots \quad (2.40)$$

we can write

---

$$\frac{\partial \mu_k}{\partial t} + \frac{\partial}{\partial x_j}(\mu_k u_j) = r^{*k} J - \int_0^\infty r^k \frac{\partial}{\partial r}(\dot{r} f) dr. \quad (2.41)$$

The integral can be worked out as:

$$\int_0^\infty r^k \frac{\partial}{\partial r}(\dot{r} f) dr = r^k \dot{r} f \Big|_0^\infty - k \int_0^\infty r^{k-1} \dot{r} f dr. \quad (2.42)$$

The first term on the right hand side is equal to zero since there are no droplets with infinite radius. To be able to take the droplet growth rate  $\dot{r}$  out of the integral, Hill [31] introduced an averaged droplet radius:

$$r_H = \sqrt{\frac{\mu_2}{\mu_0}}, \quad (2.43)$$

so that the droplet growth rate no longer depends on the droplets radius  $r$ , but on the “Hill” radius  $r_H$ ,  $\dot{r} = \dot{r}(r_H, \vec{x}, t)$ . Eq. (2.42) becomes:

$$\int_0^\infty r^k \frac{\partial}{\partial r}(\dot{r} f) dr = -k \dot{r} \int_0^\infty r^{k-1} f dr = -k \dot{r} \mu_{k-1}. \quad (2.44)$$

Finally, Eq. (2.41) becomes

$$\frac{\partial \mu_k}{\partial t} + \frac{\partial}{\partial x_j}(\mu_k u_j) = r^{*k} J + k \dot{r} \mu_{k-1}. \quad (2.45)$$

This is a recurrent relation for  $\mu_k$ , and for  $k = 0, \dots, 3$  we find the following closed set of equations:

$$k = 0 : \frac{\partial \mu_0}{\partial t} + \frac{\partial \mu_0 u_j}{\partial x_j} = J, \quad (2.46-a)$$

$$k = 1 : \frac{\partial \mu_1}{\partial t} + \frac{\partial \mu_1 u_j}{\partial x_j} = r^* J + \dot{r} \mu_0, \quad (2.46-b)$$

$$k = 2 : \frac{\partial \mu_2}{\partial t} + \frac{\partial \mu_2 u_j}{\partial x_j} = r^{*2} J + 2 \dot{r} \mu_1, \quad (2.46-c)$$

$$k = 3 : \frac{\partial \mu_3}{\partial t} + \frac{\partial \mu_3 u_j}{\partial x_j} = r^{*3} J + 3 \dot{r} \mu_2. \quad (2.46-d)$$

By introducing the following identity

$$\mu_k \equiv \rho Q_k, \quad (2.47)$$

with  $Q_k$  the so called liquid moments, the following set of equations results:

---

$$\frac{\partial \rho Q_0}{\partial t} + \frac{\partial \rho Q_0 u_j}{\partial x_j} = J, \quad (2.48-a)$$

$$\frac{\partial \rho Q_1}{\partial t} + \frac{\partial \rho Q_1 u_j}{\partial x_j} = r^* J + \dot{r} \rho Q_0, \quad (2.48-b)$$

$$\frac{\partial \rho Q_2}{\partial t} + \frac{\partial \rho Q_2 u_j}{\partial x_j} = r^{*2} J + 2\dot{r} \rho Q_1, \quad (2.48-c)$$

$$\frac{\partial \rho Q_3}{\partial t} + \frac{\partial \rho Q_3 u_j}{\partial x_j} = r^{*3} J + 3\dot{r} \rho Q_2. \quad (2.48-d)$$

The liquid density  $\rho_l$ , expressed in terms of the distribution function, follows from

$$\rho_l = \int_0^\infty \frac{4}{3} \pi \varrho_l r^3 f dr. \quad (2.49)$$

If we assume that the condensate density  $\varrho_l$  (which is a material property) is constant, then we have from Eqs. (2.40) and (2.49)

$$\rho_l = \frac{4}{3} \pi \varrho_l \int_0^\infty r^3 f dr = \frac{4}{3} \pi \varrho_l \mu_3, \quad (2.50)$$

and with Eqs. (2.25) and (2.47) we find

$$g = \frac{4}{3} \pi \varrho_l Q_3. \quad (2.51)$$

Eq. (2.48-d) can now be written in terms of the liquid mass fraction  $g$ , and with this we arrive at the four equations known as “Hill’s Method of Moments”:

$$\frac{\partial \rho Q_0}{\partial t} + \frac{\partial \rho Q_0 u_j}{\partial x_j} = J, \quad (2.52-a)$$

$$\frac{\partial \rho Q_1}{\partial t} + \frac{\partial \rho Q_1 u_j}{\partial x_j} = r^* J + \dot{r} \rho Q_0, \quad (2.52-b)$$

$$\frac{\partial \rho Q_2}{\partial t} + \frac{\partial \rho Q_2 u_j}{\partial x_j} = r^{*2} J + 2\dot{r} \rho Q_1, \quad (2.52-c)$$

$$\frac{\partial \rho g}{\partial t} + \frac{\partial \rho g u_j}{\partial x_j} = \frac{4}{3} \pi \varrho_l (r^{*3} J + 3\dot{r} \rho Q_2). \quad (2.52-d)$$

Hill’s average droplet radius follows from the liquid moments  $Q_k$  by substitution of Eq.(2.47) in Eq. (2.43), resulting in

$$r_H = \sqrt{\frac{Q_2}{Q_0}}. \quad (2.53)$$

In summary, in order to arrive at Hill’s Method of Moments as a closed set of PDE’s for the liquid mass fraction we had to assume:

---



- (i) no slip between the gas/vapour phase and the liquid phase,
- (ii) droplet growth rate  $\dot{r}$  independent of droplet radius,
- (iii) condensate density  $\varrho_l$  constant.

Assumption (i) implies that the droplets remain small, i.e. that the “Langmuir” parameter, that appears as dimensionless parameter in the differential equation for the trajectory of a droplet subject to Stokes’ drag force, should be large. The Langmuir parameter is

$$K = \frac{2}{9} \frac{1}{Re_{ref}} \frac{\rho_v}{\varrho_l} \left( \frac{r}{L_{ref}} \right)^{-2}, \quad (2.54)$$

with  $Re_{ref} = (U_{ref} L_{ref})/\nu_v$  and  $U_{ref}$  and  $L_{ref}$  a global velocity and length scale, respectively, and  $\nu_v$  the kinematic viscosity of the vapour. Assumption (ii) is essential for the closure of Hill’s derivation. The droplet radius appears in the denominator of the exponential power in Eq. (2.12), and for large enough droplets,  $\dot{r}$  is indeed nearly independent of  $r$ . As far as assumption (iii) is concerned, it can be shown that in case  $\varrho_l$  is *not* constant the PDE for  $g$  remains the same, but those for  $Q_0$ ,  $Q_1$ ,  $Q_2$  change slightly. This is not considered further in the present study.

### 2.3.4 Alternative derivation of Hill’s Method of Moments

As an alternative, Hill’s Method of Moments can also be derived from the following expression for the liquid mass fraction  $g$  (Oswatitsch [49], Hill [31]):

$$g(t) = \int_0^t \frac{4}{3} \pi \varrho_l(t) r^3(t, \tau) \frac{J(\tau)}{\rho(\tau)} d\tau. \quad (2.55)$$

In contrast to the previous section, this expression is based on physical intuition instead of definition in terms of the third moment. It is noted that the above expression is valid under the assumption that there are no droplets at  $t = 0$ , and that there is no coagulation or segregation. When the time dependence of the liquid density  $\varrho_l$  is neglected, the time derivative of  $g$  follows from Eq. (2.55) as

$$\frac{dg}{dt} = \frac{4}{3} \pi \varrho_l r^{*3} \frac{J(t)}{\rho(t)} + 4 \pi \varrho_l \int_0^t \frac{J(\tau)}{\rho(\tau)} \dot{r} r^2(t, \tau) d\tau. \quad (2.56)$$

Introducing, as before in section 2.3.3, the Hill radius  $r_H$ , the droplet-growth rate  $\dot{r}$  can be taken outside the integral. With the auxiliary variables:

$$Q_2 = \int_0^t r^2(t, \tau) \frac{J(\tau)}{\rho(\tau)} d\tau, \quad (2.57-a)$$

$$Q_1 = \int_0^t r(t, \tau) \frac{J(\tau)}{\rho(\tau)} d\tau, \quad (2.57-b)$$

$$Q_0 = \int_0^t \frac{J(\tau)}{\rho(\tau)} d\tau, \quad (2.57-c)$$

$$r_H = \sqrt{\frac{Q_2}{Q_0}}, \quad (2.57-d)$$

the following system is obtained

$$\frac{\partial \rho Q_0}{\partial t} + \frac{\partial \rho Q_0 u_j}{\partial x_j} = J, \quad (2.58-a)$$

$$\frac{\partial \rho Q_1}{\partial t} + \frac{\partial \rho Q_1 u_j}{\partial x_j} = r^* J + \dot{r} \rho Q_0, \quad (2.58-b)$$

$$\frac{\partial \rho Q_2}{\partial t} + \frac{\partial \rho Q_2 u_j}{\partial x_j} = r^{*2} J + 2\dot{r} \rho Q_1, \quad (2.58-c)$$

$$\frac{\partial \rho g}{\partial t} + \frac{\partial \rho g u_j}{\partial x_j} = \frac{4}{3} \pi \varrho_l (r^{*3} J + 3\dot{r} \rho Q_2). \quad (2.58-d)$$

The expressions for the liquid moments here are represented as integrals in time, while in section 2.3.3 they are defined as integrals over the droplets radius. Hagmeijer [27] has shown that the two different integral representations are equivalent, and consistent with the GDE. Therefore, Eqs. (2.58-a)-(2.58-d) are identical to Eqs. (2.52-a)-(2.52-d).

### 2.3.5 Alternative approximate closure using two moment equations

Apart from Hill's Method of Moments, consisting of four differential equations, an alternative approximate closure, consisting of two moment equations, exists in literature, see e.g. Heiler [29]. In this method, the differential equation for the number of particles per unit mass  $Q_0$  and that for the liquid mass fraction  $g$  are:

$$\frac{\partial \rho Q_0}{\partial t} + \frac{\partial \rho Q_0 u_j}{\partial x_j} = J, \quad (2.59-a)$$

$$\frac{\partial \rho g}{\partial t} + \frac{\partial \rho g u_j}{\partial x_j} = \frac{4}{3} \pi \varrho_l (r^{*3} J + 3\dot{\bar{r}}^2 \rho Q_0), \quad (2.59-b)$$

with  $\bar{r}$  an average droplet radius, calculated as

$$\bar{r} = \left( \frac{g}{\frac{4}{3} \pi \varrho_l Q_0} \right)^{\frac{1}{3}}. \quad (2.60)$$

Heiler [29] claims that the method gives comparable results for the liquid mass fraction as the four-equation method by Hill. The method is computationally less expensive, however, it is also less accurate, since, in contrast to Hill's Method of Moments, the average droplet radius  $\bar{r}$  is present in the differential equation for  $g$ . Therefore, the two-moment method is not considered further in this thesis.

---

### 2.3.6 Equation of state for the mixture

The governing set of equations, consisting of the Euler equations and Hill's Method of Moments, need to be augmented with an equation of state. The equation of state will give an expression for the pressure  $p$  and the temperature  $T$ , which are needed for the calculation of the fluxes and the condensation source term.

The static pressure of the mixture is the sum of the partial pressure of the vapour and that of the inert gas,

$$p = p_a + p_v. \quad (2.61)$$

For the moment, the inert gas and the vapour are treated as perfect gases (a perfect gas is one in which intermolecular forces are neglected, Anderson [6]), with specific gas constants  $R_a$  and  $R_v$ , respectively, i.e. the thermal equations of state read, see also chapter 3:

$$p_a = \rho_a R_a T_a, \quad (2.62-a)$$

$$p_v = \rho_v R_v T_v. \quad (2.62-b)$$

In chapter 3 we also consider the case of non-perfect gases. Assuming thermal equilibrium, the temperature of the inert gas and the vapour are identical,

$$T_a = T_v = T, \quad (2.63)$$

and the equation of state for the mixture thus becomes

$$p = \rho R T, \quad (2.64)$$

with  $R$  the gas constant of the mixture,

$$R = (R_0 - g R_v), \quad (2.65)$$

and  $R_0$  the gas constant for the case of zero liquid mass fraction,

$$R_0 = (1 - g_{max}) R_a + g_{max} R_v. \quad (2.66)$$

The enthalpy  $h\rho$  of the mixture follows from the sum of the enthalpies of the gas components and the condensate:

$$h\rho = h_a \rho_a + h_v \rho_v + h_l \rho_l, \quad (2.67)$$

which can be rewritten using Eqs. (2.22), (2.24-a) and (2.24-b), giving an expression for the specific (per unit of mass) enthalpy  $h$ :

$$h = (1 - g_{max}) h_a + (g_{max} - g) h_v + g h_l. \quad (2.68)$$

The vaporization heat  $L$  is defined as the difference between the specific enthalpy  $h_v$  of the vapour and that of the condensate  $h_l$ :

$$L \equiv h_v - h_l, \quad L > 0, \quad (2.69)$$

so that we can write

$$h = (1 - g_{max})h_a + g_{max}h_v - gL. \quad (2.70)$$

In analogy to Eq. (2.68), an expression for the specific internal energy can be derived:

$$e = (1 - g_{max})e_a + (g_{max} - g)e_v + ge_l. \quad (2.71)$$

Using the definition of the enthalpy  $h = e + p/\rho$  and Eq. (2.69) we can write

$$e = (1 - g_{max})e_a + g_{max}e_v - gL + g(p_v/\rho_v - p_l/\rho_l). \quad (2.72)$$

The pressure acting on the liquid is assumed to be equal to the mixture pressure,  $p = p_l$ , so we can write, using the perfect gas assumption,

$$e = (1 - g_{max})e_a + g_{max}e_v - gL + g(R_v - \frac{\rho}{\rho_l}R)T. \quad (2.73)$$

For a calorically perfect gas we have, see chapter 3:

$$e = c_v T, \quad (2.74)$$

where  $c_v$  is the specific heat at constant volume, defined as

$$c_v \equiv \left( \frac{\partial e}{\partial T} \right)_v. \quad (2.75)$$

The inert gas and the vapour are both treated as calorically perfect gases, so that Eq. (2.73) becomes

$$e = c_{v0}T - gL + g(R_v - \frac{\rho}{\rho_l}R)T, \quad (2.76)$$

where  $c_{v0}$  is the specific heat at constant volume for the case of zero liquid mass fraction,

$$c_{v0} = (1 - g_{max})c_{va} + g_{max}c_{vv}. \quad (2.77)$$

Once the specific internal energy  $e$ , the density  $\rho$ , and the liquid mass fraction  $g$  are known, the temperature of the mixture can be obtained from Eq. (2.76) and subsequently the pressure of the mixture follows from Eq. (2.64).

The last term in Eq. (2.76) is usually neglected since  $\rho \ll \rho_l$ , so that

$$e = c_{v,0}T + g(R_v T - L). \quad (2.78)$$

In case a linear expression for the latent heat is available, as is the case for the air-water mixture, Eq. (2.107), we have, from Eq. (2.78),

$$T = \frac{e + gL_0}{c_{v,0} + g(R_v - L_1)}. \quad (2.79)$$


---

### 2.3.7 Resulting set of governing equations

The resulting set of governing equations, consists of the Euler equations (2.13) augmented with Hill's Method of Moments, and is given by:

$$\frac{\partial \mathbf{U}}{\partial t} + \frac{\partial}{\partial x_j} \{ \mathbf{F}_j(\mathbf{U}) \} = \mathbf{W}(\mathbf{U}), \quad (2.80)$$

where  $\mathbf{U}$  denotes the vector of conservative variables:

$$(\mathbf{U})^T = (\rho, \rho u_1, \rho u_2, \rho u_3, \rho e_t, \rho Q_0, \rho Q_1, \rho Q_2, \rho g)^T, \quad (2.81)$$

and  $\mathbf{F}$  denotes the vector of the convective fluxes:

$$(\mathbf{F}_j(\mathbf{U}))^T = \left( F_j^{(1)}, \dots, F_j^{(9)} \right)^T, \quad (2.82)$$

with

$$\begin{aligned} F_j^{(1)}(\mathbf{U}) &= \rho u_j, \\ F_j^{(i+1)}(\mathbf{U}) &= \rho u_j u_i + \delta_{ij} p, \quad i = 1, 2, 3 \\ F_j^{(5)}(\mathbf{U}) &= \rho u_j h_t, \\ F_j^{(i+6)}(\mathbf{U}) &= \rho u_j Q_i, \quad i = 0, 1, 2 \\ F_j^{(9)}(\mathbf{U}) &= \rho u_j g. \end{aligned} \quad (2.83)$$

The condensation source term  $\mathbf{W}$  is given by:

$$(\mathbf{W}(\mathbf{U}))^T = \left( W^{(1)}, \dots, W^{(9)} \right)^T, \quad (2.84)$$

with

$$\begin{aligned} W^{(1), \dots, (5)}(\mathbf{U}) &= 0, \\ W^{(k+6)}(\mathbf{U}) &= r^{*k} J + k \dot{r} \rho Q_{k-1}, \quad k = 0, 1, 2 \\ W^{(9)}(\mathbf{U}) &= \frac{4}{3} \pi \varrho_l (r^{*3} J + 3 \dot{r} \rho Q_2). \end{aligned} \quad (2.85)$$

### 2.3.8 Speed of sound

The speed of sound is a very important quantity, because it determines the speed at which infinitesimally small disturbances propagate through a medium. Since the composition of the mixture is not constant when condensation is taking place, instead of the speed of sound, the frozen speed of sound is introduced here. This is the speed at which infinitesimally small disturbances propagate through a medium with fixed composition,

$$a_f^2 \equiv \left( \frac{\partial p}{\partial \rho} \right)_{s,g}, \quad (2.86)$$

where  $s$  is the specific entropy. In general, the equation of state is given by

$$p = p(\rho, e, g). \quad (2.87)$$

The increment of the pressure, at constant  $g$ , then follows as

---

$$dp = \left( \frac{\partial p}{\partial \rho} \right)_{e,g} d\rho + \left( \frac{\partial p}{\partial e} \right)_{\rho,g} de. \quad (2.88)$$

The first law of thermodynamics can be written in the following form

$$de = Tds + \frac{p}{\rho^2} d\rho, \quad (2.89)$$

which, upon substitution in Eq. (2.88), gives

$$dp = \left[ \left( \frac{\partial p}{\partial \rho} \right)_{e,g} + \frac{p}{\rho^2} \left( \frac{\partial p}{\partial e} \right)_{\rho,g} \right] d\rho + T \left( \frac{\partial p}{\partial e} \right)_{\rho,g} ds. \quad (2.90)$$

Expressing  $p$  directly as function of  $\rho$ ,  $s$  and  $g$  gives for constant  $g$ :

$$dp = \left( \frac{\partial p}{\partial \rho} \right)_{s,g} d\rho + \left( \frac{\partial p}{\partial s} \right)_{\rho,g} ds. \quad (2.91)$$

Equating the increments  $d\rho$  in Eqs. (2.90) and (2.91) then yields

$$\left( \frac{\partial p}{\partial \rho} \right)_{s,g} = \left( \frac{\partial p}{\partial \rho} \right)_{e,g} + \frac{p}{\rho^2} \left( \frac{\partial p}{\partial e} \right)_{\rho,g}, \quad (2.92)$$

which is the definition of the frozen speed of sound. Substitution of Eqs. (2.64) and (2.79) in Eq. (2.92) yields

$$a_f^2 = RT \left[ 1 + \frac{R}{c_{v,0} + g(R_v - L_1)} \right] \quad (2.93)$$

### 2.3.9 Relation between the liquid mass fraction and the saturation

For a mixture with temperature  $T_0$ , pressure  $p_0$ , zero liquid mass fraction and a maximum liquid mass fraction  $g_{max}$  the saturation ratio  $\Phi_0$  can be calculated as:

$$\Phi_0 = \frac{p_{v_0}}{p_{v,eq}(T_0)} = \frac{\rho_{v_0} R_v T_v}{p_{v,eq}(T_0)} = \frac{g_{max} \rho_0 R_v T_0}{p_{v,eq}(T_0)} = \frac{g_{max} p_0 R_v / R_0}{p_{v,eq}(T_0)}. \quad (2.94)$$

If, instead of the maximum liquid mass fraction, the saturation ratio  $\Phi_0$  of the mixture is known, then  $g_{max}$  follows from the last equation as:

$$g_{max} = \frac{1}{1 + \frac{R_v}{R_a} \left( \frac{p_0}{p_{v,eq}(T_0) \Phi_0} - 1 \right)}. \quad (2.95)$$

## 2.4 Material properties and constants

In the expressions for the nucleation rate, the droplet growth and the equation of state, several material properties and constants occur. For water and xenon, these quantities are given in the following subsections.

---

### 2.4.1 Surface tension

During rapid expansion in both converging-diverging nozzles and underexpanded jets, temperatures often drop far below the triple-point temperature of the condensing substance. When this happens, no definite statements can be made whether the condensate is liquid or solid. For steady flows of humid air, however, Dohrmann [23] finds good agreement with experiments under the assumption of liquid condensate. It is therefore assumed that the formed condensate is only present in the form of liquid.

The expression for the surface tension of water is taken from Dohrmann [23] and can be written in the following form:

$$\sigma(T) = \begin{cases} 19.861(T/T_c)^4 - 42.150(T/T_c)^5 \\ -5.6464 \times 10^{-6} \text{ [N/m]} & \text{for } T < 249.39 \text{ K} \\ 0.118 - 0.100(T/T_c) \text{ [N/m]} & \text{for } T \geq 249.39 \text{ K} \end{cases} \quad (2.96)$$

with  $T$  in Kelvin and  $T_c = 647.3 \text{ K}$ , the critical temperature of water. The triple-point temperature of water is  $T_{tr} = 273.15 \text{ K}$ .

Lamanna [38] uses a different expression for the surface tension at low temperatures. Her expression gives good correlation with experimentally obtained density distributions along the axis for the condensing flow in the G1-nozzle (see Lamanna [38]), for subcoolings as low as  $T = 219 \text{ K}$ . Lamanna's expression can be written in the following form:

$$\sigma(T) = \begin{cases} 8.52000 \times 10^{-2} - 0.229297(T/T_c) + 1.46999(T/T_c)^2 \\ -2.36417(T/T_c)^3 \text{ [N/m]} & \text{for } T < 250 \text{ K} \\ 0.118 - 0.100(T/T_c) \text{ [N/m]} & \text{for } T \geq 250 \text{ K} \end{cases} \quad (2.97)$$

Note that both Lamanna's expression for  $T < 250 \text{ K}$  and Dohrmann's expression for  $T < 249.39 \text{ K}$  are not based on experimentally obtained values, but merely a carefully constructed extrapolation to lower temperatures. Both expressions for the surface tension of water are plotted in Fig. 2.4.

The surface tension of liquid xenon is described by an expression first suggested by Van der Waals

$$\sigma(T) = \sigma_0(1 - T/T_c)^p \text{ [N/m]}, \quad T < T_c, \quad (2.98)$$

where  $T_c$  is the critical temperature. According to Croxton [19], this empirical relation appears to describe the behavior of simple liquids remarkably well. Smith et al. [60] find the following values:  $\sigma_0 = (5.46 \pm 0.1) \times 10^{-2} \text{ N/m}$  and  $p = 1.282 \pm 0.017$ . The critical temperature of xenon is  $T_c = 289.74 \text{ K}$ . These values were derived from measurements in the temperature range of 189 to 286 K. Croxton [19] argues that there is no guarantee that the parametric representation (2.98) will hold right down to the triple point, which, for xenon, is about 160.3 K at 0.816 bar. The relation may be expected to hold only for molecules of high symmetry and low eccentric factor in the vicinity of the critical point. Smith et al. [60] compare expression (2.98) with experimentally obtained values by Leadbetter and Thomas [39] of the surface tension in the temperature range 161.9 to 164.6 K. Their results are concluded to be in reasonable agreement, which is the motivation to use Eq. (2.98) also for temperatures lower than the triple-point temperature. The surface tension of xenon is plotted in Fig. 2.5.

---

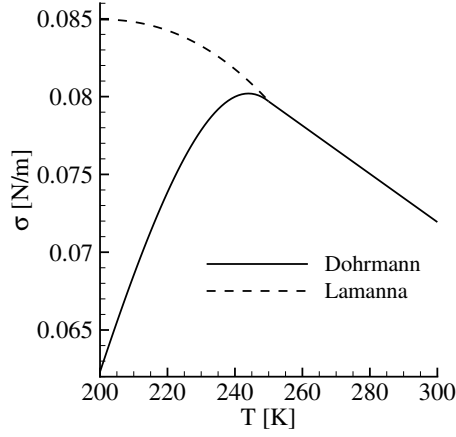


FIGURE 2.4: Surface tension  $\sigma$  of liquid water according to Dohrmann [23], Eq. (2.96), and Lamanna [38], Eq. (2.97).

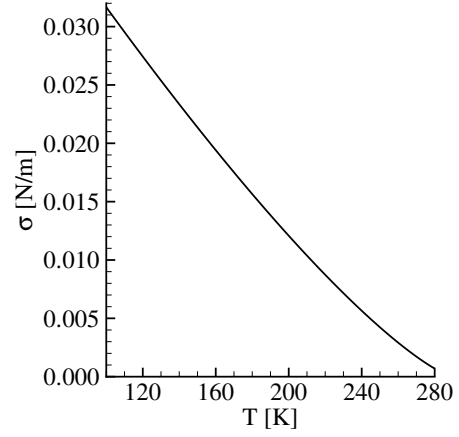


FIGURE 2.5: Surface tension  $\sigma$  of liquid xenon according to Eq. (2.98).

### 2.4.2 Liquid density

The density of water is a function of the temperature, and is obtained from Pruppacher and Klett [54], who give an expression in terms of the temperature in degrees Celsius. This expression can be rewritten in terms of the temperature in Kelvin, and becomes:

$$\varrho_l(T) = \varrho_0 \begin{cases} \sum_{i=0}^5 A_i (T/T_{tr})^i / \sum_{i=0}^1 B_i (T/T_{tr})^i & [\text{kg/m}^3] \quad T \geq T_{tr} \\ \sum_{i=0}^2 C_i (T/T_{tr})^i & [\text{kg/m}^3] \quad T < T_{tr} \end{cases} \quad (2.99)$$

with  $\varrho_0 = 999.84 \text{ kg/m}^3$  the liquid density at the triple-point temperature  $T_{tr} = 273.15 \text{ K}$ . The constants (dimensionless) in Eq. (2.99) are given in table 2.2.

$A_0 = -2.0079$	$A_3 = -10.447$	$B_0 = -3.9603$	$C_0 = 0.17058$
$A_1 = -3.5552$	$A_4 = 3.8244$	$B_1 = 4.9603$	$C_1 = 1.6353$
$A_2 = 13.784$	$A_5 = -0.59812$		$C_2 = -0.80593$

TABLE 2.2: Constants for equation (2.99)

The saturated liquid density of xenon is taken from Theeuwes and Bearman [64] who find the following expression

$$\varrho_l - \varrho_{l,c} = \sum_{i=1}^6 A_i (1 - T/T_c)^{i/3} \quad [\text{kg/m}^3], \quad (2.100)$$

in which the critical density  $\varrho_{l,c} = 1099 \text{ kg/m}^3$  and the critical temperature  $T_c = 289.74 \text{ K}$ . The constants in this equation were obtained by the method of least squares and are given in



table 2.3.

$A_1 = -0.2184099 \times 10^6 \text{ [kg/m}^3\text{]}$	$A_4 = 0.8705383 \times 10^7 \text{ [kg/m}^3\text{]}$
$A_2 = 0.1748818 \times 10^7 \text{ [kg/m}^3\text{]}$	$A_5 = -0.6824710 \times 10^7 \text{ [kg/m}^3\text{]}$
$A_3 = -0.5528331 \times 10^7 \text{ [kg/m}^3\text{]}$	$A_6 = 0.2131116 \times 10^7 \text{ [kg/m}^3\text{]}$

TABLE 2.3: Constants for equation (2.100)

The temperature range of the experimental data on which Eq. (2.100) is based is 176 to 237 K, and the maximum deviation between Eq. (2.100) and the experimental data is about 0.11%. The liquid density at the boiling point ( $T = 165.11 \text{ K}$  at 1 atmosphere) is  $2953 \text{ kg/m}^3$ . The melting point of xenon at 1.0 atm is  $161.4 \text{ K}$ . Experimental data for the liquid density below the melting point is not available. However, since the temperature in practical applications often drops below the melting point, equation (2.100) is extrapolated to lower temperatures, using a linear extrapolation which coincides both in function value as in slope at  $T = 166 \text{ K}$ . This leads to the following expression:

$$\rho_l(T) = \rho_{l,c}[3.786267 - 1.935229(T/T_c)] \text{ [kg/m}^3\text{]}, \quad T < 166 \text{ K}. \quad (2.101)$$

The liquid densities of water and xenon are plotted in Figs. 2.6 and 2.7, respectively.

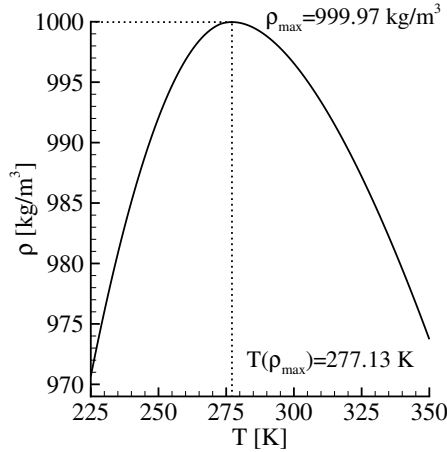


FIGURE 2.6: Liquid density of water.

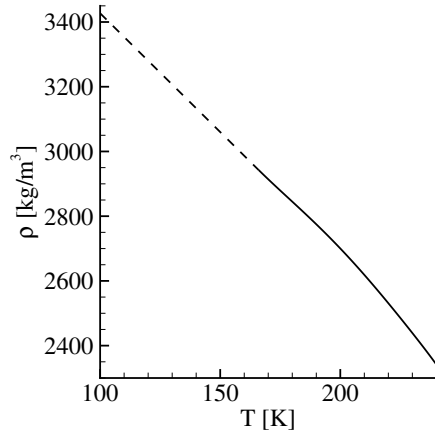


FIGURE 2.7: Liquid density of xenon, dashed line denotes linear extrapolation.

### 2.4.3 Vapour pressure

For the calculation of the phase-boundary curve of water, the formulation after Sonntag and Heinze [62] is used,

$$p_{v,eq}(T) = e^{A_9 + A_{10}T + A_{11}T^2 + B_1 \ln(T) + C_o T^{-1}} \text{ [N/m}^2\text{]}, \quad (2.102)$$

with constants

$$\begin{aligned} A_9 &= 21.125; & B_1 &= 2.4576; \\ A_{10} &= -2.7246 \times 10^{-2}; & C_0 &= -6094.4642; \\ A_{11} &= 1.6853 \times 10^{-5}. \end{aligned}$$

For xenon, a survey of available experimental data for vapour pressure over liquid and solid phase is given in Šifner and Klomfar [61]. Bowman et al. [13] find the following expression for the liquid phase, based on fitting experimental data with a least-squares method over the temperature range 162.02 to 288.97 K:

$$p_{v,eq}(T) = e^{A_{12} + A_{13}T + B_2 \ln(T) + C_1 T^{-1}} \quad [\text{N/m}^2], \quad (2.103)$$

with constants

$$\begin{aligned} A_{12} &= 55.9772; & B_2 &= -6.58218; \\ A_{13} &= 0.015775; & C_1 &= -2219.02. \end{aligned}$$

The coexistence curves of water and xenon are shown in Figs. 2.8 and 2.9, respectively.

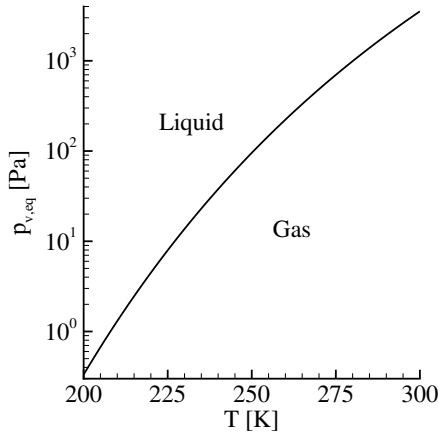


FIGURE 2.8: *Gas-liquid coexistence curve of water.*

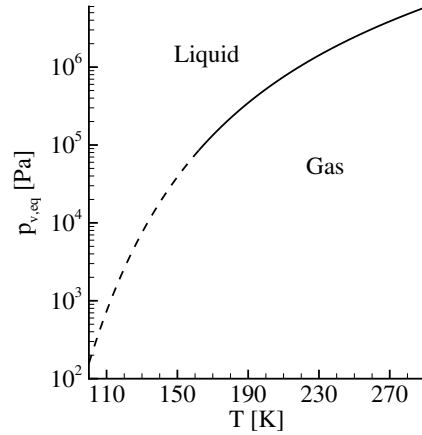


FIGURE 2.9: *Gas-liquid coexistence curve of xenon, dashed line denotes extrapolation.*

#### 2.4.4 Latent heat

The latent heat  $L$  can be determined from the Clausius-Clapeyron equation

$$\frac{dp_{v,eq}}{dT} = \frac{L p_{v,eq}}{R_v T^2}, \quad (2.104)$$

from which the latent heat follows as

$$L = R_v T^2 \left( \frac{1}{p_{v,eq}} \frac{dp_{v,eq}}{dT} \right). \quad (2.105)$$

With Eq. (2.102), the following expression for the latent heat of water is obtained

$$L(T) = R_v(A_{10}T^2 + 2A_{11}T^3 + B_1T - C_0) \quad [\text{J/kg}]. \quad (2.106)$$

In the temperature range of 200 to 300 K the latent heat after Eq. (2.106) decreases nearly linearly with temperature, and with a maximum error of about 0.05% can be approximated by

$$L(T) = L_0 + L_1T \quad [\text{J/kg}], \quad (2.107)$$

with constants

$$\begin{aligned} L_0 &= 3105913.39 \quad [\text{J/kg}] \\ L_1 &= -2212.97 \quad [\text{J/kg}\cdot\text{K}] \end{aligned}$$

The latent heat of xenon follows from Eqs. (2.105) and (2.103) as

$$L(T) = R_v(A_{13}T^2 + B_2T - C_1) \quad [\text{J/kg}]. \quad (2.108)$$

The latent heat of water and xenon are shown in Figs. 2.10 and 2.11, respectively. Note that

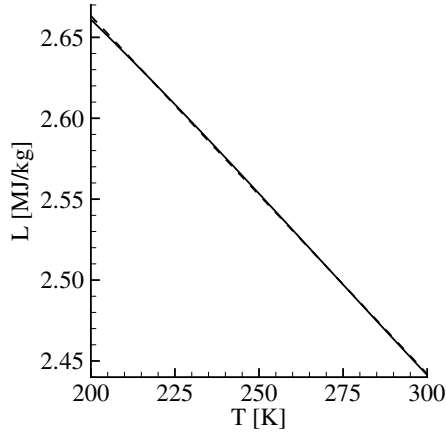


FIGURE 2.10: *Formation heat (gas to liquid) of water; solid line Eq. (2.106), dashed line Eq. (2.107).*

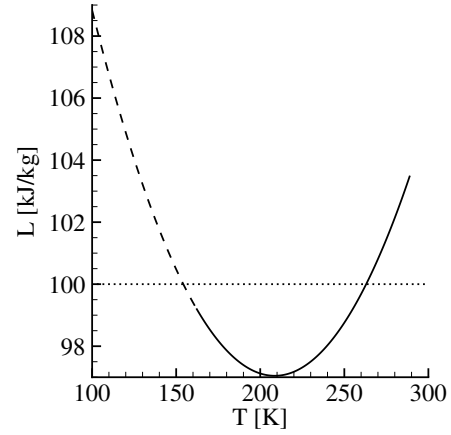


FIGURE 2.11: *Formation heat (gas to liquid) of xenon, dashed line denotes extrapolation. Dotted line is the constant value of  $L$  chosen in the numerical simulations.*

typical values for the latent heat of water ( $2.5 \times 10^6$  J/kg) and xenon ( $1.0 \times 10^5$  J/kg) differ more than one order of magnitude. Because the variation of  $L$  with  $T$  is small for xenon, in the numerical simulations, as a first approximation, the latent heat is taken as a constant ( $L = L_0 = 100$  kJ/kg).

### 2.4.5 Material properties of the gas phase

The values of the specific gas constant  $R$ , the specific heat capacities  $c_p$  and  $c_v$  and the ratio of specific heats  $\gamma$  are:

$$\begin{array}{rcl} & R & = 287.04 \quad [\text{J/kg}\cdot\text{K}] \\ \text{dry air:} & c_p & = 1004.0 \quad [\text{J/kg}\cdot\text{K}] \\ & c_v & = 716.96 \quad [\text{J/kg}\cdot\text{K}] \\ & \gamma & = 1.4004 \end{array}$$

$$\begin{array}{rcl} & R & = 461.52 \quad [\text{J/kg}\cdot\text{K}] \\ \text{water:} & c_p & = 1859.0 \quad [\text{J/kg}\cdot\text{K}] \\ & c_v & = 1397.5 \quad [\text{J/kg}\cdot\text{K}] \\ & \gamma & = 1.3302 \end{array}$$

$$\begin{array}{rcl} & R & = 63.329 \quad [\text{J/kg}\cdot\text{K}] \\ \text{xenon:} & c_p & = 158.32 \quad [\text{J/kg}\cdot\text{K}] \\ & c_v & = 94.991 \quad [\text{J/kg}\cdot\text{K}] \\ & \gamma & = 1.6667 \end{array}$$

The mass of a water molecule is  $m = 2.991 \times 10^{-26}$  kg, and the mass of a xenon molecule is  $m = 2.180 \times 10^{-25}$  kg.

---

# EQUATION OF STATE FOR REAL GAS

---



## 3.1 Thermodynamics

### 3.1.1 Basics

The Thermodynamic State Principle states that for a gas with fixed chemical composition, the local thermodynamic state is completely fixed by two independent thermodynamic quantities. So, if we have a system with three thermodynamic quantities, namely the pressure  $p$ , the specific volume  $v$  ( $\equiv 1/\rho$ ) and the temperature  $T$ , then there must be an Equation Of State (EOS) that describes a relation between these thermodynamic quantities of the system. In this specific example this EOS is a so-called *thermal* EOS. In case the system in addition also involves an energy-like quantity, like internal energy, entropy or enthalpy, we have to consider the first and second law of thermodynamics, and relations derived from this, the so-called Maxwell relations.

The first law of thermodynamics reads

$$de = dq - p dv, \quad (3.1)$$

with  $dq$  the added amount of heat per unit mass. In thermodynamics the specific heats (heat capacity per unit mass) play an important role. They are defined as the amount of heat that must be added to a unit mass in order to raise its temperature one K in a small reversible change, either at constant pressure ( $c_p$ ) or at constant volume ( $c_v$ ):

$$c_v \equiv \left( \frac{\partial q}{\partial T} \right)_v \quad \text{and} \quad c_p \equiv \left( \frac{\partial q}{\partial T} \right)_p. \quad (3.2)$$

For state changes at constant volume, the first law of thermodynamics, Eq. (3.1) reduces to

$$de = dq, \quad (3.3)$$

so that the specific heat at constant volume  $c_v$  can be expressed as

$$c_v(T, v) = \left( \frac{\partial e}{\partial T} \right)_v. \quad (3.4)$$

With the definition of the specific enthalpy,

---

$$h \equiv e + p v, \quad (3.5)$$

we can write the first law of thermodynamics as

$$dh = dq + v dp. \quad (3.6)$$

For state changes at constant pressure, we thus have

$$dh = dq, \quad (3.7)$$

so that the specific heat at constant pressure  $c_p$  can be expressed as

$$c_p(T, p) = \left( \frac{\partial h}{\partial T} \right)_p. \quad (3.8)$$

The Maxwell relations are obtained by combining the first and second law of thermodynamics, resulting in the *fundamental equation of Gibbs*, e.g. see Kuiken [37],

$$de = T ds - p dv, \quad (3.9)$$

with  $s$  the specific entropy. A first set of Maxwell relations is obtained by choosing  $(T, v)$  as the independent variables. Then we can express the differentials  $de$  and  $ds$  as

$$de = \left( \frac{\partial e}{\partial T} \right)_v dT + \left( \frac{\partial e}{\partial v} \right)_T dv, \quad (3.10)$$

$$ds = \left( \frac{\partial s}{\partial T} \right)_v dT + \left( \frac{\partial s}{\partial v} \right)_T dv. \quad (3.11)$$

Substituting the expressions for the differentials  $de$  and  $ds$  in Eq. (3.9) yields, with Eq. (3.2),

$$\left( \frac{\partial s}{\partial T} \right)_v = \frac{1}{T} \left( \frac{\partial e}{\partial T} \right)_v = \frac{1}{T} c_v(T, v), \quad (3.12)$$

$$\left( \frac{\partial s}{\partial v} \right)_T = \frac{1}{T} \left[ \left( \frac{\partial e}{\partial v} \right)_T + p \right]. \quad (3.13)$$

Differentiating Eq. (3.12) with respect to  $v$  and Eq. (3.13) with respect to  $T$ , and equating the two results yields the equation of Helmholtz:

$$\left( \frac{\partial e}{\partial v} \right)_T = -p + T \left( \frac{\partial p}{\partial T} \right)_v. \quad (3.14)$$

Combination of Eqs. (3.11) to (3.14) then gives the following expression for the differential of the specific entropy:

$$ds = \frac{1}{T} c_v(T, v) dT + \left( \frac{\partial p}{\partial T} \right)_v dv. \quad (3.15)$$

Substitution of the Helmholtz equation in Eq. (3.13) leads to

---

$$\left(\frac{\partial s}{\partial v}\right)_T = \left(\frac{\partial p}{\partial T}\right)_v. \quad (3.16)$$

Differentiating Eq. (3.12) with respect to  $v$  and Eq. (3.16) with respect to  $T$ , and equating the two results yields

$$\left(\frac{\partial c_v}{\partial v}\right)_T = T \left(\frac{\partial^2 p}{\partial T^2}\right)_v. \quad (3.17)$$

In a very similar fashion, by choosing  $(p, T)$  as the two independent thermodynamic variables, we can derive a second set of Maxwell relations

$$\left(\frac{\partial s}{\partial T}\right)_p = \frac{1}{T} c_p(T, p), \quad (3.18)$$

$$\left(\frac{\partial s}{\partial p}\right)_T = - \left(\frac{\partial v}{\partial T}\right)_p, \quad (3.19)$$

from which we obtain the pendant of the equation of Helmholtz:

$$\left(\frac{\partial h}{\partial p}\right)_T = v - T \left(\frac{\partial v}{\partial T}\right)_p. \quad (3.20)$$

In addition, we can derive the following relation

$$\left(\frac{\partial c_p}{\partial p}\right)_T = -T \left(\frac{\partial^2 v}{\partial T^2}\right)_p. \quad (3.21)$$

#### Relation between $c_p$ and $c_v$

From Eq. (3.15) it follows that

$$\left(\frac{\partial s}{\partial T}\right)_p = \frac{1}{T} c_v(T, v) + \left(\frac{\partial p}{\partial T}\right)_v \left(\frac{\partial v}{\partial T}\right)_p, \quad (3.22)$$

and with Eq. (3.18) the relation between  $c_p$  and  $c_v$  follows as

$$c_p - c_v = \left(\frac{\partial p}{\partial T}\right)_v \left(\frac{\partial v}{\partial T}\right)_p. \quad (3.23)$$

This shows that for a given thermal EOS and a given  $c_v$ , the  $c_p$  is known.

#### 3.1.2 Discussion

It follows from Gibbs' fundamental equation (3.9) that if for example  $e$  is given as function of  $v$  and  $s$ , as a so-called caloric EOS, the temperature  $T(v, s)$  and pressure  $p(v, s)$  follow from Eq. (3.9) in terms of the partial derivatives of  $e(v, s)$ , completing the description of the thermodynamics. The same is true when choosing  $s(v, e)$  as caloric EOS.

In the present study we describe the thermodynamics in terms of the independent variables  $\rho(\equiv 1/v)$  and  $e$ , i.e. the thermodynamic quantities that appear, together with  $p$ , directly in the

---

Euler equations. We can express the fundamental equation of Gibbs (3.9) in the independent variables  $\rho$  and  $e$  as

$$T ds = de - \frac{p}{\rho^2} d\rho. \quad (3.24)$$

Taking the differential of the entropy  $s(\rho, e)$  in terms of  $\rho$  and  $e$  leads to

$$ds = \left( \frac{\partial s}{\partial e} \right)_\rho de + \left( \frac{\partial s}{\partial \rho} \right)_e d\rho, \quad (3.25)$$

so we can derive the following relations

$$\left( \frac{\partial s}{\partial e} \right)_\rho = \frac{1}{T}, \quad (3.26)$$

$$\left( \frac{\partial s}{\partial \rho} \right)_e = -\frac{p}{\rho^2 T}. \quad (3.27)$$

As discussed above, if  $s$  is given in a caloric EOS as function of  $\rho$  and  $e$ , the description would be complete. However, in practice it is inconvenient to work with the entropy, therefore we choose to use a thermal-like EOS, to be derived in section 3.4, involving  $T(\rho, e)$  and  $p(\rho, e)$ .

Taking the derivative of Eq. (3.26) with respect to  $\rho$  and the derivative of Eq. (3.27) with respect to  $e$  and equating the results yields

$$\frac{\partial}{\partial \rho} \left( \frac{1}{T} \right)_e = -\frac{\partial}{\partial e} \left( \frac{p}{\rho^2 T} \right)_\rho. \quad (3.28)$$

This expression can be considered as a constraint on the admissible thermodynamic relations for  $p(\rho, e)$  and  $T(\rho, e)$ . Eq. (3.28) can be expanded to

$$p \left( \frac{\partial T}{\partial e} \right)_\rho - T \left( \frac{\partial p}{\partial e} \right)_\rho + \rho^2 \left( \frac{\partial T}{\partial \rho} \right)_e = 0. \quad (3.29)$$

## 3.2 Classification of gases

In engineering applications, the most commonly used thermal EOS is the perfect gas EOS, which assumes a dilute gas in which the volume occupied by the molecules is negligible and in which the molecules do not exert a force on each other. Only during their occasional collisions they interact with each other and exchange momentum and energy. The perfect gas EOS, however, is not applicable in all conditions. At very high temperatures, for example, one has to account for effects like dissociation, recombination, ionisation and molecule-oscillations, making a *high-temperature gas* EOS necessary. For a gas at conditions of high pressure, intermolecular forces can no longer be neglected, which means that a *real gas* EOS should be used. In this chapter, the difference between a perfect and real gas EOS is reviewed, and a novel real-gas EOS obeying Maxwell's relations is derived.

For the analysis of gas dynamic problems, we can identify four categories of gases, as follows, see Anderson [7]: Calorically perfect gases, thermally perfect gases, mixtures of chemically reacting gases and real gases. Since chemically reacting gases are not considered here, this category is not discussed further.

---



### 3.2.1 Calorically perfect gas

A perfect gas is a gas that satisfies the perfect gas equation

$$pv = RT, \quad (3.30)$$

with  $R$  the specific gas constant. It follows from Eq. (3.23) that for this gas  $c_p - c_v = R$  is constant, known as Carnot's law, which is found to be satisfied to better than 1% by air at normal temperatures and pressures (Batchelor [10]). From Eq. (3.17) it follows that  $c_v = c_v(T)$  and with Eq. (3.21) also  $c_p = c_p(T)$ .

A calorically perfect gas is by definition a gas with constant specific heats  $c_v$  and  $c_p$  (according to Eq. (3.23) it is sufficient to state that  $c_v$  is constant). For this gas, it follows from Eqs. (3.4) and (3.14) that

$$e = c_v T. \quad (3.31)$$

In many compressible flow applications, the pressures and temperatures are moderate enough that the gas can be considered to be calorically perfect.

### 3.2.2 Thermally perfect gas

For relatively high temperatures, the specific heats  $c_v$  and  $c_p$  are not constant, but functions of the temperature

$$c_p = f_1(T) \quad \text{and} \quad c_v = f_2(T), \quad (3.32)$$

with the constraint that  $f_1(T) - f_2(T) = R$  is constant. The specific internal energy follows from Eqs. (3.4) and (3.14):

$$e(T) = \int f_2(T) dT, \quad (3.33)$$

and the specific enthalpy then follows as  $h(T) = e(T) + RT$ .

### 3.2.3 Real gas

For relatively high pressures, intermolecular forces can no longer be neglected. In practice, a gas behaves as a real gas under conditions of very high pressure and moderate (room) temperature, conditions which accentuate the influence of intermolecular forces on the thermodynamics. For a real gas, the perfect gas EOS (3.30) is no longer valid. Instead, we must use a "real gas" thermal EOS, of which there are many versions. Also,  $c_v$  will be a function of both  $T$  and  $v$ , with  $c_p$  given by Eq. (3.23). Perhaps the most familiar real-gas thermal EOS is the van der Waals equation, described in section 3.3. However, this EOS describes a relation between the density, the pressure and the temperature of the gas only. Since the temperature and pressure are both dependent variables, an additional expression is needed in terms of the specific internal energy or the specific enthalpy. To this end, a novel EOS is developed, which is described in section 3.4.

---

### 3.3 EOS of van der Waals

An EOS that takes into account the effects of intermolecular forces, is the EOS derived by van der Waals. Based on molecular-theoretical considerations, see Wisman [70], this EOS gives a qualitatively good description of the influence of intermolecular forces. Van der Waals' considerations can be summarized as follows:

1. Molecules repulse one another at very close distance. As a consequence, a part of the volume in which the gas is situated, is not accessible. The presence of a molecule at a certain location excludes the possibility that another molecule can be present at that very same location. The volume in which a molecule can be situated is therefore smaller than the whole volume. The excluded volume is called *co-volume*, and is denoted by  $b$ . The freely available volume is then  $(v - b)$ , and the thermal EOS for a perfect gas then becomes:  $p(v - b) = RT$ .
2. At large distance molecules attract each other with a force that decreases rapidly with increasing distance. This is simplified by the assumption that molecule  $\beta$  is only attracted by molecule  $\alpha$  if  $\beta$  is located within a sphere with radius  $r$  and  $\alpha$  as center. This sphere is referred to as the *attraction-sphere*. In the interior of the gas, there will be an equal number of molecules within each attraction-sphere, so that the net-effect of all attracting forces is zero. At a wall, parts of the attraction-sphere will poke through the wall, so that gas molecules in the opposite part of the attraction-sphere exert a resulting force. This resultant is directed inward. This implies that the pressure in the gas is different from the pressure at the wall. The pressure correction is proportional to the number of molecules in a layer along the wall, which has a thickness  $r_0$ , equal to the radius  $r$  of the attraction-sphere, see Fig. 3.1. This means that the pressure correction is

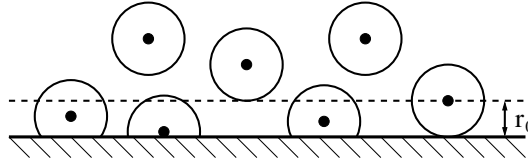


FIGURE 3.1: Gas molecules and their attraction sphere at a wall.

proportional to the number of molecules per unit of volume, or inversely proportional to  $v$ . The force exerted on each molecule is proportional to the number of molecules within the attraction-sphere, i.e. also inversely proportional with  $v$ . The resulting pressure correction is therefore inversely proportional to  $v^2$ , and the pressure  $p$  is replaced by the expression  $(p + a/v^2)$ .

In conclusion, the thermal EOS of van der Waals reads:

$$(p + \frac{a}{v^2})(v - b) = RT, \quad (3.34)$$

where  $R$  is the gas constant, and  $a$  and  $b$  are constants depending on the gas. It follows from Maxwell relation (3.17) that  $c_v = c_v(T)$  and from (3.21) that  $c_p = f(T, p)$ .

### 3.4 Novel real gas EOS

The van der Waals thermal EOS gives a qualitatively good description of the phenomena that occur at high pressure. However, here we follow a somewhat different approach. To account for real-gas effects, the concept of the compressibility factor  $z$ , see Wisman [70], is introduced, which is defined by the relation

$$z \equiv \frac{p}{\rho RT}, \quad (3.35)$$

so that the thermal EOS now reads

$$p = z\rho RT, \quad (3.36)$$

with  $R$  the specific gas-constant as before (note that  $\rho \equiv 1/v$ ). For the van der Waals gas we find, for example,

$$z = z(T, v) = \frac{v}{v - b} - \frac{a}{vRT}. \quad (3.37)$$

In solving the Euler equations, we need an expression for the pressure in terms of the specific internal energy  $e$  and the density  $\rho$ , since these two thermodynamic quantities are part of the state vector  $\mathbf{U}$  in the conservation formulation, and the pressure  $p$  is not. Therefore, such an expression is derived here for the pressure, and also for the temperature, since this thermodynamic property is needed in the calculation of flows with condensation (note that the temperature is not needed for the Euler equations).

Recall that the thermodynamic state for a gas of constant composition is fixed by specifying only two thermodynamic quantities. Thus, by specifying the density and the specific internal energy, the thermodynamic state of the gas is fixed and the pressure can be written as a function of the density and the specific internal energy:

$$p = p(\rho, e). \quad (3.38)$$

Hence, with Eq. (3.36), the temperature and compressibility factor also have to be functions of density and specific internal energy:

$$p(\rho, e) = z(\rho, e)\rho RT(\rho, e). \quad (3.39)$$

The explicit expressions for both  $z$  and  $T$  can be of any form, for example first, second or higher order polynomials can be chosen, as long as they satisfy Eq. (3.28) or (3.29). The values of the constants occurring in these polynomials are then determined from experimental data, i.e. it is assumed that we have at our disposal a data-base in the form of table 3.1.

Substitution of Eq. (3.39) in Maxwell relation (3.28) results in

$$\frac{\partial}{\partial \rho} \left( \frac{1}{T} \right)_e = -\frac{R}{\rho} \left( \frac{\partial z}{\partial e} \right)_\rho. \quad (3.40)$$

Integrating gives

$$\frac{1}{T} = -R \int \frac{1}{\rho} \left( \frac{\partial z}{\partial e} \right)_\rho d\rho + f(e). \quad (3.41)$$

density	specific internal energy	pressure	temperature
$\rho$	$e$	$p$	$T$
.	.	.	.
.	.	.	.
.	.	.	.

TABLE 3.1: experimental data for gas at high pressure

We take the following polynomial form for the compressibility factor  $z$

$$z(\rho, e) = z_{00} + z_{10}\rho + z_{01}e + z_{20}\rho^2 + z_{11}\rho e + z_{02}e^2, \quad (3.42)$$

where  $z_{00}, z_{10}, \dots, z_{02}$  are constants. Note that this expression is valid only in a restricted region of  $\rho$  and  $e$ . In this way we find for the derivative of  $z$  with respect to  $e$

$$\left(\frac{\partial z}{\partial e}\right)_\rho = z_{01} + z_{11}\rho + 2z_{02}e, \quad (3.43)$$

and for the reciprocal of  $T$  we thus find

$$\frac{1}{T(\rho, e)} = -R\{z_{11}\rho + (z_{01} + 2z_{02}e)\ln(\rho)\} + f(e). \quad (3.44)$$

We are free to choose the function  $f(e)$ , and we choose here, analogous to the compressibility factor  $z$ , a polynomial function. We want our real-gas model to include the perfect gas model when choosing appropriate values for the constants of the polynomial for the compressibility factor  $z$ , i.e. to recover  $e = c_v T$  when  $z = 1$ . We then see that we have to include a term  $T_0 e^{-1}$  in  $f(e)$ . The chosen polynomial is

$$f(e) = T_0 e^{-1} + T_1 + T_2 e, \quad (3.45)$$

giving us the full expression for the temperature as

$$T(\rho, e) = \frac{1}{-R\{z_{11}\rho + (z_{01} + 2z_{02}e)\ln(\rho)\} + T_0 e^{-1} + T_1 + T_2 e}. \quad (3.46)$$

We can use the constants  $T_0$ ,  $T_1$  and  $T_2$  to fit the polynomial expression for  $T(\rho, e)$  to the data points given in table 3.1. With the expressions for  $z(\rho, e)$  and  $T(\rho, e)$  known, we can obtain the pressure from Eq. (3.39), which makes the system of thermodynamic equations closed. Eq. (3.39) can be considered as the thermal EOS, while Eq. (3.46) can be considered as the caloric EOS. These relations contain 9 parameters, which can be chosen arbitrarily.

So, in summary, we chose  $\rho$  and  $e$  as the independent set of thermodynamic quantities, and by specifying the thermal EOS (3.36) with specified  $z(\rho, e)$ , Eq. (3.42), and the expression for  $T(\rho, e)$ , Eq. (3.46), we have the thermodynamics described completely.

### 3.5 Derived quantities of the real gas EOS

With the system of thermodynamic equations closed, we can find expressions for important derived quantities, such as the entropy, and the isobaric and isochoric specific heats.

---

### 3.5.1 Entropy

With Eqs. (3.26) and (3.27) we can find an expression for the entropy. By integrating Eq. (3.26), making use of Eq. (3.46)

$$s(\rho, e) = -R\{z_{11}\rho e + (z_{01}e + z_{02}e^2)\ln(\rho)\} + T_0 \ln(e) + T_1 e + \frac{1}{2}T_2 e^2 + \tilde{s}(\rho). \quad (3.47)$$

Differentiating with respect to  $\rho$  gives

$$\left(\frac{\partial s}{\partial \rho}\right)_e = -R\{z_{11}e + z_{01}\frac{e}{\rho} + z_{02}\frac{e^2}{\rho}\} + \tilde{s}'(\rho). \quad (3.48)$$

From Eq. (3.27) we have

$$\left(\frac{\partial s}{\partial \rho}\right)_e = -R\frac{z}{\rho} = -R\{z_{00}\frac{1}{\rho} + z_{10} + z_{01}\frac{e}{\rho} + z_{20}\rho + z_{11}e + z_{02}\frac{e^2}{\rho}\}. \quad (3.49)$$

Setting Eq. (3.48) equal to Eq. (3.49) we find the expression for  $\tilde{s}'(\rho)$

$$\tilde{s}'(\rho) = -R\{z_{00}\frac{1}{\rho} + z_{10} + z_{20}\rho\}, \quad (3.50)$$

and we see that the right-hand side of this equation is indeed only a function of  $\rho$ , enabling us to integrate this expression, yielding

$$\tilde{s}(\rho) = -R\{z_{00}\ln(\rho) + z_{10}\rho + \frac{1}{2}z_{20}\rho^2\} + s_0. \quad (3.51)$$

Now we have found an equation for the entropy

$$s(\rho, e) = s_0 - R[\{z_{00} + z_{01}e + z_{02}e^2\}\ln(\rho) + \{z_{10} + \frac{1}{2}z_{20}\rho + z_{11}e\}\rho] + T_0 \ln(e) + T_1 e + \frac{1}{2}T_2 e^2. \quad (3.52)$$

For a calorically perfect gas we have

$$\begin{aligned} z_{00} &= 1, \\ z_{10} &= 0; z_{20} = 0; z_{11} = 0; z_{01} = 0; z_{02} = 0, \\ T_0 &= c_v, \\ T_1 &= 0; T_2 = 0, \end{aligned}$$

and by substituting these values in Eq. (3.52) we find the expression for the entropy of a calorically perfect gas

$$s(\rho, e) = s_0 + \ln(\rho^{-R} e^{c_v}). \quad (3.53)$$

This shows that in isentropic flow of a calorically perfect gas  $e = \text{const } \rho^{\gamma-1}$ , where we have used the perfect gas relation  $R = c_p - c_v$  and the definition  $\gamma \equiv c_p/c_v$ .

---

### 3.5.2 Isobaric and Isochoric Specific Heat

To determine the specific heat at constant volume  $c_v$  and the specific heat at constant pressure  $c_p$ , we have the following set of equations available:

$$p = p(\rho, e) = z(\rho, e)\rho RT(\rho, e), \quad (3.54)$$

$$T = T(\rho, e). \quad (3.55)$$

First we will derive an expression for the specific heat at constant volume. We start with the relation for the isochoric specific heat as derived in Eq. (3.4), with  $v \equiv 1/\rho$ ,

$$c_v \equiv \left( \frac{\partial e}{\partial T} \right)_\rho. \quad (3.56)$$

Since the independent variables are  $\rho$  and  $e$ , we can immediately rewrite this as

$$c_v = \frac{1}{\left( \frac{\partial T}{\partial e} \right)_\rho}. \quad (3.57)$$

Now an expression for the specific heat at constant pressure will be derived. We start from the relation for the isochoric specific heat as derived in Eq. (3.8):

$$c_p = \left( \frac{\partial h}{\partial T} \right)_p, \quad (3.58)$$

where the enthalpy  $h$  is defined as  $h \equiv e + p/\rho$ . By replacing  $h$  we get

$$c_p = \left( \frac{\partial e}{\partial T} \right)_p - \frac{p}{\rho^2} \left( \frac{\partial \rho}{\partial T} \right)_p. \quad (3.59)$$

Taking the derivative of the set of Eqs. (3.54) and (3.55) with respect to  $T$  at constant pressure  $p$ , we get

$$\left( \frac{\partial}{\partial T} \begin{Bmatrix} \text{Eq. (3.54)} \\ \text{Eq. (3.55)} \end{Bmatrix} \right)_p \rightsquigarrow \begin{cases} 0 = \left( \frac{\partial p}{\partial e} \right)_\rho \left( \frac{\partial e}{\partial T} \right)_p + \left( \frac{\partial p}{\partial \rho} \right)_e \left( \frac{\partial \rho}{\partial T} \right)_p, \\ 1 = \left( \frac{\partial T}{\partial e} \right)_\rho \left( \frac{\partial e}{\partial T} \right)_p + \left( \frac{\partial T}{\partial \rho} \right)_e \left( \frac{\partial \rho}{\partial T} \right)_p, \end{cases} \quad (3.60)$$

enabling us to derive the following relations

$$\left( \frac{\partial e}{\partial T} \right)_p = \left( \frac{\partial p}{\partial \rho} \right)_e \left/ \left[ \left( \frac{\partial p}{\partial \rho} \right)_e \left( \frac{\partial T}{\partial e} \right)_\rho - \left( \frac{\partial p}{\partial e} \right)_\rho \left( \frac{\partial T}{\partial \rho} \right)_e \right] \right., \quad (3.61)$$

$$\left( \frac{\partial \rho}{\partial T} \right)_p = - \left( \frac{\partial p}{\partial e} \right)_\rho \left/ \left[ \left( \frac{\partial p}{\partial \rho} \right)_e \left( \frac{\partial T}{\partial e} \right)_\rho - \left( \frac{\partial p}{\partial e} \right)_\rho \left( \frac{\partial T}{\partial \rho} \right)_e \right] \right.. \quad (3.62)$$

By substituting Eqs. (3.61) and (3.62) in Eq. (3.59) we have derived an expression for the isobaric specific heat in the desired form:

---

$$c_p = \left[ \left( \frac{\partial p}{\partial \rho} \right)_e + \frac{p}{\rho^2} \left( \frac{\partial p}{\partial e} \right)_\rho \right] / \left[ \left( \frac{\partial p}{\partial \rho} \right)_e \left( \frac{\partial T}{\partial e} \right)_\rho - \left( \frac{\partial p}{\partial e} \right)_\rho \left( \frac{\partial T}{\partial \rho} \right)_e \right]. \quad (3.63)$$

Though it requires some algebraic manipulations, above expression can also be obtained from Eq. (3.23), making use of Eq. (3.29) and deriving from  $p = p(\rho, e)$  via the differentials

$$\left( \frac{\partial p}{\partial T} \right)_\rho = \left( \frac{\partial p}{\partial e} \right)_\rho / \left( \frac{\partial T}{\partial e} \right)_\rho. \quad (3.64)$$

### 3.5.3 Total pressure

When adiabatically bringing a gas to rest, the total specific enthalpy is conserved. Therefore, the stagnation specific enthalpy  $h_0$  (subscript 0 denotes stagnation) is equal to the total specific enthalpy  $h_t$ ,

$$h_0 = h_t. \quad (3.65)$$

The total specific enthalpy is the sum of the specific enthalpy and the specific kinetic energy,

$$h_t = h + \frac{1}{2} |\vec{u}|^2. \quad (3.66)$$

The specific enthalpy can be expressed in terms of specific internal energy, density and pressure through its definition

$$h \equiv e + \frac{p}{\rho}, \quad (3.67)$$

so that

$$e_0 + \frac{p_0}{\rho_0} = e + \frac{p}{\rho} + \frac{1}{2} |\vec{u}|^2. \quad (3.68)$$

We can eliminate the stagnation pressure  $p_0$  and the static pressure  $p$  by substituting the thermal EOS  $p = z\rho RT$ , resulting in a relation for  $\rho_0$  and  $e_0$  in terms of the local values of  $\rho$  and  $e$ :

$$e_0 + z(\rho_0, e_0)RT(\rho_0, e_0) = e + z(\rho, e)RT(\rho, e) + \frac{1}{2} |\vec{u}|^2. \quad (3.69)$$

When isentropically bringing a gas to rest the following relation is valid:

$$s(\rho_0, e_0) = s(\rho, e). \quad (3.70)$$

We now have two non-linear relations for  $\rho_0$  and  $e_0$ , which can be solved for a given state  $(\rho, e)$  and  $|\vec{u}|$  by, for example, a Newton iteration method. Once we have found  $\rho_0$  and  $e_0$  we can calculate the total temperature  $T_0 = T(\rho_0, e_0)$  from Eq. (3.46), and the total pressure  $p_0 = p(\rho_0, e_0)$  from Eqs. (3.42) and (3.39).

---

### 3.5.4 Speed of Sound

In section 2.3.8 an expression for the frozen speed of sound (2.92) was derived. Dropping the subscript  $g$  (the gas has constant composition) we have

$$\left(\frac{\partial p}{\partial \rho}\right)_s = \left(\frac{\partial p}{\partial \rho}\right)_e + \frac{p}{\rho^2} \left(\frac{\partial p}{\partial e}\right)_\rho. \quad (3.71)$$

The first and second term between brackets at the right-hand side are found from the real-gas EOS as

$$\left(\frac{\partial p}{\partial \rho}\right)_e = \rho RT \left(\frac{\partial z}{\partial \rho}\right)_e + z \rho R \left(\frac{\partial T}{\partial \rho}\right)_e + z RT, \quad (3.72-a)$$

$$\left(\frac{\partial p}{\partial e}\right)_\rho = \rho RT \left(\frac{\partial z}{\partial e}\right)_\rho + z \rho R \left(\frac{\partial T}{\partial e}\right)_\rho. \quad (3.72-b)$$

The derivatives of the compressibility factor and the temperature with respect to the density and the specific internal energy can be found from Eqs. (3.42) and (3.46). They are

$$\left(\frac{\partial z}{\partial \rho}\right)_e = z_{10} + z_{11}e + 2z_{20}\rho, \quad (3.73-a)$$

$$\left(\frac{\partial z}{\partial e}\right)_\rho = z_{01} + z_{11}\rho + 2z_{02}e, \quad (3.73-b)$$

$$\left(\frac{\partial T}{\partial \rho}\right)_e = RT^2 \left\{ z_{11} + \frac{z_{01} + 2z_{02}e}{\rho} \right\}, \quad (3.73-c)$$

$$\left(\frac{\partial T}{\partial e}\right)_\rho = T^2 \left\{ 2Rz_{02} \ln(\rho) + \frac{T_0}{e^2} - T_2 \right\}. \quad (3.73-d)$$

With Eqs. (3.72-a) to (3.73-d) and Eq. (3.71) we have found an explicit equation for the speed of sound in the real gas.

## 3.6 Real-gas EOS for a condensing gas mixture

If the thermodynamic state of the gas-mixture is such that one or more components condense, then the thermodynamic state of the mixture is not fixed by specifying the density and the specific internal energy only. During the condensation process, the mixture is continuously changing in composition, so that the thermodynamic state depends also on the composition. Therefore, the liquid mass fractions  $g_k$  of the individual components  $k$  need to be incorporated in the EOS. In this way, the pressure of the mixture becomes a function of the density, the specific internal energy, and the liquid mass fractions of the individual components of the mixture:

$$p = p(\rho, e, g_k). \quad (3.74)$$



Since the real-gas EOS Eq. (3.39) does not account for the liquid mass fractions  $g_k$ , we are faced with the problem of determining the pressure. However, if the volume occupied by the liquid droplets is small compared to the volume occupied by the vapour, then the pressure of the mixture  $p$  is equal to the pressure  $p_v$  of the vapour mixture,

$$p = p_v. \quad (3.75)$$

For the vapour mixture (excluding the liquid), we can determine the pressure from the real-gas EOS (3.39). The composition of the mixture is not constant, and therefore  $R$  is a function of the composition:

$$p_v = p(\rho_v, e_v, g_k) = z(\rho_v, e_v) R_v(g_k) \rho_v T(\rho_v, e_v), \quad (3.76)$$

where  $\rho_v$  and  $e_v$  are the density and the specific internal energy of the vapour part of the mixture. We can determine  $R_v(g_k)$  from

$$R_v(g_k) = R_0 \frac{1 - \sum_{k=1}^K g_k \frac{R_k}{R_0}}{1 - g}, \quad g < 1, \quad (3.77)$$

where  $R_k$  is the gas-constant of component  $k$ ,  $R_0$  is the gas constant of the mixture in case of zero liquid mass fraction, and  $g$  is the total liquid mass fraction, equal to the sum of liquid mass fraction of the individual components

$$g = \sum_{k=1}^K g_k. \quad (3.78)$$

The vapour density follows from Eq. (2.24-b), and by regarding all components as vapour (note that in principle every gas can condense under the right circumstances) we have  $g_{max} \equiv 1$  and thus

$$\rho_v = \rho(1 - g). \quad (3.79)$$

By using the definition of the enthalpy,  $h \equiv e + p/\rho$ , we can express the specific internal energy of the vapour as

$$e_v = h_v - \frac{p_v}{\rho_v}, \quad (3.80)$$

where  $h_v$  is the specific enthalpy of the vapour. Then we can sum the contributions to the specific enthalpy  $h$  of the vapour and the liquid to get the specific enthalpy of the mixture, i.e.

$$\begin{aligned} \rho h &= \rho_v h_v + \rho_l h_l \Rightarrow \\ h &= (1 - g) h_v + g h_l. \end{aligned} \quad (3.81)$$

The difference between the enthalpy of the vapour and the enthalpy of the liquid of a condensing component, is equal to the heat of formation

---

$$L = h_v - h_l, \quad (3.82)$$

where  $L$  is the latent heat (heat of formation). Substitution of Eq. (3.82) in Eq. (3.81) gives

$$h = (1 - g)h_v + g(h_v - L) = h_v - gL, \quad (3.83)$$

so that the enthalpy of the gaseous phase is equal to

$$h_v = h + gL. \quad (3.84)$$

The latent heat  $L$  is found by summing the individual contributions per component (heat is released by the liquid, this explains why subscript  $l$  is attached to the density):

$$\begin{aligned} \rho_l L &= \sum_{k=1}^K \rho_{l,k} L_k \Rightarrow \\ L &= \sum_{k=1}^K \frac{g_k}{g} L_k, \end{aligned} \quad (3.85)$$

where  $K$  is the number of components, and  $\rho_{l,k}$  is the liquid density of component  $k$ . The latent heat  $L_k$  of a component can be calculated, for example, with the law of Watson, see Reid et al. [57]. Substituting Eq. (3.85) into Eq. (3.84) gives an expression for the enthalpy of the gaseous phase

$$h_v = h + \sum_{k=1}^K g_k L_k. \quad (3.86)$$

If we substitute this expression in Eq. (3.80) we find

$$e_v = h - \frac{p_v}{\rho_v} + \sum_{k=1}^K g_k L_k, \quad (3.87)$$

or equivalently

$$e_v = e + \frac{p}{\rho} - \frac{p_v}{\rho_v} + \sum_{k=1}^K g_k L_k. \quad (3.88)$$

With the assumption of equal mixture and vapour pressure, we find an implicit relation for the specific internal energy  $e_v$  of the vapour:

$$e_v = e - g \frac{p_v(\rho_v, e_v)}{\rho_v} + \sum_{k=1}^K g_k L_k. \quad (3.89)$$

This equation can be solved, for example, with Newton iteration. Once the specific internal energy  $e_v$  of the vapour is known, with the density of the vapour given in Eq. (3.79), the pressure follows from Eq. (3.76).

---

## 4.1 Governing equations in cylindrical coordinates and two dimensions

Since one of the main aims of this thesis is to simulate condensing flows in axi-symmetric configurations, the set of governing equations (2.80) is transformed from Cartesian coordinates  $(x, y, z)$  to cylindrical coordinates  $(r, \theta, z)$ . For flows without swirl, the governing equations, in cylindrical coordinates, become (see appendix A)

$$\frac{\partial r\mathbf{U}}{\partial t} + \frac{\partial r\mathbf{F}}{\partial z} + \frac{\partial r\mathbf{G}}{\partial r} = \mathbf{H} + r\mathbf{W}. \quad (4.1)$$

This equation can be rewritten by taking  $r$  out of the derivative terms and dividing by  $r$ :

$$\frac{\partial \mathbf{U}}{\partial t} + \frac{\partial \mathbf{F}}{\partial z} + \frac{\partial \mathbf{G}}{\partial r} = \frac{\mathbf{H} - \mathbf{G}}{r} + \mathbf{W}. \quad (4.2)$$

The governing equations in two dimensions are found from the ones in 3D by omitting the momentum equation in the  $z$ -direction, and by setting the velocity and the derivatives in the  $z$ -direction equal to zero,  $w = 0$ ;  $\frac{\partial}{\partial z} = 0$ . We find then:

$$\frac{\partial \mathbf{U}}{\partial t} + \frac{\partial \mathbf{F}}{\partial x} + \frac{\partial \mathbf{G}}{\partial y} = \mathbf{W}. \quad (4.3)$$

The governing equations for axi-symmetric flows and those for two-dimensional flows thus differ only by the source term  $(\mathbf{H} - \mathbf{G})/r$  in the axi-symmetric form. For convenience, we replace the  $z$ -coordinate with  $x$  and the  $r$ -coordinate with  $y$ , so that the governing equations become

$$\frac{\partial \mathbf{U}}{\partial t} + \frac{\partial \mathbf{F}}{\partial x} + \frac{\partial \mathbf{G}}{\partial y} = \frac{\mathbf{H} - \mathbf{G}}{y} + \mathbf{W}. \quad (4.4)$$

where the first term on the right-hand side is zero for two-dimensional flows. The state vector  $\mathbf{U}$ , the flux vectors in  $x$ - and  $y$ -direction  $\mathbf{F}$  and  $\mathbf{G}$ , respectively, the axi-symmetric source term  $\mathbf{H}$  and the condensation source term  $\mathbf{W}$  are given by:

---

$$\mathbf{U} = \begin{pmatrix} \rho \\ \rho u \\ \rho v \\ \rho e_t \\ \rho Q_0 \\ \rho Q_1 \\ \rho Q_2 \\ \rho g \end{pmatrix} \quad \mathbf{F} = \begin{pmatrix} \rho u \\ \rho u^2 + p \\ \rho uv \\ \rho u h_t \\ \rho u Q_0 \\ \rho u Q_1 \\ \rho u Q_2 \\ \rho u g \end{pmatrix} \quad \mathbf{G} = \begin{pmatrix} \rho v \\ \rho v u \\ \rho v^2 + p \\ \rho v h_t \\ \rho v Q_0 \\ \rho v Q_1 \\ \rho v Q_2 \\ \rho v g \end{pmatrix} \quad (4.5)$$

$$\mathbf{H} = \begin{pmatrix} 0 \\ 0 \\ p \\ 0 \\ 0 \\ 0 \\ 0 \\ 0 \end{pmatrix} \quad \mathbf{W} = \begin{pmatrix} 0 \\ 0 \\ 0 \\ 0 \\ J \\ r^* J + \dot{r} \rho Q_0 \\ r^{*2} J + 2 \dot{r} \rho Q_1 \\ \frac{4}{3} \pi \varrho_l (r^{*3} J + 3 \dot{r} \rho Q_2) \end{pmatrix} \quad (4.6)$$

For axi-symmetric flow  $u$  and  $v$  are the axial and radial velocity component, respectively.

## 4.2 Non-dimensionalisation of the governing equations

By choosing an independent set of reference quantities, the governing equations can be non-dimensionalised. The chosen set of independent reference quantities are length  $L_{ref}$  (m), pressure  $p_{ref}$  (kg/m·s<sup>2</sup>), temperature  $T_{ref}$  (K), and specific gas-constant of the mixture  $R_0$  (m/s<sup>2</sup>·K). With these reference quantities the following dimensionless variables result:

$$\begin{aligned} \hat{t} &= \frac{t \sqrt{R_0 T_{ref}}}{L_{ref}}, \quad \hat{x} = \frac{x}{L_{ref}}, \quad \hat{y} = \frac{y}{L_{ref}}, \quad \hat{r}^* = \frac{r^*}{L_{ref}}, \\ \hat{u} &= \frac{u}{\sqrt{R_0 T_{ref}}}, \quad \hat{v} = \frac{v}{\sqrt{R_0 T_{ref}}}, \quad \hat{\dot{r}} = \frac{\dot{r}}{\sqrt{R_0 T_{ref}}}, \quad \hat{p} = \frac{p}{p_{ref}}, \\ \hat{\rho} &= \frac{\rho R_0 T_{ref}}{p_{ref}}, \quad \hat{T} = \frac{T}{T_{ref}}, \quad \hat{e}_t = \frac{e_t}{R_0 T_{ref}}, \\ \hat{R} &= \frac{R}{R_0}, \quad \hat{Q}_k = \frac{Q_k p_{ref} L_{ref}^{(3-k)}}{R_0 T_{ref}}, \quad \hat{J} = \frac{J L_{ref}^4}{\sqrt{R_0 T_{ref}}}. \end{aligned}$$

The quantities appearing in the expressions for the nucleation rate  $J$  and the droplet growth-rate  $\dot{r}$  are non-dimensionalised in the same way as the quantities above. If we substitute all the dimensionless variables into the governing equations, we obtain

$$\frac{\partial \hat{\mathbf{U}}}{\partial \hat{t}} + \frac{\partial \hat{\mathbf{F}}}{\partial \hat{x}} + \frac{\partial \hat{\mathbf{G}}}{\partial \hat{y}} = \frac{\hat{\mathbf{H}} - \hat{\mathbf{G}}}{\hat{y}} + \hat{\mathbf{W}}. \quad (4.7)$$

where the state vector  $\hat{\mathbf{U}}$ , the flux vectors in  $x$ - and  $y$ -direction  $\hat{\mathbf{F}}$  and  $\hat{\mathbf{G}}$ , respectively, the axi-symmetric source term  $\hat{\mathbf{H}}$  and the condensation source term  $\hat{\mathbf{W}}$  are as given in Eqs. (4.5) and

(4.6), except that all the quantities now carry a hat, indicating that they are all dimensionless. For convenience, the hat is omitted from here on.

### 4.3 Numerical Algorithm

For the numerical solution of the non-linear, coupled system of governing equations (4.7), a finite-volume method is used. For all current applications, the computational domain is two dimensional, and is discretized by triangular elements, from which median dual mesh control volumes are constructed. The flux terms  $\mathbf{F}$  and  $\mathbf{G}$  are calculated at the center of the edges of the median dual mesh, using either van Leer's Flux Vector Splitting scheme (FVS) or Liou's AUSM<sup>+</sup> FVS scheme. Second-order extrapolation of the solution from the nodes to the edges is achieved using van Leer's MUSCL-scheme. The control-volume-averaged solution vector  $\mathbf{U}$  is assigned to the value of  $\mathbf{U}$  at the center of gravity of the control volume. The solution at the nodes is then obtained from the solution at the center of gravity by linear interpolation, employing the gradient of the solution vector at the center of gravity. The condensation source term and the axi-symmetric source term are calculated from the solution in the center of gravity of the control volume. The change in time of the discretized solution follows from the sum of the fluxes and the source terms.

### 4.4 Finite-volume method

For the formulation of the finite-volume method, the governing equations (4.7) are integrated over a stationary control surface with area  $A$ :

$$\iint_A \left( \frac{\partial \mathbf{U}}{\partial t} + \frac{\partial \mathbf{F}}{\partial x} + \frac{\partial \mathbf{G}}{\partial y} \right) dA = \iint_A \left( \frac{\mathbf{H} - \mathbf{G}}{y} + \mathbf{W} \right) dA. \quad (4.8)$$

By applying Gauss' divergence theorem we can express the surface integral for the flux terms in a contour integral:

$$\iint_A \frac{\partial \mathbf{U}}{\partial t} dA + \int_{\partial A} (\mathbf{F}n_x + \mathbf{G}n_y) dC = \iint_A \frac{1}{y} (\mathbf{H} - \mathbf{G}) dA + \iint_A \mathbf{W} dA, \quad (4.9)$$

where  $\vec{n} = (n_x, n_y)^T$  is the boundary normal and  $C = \partial A$  is the closed contour that forms the boundary of surface  $A$ . By introducing control-volume averaged quantities in the following way

$$\bar{\phi} = \frac{1}{A} \iint_A \phi dA, \quad (4.10)$$

and by discretizing the flux terms we can rewrite Eq. (4.9) for a control volume as

$$\frac{\partial \bar{\mathbf{U}}_i}{\partial t} A_i + \underbrace{\sum_{j=1}^N (\mathbf{F}n_x + \mathbf{G}n_y)_{i,j} C_{i,j}}_{\text{I}} = \underbrace{\left( \frac{\mathbf{H}_i - \mathbf{G}_i}{y_i} \right) A_i}_{\text{II}} + \underbrace{\bar{\mathbf{W}}_i A_i}_{\text{III}}, \quad (4.11)$$


---

where  $i$  is the index of the control volume,  $N$  the total number of interfaces that form the boundary of control volume  $i$  and  $j$  the index of the interfaces of the control volume  $i$ . Eq. (4.11) is grouped in several terms, which will be referred to as

- I: convective flux term,
- II: axi-symmetric source term, and
- III: condensation source term,

respectively. The numerical treatment of each term is different and is described in the following sections. For convenience the bar, denoting the volume averaged value, is omitted from here on.

## 4.5 Construction of the median dual mesh

The 2D computational domain is divided into elements that are triangular. The median dual mesh is constructed from the triangular elements by connecting the midpoints of the edges of the triangle with the centroids (center of gravity) of the triangles, as is illustrated in Fig. 4.1.

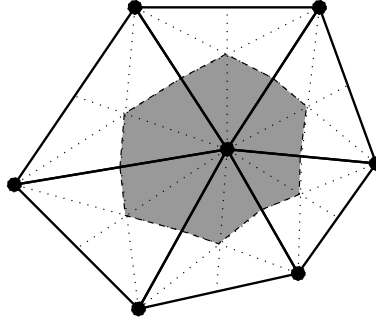


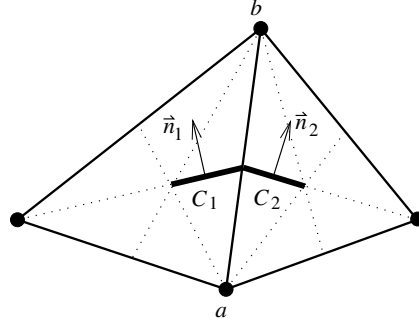
FIGURE 4.1: Construction of the median dual mesh from the triangular elements.

## 4.6 The convective flux term

### 4.6.1 Edge-wise flux computation and distribution

If Eq. (4.11) is solved for the control-volume-averaged value of  $\mathbf{U}$  associated with the control volume constructed around each node of the computational domain, we need to compute the fluxes over the interfaces which form the boundary of the control volumes. In this way, for every internal interface (not for the interfaces at the boundaries of the computational domain), the fluxes are computed twice. To prevent this, the internal interfaces are uniquely associated with the edges of the triangles as demonstrated in Fig. 4.2.

The fluxes at the contours  $C_1$  and  $C_2$  are computed with the same method using the same data, so that they can be treated as one interface. For convenience, the product of the normal vector  $\vec{n}$  and the contour  $C$  is stored as the contour vector  $\vec{C}$ , so that  $\vec{C}_{ab} = \vec{n}_1 C_1 + \vec{n}_2 C_2$ ,

FIGURE 4.2: Edge  $a$ - $b$  with its interfaces  $C_1$  and  $C_2$ .

which, for uniqueness, is defined to point from node  $a$  to node  $b$ . A loop over all edges starting at node  $a$  then gives the flux over all interfaces forming the boundary of the control volume associated with node  $a$ . So, in the method, one loop over all edges in which for each edge  $a$ - $b$  the calculated flux is added to the control volume associated with node  $a$  and subtracted from the control volume associated with node  $b$ , leads to the net flux for all control volumes.

#### 4.6.2 Flux-vector splitting schemes

The convective fluxes at the interfaces are evaluated by either the AUSM<sup>+</sup> flux splitting scheme, proposed by Liou [41], or Van Leer's FVS scheme [65]. Every face is appointed a left ( $l$ ) and right ( $r$ ) state, also indicated as plus (+) or minus (−) states, respectively. The left and right states are either taken equal to the state in nodes  $a$  and  $b$ , respectively, or are constructed from a higher-order method as is explained in section 4.6.3.

##### AUSM<sup>+</sup> scheme

Let the left and right states be given, then the left and right AUSM<sup>+</sup> Mach numbers are

$$M_l = \frac{\vec{u}_l \cdot \vec{C}}{a_{1/2} |\vec{C}|}, \quad (4.12-a)$$

$$M_r = \frac{\vec{u}_r \cdot \vec{C}}{a_{1/2} |\vec{C}|}, \quad (4.12-b)$$

respectively, where  $\vec{u}_l$  and  $\vec{u}_r$  are the left and right velocity vector, respectively, and  $a_{1/2}$  is the speed of sound at the interface, which is calculated as  $a_{1/2} = \frac{1}{2}(a_l + a_r)$ . Based on the left and right Mach numbers, the following split Mach numbers are defined:

$$\mathcal{M}^+(M_l) = \begin{cases} \frac{1}{4}(M_l + 1)^2 + \beta(M_l^2 - 1)^2 & |M_l| < 1 \\ \frac{1}{2}(M_l + |M_l|) & |M_l| \geq 1 \end{cases} \quad (4.13-a)$$

$$\mathcal{M}^-(M_r) = \begin{cases} -\frac{1}{4}(M_r - 1)^2 - \beta(M_r^2 - 1)^2 & |M_r| < 1 \\ \frac{1}{2}(M_r - |M_r|) & |M_r| \geq 1 \end{cases} \quad (4.13-b)$$

with  $\beta$  a user-defined parameter in the range:  $-\frac{1}{16} \leq \beta \leq \frac{1}{2}$ . With the split Mach numbers the interface Mach number is constructed as

$$m_{1/2} = \mathcal{M}^+(M_l) + \mathcal{M}^-(M_r), \quad (4.14)$$

from which the split interface Mach numbers follow as

$$m_{1/2}^+ = \frac{1}{2}(m_{1/2} + |m_{1/2}|), \quad (4.15-a)$$

$$m_{1/2}^- = \frac{1}{2}(m_{1/2} - |m_{1/2}|). \quad (4.15-b)$$

In analogy with the split Mach numbers, the following split pressures are defined:

$$\mathcal{P}^+(M_l) = \begin{cases} \frac{1}{4}(M_l + 1)^2(2 - M_l) + \alpha M_l(M_l^2 - 1)^2 & |M_l| < 1 \\ \frac{1}{2}(1 + M_l/|M_l|) & |M_l| \geq 1 \end{cases} \quad (4.16-a)$$

$$\mathcal{P}^-(M_r) = \begin{cases} \frac{1}{4}(M_r - 1)^2(2 + M_r) - \alpha M_r(M_r^2 - 1)^2 & |M_r| < 1 \\ \frac{1}{2}(1 - M_r/|M_r|) & |M_r| \geq 1 \end{cases} \quad (4.16-b)$$

with  $\alpha$  a user defined parameter in the range:  $-\frac{3}{4} \leq \alpha \leq \frac{3}{16}$ . With the split pressures, the interface pressure follows as

$$p_{1/2} = \mathcal{P}^+(M_l) p_l + \mathcal{P}^-(M_r) p_r. \quad (4.17)$$

With the split interface Mach-numbers  $m_{1/2}^\pm$  and the interface pressure  $p_{1/2}$  known, the numerical convective flux for the 8 governing equations is constructed as follows

$$F_1 = |\vec{C}|(m_{1/2}^+ a_l U_{l,1} + m_{1/2}^- a_r U_{r,1}), \quad (4.18-a)$$

$$F_2 = |\vec{C}|(m_{1/2}^+ a_l U_{l,2} + m_{1/2}^- a_r U_{r,2}) + p_{1/2} C_x, \quad (4.18-b)$$

$$F_3 = |\vec{C}|(m_{1/2}^+ a_l U_{l,3} + m_{1/2}^- a_r U_{r,3}) + p_{1/2} C_y, \quad (4.18-c)$$

$$F_4 = |\vec{C}|(m_{1/2}^+ a_l \{U_{l,4} + p_l\} + m_{1/2}^- a_r \{U_{r,4} + p_r\}), \quad (4.18-d)$$

$$F_5 = |\vec{C}|(m_{1/2}^+ a_l U_{l,5} + m_{1/2}^- a_r U_{r,5}), \quad (4.18-e)$$

$$F_6 = |\vec{C}|(m_{1/2}^+ a_l U_{l,6} + m_{1/2}^- a_r U_{r,6}), \quad (4.18-f)$$

$$F_7 = |\vec{C}|(m_{1/2}^+ a_l U_{l,7} + m_{1/2}^- a_r U_{r,7}), \quad (4.18-g)$$

$$F_8 = |\vec{C}|(m_{1/2}^+ a_l U_{l,8} + m_{1/2}^- a_r U_{r,8}), \quad (4.18-h)$$

where  $U_{l,i}$  and  $U_{r,i}$  are the  $i$ -th component of  $\mathbf{U}_l$  and  $\mathbf{U}_r$ , respectively. Liou [41] argues that the AUSM<sup>+</sup> scheme has the following features: (1) exact resolution of a stationary normal shock or contact discontinuity, (2) positivity-preserving property, and (3) improvement in accuracy over its predecessor AUSM and other popular schemes, (4) simplicity and easy generalization to other conservation laws.

---



### Van Leer's FVS scheme

Van Leer's FVS scheme closely resembles the AUSM<sup>+</sup> scheme and is obtained by replacing  $a_{1/2}$  by  $a_l$  and  $a_r$  in Eq. (4.12-a) and Eq. (4.12-b), respectively. Furthermore, in Eqs. (4.13-a) and (4.13-b) parameter  $\beta = 0$  and in Eqs. (4.16-a) and (4.16-b) parameter  $\alpha = 0$ . The split interface Mach numbers are replaced by

$$m_{1/2}^+ = \mathcal{M}^+(M_l), \quad (4.19-a)$$

$$m_{1/2}^- = \mathcal{M}^-(M_r). \quad (4.19-b)$$

The numerical convective flux is then given by Eqs. (4.18-a) to (4.18-h). A drawback of the Van Leer FVS is that it fails to recognize a contact-discontinuity, leading to excessive numerical diffusion, see Liou & Steffen [40].

### 4.6.3 Higher-order fluxes

#### Associating the solution with the center of gravity

If we assume that the solution is constant throughout the control volume, the solution at the faces of the control volume is equal to the solution at the node associated with that control volume. When we assume that the solution varies linearly inside the control volume, the solution at the face of the control volume is no longer equal to the solution at the node of the control volume. Assuming linear variation inside the control volume, the solution  $\phi$  at any point in the control volume is given by

$$\phi(\vec{x}) = \phi_0 + (\vec{\nabla}\phi)_0 \cdot (\vec{x} - \vec{x}_0), \quad (4.20)$$

where  $\phi_0$  is the solution in a certain fixed point inside the control volume. If we integrate  $\phi(\vec{x})$  over the control volume, and divide the result by the surface  $A$  of the control volume, we get

$$\frac{1}{A} \iint_A \phi(\vec{x}) dA = \frac{1}{A} \iint_A \phi_0 dA + \frac{1}{A} \iint_A (\vec{\nabla}\phi)_0 \cdot (\vec{x} - \vec{x}_0) dA. \quad (4.21)$$

Since the gradient of the solution  $(\vec{\nabla}\phi)_0$  is constant throughout the control volume, this term can be taken out of the integral

$$\frac{1}{A} \iint_A \phi(\vec{x}) dA = \frac{1}{A} \iint_A \phi_0 dA + \frac{1}{A} (\vec{\nabla}\phi)_0 \cdot \iint_A (\vec{x} - \vec{x}_0) dA. \quad (4.22)$$

If we locate the fixed point indicated by subscript 0 at the center of gravity, then the last term in Eq. (4.22) represents the static moment around the center of gravity, which is by definition equal to zero. Therefore, the last term vanishes, and we have

$$\frac{1}{A} \iint_A \phi(\vec{x}) dA = \frac{1}{A} \iint_A \phi_{cg} dA. \quad (4.23)$$


---

The term on the left-hand side is the cell-averaged value  $\bar{\phi}$ , see Eq. (4.10). Therefore, the assumption of a linear variation of the solution inside the control volume necessitates the association of the control-volume-averaged solution with the solution at the center of gravity, and not at the node of the control volume, which is in general not located at the center of gravity of the control volume.

### Reconstructing the solution in the nodes

Every control volume has a center of gravity, and since the number of control volumes is equal to the number of nodes, the number of centers of gravity is equal to the number of nodes. This allows the construction of a triangular mesh based on the centers of gravity of the median dual mesh control-volumes, as shown in Fig. 4.3.

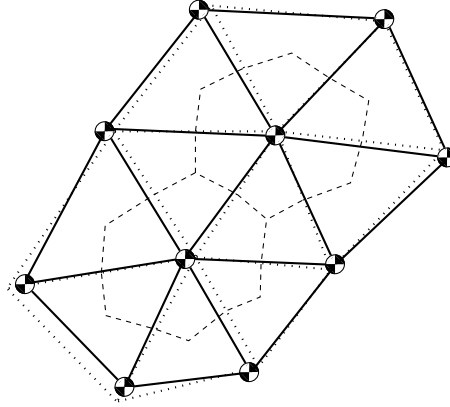


FIGURE 4.3: *Centers of gravity of the median dual mesh control volumes. Dotted lines form the node triangles, solid lines form the center of gravity triangles.*

With the solution in each corner point of the center of gravity based triangles known, we can reconstruct the gradient of the solution inside each triangle (see section 4.6.4). The gradient of the solution at the center of gravity is taken as the weighed sum of the gradient in the surrounding triangles:

$$(\vec{\nabla}\phi)_{cg} = \frac{1}{\sum_j \omega_j} \sum_j \omega_j (\vec{\nabla}\phi)_j, \quad (4.24)$$

where  $j$  is the index of the triangle surrounding the center of gravity. The weights  $\omega_j$  are given by

$$\omega_j = \frac{1}{A_j}, \quad (4.25)$$

so that small triangles contribute more to the gradient in the center of gravity than large triangles. Note that if the gradient in all surrounding triangles is the same, then the reconstruction

of the gradient at the center of gravity is exact. With the gradient at the center of gravity known, the solution in the node is found as

$$\phi_{node} = \phi_{cg} + (\vec{\nabla}\phi)_{cg} \cdot (\vec{x}_{node} - \vec{x}_{cg}). \quad (4.26)$$

### Second-order accurate fluxes

Second-order accurate fluxes can be obtained by either interpolating fluxes at the nodal points directly, or by first interpolating conserved or primary flow variables and then calculating the fluxes. While the latter technique is computationally more expensive, it leads to solutions with fewer spurious oscillations, Hirsch [30]. For a structured, equidistant mesh, as shown in Fig. 4.4, the values of the left and right state second-order, limited, primitive variables

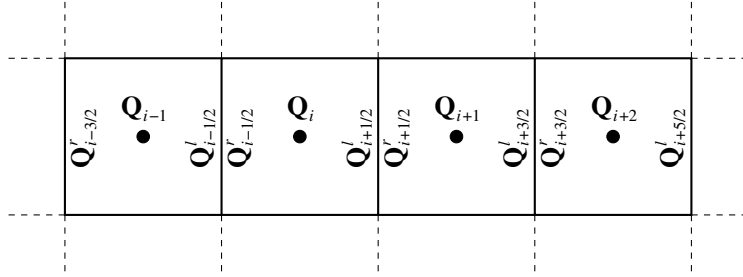


FIGURE 4.4: Cell nomenclature for one-dimensional reconstruction and limiting.

$\mathbf{Q} = \mathbf{Q}(\mathbf{U})$  with  $\mathbf{Q} = (\rho, u, v, p, Q_0, Q_1, Q_2, g)^T$  at interface  $i + \frac{1}{2}$  are obtained using the  $\kappa$ -scheme of Anderson et al. [8]

$$\mathbf{Q}_{i+1/2}^l = \mathbf{Q}_i + \left\{ \frac{1}{4}s[(1 - \kappa s)\Delta^- + (1 + \kappa s)\Delta^+] \right\}_i, \quad (4.27-a)$$

$$\mathbf{Q}_{i+1/2}^r = \mathbf{Q}_i - \left\{ \frac{1}{4}s[(1 - \kappa s)\Delta^+ + (1 + \kappa s)\Delta^-] \right\}_{i+1}, \quad (4.27-b)$$

where

$$\Delta_i^+ \equiv \mathbf{Q}_{i+1} - \mathbf{Q}_i, \quad (4.28-a)$$

$$\Delta_i^- \equiv \mathbf{Q}_i - \mathbf{Q}_{i-1}. \quad (4.28-b)$$

Furthermore,  $s$  is the nonlinear limiter defined as

$$s = \frac{2\Delta^+\Delta^- + \epsilon}{(\Delta^+)^2 + (\Delta^-)^2 + \epsilon}. \quad (4.29)$$

with  $\epsilon$  a small number, typically  $1 \times 10^{-12}$ , to prevent division by zero in parts of the domain where the gradient of  $\mathbf{Q}$  becomes zero. The value of  $\kappa$  is restricted to  $-1 \leq \kappa \leq 1$ . For  $\kappa = -1$  pure one-sided second-order extrapolation is obtained, while for  $\kappa = +1$  second-order central differencing is obtained. A value of  $\kappa = 1/3$  leads to a third-order accurate

upwind-approximation, see Anderson et al. [8]. Near discontinuities the limiter  $s$  reduces the scheme to first-order ( $s \rightarrow 0$ ).

For an unstructured, triangular mesh with constant mesh size, as shown in Fig. 4.5, the

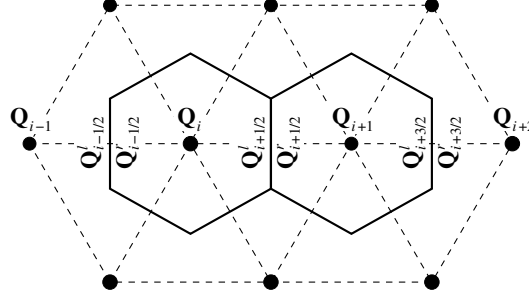


FIGURE 4.5: *One-dimensional reconstruction and limiting on an unstructured equidistant mesh.*

extrapolation to the interface  $i + \frac{1}{2}$  using values at the nodes  $i - 1, i, i + 1$  and  $i + 2$  is straightforward, but for an unstructured, triangular mesh with varying size, as shown in Fig. 4.6, the

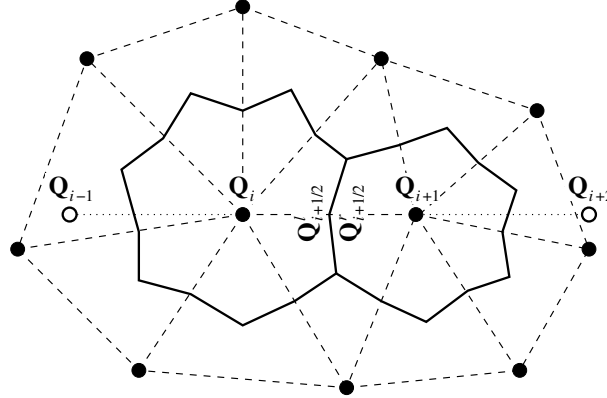


FIGURE 4.6: *One-dimensional reconstruction and limiting on an unstructured mesh with varying mesh size.*

only information which is readily available at the interface is the state at nodes  $i$  and  $i + 1$ . The state at nodes  $i - 1$  and  $i + 2$  however, is not known, since these ghost nodes, as they will be referred to, are not part of the mesh. To be able to apply Eqs. (4.27-a) and (4.27-b) without modification, the values at ghost nodes  $i - 1$  and  $i + 2$  are reconstructed from the states at the surrounding nodes of the triangle in which the ghost node is located. This reconstruction is second-order accurate and is described in section 4.6.4.

#### 4.6.4 Second-order solution reconstruction in a triangle

Consider a triangle in the  $(x, y)$ -plane, defined by its three nodes, labeled 1, 2 and 3, respectively, see Fig. 4.7. If we assume the quantity  $\varphi$  to vary linearly inside the triangle, the value

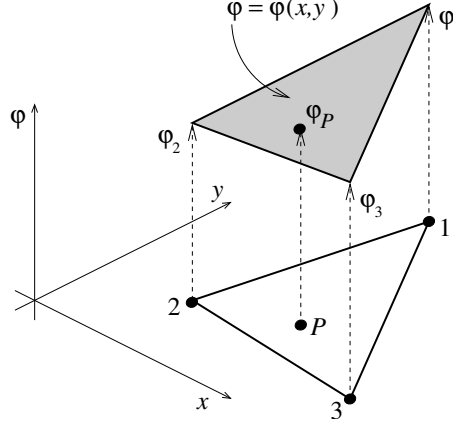


FIGURE 4.7: *Linear reconstruction in a triangle*

of  $\varphi$  at any point  $P$  inside the triangle is given by

$$\varphi(x_P, y_P) = Ax_P + By_P + C, \quad (4.30)$$

which is the general description of a plane in three dimensions. The constants  $A, B$  and  $C$  follow from the solution of the following system of equations

$$\varphi_1 = Ax_1 + By_1 + C, \quad (4.31\text{-a})$$

$$\varphi_2 = Ax_2 + By_2 + C, \quad (4.31\text{-b})$$

$$\varphi_3 = Ax_3 + By_3 + C, \quad (4.31\text{-c})$$

so that

$$\begin{pmatrix} A \\ B \\ C \end{pmatrix} = \begin{bmatrix} x_1 & y_1 & 1 \\ x_2 & y_2 & 1 \\ x_3 & y_3 & 1 \end{bmatrix}^{-1} \begin{pmatrix} \varphi_1 \\ \varphi_2 \\ \varphi_3 \end{pmatrix}, \quad (4.32)$$

with

$$\begin{bmatrix} x_1 & y_1 & 1 \\ x_2 & y_2 & 1 \\ x_3 & y_3 & 1 \end{bmatrix}^{-1} = \frac{1}{\begin{vmatrix} x_1 & y_1 & 1 \\ x_2 & y_2 & 1 \\ x_3 & y_3 & 1 \end{vmatrix}} \begin{bmatrix} y_2 - y_3 & y_3 - y_1 & y_1 - y_2 \\ x_3 - x_2 & x_1 - x_3 & x_2 - x_1 \\ x_2 y_3 - x_3 y_2 & x_3 y_1 - x_1 y_3 & x_1 y_2 - x_2 y_1 \end{bmatrix}. \quad (4.33)$$

It can be shown that the value in point  $P$  is given by the following equation

$$\varphi_P = \alpha_1 \varphi_1 + \alpha_2 \varphi_2 + \alpha_3 \varphi_3, \quad (4.34)$$

where

$$\alpha_1 = \frac{\begin{vmatrix} x_P & y_P & 1 \\ x_2 & y_2 & 1 \\ x_3 & y_3 & 1 \end{vmatrix}}{\begin{vmatrix} x_1 & y_1 & 1 \\ x_2 & y_2 & 1 \\ x_3 & y_3 & 1 \end{vmatrix}}, \quad \alpha_2 = \frac{\begin{vmatrix} x_1 & y_1 & 1 \\ x_P & y_P & 1 \\ x_3 & y_3 & 1 \end{vmatrix}}{\begin{vmatrix} x_1 & y_1 & 1 \\ x_2 & y_2 & 1 \\ x_3 & y_3 & 1 \end{vmatrix}}, \quad \alpha_3 = \frac{\begin{vmatrix} x_1 & y_1 & 1 \\ x_2 & y_2 & 1 \\ x_P & y_P & 1 \end{vmatrix}}{\begin{vmatrix} x_1 & y_1 & 1 \\ x_2 & y_2 & 1 \\ x_3 & y_3 & 1 \end{vmatrix}}. \quad (4.35)$$

It is worth noting that  $\alpha_1$ ,  $\alpha_2$  and  $\alpha_3$  denote the area of the inner triangles  $\triangle_{P,2,3}$ ,  $\triangle_{P,3,1}$  and  $\triangle_{P,1,2}$  as fraction of the area of triangle  $\triangle_{1,2,3}$ , respectively, see Fig. 4.8.

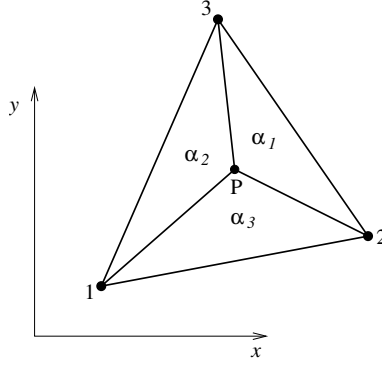


FIGURE 4.8: Triangles  $\triangle_{P,2,3}$ ,  $\triangle_{P,3,1}$  and  $\triangle_{P,1,2}$ .

## 4.7 The axi-symmetric source term

The main concern when discretizing the axi-symmetric source term is the occurrence of the coordinate  $y$  in the denominator, see Eq. (4.11). Since  $y$  is zero for nodes which are situated on the axis, we cannot simply use the state at the node associated with the control volume  $i$  to determine the axi-symmetric source term. Instead, the solution in the center of gravity is used, and since the center of gravity, unlike the node, is not located on the axis, we have  $y_{cg} \neq 0$ .

The axi-symmetric source term consists of two terms:  $\mathbf{H}$ , and  $\mathbf{G}$ . The two terms are determined from the state vector at the center of gravity  $\mathbf{U}_{cg}$ :

$$(\mathbf{H}_i - \mathbf{G}_i) \frac{A_i}{y_i} = [\mathbf{H}(\mathbf{U}_{cg}) - \mathbf{G}(\mathbf{U}_{cg})]_i \frac{A_i}{y_{cg,i}}. \quad (4.36)$$

## 4.8 The condensation source term

Since the axi-symmetric source term is calculated in the center of gravity of the control volume, the condensation source term  $\mathbf{W}$  is also calculated in the center of gravity,

$$\mathbf{W}_i = \mathbf{W}(\mathbf{U}_{cg}). \quad (4.37)$$

The nucleation rate  $J$ , as given in Eqs. (2.9) and (2.10), and the expression for the critical droplet radius (2.6), contain the natural logarithm of the super-saturation ratio  $\Phi$ , which, in condensing flows, usually increases from a value smaller than one to a value larger than one. To prevent division by zero, which occurs when  $\Phi = 1$ , the nucleation rate is only calculated for  $\Phi > 1$  (note that the  $J \equiv 0$  for  $\Phi < 1$ ). In the computational method, the threshold condition  $\Phi > 1$  is replaced by  $\Phi > 1 + \epsilon$  where  $\epsilon$  is a small number, larger than machine zero, the smallest number that can be represented on the computer compared to the number one.

The expression for the droplet growth rate (2.11) contains the radius  $r$  of a droplet. Since the radius is not defined when there are no droplets, calculation of  $\dot{r}$  can only be done when the number of droplets is larger than one. The number of droplets  $Q_0$  however, has a dimension of droplets per kilogram of mixture. The threshold is therefore replaced by the number of droplets per control volume,  $\rho Q_0 A^{3/2} > 1 + \epsilon$ , where  $\epsilon$  is introduced for the same reason as used for the threshold in the nucleation rate.

## 4.9 Time integration

For the present applications, we are only interested in finding the steady-state solution. Time-updates are used as a relaxation method to obtain this steady-state solution. Since the time scale of the condensation source term can be very different from that of the other three terms in Eq. (4.11), the time-update is split into two parts. This splitting method is called fractional time-stepping and is described in Oran & Boris [48]

$$\frac{\partial \mathbf{U}_i}{\partial t} = -\mathcal{R}_i, \quad (4.38\text{-a})$$

$$\frac{\partial \mathbf{U}_i}{\partial t} = \mathcal{S}_i, \quad (4.38\text{-b})$$

with

$$\begin{aligned} \mathcal{R}_i &= \frac{1}{A_i} [(4.11)\text{I} - (4.11)\text{II}], \\ \mathcal{S}_i &= \mathbf{W}_i. \end{aligned}$$

The first part (4.38-a) is solved using Heun's two-step predictor-corrector method, which is second order accurate,

$$\mathbf{U}_i^{(0)} = \mathbf{U}_i^{(n)}$$


---

$$\begin{aligned}
\mathbf{U}_i^{(1/2)} &= \mathbf{U}_i^{(0)} - \Delta t_i \mathcal{R}_i^{(0)} \\
\mathbf{U}_i^{(*)} &= \mathbf{U}_i^{(0)} - \Delta t_i \mathcal{R}_i^{(1/2)} \\
\mathbf{U}_i^{(**)} &= \frac{1}{2}(\mathbf{U}_i^{(1/2)} + \mathbf{U}_i^{(*)})
\end{aligned} \tag{4.39}$$

with  $n$  the current time-level. For steady flows, local time-stepping is performed, which means that the magnitude of the time-step  $\Delta t_i$  is the maximum allowable local time-step per control volume. The local time-step is calculated from the CFL-criterion (named after Courant, Friedrich and Lewy). The local time-step is a function of the maximum signal propagation speed and the control-volume geometry

$$\Delta t_i = \frac{1}{2} \text{CFL} \frac{\sqrt{A_i}}{(|\vec{u}| + a)_i}, \tag{4.40}$$

where  $a$  is the speed of sound and  $\vec{u}$  the velocity vector. The square root of the area provides a characteristic length for the control volume, while the prefactor  $\frac{1}{2}$  is included to account for the irregular shape of the median-dual mesh control-volume. Typical values for the CFL-number are in the range of 0.9 – 1.0. For flows without condensation the solution at the next time level  $n + 1$  is

$$\mathbf{U}^{(n+1)} = \mathbf{U}^{(**)}. \tag{4.41}$$

For flows with condensation, the second part (4.38-b) is solved using  $k$  steps of the predictor-corrector method

$$\begin{aligned}
\mathbf{U}_i^{(0)} &= \mathbf{U}_i^{(**)} \\
\mathbf{U}_i^{(s+1/2)} &= \mathbf{U}_i^{(s)} + \Delta t_i^{(s)} \mathcal{S}_i^{(s)} \\
\mathbf{U}_i^{(s+1)} &= \frac{1}{2}(\mathbf{U}_i^{(s+1/2)} + \mathbf{U}_i^{(s)} + \Delta t_i^{(s)} \mathcal{S}_i^{(s+1/2)}) \\
\mathbf{U}_i^{(n+1)} &= \mathbf{U}_i^{(k)}, \quad s = 0, 1, \dots, k-1
\end{aligned} \tag{4.42}$$

The fractional time-steps  $\Delta t^{(s)}$  are chosen such, that the production of liquid per time-step - and thus the amount of latent heat release - is limited

$$\Delta t_i^{(s)} W_8(\mathbf{U}_i^{(s)}) < \alpha_g, \tag{4.43}$$

where  $W_8$  is the eighth component of the condensation source vector  $\mathbf{W}$ . Since the latent heat of water and xenon differ significantly, the value of  $\alpha_g$  is chosen differently for each substance. For water, a typical value is  $\alpha_g = 10^{-4} \text{ kg/m}^3$ , and for xenon  $\alpha_g = 10^{-3} \text{ kg/m}^3$ . The last fractional time-step  $\Delta t_i^{(s-1)}$  is adjusted such that after  $k$  time-steps the sum of the fractional time-steps is equal to  $\Delta t_i$

$$\sum_{s=0}^{k-1} \Delta t_i^{(s)} = \Delta t_i. \tag{4.44}$$

For unsteady flows, local time-stepping cannot be applied, since the time-step at every control-volume needs to be equal. The local time-step  $\Delta t_i$  is then replaced by the global time-step, which is



$$\Delta t_g = \min(\Delta t_i) \quad i = 1, \dots, N, \quad (4.45)$$

where  $N$  is the number of control volumes.

## 4.10 Boundary conditions

At the boundaries of the computational domain, the control volumes are closed as shown in Fig. 4.9. To determine the fluxes over the boundary interfaces, dummy nodes are introduced

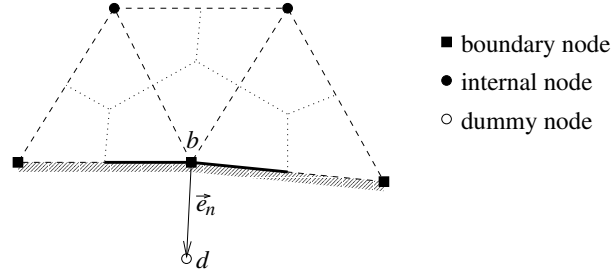


FIGURE 4.9: Closure of the median dual mesh at a boundary, denoted by the solid line.

across the boundary surfaces. These dummy nodes are outside of the computational domain, and have associated with them a state vector which is updated employing the boundary conditions. In the present computational method boundaries are divided into three main classes:

1. Inflow and outflow boundaries, which allow the flow of fluid through the boundary;
2. Far-field boundaries, representing the flow state in the far field;
3. Solid walls which have zero net mass flux.

The state vector in the dummy node is updated according to the type of the boundary condition. The flux at the boundary face is then computed using the flux operator, that is also used in the interior domain.

### 4.10.1 Inflow and Outflow Boundaries

In the present computational method, the flow at the inflow and outflow boundaries is assumed to be nearly one-dimensional. The equations for 1D flow follow from Eq. (4.7) as

$$\frac{\partial}{\partial t} \begin{pmatrix} \rho \\ u \\ p \\ Q_0 \\ Q_1 \\ Q_2 \\ g \end{pmatrix} + \begin{pmatrix} u & \rho & 0 & 0 & 0 & 0 & 0 \\ 0 & u & \frac{1}{\rho} & 0 & 0 & 0 & 0 \\ 0 & \rho a^2 & u & 0 & 0 & 0 & 0 \\ 0 & 0 & 0 & u & 0 & 0 & 0 \\ 0 & 0 & 0 & 0 & u & 0 & 0 \\ 0 & 0 & 0 & 0 & 0 & u & 0 \\ 0 & 0 & 0 & 0 & 0 & 0 & u \end{pmatrix} \frac{\partial}{\partial x} \begin{pmatrix} \rho \\ u \\ p \\ Q_0 \\ Q_1 \\ Q_2 \\ g \end{pmatrix} = \frac{1}{\rho} \begin{pmatrix} 0 \\ 0 \\ 0 \\ W_5 \\ W_6 \\ W_7 \\ W_8 \end{pmatrix}. \quad (4.46)$$

From Eq. (4.46) we find the eigenvalues from the (7x7) Jacobian matrix as the solutions of

$$(u - \lambda)^5[(u - \lambda)^2 - a^2] = 0. \quad (4.47)$$

So it follows that the 7 eigenvalues, all real, are  $\lambda_1 = u, \lambda_2 = u + a, \lambda_3 = u - a, \lambda_4 = u, \lambda_5 = u, \lambda_6 = u, \lambda_7 = u$ . This clearly indicates that 5 characteristic directions correspond with the streamline directions and the remaining two directions correspond with acoustic waves identical to the ones for single-phase flow.

The propagation properties in a one-dimensional flow are expressed in a straightforward way by the characteristic variables, which are described by the compatibility relations for one-dimensional flow. The compatibility relations are found by multiplying Eq. (4.46) with the left eigenvectors, related to the eigenvalues  $\lambda_1, \lambda_2, \dots, \lambda_7$ :

$$\frac{\partial \rho}{\partial t} - \frac{1}{a^2} \frac{\partial p}{\partial t} + u \left( \frac{\partial \rho}{\partial x} - \frac{1}{a^2} \frac{\partial p}{\partial x} \right) = 0, \quad (4.48-a)$$

$$\frac{\partial u}{\partial t} + \frac{1}{\rho a} \frac{\partial p}{\partial t} + (u + a) \left( \frac{\partial u}{\partial x} + \frac{1}{\rho a} \frac{\partial p}{\partial x} \right) = 0, \quad (4.48-b)$$

$$\frac{\partial u}{\partial t} - \frac{1}{\rho a} \frac{\partial p}{\partial t} + (u - a) \left( \frac{\partial u}{\partial x} - \frac{1}{\rho a} \frac{\partial p}{\partial x} \right) = 0, \quad (4.48-c)$$

$$\frac{\partial Q_0}{\partial t} + u \frac{\partial Q_0}{\partial x} = W_5, / \rho \quad (4.48-d)$$

$$\frac{\partial Q_1}{\partial t} + u \frac{\partial Q_1}{\partial x} = W_6, / \rho \quad (4.48-e)$$

$$\frac{\partial Q_2}{\partial t} + u \frac{\partial Q_2}{\partial x} = W_7, / \rho \quad (4.48-f)$$

$$\frac{\partial g}{\partial t} + u \frac{\partial g}{\partial x} = W_8, / \rho \quad (4.48-g)$$

where  $W_k$  is the  $k$ -th component of  $\mathbf{W}$ , as given in Eq. (4.6). To be able to apply the one-dimensional compatibility relations at a two-dimensional boundary, we have to prescribe a direction for the velocity  $u$  and the direction  $x$ . For the velocity the direction of the velocity vector normal to the boundary is chosen, so that  $u = \vec{u} \cdot \vec{e}_n$ . For the direction  $x$  the local normal direction to the boundary is chosen, i.e.  $x = n$ , see Fig. 4.9. The direction of the velocity vector at the dummy node  $d$  is taken equal to the direction of the velocity vector at the boundary node  $b$ .

The boundary conditions may be divided into numerical and physical boundary conditions. The number of physical boundary conditions which may be specified depends on whether the flow is subsonic or supersonic.

### Subsonic inflow

At a one-dimensional subsonic inflow boundary ( $0 < u < a$ ), there are 6 inward-running characteristics ( $u, u + a, u, u, u, u$ ) and one outward-running characteristic ( $u - a$ ). We can thus prescribe 6 physical conditions leaving one numerical condition. This numerical condition is determined by the third of the compatibility relations, Eq. (4.48-c), which describes the

---

upstream-traveling acoustic wave. In the numerical method, two different boundary conditions are implemented. The first one prescribes the liquid moments ( $\rho Q_0, \rho Q_1, \rho Q_2, \rho g$ ) and the *total* pressure  $p_0$  and *total* temperature  $T_0$ , the second one prescribes the liquid moments and the *static* pressure  $p$  and *static* temperature  $T$ .

- **Total-value preserving subsonic inflow boundary condition**

If we specify the total pressure  $p_0$  and total temperature  $T_0$ , we get, using a general equation of state,

$$p_0 = p(\rho_0, e_0), \quad (4.49-a)$$

$$T_0 = T(\rho_0, e_0). \quad (4.49-b)$$

These two (non-linear) relations provide the total density,  $\rho_0$ , and the total specific internal energy,  $e_0$ . Next, the total specific enthalpy and the specific entropy follow as

$$h_0 = e_0 + \frac{p_0}{\rho_0}, \quad (4.50-a)$$

$$s_0 = s(\rho_0, e_0), \quad (4.50-b)$$

where  $s$  is a given expression for the specific entropy. Furthermore, the following expressions also apply to the inflow boundary

$$h_0 = e + \frac{p}{\rho} + \frac{1}{2}u^2, \quad (4.51-a)$$

$$s_0 = s(\rho, e), \quad (4.51-b)$$

which upon differentiation with respect to time lead to

$$0 = \frac{\partial e}{\partial t} + \frac{1}{\rho} \frac{\partial p}{\partial t} - \frac{p}{\rho^2} \frac{\partial \rho}{\partial t} + u \frac{\partial u}{\partial t}, \quad (4.52-a)$$

$$0 = \left( \frac{\partial s}{\partial \rho} \right)_e \frac{\partial \rho}{\partial t} + \left( \frac{\partial s}{\partial e} \right)_\rho \frac{\partial e}{\partial t}. \quad (4.52-b)$$

The first and third term on the right-hand side of Eq. (4.52-b) follow from Maxwell relations (3.26) and (3.27), which are repeated here for convenience:

$$\left( \frac{\partial s}{\partial e} \right)_\rho = \frac{1}{T}, \quad (4.53-a)$$

$$\left( \frac{\partial s}{\partial \rho} \right)_e = -\frac{p}{\rho^2 T}. \quad (4.53-b)$$

Upon substitution in Eq. (4.52-b) we find

$$0 = -\frac{p}{\rho^2 T} \frac{\partial \rho}{\partial t} + \frac{1}{T} \frac{\partial e}{\partial t}, \quad (4.54)$$

or

$$\frac{\partial e}{\partial t} = \frac{p}{\rho^2} \frac{\partial \rho}{\partial t}. \quad (4.55)$$

This last expression can now be substituted in Eq. (4.52-a), leading to

$$\frac{\partial u}{\partial t} = -\frac{1}{\rho u} \frac{\partial p}{\partial t}, \quad (4.56)$$

which gives a relation between the time-rate of change of the pressure and the time-rate of change of the velocity. Eq. (4.56) can be used to eliminate  $\frac{\partial u}{\partial t}$  from (4.48-c), leading to the following expression

$$\frac{\partial p}{\partial t} = \mathcal{R}, \quad (4.57)$$

where  $\mathcal{R}$  is the residual

$$\mathcal{R} = \frac{u(u-a)}{u+a} \left( \rho a \frac{\partial u}{\partial n} - \frac{\partial p}{\partial n} \right). \quad (4.58)$$

Integration in time of the pressure at the boundary is done with Heun's predictor-corrector method, see section 4.9. For simplicity, we consider only the predictor step. The pressure at the intermediate time level becomes

$$p^{(1/2)} = p^{(0)} + \Delta t \mathcal{R}^{(0)}. \quad (4.59)$$

Next, the density  $\rho$  and specific internal energy  $e$  at the dummy node are calculated from the following set of equations:

$$p^{(1/2)} = p(\rho, e), \quad (4.60-a)$$

$$s_0 = s(\rho, e), \quad (4.60-b)$$

and the components of the velocity at the dummy node follow from

$$h_0 = e + p^{(1/2)}/\rho + \frac{1}{2}u^2, \quad (4.61-a)$$

$$u_d/v_d = u_b/v_b, \quad (4.61-b)$$

where  $u$  and  $v$  are the  $x$ - and  $y$ -component of the velocity vector  $\vec{u}$ . Subscript  $b$  denotes the boundary node and subscript  $d$  denotes the dummy node. The last relation implies that the direction of the velocity at the dummy node is equal to the direction of the velocity at the boundary node.

---

- **Static-value preserving subsonic inflow boundary condition**

In case the static pressure at the boundary is known, the time-rate of change of the pressure is zero. Therefore, the second term on the left-hand side of Eq. (4.48-c) cancels. Integration in time of the velocity at the boundary is done in the same way as for the total value preserving inflow boundary condition.

Note that the space derivatives (terms with  $\frac{\partial}{\partial n}$ ) in both inflow boundary conditions are discretized using first order differences. Thus, for example

$$\frac{\partial u}{\partial n} = \frac{u_b - u_d}{n_b - n_d}. \quad (4.62)$$

### Supersonic inflow

For a supersonic inflow, all the characteristics are inward-running, and we are free to specify all of the flow variables.

### Subsonic outflow

At a one-dimensional subsonic outflow boundary ( $0 < u < a$ ), there are 6 outward-running characteristics (u,u+a,u,u,u,u) and one inward-running characteristic (u-a). Therefore only one physical condition may be prescribed, for example the static pressure (independent of time), as is done in the present numerical method, and determine the remaining variables, i.e.  $\rho$  and  $u$ , and the liquid moments, using compatibility relations (4.48-a) and (4.48-b), and (4.48-d)-(4.48-g). Since the pressure is fixed, the second term on the left-hand side of Eqs. (4.48-a) and (4.48-b) cancels, and the time-rate of change of the density and velocity follow as

$$\frac{\partial \rho}{\partial t} = -u \left( \frac{\partial \rho}{\partial n} - \frac{1}{a^2} \frac{\partial p}{\partial n} \right), \quad (4.63-a)$$

$$\frac{\partial u}{\partial t} = -(u+a) \left( \frac{\partial u}{\partial n} + \frac{1}{\rho a} \frac{\partial p}{\partial n} \right), \quad (4.63-b)$$

while for the liquid moments we find

$$\frac{\partial Q_0}{\partial t} = -u \frac{\partial Q_0}{\partial n} + W_5/\rho, \quad (4.63-c)$$

$$\frac{\partial Q_1}{\partial t} = -u \frac{\partial Q_1}{\partial n} + W_6/\rho, \quad (4.63-d)$$

$$\frac{\partial Q_2}{\partial t} = -u \frac{\partial Q_2}{\partial n} + W_7/\rho, \quad (4.63-e)$$

$$\frac{\partial g}{\partial t} = -u \frac{\partial g}{\partial n} + W_8/\rho. \quad (4.63-f)$$


---

### Supersonic outflow

For a supersonic outflow, no physical conditions may be specified and the time rate of change of the state at the dummy nodes is completely determined by all compatibility relations. For simplicity, the compatibility relations are not used to determine the state at the dummy node, but all state variables are extrapolated from the interior of the computational domain to the outflow boundary,

$$\mathbf{U}_d = \mathbf{U}_b. \quad (4.64)$$

### 4.10.2 Far-field boundaries

Far-field boundaries are needed to limit the size of the computational domain. At the far-field boundaries, it is checked whether there is inflow or outflow. For the current flow simulations, the velocity normal to the boundary is small (subsonic). In the case of inflow, the total-value preserving inflow boundary condition is applied. In the case of outflow, the subsonic outflow boundary condition is applied.

### 4.10.3 Solid Walls

At solid walls there is no flow through the boundary. This implies that there is only a pressure contribution to the flux at the wall. Deconick & Struys [22] derived an expression for the pressure at the wall, consistent with the Van Leer FVS scheme

$$p_d = p_b(M_n + 1)^2 \left(1 + \frac{\gamma - 1}{2} M_n\right), \quad (4.65)$$

where  $\gamma$  is the ratio of specific heats, and  $M_n$  is the Mach-number normal to the wall,

$$M_n = \frac{\vec{u} \cdot \vec{e}_n}{a}, \quad (4.66)$$

with normal vector  $\vec{e}_n$  defined to point outwards as in Fig. 4.9. The flux at the wall is now calculated based on the pressure  $p_d$  at the dummy node. From Eq. (4.65), we see that the pressure at the dummy node is larger than pressure at the boundary node, in case of outflow. The increased pressure will have the effect of turning the velocity vector more in line with the boundary tangent. In practice, using the modified pressure  $p_d$  instead of  $p_b$  leads to a smaller numerical entropy production at the wall.

## 4.11 Solution continuation on subsequent meshes

As a starting point for the numerical calculation of the flow in or over a given geometry, everywhere in the field initial conditions have to be known. Since these initial conditions can deviate substantially from the final solution, a relatively large amount of computational time is spent on iterating the flow solution from its given initial state to a state close to the final, converged, solution.

After establishing the flow in a certain geometry on a given mesh, it is important to show that the solution is sufficiently grid independent. In practice this usually implies that one first computes a flow solution on a relatively coarse mesh, and subsequently refines the mesh until the changes in the solution become small in some norm. As initial solution on the finer

mesh, we want to use the solution on the coarser mesh. Thus, for every node of the fine mesh, we want to determine the solution of the coarse mesh as initial solution. For an equidistant structured mesh, this procedure is rather straightforward, since it is easy to determine in which square of the coarse mesh a node of the fine mesh is located. For unstructured meshes however, this procedure is not as straightforward as it may seem. If, for every node of the fine mesh, one has to loop over all control volumes of the coarse mesh to find where it is located, this can be computationally very expensive, especially for three dimensional meshes, which consist of many nodes. When halving the mesh-size, for example, the number of nodes will increase with  $\sim 2^3$  (in three dimensions), so that for a coarse mesh consisting of  $N_c$  nodes, the number of nodes in the fine mesh  $N_f$  will be  $\sim 2^3 N_c$ . The number of computational operations needed to calculate the initial solution on the fine mesh will then be proportional to  $N^2$ , where  $N = \sqrt{N_c N_f}$ .

Appendix B presents a mesh-to-mesh interpolation method that is computationally less expensive.

---





The numerical results for steady flows without condensation (“dry flows”) and steady flows with non-equilibrium condensation, presented in this chapter, are utilized to validate the present numerical method. The numerical method is based on the numerics presented in chapter 4, and contains the physical models which were presented in chapter 2. The results will also give insight into the effects of condensation in transonic flows.

All triangular meshes were created with Delaundo, see Müller [47], a program that creates triangular grids based on the Frontal Delaunay Method.

## 5.1 NACA 0012 airfoil

Well-known airfoils of a certain class including the Göttingen 398 and the Clark Y airfoils, which have proved to be efficient, are nearly alike when their camber is removed (mean line straightened) and they are reduced to the same maximum thickness, see Abbott & Von Doenhoff [2]. A thickness variation similar to that of these airfoils was chosen for the development of the N.A.C.A. airfoils. An equation defining the shape was used as a method of producing a family of airfoil sections.

If the chord is taken along the  $x$  axis from 0 to 1 the ordinates  $y$  are given by an equation of the form

$$\pm y = a_0\sqrt{x} + a_1x + a_2x^2 + a_3x^3 + a_4x^4. \quad (5.1)$$

This equation was adjusted to give the desired shape by imposing the following conditions to determine the constants:

1. Maximum ordinate 0.1 at 0.3 chord,  $x = 0.3 : y = 0.1, dy/dx = 0$ .
2. Ordinate at trailing edge  $x = 1 : y = 0.002$
3. Trailing-edge angle  $x = 1 : dy/dx = -0.234$
4. Nose shape  $x = 0.1 : y = 0.078$

The following equation satisfying approximately the above-mentioned conditions represents a profile having a thickness of approximately 20 percent of the chord:

$$\pm y = 0.29690\sqrt{x} - 0.12600x - 0.35160x^2 + 0.28430x^3 - 0.10150x^4. \quad (5.2)$$


---

Sections having any desired maximum thickness are obtained by multiplying the basic ordinates by the proper factor; that is

$$\pm y_t = \frac{t}{0.20}(0.29690\sqrt{x} - 0.12600x - 0.35160x^2 + 0.28430x^3 - 0.10150x^4), \quad (5.3)$$

where  $t$  is the maximum thickness. For the NACA 0012 airfoil, the maximum thickness is  $t = 0.12$ . The shape of the airfoil is shown in Fig. 5.1.

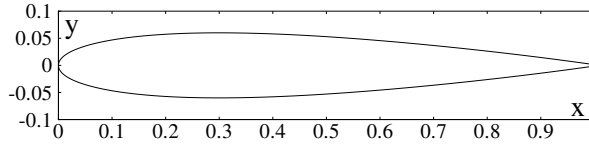


FIGURE 5.1: NACA0012 airfoil

There is a vast amount of data available for the flow over the NACA 0012 airfoil at free-stream Mach-number  $M_\infty = 0.8$  and angle of attack  $\alpha = 1.25^\circ$ . Six numerical results, obtained independently by different authors, are reported in ref. [4]. In this AGARD report the static pressure, Mach and total pressure distribution along the upper and lower surface of the airfoil are given. Also, the lift-coefficient  $c_l$ , the drag-coefficient  $c_d$ , and the moment-coefficient around the 1/4 chord point  $c_m$ , for the airfoil are given. The results reported in ref. [4] were all obtained on structured grids of either C or O type.

### 5.1.1 Generation of the unstructured mesh

A problem which is encountered when generating a mesh around the NACA 0012 airfoil, is that the trailing edge of the airfoil has a finite thickness,  $\pm y_{te} = 0.0105t$ , which is an undesirable property since a finite trailing edge thickness will introduce unwanted vortices as well as some unsteadiness at the trailing edge. Therefore, the trailing edge should have zero thickness. Rivers and Wahls [58] discuss different methods used to overcome the finite trailing edge thickness problem. Based on the work by Rivers and Wahls [58], a sliver of thickness is removed from the lower and upper surface, varying linearly from the trailing edge to the leading edge, so that

$$\begin{aligned} \pm y_{t,c} &= \pm y_t \mp 0.0105tx \\ &= \frac{t}{0.20}(0.29690\sqrt{x} - 0.12810x - 0.35160x^2 + 0.28430x^3 - 0.10150x^4) \end{aligned} \quad (5.4)$$

where  $y_{t,c}$  is the ordinate of the airfoil with zero thickness at the trailing edge.

Since the flow-field over the NACA 0012 airfoil is known from other numerical methods, this solution can be used to refine the mesh at places of high solution gradient. Large gradients occur around the stagnation point at the nose, the trailing edge, and at the shock on the upper surface as well as the (weak) shock on the lower surface.

The distance between two nodes will be referred to as the mesh size  $h$ . The mesh is refined at the nose, to capture the large gradient of the flow expanding from the stagnation point over

the sharply curved nose. The refined mesh at the nose has a constant mesh size  $h_{nose}$  and runs from  $x/c = 0$  to  $x/c = 0.03$ . The mesh at the surface is also refined at both the upper and lower shock location. The mesh size at both shocks is equal to  $h_{shock}$ . The mesh size between the nose and the shock is increased with 10% every successive node until the mesh size reaches a given maximum size  $h_{max}$ . To capture the shock at the upper surface, which has a height of approximately one chord length, the mesh around the shock is also refined, again with mesh size  $h_{shock}$ .

The inflow and outflow boundary, and the far-field boundaries at the lower and upper part of the domain are located at 50 chord lengths from the airfoil. Since the flow field far from the airfoil is uniform, the mesh can be chosen conveniently coarse at these boundaries. The number of nodes on the far-field boundaries and the inflow and outflow boundary is set to 10.

The mesh-size at the nose and the mesh size at the shocks on the lower and upper surface, are input parameters of a program which creates the nodes on the surface of the airfoil and at the inflow, outflow and far-field boundaries. These nodes are then used as input for Delaundo, the program which creates the triangular mesh. Four different meshes have been created, indicated by mesh I, II, III and IV, respectively. The corresponding mesh parameters are listed in table 5.1.

mesh	mesh size $h$ [x/c]			number of nodes	
	nose	shock	max	total	on airfoil (upper-lower)
I	0.003	0.005	0.015	4019	103 - 106
II	0.001	0.005	0.015	4803	143 - 143
III	0.001	0.003	0.010	6249	171 - 174
IV	0.001	0.002	0.008	7536	202 - 207

TABLE 5.1: NACA 0012 mesh parameters

In comparison with the structured meshes given in ref. [4], the unstructured meshes I to IV combine a higher number of nodes on the airfoil with a lower number of total nodes. The finest structured mesh, for example, is of O-type and consists of  $320 \times 64$  nodes with 320 nodes on the airfoil. The ratio of total nodes and nodes on the airfoil is therefore 64, while for unstructured mesh IV this ratio is around 18. It is therefore expected that the computational effort to obtain a converged solution with similar accuracy is lower for the present unstructured meshes.

In Fig. 5.2 mesh I is shown. In the left plot we see the complete mesh, and in the right plot, a close-up of the mesh around the airfoil is shown.

### 5.1.2 Results

The flow is solved with the 2D version of the numerical method, using the AUSM<sup>+</sup> scheme with  $\alpha = 3/16$  and  $\beta = 1/8$ , and second-order accurate fluxes with  $\kappa = 1/3$ . Since the total pressure is of atmospheric level, the air is treated as a perfect gas. The boundary condition at the inflow is the total-value preserving subsonic inflow boundary condition with  $p_0 = 1.0$  bar and  $T_0 = 300$  K. At the outflow the subsonic outflow boundary condition is used, with static pressure  $p/p_0 = 0.656$ . Assuming that we have the same static pressure far upstream and downstream of the profile, the resulting free-stream Mach number is  $M_\infty = 0.8$ . At

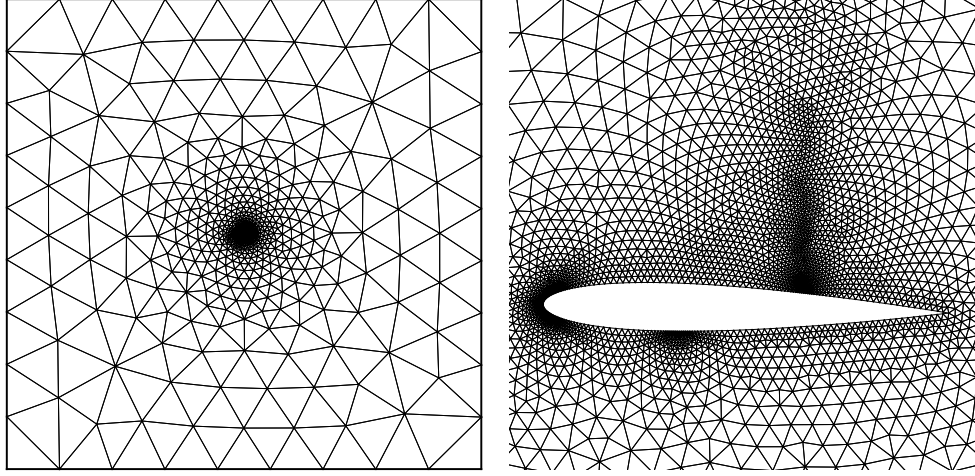


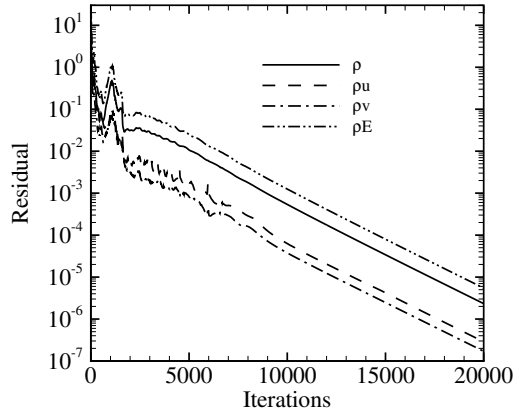
FIGURE 5.2: NACA0012 airfoil: triangular mesh I.

the upper and lower boundaries of the domain the far-field boundary conditions are imposed, with the same total flow conditions as at the inlet boundary.

The  $L_2$ -norm of the residuals of the state vector, defined as

$$L_2(\mathbf{U}) = \frac{1}{N} \sqrt{\sum_{i=1}^N \left( \frac{\mathbf{U}_i^{n+1} - \mathbf{U}_i^n}{\Delta t_i} \right)^2}, \quad (5.5)$$

where  $N$  is the number of nodes, and  $n$  the iteration number, for mesh I is shown in Fig. 5.3. After 10,000 iterations the  $L_2$ -norm of the residual of the density has dropped below  $10^{-3}$ .

FIGURE 5.3: NACA 0012,  $M_\infty = 0.8$ ,  $\alpha = 1.25^\circ$ .  $L_2$  norm of the residuals for mesh I.

The evolution of the residuals hereafter exhibits no bumps, and the location of the shock on

the upper side of the airfoil after 10,000 iterations remains the same. The lift-, drag- and moment-coefficient after 15,000 iterations and 20,000 iterations are identical up to the fourth decimal. Since the coefficients given in ref. [4], have only four decimals, it is concluded that the solution is accurate enough once the L2-norm of the residual of the density is lower than  $0.5 \times 10^{-4}$ .

For the solution obtained on mesh I, the total pressure loss is calculated along the upper and lower surface. The result is shown in Fig. 5.4. As a reference, the distribution given in

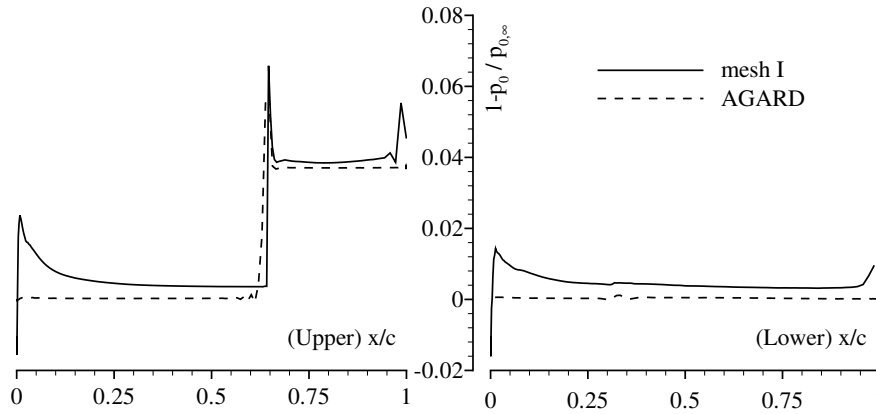


FIGURE 5.4: NACA 0012,  $M_\infty = 0.8$ ,  $\alpha = 1.25^\circ$ . Total pressure loss on the upper and lower surface.

ref. [4] for the  $320 \times 64$  O-type mesh, which is the only solution provided in tabular form, is also plotted in this figure. This solution will be referred to as the “AGARD” solution. The “AGARD” solution is used here for comparison with the present results.

From Fig. 5.4 we see that there is a relatively large total-pressure loss on the nose at both the upper and lower surface of the mesh. Since the flow should be isentropic here, the total pressure loss is purely numerical. The jump in the total pressure loss across the shock wave as obtained with the present method agrees well with that of ref. [4], while the shock in the present result is slightly downstream of the shock in the results of ref. [4]. Also, at the trailing edge the present method features a peak in the total-pressure loss due to numerical effects.

To appreciate this, one should realize that, in theory, at the trailing edge the total pressure is two-valued, caused by the difference in shock strength for the shocks on the upper and the lower surface. At the trailing edge the static pressure is continuous, so that the difference in total pressure results in a difference in velocity (Mach-number). This implies that the streamline (contact surface) from the trailing edge is tangential to the lower surface, i.e. the upper-surface trailing edge point is a stagnation point and the lower surface trailing-edge point is a point where  $M \neq 0$ . In the numerical method, the trailing-edge is a node and uniquely associated with it is a control volume, i.e. we cannot accommodate a two-valued solution at the trailing edge.

In an attempt to reduce the total pressure loss at the nose, the mesh-size at the nose is reduced (mesh II). The solution is iterated until the L2-norm of the residual of the density is

lower than  $0.5 \times 10^{-4}$ , which is after approximately 8,400 additional iterations. The total-pressure loss along the upper and lower surface for mesh II after 10,000 iterations is plotted in figure 5.5. As can be seen from Figs. 5.4 and 5.5, the total pressure loss at the nose has

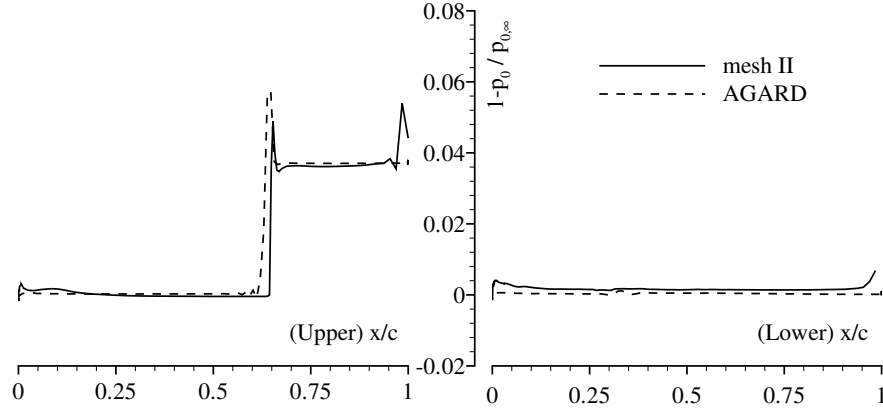


FIGURE 5.5: *NACA 0012*,  $M_\infty = 0.8$ ,  $\alpha = 1.25^\circ$ . Total pressure loss on the upper and lower surface.

reduced considerably, and it can be concluded that the mesh-size at the nose is now small enough. The position of the shock on the upper surface, however, has also changed (further downstream). To investigate the sensitivity of the shock location on the mesh-size, a solution is obtained on mesh III and IV, which have a smaller mesh size in the shock region and a smaller maximum mesh size. Again, the same criterion for convergence of the solution as was used on mesh I and II is used. For all meshes, the position of the shock on the upper surface is tabulated in table 5.2. The position of the shock is different for each mesh, but the

mesh	upper shock (x/c)	$c_l$	$c_d$	$c_m$
I	0.647	0.3791	0.0271	-0.0460
II	0.650	0.3861	0.0269	-0.0478
III	0.654	0.3908	0.0271	-0.0488
IV	0.655	0.3902	0.0267	-0.0485

TABLE 5.2: *NACA 0012*,  $M_\infty = 0.8$ ,  $\alpha = 1.25^\circ$ . Aerodynamic coefficients and shock position for the different meshes.

changes in position are small, and the difference in position for mesh III and mesh IV are very small. Furthermore, if we consider the pressure distribution over the airfoil, shown in Fig. 5.6, we see that the shock on the upper surface is steeper than the shock in the reference AGARD solution, but that the end-point of the shock for both the present result (mesh IV) and the reference AGARD solution is located at the same position. From Fig. 5.6 we also observe that for the lower surface, the (weak) shock is more smeared.

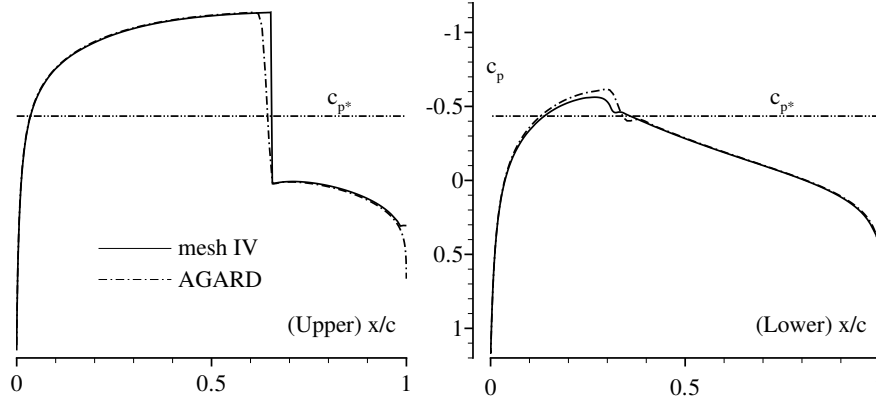


FIGURE 5.6: NACA 0012,  $M_\infty = 0.8$ ,  $\alpha = 1.25^\circ$ . Pressure coefficient  $c_p = (p - p_\infty)/(\frac{1}{2}\gamma p_\infty M_\infty^2)$ , mesh IV compared with ref. [4].  $c_{p^*} = 0.43464$ .

In table 5.2, the lift-coefficient  $c_l$ , drag-coefficient  $c_d$ , and moment-coefficient  $c_m$  around the  $\frac{1}{4}$ -chord point are also given. These aerodynamic coefficients are found by integrating the static pressure over the surface, see Anderson [6]. Since the  $x$ -direction corresponds with the free-stream direction, we find:

$$c_l = \frac{l}{\frac{1}{2}\gamma p_\infty M_\infty^2 c} = \frac{-1}{\frac{1}{2}\gamma p_\infty M_\infty^2 c} \int_{\partial A} p n_y dC, \quad (5.6)$$

$$c_d = \frac{d}{\frac{1}{2}\gamma p_\infty M_\infty^2 c} = \frac{-1}{\frac{1}{2}\gamma p_\infty M_\infty^2 c} \int_{\partial A} p n_x dC, \quad (5.7)$$

$$c_m = \frac{m}{\frac{1}{2}\gamma p_\infty M_\infty^2 c^2} = \frac{1}{\frac{1}{2}\gamma p_\infty M_\infty^2 c^2} \int_{\partial A} p \{y n_x - (x - \frac{1}{4}c) n_y\} dC, \quad (5.8)$$

where  $\vec{n}$  is the outward-pointing contour normal on the airfoil contour  $\partial A$ .

The calculated values of the lift-, drag-, and moment-coefficient are different for each mesh, but converge to a certain value with decreasing mesh size. The aerodynamic coefficients are all somewhat larger than those reported in ref. [4]. In ref. [4] there is also some scatter in the values of  $c_l$ ,  $c_d$ , and  $c_m$  contributed by the different authors. The values corresponding to the “AGARD” solution are:  $c_l = 0.3632$ ,  $c_d = 0.0230$ ,  $c_m = -0.0397$ . The scatter in the data provided by the different authors amounts to  $\Delta c_l = 0.0273$ ,  $\Delta c_d = 0.0023$ ,  $\Delta c_m = 0.0072$ .

The difference between the present results and the “AGARD” solution are caused by the different pressure distributions over the airfoil, see Fig. 5.6. Since the lift- and drag-coefficients are found by integrating the pressure over the surface, they are proportional to the area enclosed by the  $c_p$ -curve. For the upper surface, the positive contribution to the lift is larger than for the reference case, primarily because in our result the shock is steeper than in the reference case. For the lower surface, the negative contribution to the lift is smaller be-

cause in our result the (weak) shock is more smeared. The net result is a higher lift-coefficient for the present results in comparison to the reference case.

Fig. 5.7 shows the map of Mach iso-contours for the solution on mesh IV. Clearly visible

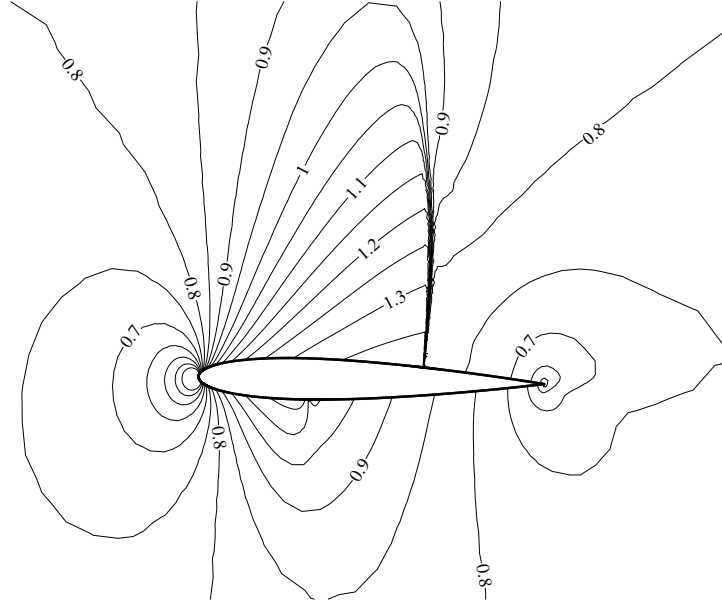


FIGURE 5.7: NACA 0012,  $M_\infty = 0.8$ ,  $\alpha = 1.25^\circ$ . *Iso-Mach lines, mesh IV* ( $\Delta M = 0.05$ ).

is the shock on the upper side of the profile, extending almost one chord length into the flow-field. The shock on the lower side of the profile is weak and not as clearly visible as the stronger shock on the upper side.



## 5.2 Parallel-jet nozzle A1

The parallel-jet nozzle A1 is a nozzle with relatively little divergence downstream of the throat section, and has a straight outflow section downstream of the divergent part of the nozzle. The flow in the nozzle is therefore very sensitive to variations in the back pressure, and to variations in the inlet vapour fraction. The flow in this 2D nozzle has been extensively investigated, numerically as well as experimentally, by Schnerr and Adam [3], which makes this a very suitable test-case to validate the present numerical method.

The geometry of the nozzle is given in Fig. 5.8. The nozzle has a straight outflow section

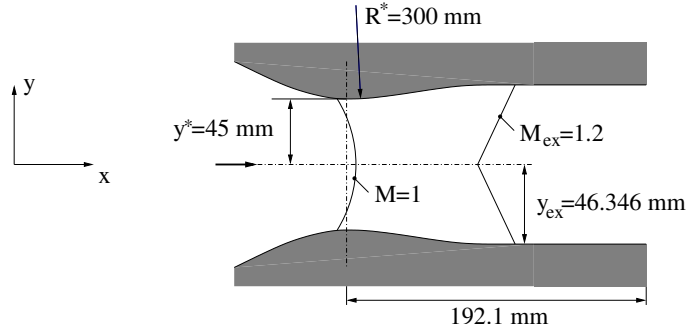


FIGURE 5.8: Geometry of the parallel-jet nozzle A1 (schematic).

with a length of  $\approx 104.5$  mm, starting at  $\approx 87.6$  mm downstream of the throat. The throat of the nozzle has a height of  $2y^* = 90$  mm, and has the shape of an arc with a radius  $R^* = 300$  mm. The height of the nozzle at the outflow boundary is  $2y^* \approx 92.69$  mm, so that for an isentropic flow of air through the nozzle, the outflow Mach number is  $M_{ex} = 1.2$ . More details can be found in Adam ([3], section 5.2)

We will consider the flow of dry air and the flow of wet air through the parallel-jet nozzle. In the experiments, the parallel outflow section of the nozzle is connected to an adjustable diffuser, which makes it possible to control the pressure at the outflow of the nozzle. The experimental setup is sketched in Fig. 5.9. For the flow of wet air, the diffuser is adjusted such that the cross-sectional area of the diffuser is larger than the cross-sectional area of the parallel outflow section of the nozzle. In this way, the flow in the nozzle is completely determined by the geometry of the nozzle, and not by the pressure at the parallel outflow boundary of the nozzle. The flow of wet air exhibits a shock in the diverging part of the nozzle, upstream of the parallel outflow section of the nozzle. The location of the shock is completely determined by the geometry of the nozzle, since the flow expands into vacuum downstream of the diffuser. For the flow of dry air, the diffuser was adjusted such that the flow exhibits a shock at the same location as is the case for the flow of wet air.

In the numerical simulations, two different geometries are used. Flows with condensation are calculated on a mesh, in which the flow due to a slight divergence downstream of the parallel part of the nozzle is expanded once more. In this way, the flow is accelerated to supersonic velocity, in the same way as in the experiments due to the expansion into the vacuum. The flow with condensation is therefore solely determined by the geometry of the

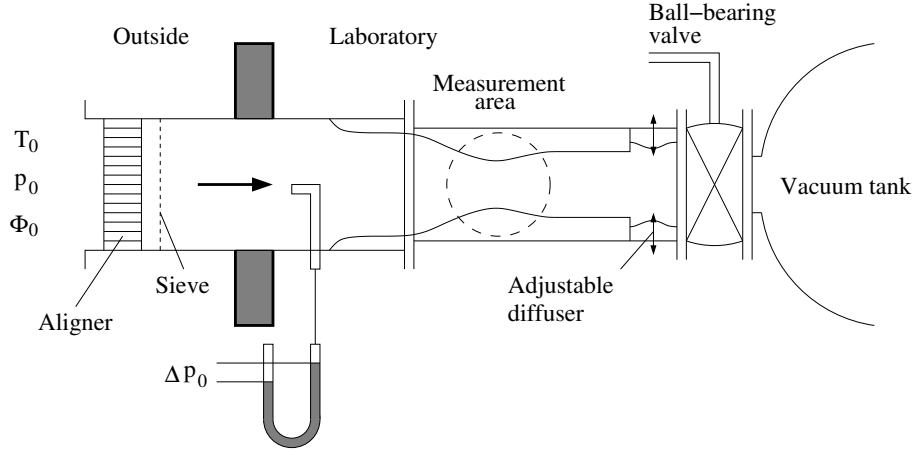


FIGURE 5.9: Schematic construction of the supersonic wind-tunnel, figure reproduced from Adam's thesis [3].

nozzle, independent of the outflow boundary condition. On the other hand, the flow of dry air, without condensation, is calculated on a mesh that does not have a divergent part downstream of the parallel part of the nozzle. In this way, a back pressure can be imposed at the outflow boundary, which in its turn can be adjusted such that a shock will be located at the same location as for the flow with condensation.

The shape of the nozzle wall, which is needed to create the triangular mesh, was obtained from the structured mesh generated by Adam [3]. Two different geometries are available for the A1 nozzle, one with a straight outflow section, used for the dry flow simulations (dry air mesh), and one with an added divergent part downstream of the straight outflow section, used for the wet air flow simulations (wet air mesh).

The dry air mesh consists of  $211 \times 41$  nodes in  $x$ - and  $y$ -direction, respectively. The wet air mesh consists of  $221 \times 41$  nodes in  $x$ - and  $y$ -direction, respectively. From the dry air structured mesh, two different meshes were created, one using every second node of the structured nozzle mesh boundaries, and one using all nodes of the boundaries. The first triangular mesh thus has 250 boundary nodes and consists in total of 3519 nodes and 6786 triangles, and will be referred to as the dry air coarse mesh. The second triangular mesh has 500 boundary nodes and consists in total of 13805 nodes and 27108 triangles, and will be referred to as the dry air fine mesh.

In a similar way as for the dry air structured mesh, a coarse and a fine wet air unstructured mesh were created. The wet air coarse mesh consists of 3646 nodes and 7030 triangles, and the wet air fine mesh consists of 14294 nodes and 28066 triangles. The dry air coarse mesh and the wet air coarse mesh are shown in Fig. 5.10. Note that the meshes are not symmetric around the axis  $y = 0$ . For flows with bifurcation, an additional symmetric mesh would be needed, which can be constructed by mirror imaging an unstructured mesh for  $y \geq 0$  around the  $x$ -axis. Since bifurcation is not studied for the flow in the A1 nozzle in this thesis, this is not considered further.

Since the coarse meshes consists of considerably less nodes, the number of iterations needed to obtain a converged solution is substantially lower for the coarse meshes than for

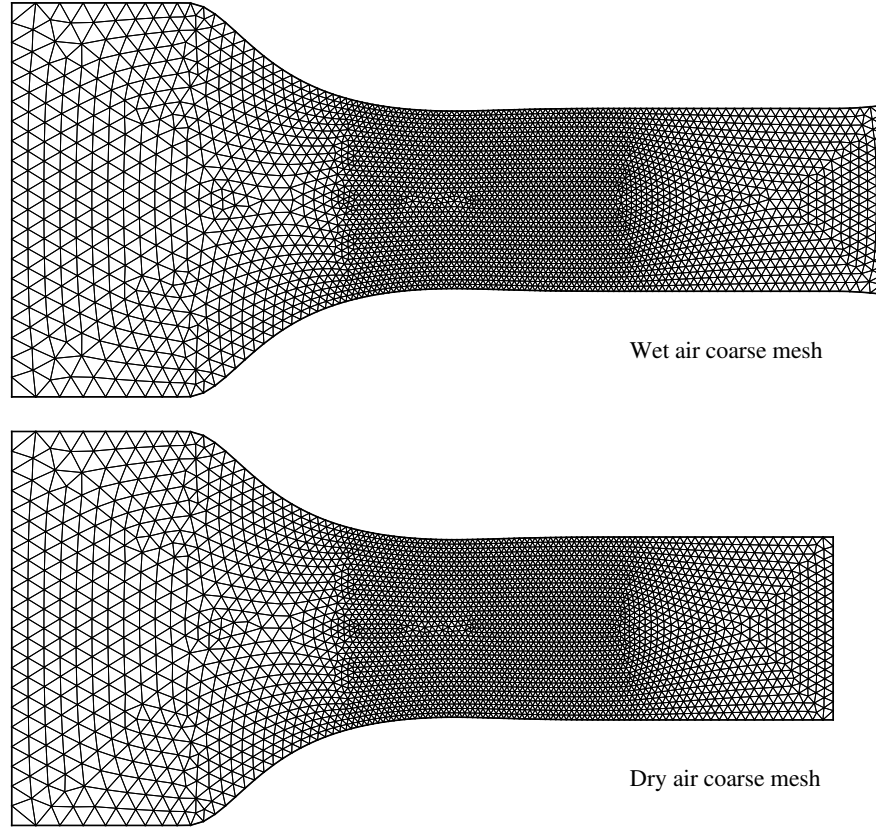


FIGURE 5.10: A1-nozzle: coarse triangular meshes created with Delaundo, for dry air and wet air flow simulations.

the fine meshes. The amount of work needed to perform one iteration is also less for the coarse meshes. Results obtained on the coarse meshes are used as initial solution on the fine meshes (using the linear solution interpolation method described in appendix B), and the results obtained on the fine meshes are compared with those obtained on the coarse meshes.

For both the dry air and wet air test cases, the reservoir (total) pressure and temperature at the inlet are  $T_0 = 298.7$  K and  $p_0 = 1.004$  bar, respectively. The wet air has a reservoir saturation of  $\Phi_0 = 35.6\%$ . The maximum liquid mass fraction follows from Eq. (2.95),  $g_{max} = 7.253$  g/kg. The imposed pressure at the outflow boundary for the dry air is  $p = 0.6339$  bar. The flow is solved with 2D version of the computational method, using the AUSM<sup>+</sup> scheme with  $\alpha = 3/16$  and  $\beta = 1/8$ , and second-order accurate fluxes with  $\kappa = 1/3$ . Since the total pressure is of atmospheric level, the air/water mixture is treated as a perfect gas. Nucleation is calculated with the CNT model.

### 5.2.1 Dry flow with shock

First, the flow of dry air with a shock is calculated on the coarse dry air mesh. An initial solution with a Mach number of  $M = 0.7$  is imposed everywhere in the nozzle. The boundary

condition at the inflow is the total-value preserving subsonic inflow boundary condition. At the outflow the subsonic outflow boundary condition is used. The  $L_2$ -norm of the residuals, given by Eq. (5.5), is shown in Fig. 5.11. After approximately 2,000 iterations the flow

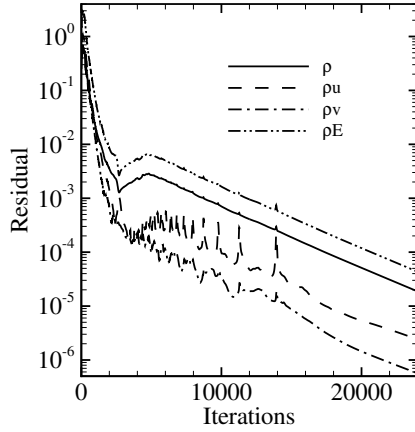


FIGURE 5.11: *A1-nozzle, coarse mesh. Residuals for dry flow with shock.*

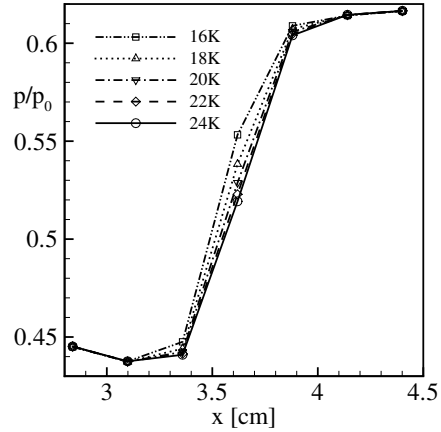


FIGURE 5.12: *A1-nozzle, coarse mesh, dry flow with compression shock. Pressure at symmetry line of the nozzle for different iteration levels.*

becomes supersonic in the throat, and after approximately 5,000 iterations a shock starts to form directly downstream of the throat. As the iteration process continues, the shock moves further downstream. The bumps in the residuals, best seen in the residuals of  $\rho u$  and  $\rho v$ , indicate the shock moving downstream from one control volume to the next one. Finally, after more than 14,000 iterations, the shock stays at the same discrete location, and only minor changes are taking place in the flow field, as can be seen from the smooth decrease of the residuals. The pressure rise through the steady shock is shown in Fig. 5.12, from which we can also see that the shock stays at the same location, and the small changes in pressure at the shock become smaller per iteration, indicating that the solution is converging to a final, steady-state solution.

With the solution interpolation method, the solution on the coarse mesh obtained after 24,000 iterations, is used to generate an initial solution on the fine mesh. The flow conditions are kept the same, and the computational 2D flow method is run for another 50,000 iterations. The residuals of the iteration process are shown in Fig. 5.13. As can be seen from the residuals, the convergence is considerably slower than for the coarse mesh. After 50,000 iterations, the residuals have decreased more than five orders in magnitude, and the solution is considered to be sufficiently converged.

The solution on the fine mesh after 50,000 iterations is shown in Fig. 5.14. The flow reaches a maximum Mach number of  $M = 1.159$  (compared to  $M = 1.154$  for the coarse mesh) at the symmetry line directly upstream of the shock, indicating that the shock is weak. The total pressure loss resulting from the shock is  $1 - p_t/p_0 = 0.0046$  (compared to  $1 - p_t/p_0 = 0.0051$  for the coarse mesh). Theoretically, following from the Rankine-Hugoniot relations for a

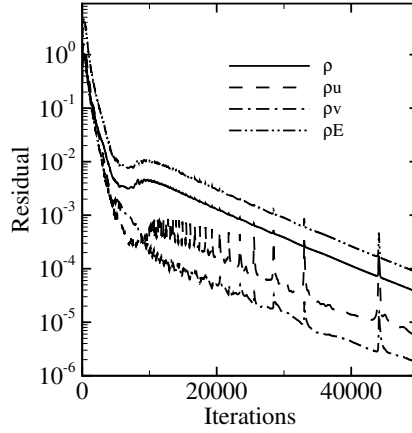


FIGURE 5.13: A1-nozzle, fine mesh. Residuals for dry flow with shock.

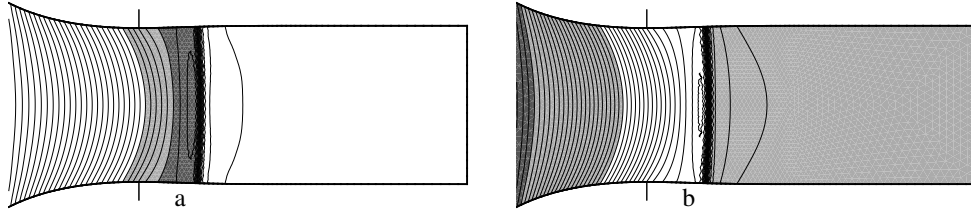


FIGURE 5.14: Numerical simulation on fine mesh of dry flow with shock in parallel-jet nozzle A1;

	quantity	symbol	light grey	dark grey	increment
a	Mach-number	$M$	$> 1$	$> 1.1$	0.02
b	pressure	$p/p_0$	$> 0.6$	$> 0.8$	0.01

normal shock with upstream Mach number  $M = 1.159$ , the shock should result (for dry air) in a total pressure loss of  $1 - p_t/p_0 = 0.0049$ . At the outflow boundary the Mach number is  $M_{ex} = 0.83$  (which is the same as for the coarse mesh).

### 5.2.2 Flow with condensation

Now that the dry flow field with a steady compression shock is achieved, it can be used as initial solution for the flow with condensation. First, an initial solution on the coarse wet air mesh is obtained from the solution on the fine dry air mesh, with the solution interpolation method described in appendix B. The saturation is changed from  $\Phi_0 = 0$  to  $\Phi_0 = 0.356$ , corresponding to a maximum liquid mass fraction of  $g_{max} = 7.25$  g/kg. The boundary condition at the outflow is changed to the supersonic outflow boundary condition.

The residual during the iteration process is shown in Fig. 5.15. As can be seen, the solution converges to machine zero in about 50,000 iterations.

The solution interpolation method is used to obtain an initial solution on the fine mesh,

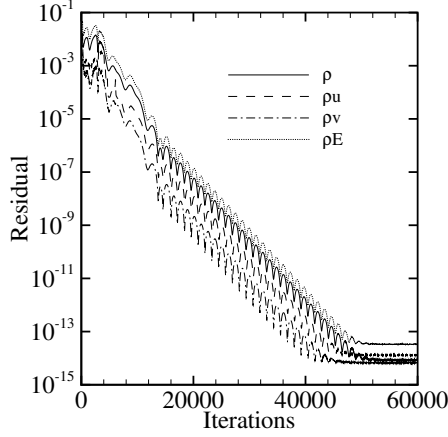


FIGURE 5.15: *A1-nozzle: residuals, flow with condensation and shock, coarse mesh.*

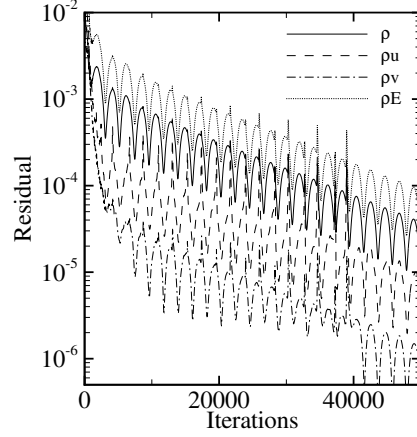


FIGURE 5.16: *A1 nozzle: residuals, flow with condensation and shock, fine mesh.*

based on the converged, wet flow solution on the coarse mesh. The residuals of the iteration process are shown in Fig. 5.16. Here, only the evolution of the residuals up to 50,000 iterations is shown, to emphasize the relatively slow convergence compared to the convergence on the coarse mesh. After approximately 300,000 iterations the residuals stop decreasing and become machine zero. The solution after 300,000 iterations is shown in Fig. 5.17. Note that the solution in the divergent part downstream of the parallel part of the nozzle is not shown, since we are not interested in this part of the solution. Recall that the divergent part was only added to the nozzle to ensure supersonic velocity at the outflow boundary, so that the outflow boundary does not have any influence on the solution upstream of the added divergent part. In Fig. 5.17a we see the expansion of the mixture to supersonic speed with a maximum Mach number of  $M_f = 1.157$  at the symmetry line. Downstream of the throat, the supersonic flow is terminated by a normal shock, represented on the mesh by three nodes. The location of these points is  $x = 3.39$ ,  $x = 3.51$  and  $x = 3.64$  cm (at the symmetry line). In Fig. 5.17b we see the saturation of the flow increasing from  $\Phi < 1$  upstream of the throat to a super-saturation with maximum value of  $\Phi = 20.1$  one cell upstream of the shock. As soon as the air/water-vapour mixture becomes super-saturated, droplets start to form in the nucleation process, as can be seen in Fig. 5.17c, where the logarithm of the nucleation rate is shown. The nucleation rate reaches a maximum of  $J = 2.03 \times 10^{19} \text{ m}^{-3}\text{s}^{-1}$  in the central part of the nozzle just upstream of the shock. The shock interacts with the condensation process, as it cuts off the process of nucleation which is a direct result of the decrease of the super-saturation. Fig. 5.17d gives the number of droplets formed during nucleation, most in the central region of the nozzle, where the super-saturation was highest. The number of droplets becomes significant in the nucleation zone just upstream of the shock. The droplets formed here, do not evaporate completely when passing through the shock. Downstream of the shock the droplets grow again, because, despite the shock, there is still super-saturation. From the shock, the droplets are convected downstream with the flow. The release of latent heat during the condensation, caused by the growing droplets, is an internal source of energy to the fluid in the gaseous phase. As a result, the fluid at subsonic speed downstream of the shock, expands in the straight outflow section to nearly sonic speed just upstream of the

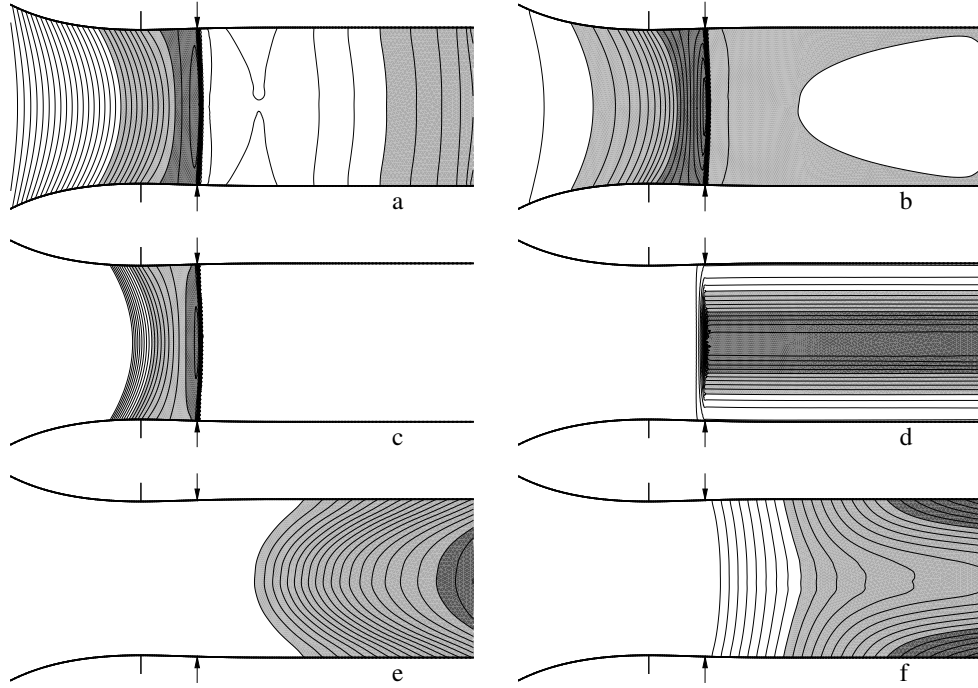


FIGURE 5.17: Numerical simulation on fine mesh of wet flow in parallel-jet nozzle A1. The arrow indicates the shock position. The results are shown up to the diverging outflow section.

	quantity	symbol	light grey	dark grey	increment
a	Mach-number	$M_f$	$> 0.9$	$> 1.1$	0.02
b	super-saturation	$\Phi$	$> 2$	$> 12$	1
c	nucleation rate	$\log_{10} J [\text{m}^{-3}\text{s}^{-1}]$	$> 10$	$> 18$	1
d	number of droplets	$Q_0 [10^{14}\text{kg}^{-1}]$	$> 1$	$> 2$	0.2
e	liquid mass fraction	$g/g_{max}$	$> 0.05$	$> 0.5$	0.025
f	Hill droplet radius	$r_H [\mu\text{m}]$	$> 0.1$	$> 0.2$	0.01

added divergent outflow section. The distribution of the liquid-mass fraction and that of the droplet radius, shown in Figs. 5.17e and 5.17f, respectively, are quite smooth. The liquid-mass fraction increases downstream of the shock to a maximum value of  $0.535 g/g_{max}$  on the symmetry line just upstream of the divergent outflow section. The droplets reach a maximum radius of  $0.258 \mu\text{m}$  near the wall just upstream of the divergent part of the wall. That the droplets near the wall are larger is because the number of droplets at the wall is smaller, and have the opportunity to grow larger than the larger amount of droplets in the central region of the nozzle. However, still most liquid is in the central region, see Fig. 5.17c.

### 5.2.3 Comparison between fine and coarse mesh wet flow solution

For the flow with condensation, the results obtained on the coarse and the fine mesh are compared by considering the flow solution along the symmetry line. The results are shown in Fig. 5.18. The properties such as Mach-number  $M_f$ , temperature  $T$  and pressure  $p$  agree very

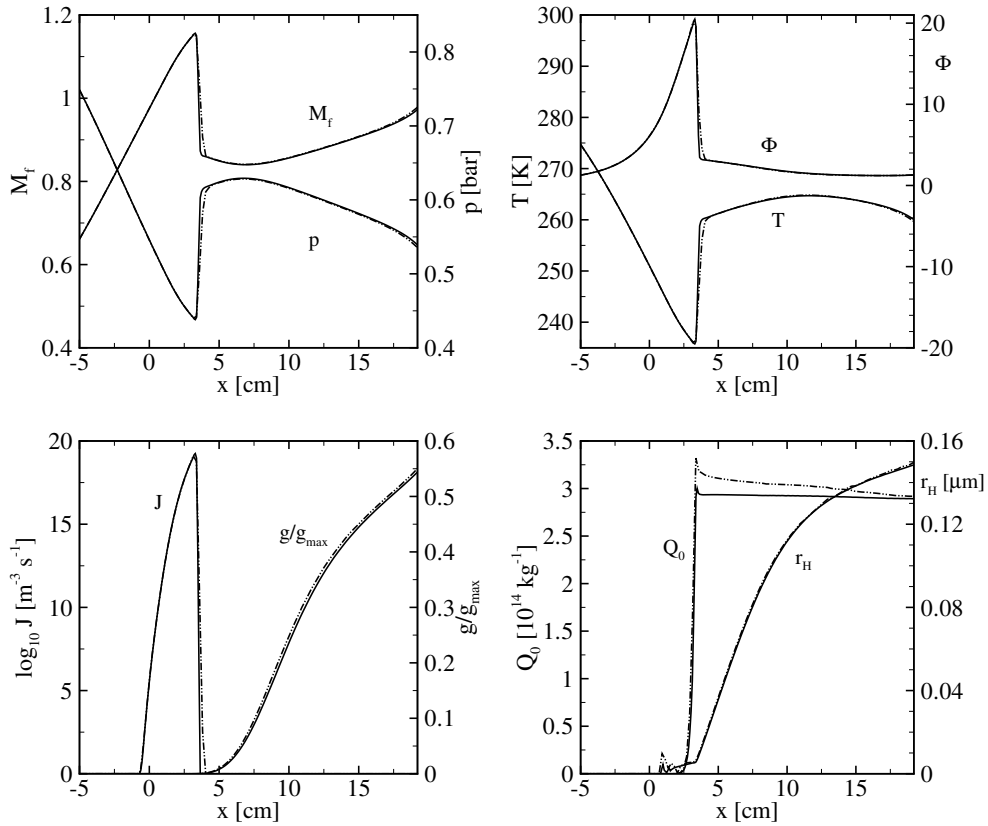


FIGURE 5.18: A1-nozzle, wet flow. Coarse (---) and fine (—) mesh solution along the symmetry line. The results are shown up to the diverging outflow section.

well, with the results for the coarse mesh somewhat more smeared at the shock. Although not clearly visible from Fig. 5.18, the super-saturation  $\Phi$  on the coarse mesh is somewhat larger upstream of the shock, with the maximum super-saturation just upstream of the shock somewhat smaller than on the fine mesh.

This results, for the coarse mesh, in a slightly larger region with significant nucleation rate  $J$ , with the maximum nucleation rate somewhat smaller, all in all resulting in a larger number of droplets  $Q_0$ . Also, as can be seen from Fig. 5.18, the liquid-mass fraction  $g$  is slightly larger for the coarse mesh solution. As a consequence, the Hill droplet radius  $r_H$  distribution is practically the same for the coarse and fine mesh solution.

Since the solution on the fine mesh does not differ significantly from the solution on the coarse mesh, we can conclude that on the fine mesh the solution has become sufficiently grid-independent.

#### 5.2.4 Comparison with results from literature

The thesis of Adam [3] contains experimental and numerical results for the A1 nozzle. The experimental results consist of schlieren pictures of the dry flow and the wet flow, and of



the static pressure along the centerline of the nozzle, also for both the dry flow and the wet flow. The numerical results contain the Mach number, the nucleation rate, and the liquid mass fraction.

### Experimental and numerical schlieren images

Schlieren images give a qualitative representation of the gradient of the density in a specified direction. Schlieren-like images can therefore be obtained from the numerical results by calculating the gradient of the density throughout the flow field. For the A1 nozzle, the experimental schlieren image represents the gradient in the  $x$ -direction, therefore the numerical schlieren image is calculated as  $\frac{\partial \rho}{\partial x}$ . Fig. 5.19 shows the experimental and numerical schlieren images. Comparing the two schlieren images, we see that at the centerline the shock in the

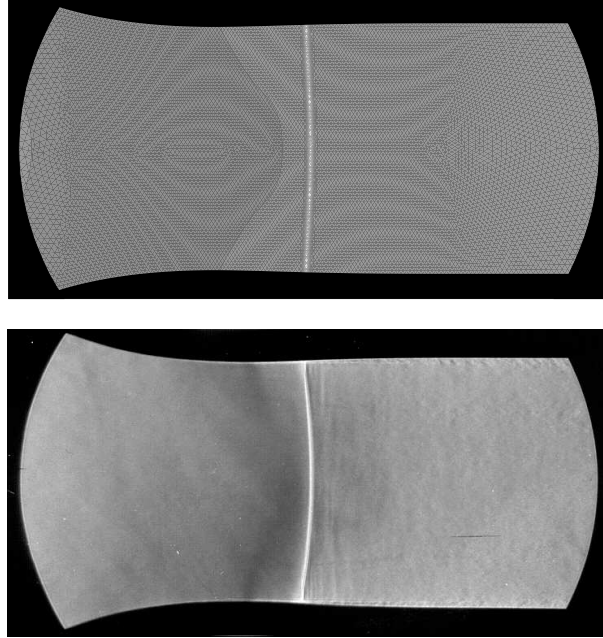


FIGURE 5.19: A1 nozzle, wet flow. Numerical schlieren image ( $\frac{\partial \rho}{\partial x}$ ) produced from present result (upper), and schlieren picture of experiment (lower).

experiment is at the same location as in the numerical result. However, contrary to the numerical result, the shock is curved in the experiment. The curvature near the wall is caused by the interaction of the shock with the boundary layer along the wall, an effect not present in our model of the flow. In the experiment, we also observe the turbulent boundary layer downstream of the shock.

### Experimental and numerical static pressure distribution

In the experimental set-up of Schnerr & Adam [3], there are pressure orifices in the side-wall along the nozzle-axis of the measurement area (see also Fig. 5.9). The static pressure distribution, as pressure difference with the atmosphere, can then be measured by means of U-tube manometers. In this way, Schnerr (see ref. [3]) obtained the static pressure along the centerline at the side-wall of the A1 nozzle for both the dry flow and the wet flow. The experimentally obtained static pressure distribution is shown in Fig. 5.20, together with the static pressure distribution obtained from the present numerical results, for both the dry flow and the wet flow. The identical pressure distribution up to a location just downstream of the shock

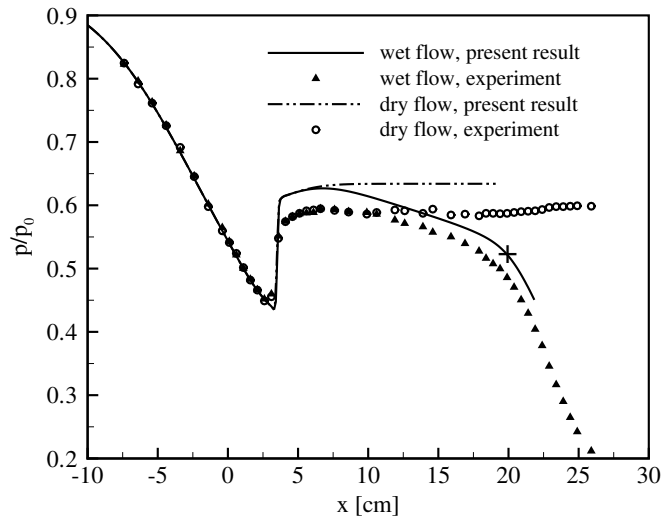


FIGURE 5.20: A1-nozzle, comparison between experimentally obtained pressure distribution and present results for the dry flow and the wet flow. The + indicates the location where the (numerically calculated) flow becomes supersonic.

for both the dry flow and the wet flow indicates, that not much heat is added over the shock. Downstream of the shock the pressure increases slightly due to the geometrical divergence of the nozzle, before the condensation sets in, releasing heat in the flow, resulting in an increase of the velocity and a monotonically decreasing pressure. For the dry flow, the pressure in the parallel part of the nozzle remains constant. Comparison between the experimental and numerical pressure distribution shows differences just upstream of the shock as well as downstream of the shock. Because of the interaction of the shock with the side-wall boundary layer in the channel, the pressure increase over the shock in the experimental pressure measurements is somewhat smeared out. In the experiment, the shock substantially increases the thickness of the boundary layer aft of the shock, so that the effective cross sectional area of the nozzle decreases. Since the flow is subsonic downstream of the shock, the decrease in effective cross sectional area will lead to an acceleration of the flow and a lower static pressure compared to the numerical results, for both the dry and the wet flow. The differ-

ence between the numerical results and the experiment is  $\sim 0.03p_0$ . Adam [3] finds very similar differences, both qualitative and quantitative, between his numerical results and the experimental data (see next section).

### Comparison with other numerical results

In the thesis of Adam [3], a numerical method is employed to simulate the wet flow in the A1-nozzle. The numerical method contains the same nucleation and droplet growth models as the present numerical method. The method applied by Adam [3] however, is based on structured grids, as opposed to the unstructured triangular grids used for the present computations.

The numerical results presented by Adam [3], contain the Mach number  $M_f$ , the nucleation rate  $J$ , the liquid mass fraction  $g$ , and the static pressure along the centerline. Adam [3] finds a maximum Mach-number of  $M_f = 1.16$  just upstream of the shock, while for the present results the maximum Mach-number is  $M_f = 1.157$ . The shock location is identical for both results. The maximum nucleation rate found by Adam is somewhat larger,  $J = 5 \times 10^{19} \text{ m}^{-3}\text{s}^{-1}$  and for the present computations  $J = 2.03 \times 10^{19} \text{ m}^{-3}\text{s}^{-1}$ . The liquid mass fraction at the outflow centerline is also somewhat larger,  $g/g_{max} = 0.56$  for Adam's computational results compared to  $g/g_{max} = 0.535$  for the present computational results.

In conclusion, the overall agreement between the present numerical results and the numerical results obtained by Adam [3], is good.

### 5.2.5 Discussion of the present numerical result

Although the present result for the wet flow in the A1 nozzle agrees quite well with experimental data and with another numerical result, the sensitivity of the solution to the expressions for the material properties, as presented in section 2.4, was not considered. For the surface tension, two expressions were presented, Eq. (2.96), obtained from Dohrmann's thesis [23], and Eq. (2.97), obtained from Lamanna's thesis [38]. The first expression was used in the numerical simulation of the wet flow in the A1 nozzle, since this expression was also used in the numerical method used by Adam [3]. In this way, utilizing the same material properties for water as Adam did, the correct implementation of the present numerical method has been validated, as presented in the preceding subsection.

To investigate the sensitivity of the solution of the wet flow in the A1 nozzle for the expression of the surface tension, expression (2.97) presented by Lamanna [38], has been implemented in the present numerical method. For the same flow conditions, the present numerical method, now containing expression (2.97) for the surface tension of water, is applied to obtain a converged solution on the fine mesh for the wet flow in the A1 nozzle, starting from the solution obtained with Dohrmann's expression for the surface tension of water.

The residuals converge to machine accuracy, in the same oscillating manner as shown in Fig. 5.16. The solution however, is slightly different from the solution presented in section 5.2.2. The shock is located somewhat further downstream, as is the region with nucleation upstream of the shock. The region in which the nucleation occurs is somewhat larger in streamwise direction. As a result, there are more droplets in the flow downstream of the shock, and with the distribution of the liquid mass fraction being more or less the same, but located further downstream, the droplets are somewhat smaller in size. This demonstrates not only the complexity of the condensation process and the need to correctly represent the material properties of the condensing substance, but also the extreme sensitivity of the flow in

---

the A1 nozzle to small changes in the conditions or model parameters. Lamanna [38] argues that “the entire set of experimental data can best be correlated with a numerical method based on the following combination: reduced ICCT for the nucleation rate, the transitional Gyarmathy model for the droplet growth process and, the newly proposed surface tension fit”. The transitional Gyarmathy model (describing the droplet growth rate) is different from the Hertz-Knudsen droplet growth model used in the present calculations in that it takes into account the variation in Knudsen number during the growth of the droplets. The transitional Gyarmathy model also takes into account the difference in the temperature of the droplets and that of the flow, caused by the latent heat released by the vapour condensing on the droplets.

From this we can conclude that the good agreement of the present numerical results for the wet flow in the A1 nozzle, which are obtained by applying the CNT model rather than the reduced ICCT model, the Hertz-Knudsen model instead of the transitional Gyarmathy model, and Dohrmann’s expression instead of Lamanna’s for the surface tension of water, is caused by a “cancellation” of effects induced by the mathematical models for the condensation process applied in the present method. However, we should take into consideration that the wet flow in the A1 nozzle is extremely sensitive to small changes in the flow conditions, which is caused by the geometry of the A1 nozzle. It is expected that the flow in or around less critical geometries than the A1 nozzle is less sensitive to (the parameters in) the mathematical models used to describe the condensation process.

---

### 5.3 Supersonic underexpanded dry jet

A supersonic underexpanded jet is generated from a sonic or a supersonic flow exhausting from an axi-symmetric nozzle into an environment with a lower static pressure. The nozzle can have a shape which is optimized for a certain application, but it can also have an arbitrary shape, e.g. a rupture in a pipe containing gas at high pressure. Underexpanded jets are found in a number of applications, for example rocket exhausts at high altitude, vehicle manoeuvring thrusters, propulsion simulation devices and fuel injectors.

The basic features of the supersonic plume are shown in Fig. 5.21.

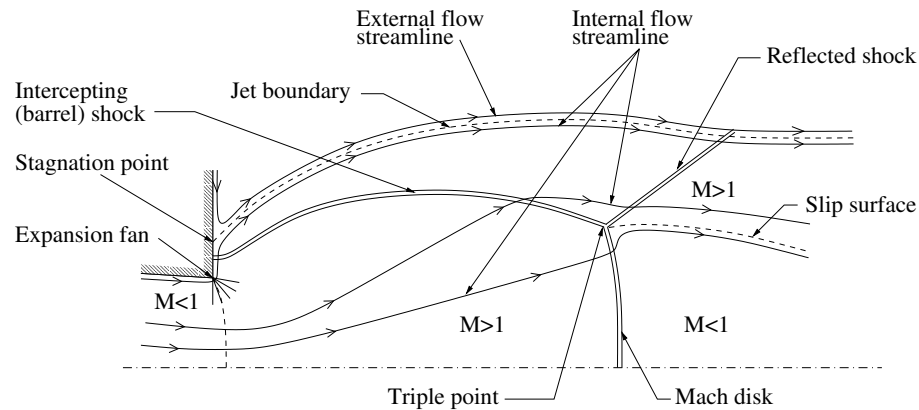


FIGURE 5.21: Schematics of the plume of an underexpanded nozzle

The flow ejecting from the nozzle at sonic velocity expands through an expansion fan centered at the edge (lip) of the nozzle. The expansion fan accelerates the flow to supersonic velocity and turns the flow away from the centerline, deflecting the flow over an angle of 90 degrees, such that it becomes adjacent to the vertical wall. The static pressure at the vertical wall just downstream of the nozzle lip becomes smaller than the ambient pressure, and a compression shock is formed which compresses the flow to the ambient pressure level. Downstream of this shock, there is a stagnation point, where the flow meets the ambient gas and separates from the vertical wall. The jet boundary, representing the contact discontinuity between the internal flow and the external ambient surroundings, is continuously curving towards the supersonic internal flow. Compression due to the curved jet boundary enhances the formation of the shock. The curved shock has the form of a barrel, and is therefore referred to as the barrel shock.

In the region enclosed by the barrel shock, streamlines seem to radiate from a single point, a “source” at a certain distance downstream of the nozzle orifice, see Ashkenas & Sherman [9]. The flow inside the barrel shock expands to a pressure which is much lower than the ambient pressure, and, depending on the pressure ratio, a shock normal to the centerline is formed, the so called Mach disk (named after its discoverer). The Mach disk decelerates the flow to subsonic velocity. Away from the centerline, the Mach disk curves towards the flow (concave when viewed from upstream) and intersects with the barrel shock. At the intersection a reflected shock is formed, which turns the streamlines, which are directed towards

the centerline just upstream of the reflected shock, in the direction of the centerline. The curvature of the Mach disk implies that the flow is being turned away from the centerline at the triple point. This corresponds to a Mach reflection, following Hornung's classification, see Hornung [32]. From the resulting triple-point, a slip line emanates to accommodate the difference in total pressure between the flow through the barrel shock and the reflected shock, and that through the Mach disk.

Detailed experimental data is available for underexpanded axi-symmetric jets. An excellent paper on this subject was written by Ashkenas & Sherman [9], who investigated the location of the Mach disk as a function of the reservoir/ambient pressure ratio for different gases, and gave a comprehensive explanation of the viscous effects in the free jet. It should be kept in mind that their results are based on measurements using a nozzle that consists of a converging part only, so that the outflow orifice is also the nozzle throat. Ashkenas & Sherman [9] conclude that the location of the Mach disk does not depend on properties of the gas, such as specific heat ratio, gas constant, etc., but only on the pressure ratio, as is evident from Fig. 5.37. From this figure, Ashkenas & Sherman [9] derived the following empirical relation for the distance of the Mach disk from the nozzle exit plane:

$$x_M/D \approx 0.67(p_r/p_a)^{1/2}, \quad (5.9)$$

where  $D$  is the nozzle throat diameter,  $p_r$  the total pressure in the reservoir, and  $p_a$  the pressure in the static ambient. The same type of relation was presented in an earlier paper by Crist et al. [18], but with a slightly different slope,

$$x_M/D \approx 0.65(p_r/p_a)^{1/2}, \quad (5.10)$$

The difference between both expressions is probably caused by the experimental difficulty of determining the exact location of the Mach disk. Crist et al. [18] study the Mach disk in more detail, and come to the following conclusions:

1. The Mach-disk location is insensitive to:
  - (a) the ratio of specific heats  $\gamma$ ,
  - (b) condensation,
  - (c) nozzle lip geometry, and,
  - (d) absolute pressure level.
2. The Mach-disk location is given by Eq. (5.10), for pressure ratios to 300,000 and probably higher.
3. Diameters of Mach disk, jet boundary, and barrel shock:
  - (a) increase with decrease in  $\gamma$ ,
  - (b) increase with condensation,
  - (c) decrease at high stagnation density for which intermolecular forces become important.
4. Ratio of Mach-disk diameter to Mach-disk distance from nozzle exit-plane is approximately a constant for high pressure ratios.
5. For the high Mach-number region, properties along the jet axis may be approximated by flow through a hypothetical conical nozzle.

Abbett [1] also gives a comprehensive explanation of the various flow features occurring in the underexpanded jet. Axi-symmetric Euler and Navier-Stokes equations have been used to

---

obtain numerical solutions for underexpanded jet plumes with impressive results, see Cumber et al. [20], [21], Gribben et al. [26], Berzins et al. [11], Prudhomme & Haj-Hariri [53]. These computational results demonstrate good agreement with experiments for a wide range of conditions using parameters such as Mach-disk location and centerline velocity and are reported to capture the complex flow structure in detail.

### 5.3.1 The computational domain

The primary goal is to simulate the flow ejecting from a circular nozzle. The injector consists of a reservoir containing quiescent gas at high pressure  $p_r$ , and a converging nozzle leading to the exit where the flow discharges into the ambient surroundings where the pressure is equal to  $p_a$ . The ratio between the pressure in the reservoir and the ambient surroundings is high enough that the nozzle flow becomes sonic and an underexpanded jet is formed at the exit. The computational domain, consisting of the nozzle and the external region (the ambient) is shown in Fig. 5.22. The outflow and far-field boundaries are preferably located at

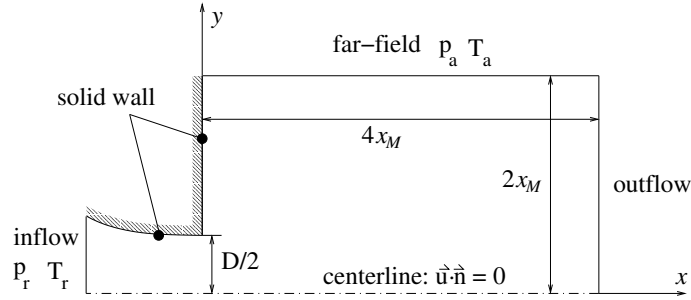


FIGURE 5.22: *Computational domain (not to scale) for axis-symmetric nozzle,  $x_M$  is the estimated Mach-disk location according to Eq. (5.9)*

a large distance from the nozzle orifice. For all calculations, the far-field boundary is placed at  $y = 2x_M$  and the outflow boundary is placed at  $x = 4x_M$ , where the location of the Mach disk  $x_M$  is determined from the empirical rule due to Ashkenas & Sherman [9], see Eq. (5.9). The influence of the location of the far-field and the outflow boundary on the solution is expected to be negligible, as is confirmed by the present computational results.

### 5.3.2 Boundary conditions

At the nozzle inflow, the stagnation conditions are the same as in the reservoir. Therefore, at the nozzle inflow, the total value preserving inlet boundary condition is applied. At the axis of rotational symmetry, the velocity normal to the boundary has to be zero. The boundary is therefore similar to that of a solid wall, and the solid wall boundary condition is applied.

At the outflow boundary, the situation is somewhat more complicated. Depending on the pressure ratio and the location of the outflow boundary, the jet wake can have either a subsonic or a supersonic core, bounded in both cases by a supersonic ring. Outside this supersonic ring the flow becomes subsonic again. For the subsonic flow in- and outside of the supersonic ring, a static pressure has to be prescribed. For the flow outside the supersonic ring, the static pressure is roughly equal to the ambient pressure, since it may be assumed that the

flow velocity is very small here. In case the jet core is subsonic, no definite statements about the outflow pressure can be made. However, as became clear from numerical experiments, a simple boundary condition that extrapolates all flow solution variables from the interior to the outflow boundary, was sufficient enough to determine the state over the whole of the outflow boundary.

At the far-field boundary, the situation is as follows. The shear layer separating the jet from the ambient surroundings would be a vortex sheet in the case of inviscid flow. In viscous flow the shear layer entrains fluid from the ambient surroundings, which results in an entrained flow in the ambient. In the numerical method for solving the Euler equations for inviscid flow, numerical effects will spread the vortex-sheet into a shear layer which entrains fluid from the ambient surroundings. Therefore, there is inflow over the complete far-field boundary. Streamlines thus emanate from far away where the flow is quiescent, and therefore at this boundary the far-field boundary condition is applied. The total pressure there is equal to the ambient pressure  $p_a$ , and the total temperature is taken equal to the total temperature in the reservoir,  $T_a = T_r$ .

### 5.3.3 The mesh

The computational domain, bounded by the boundaries as depicted in Fig. 5.22, is discretised by triangular elements. The mesh is preferably dense in regions with large gradients, and coarse in regions with small gradient. For axi-symmetric flows, it is important to limit the size of the elements on the symmetry-line, since the axi-symmetric contributions are predominant in the vicinity of the centerline. Slight errors in the radial velocity approximations can produce large errors in the solution, see Prudhomme & Haj-Hariri [53].

In the jet plume, bounded by the barrel shock and the Mach disk, the flow is expanding rapidly, and the mesh should be dense enough to capture the large flow gradients occurring in the plume. From Eq. (5.9) the downstream length of the jet is known, and from Crist et al. [18] it follows that the diameter of the jet is approximately half the length of the jet. Behind the Mach disk, flow gradients become smaller, and the mesh-size is chosen larger behind the Mach disk. Away from the rotational symmetry-line, outside the jet boundary, flow gradients are small, and the mesh-size is accordingly large.

In summary, the computational domain is divided into three regions as depicted in Fig. 5.23.

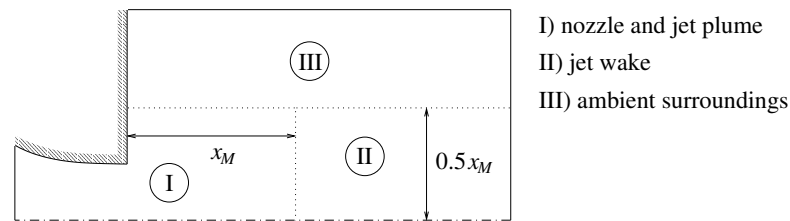


FIGURE 5.23: Division of the computational domain for the underexpanded jet into three regions with different mesh spacing.

A program that uses the desired mesh-sizes in each region as input, generates the boundary nodes, which are in turn used by the meshing program Delaundo to generate the unstructured



triangular mesh.

An example of a relatively coarse mesh, for a pressure ratio of  $p_r/p_a = 10.0$  ( $x_M \approx 2.1D$ ) is shown in Fig. 5.24. It demonstrates the utility of using an unstructured grid: nodes can be

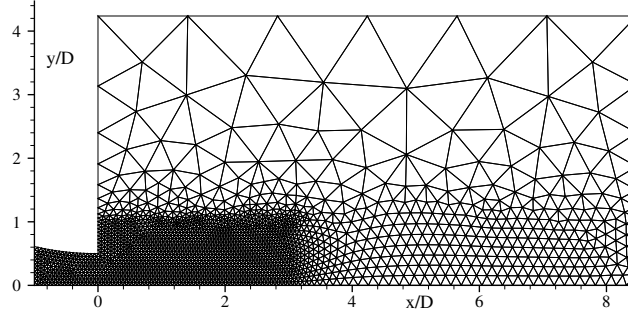


FIGURE 5.24: *Example of a (relatively coarse) triangular mesh for the underexpanded jet,  $p_r/p_a = 10$ .*

concentrated relatively easily in regions with large gradients, while away from these regions the grid becomes quickly coarse again.

#### 5.3.4 Instabilities occurring in the jet

As was already found in previous numerical investigations of the supersonic underexpanded jet, Berzins et al. [11], Cumber et al. [20] [21], Prudhomme & Haj-Hariri [53], the Euler equations, lacking a diffusive mechanism, are not well-suited to simulate strongly underexpanded jets computationally. Therefore, results obtained by other authors, are based on the Navier-Stokes equations instead.

In the inviscid plume of the underexpanded nozzle, a very well-known instability, known as the Kelvin-Helmholtz (K-H) instability, occurs. The instability can develop when two parallel streams of different velocities are adjacent to each other. At the interface, or vortex sheet (infinitesimal shear layer), the flow can be unstable to perturbations, even infinitesimal ones. This is in particular the case for shear layers of constant strength, stretching shear layers are to a lesser extent subject to instability. The shear layer will deform into waves, which grow in amplitude further downstream, and eventually the shear layer will roll up and form convective patterns called Kelvin cats eyes, shown in Fig. 5.25 (photo taken from An Album of Fluid Motion, Milton Van Dyke [24]).

In the flow-field of a strongly underexpanded jet, there are two regions where a shear layer is present: along the jet boundary, where the flow emanating from the nozzle meets the ambient surrounding gas, and at the slip-line originating from the triple-point, which is the point where the barrel shock and the Mach disk intercept and form a reflected shock, see Fig. 5.21. Without the presence of a dissipative mechanism, such as viscosity, the billows caused by the K-H instability grow without bound, and cause the flow field to become unstable, therefore preventing a steady-state solution.

Since the present computational method is based on the Euler equations, the only diffusive mechanism that is present is of numerical origin, included in the Truncation Error (T.E.),

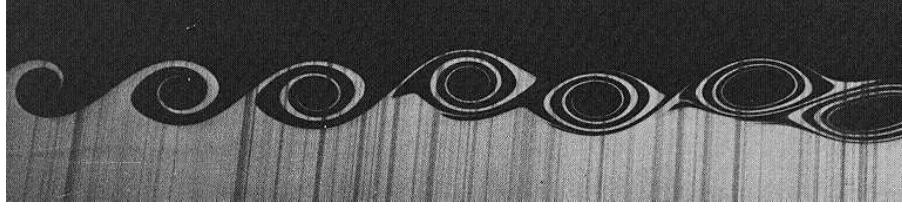


FIGURE 5.25: Example of a Kelvin-Helmholtz instability. From “An Album of Fluid Motion” by Milton van Dyke [24].

defined as the difference between the original governing equations and the discrete approximation to it, Anderson [6]. In case the fluxes are of first order, the lowest order in the T.E. of the momentum equations contain second derivatives of the velocity, so that this term is similar to the viscous terms in fluid flow equations, Anderson [6]. Thus, in case of first-order fluxes, the finite-volume method introduces an *artificial viscosity* in the solution. This is often called implicit artificial viscosity, as opposed to explicit artificial viscosity, which is purposely added to a discretization scheme. Artificial viscosity tends to reduce the gradients in the solution whether physically correct or numerically induced. This effect, which is the direct results of even derivative terms in the T.E., is called artificial dissipation.

As became evident from attempts to numerically simulate the underexpanded jet, using second-order accurate fluxes (generally referred to as a second-order method, which lacks second-order derivatives in the T.E.) leads to instability. Along the jet boundary, the Kelvin-Helmholtz (K-H) instability occurs, causing the jet boundary to oscillate with increasing amplitude downstream. As a result, the location of the intercepting barrel shock oscillates, resulting in its turn to a Mach-disk moving up- and downstream with time. In this unsteady flow, vortices are continuously shed from the jet boundary, and are convected downstream with the flow. These unsteady flow effects become more pronounced with decreasing mesh size. However, if first-order fluxes (generally referred to as a first-order method) are used instead of second-order fluxes, the solution is steady and converges to machine zero. The major drawback of first-order methods is that the T.E. decreases linearly with  $h$ , where  $h$  is the mesh-size, while for second-order methods the T.E. decreases with  $h^2$ . Therefore, the number of control volumes required to obtain an accurate (grid converged) solution of the governing equations, is in general much larger for first-order methods. Since the number of control volumes is directly related to the computational effort required to compute a solution, second-order methods are generally preferred over first-order methods, since for a desired level of accuracy they save computational time. However, it is clear that for the present computations, the second-order method does not give satisfactory results, necessitating the use of the first-order method.

A further argument to use a numerical method that suppresses the K-H instabilities is that the literature suggests that the Mach disk is quite stationary, indicating that it does not depend dominantly on the jet-plume boundary and slip-line instabilities.

### 5.3.5 Results for pressure ratio 30

The underexpanded jet of air for a pressure ratio of  $p_r/p_a = 30$  is calculated with the axisymmetric version of the computational method, using the AUSM<sup>+</sup> scheme with  $\alpha = 3/16$  and  $\beta = 1/8$ , and first-order accurate fluxes. Since the pressure in the reservoir is kept

constant and equal to  $p_r = 1$  bar, the perfect gas equation of state is used. For the pressure ratio of 30, a grid convergence study is carried out to check whether the obtained solution is sufficiently grid-independent. Three sets of meshes are generated with different mesh-sizes, to study the influence of the mesh-size on the solution. The mesh sizes in the three regions I, II and III, listed in section 5.3.3, are tabulated in table 5.3.

mesh	mesh size $h$			number of nodes
	region I	region II	region III	
coarse	$D/18$	$D/6$	$x_M/1.5$	4,708
intermediate	$D/36$	$D/12$	$x_M/3.0$	17,918
fine	$D/54$	$D/18$	$x_M/4.5$	39,840

TABLE 5.3: Mesh sizes in the different regions of the computational domain for an underexpanded jet with  $p_r/p_a = 30$ .  $x_M$  is the Mach-disk location according to Eq. (5.9) and  $D$  is the diameter of the nozzle exit.

On the three meshes, the iteration process is continued until the total temperature throughout the whole domain is constant up to the sixth digit, which is then considered as a converged solution. This corresponds roughly to a decrease in the L2-norm of the residuals in density, momentum and total energy of six orders of magnitude (if the iterative process is continued further, the residuals can be reduced to machine zero, but this has no noticeable influence on the solution). On the coarsest mesh, for  $y/D < 0.5$ , an initial solution is imposed with Mach number  $M = 1$ , total pressure  $p_r = 1$  bar and total temperature  $T_r = 300$  K. For  $y/D \geq 0.5$  the initial conditions are equal to the ambient conditions. After 4,000 iterations the solution is sufficiently converged. Subsequently, the solution on the coarse mesh is used as initial solution on the intermediate mesh. Since the initial solution is already very accurate, it takes only 3,000 iterations to obtain a sufficiently converged solution on the intermediate mesh. The solution on the intermediate mesh is then used as initial condition for the fine mesh. After a further 5,000 iterations the solution on the fine mesh is sufficiently converged.

In Fig. 5.26, the iso-contours of the Mach number are plotted, for the coarse, intermediate and fine mesh. On all meshes, the barrel shock, the Mach disk and the reflected shock are clearly visible, becoming more pronounced as the mesh size decreases. As can be seen from the left figure, the location of the intersection of the Mach disk with the rotational symmetry-line is nearly identical for both the coarse and the intermediate mesh. However, the diameter of the Mach disk is larger on the intermediate mesh. Comparing the solution on the fine and the intermediate mesh, the location of the Mach disk is again nearly identical, and also the diameters of the Mach disk are nearly identical, with the diameter on the fine mesh slightly larger.

Since the Mach disk is represented on the mesh by three nodes, it is not immediately clear which point should be chosen as “the” Mach-disk location. The diameter of the Mach disk is found as the point where the barrel shock and Mach disk intercept, and since in the numerical solution both shocks have a finite thickness, the diameter can only be determined with a limited accuracy. The centerline location and diameter of the Mach disk are shown in Fig. 5.27 as functions of the mesh-size  $h$ . In the left plot, the squares represent the first and last node of the discrete representation of the Mach disk, and the circle represents the intermediate point of the Mach-disk location on the centerline. In the right plot, the squares

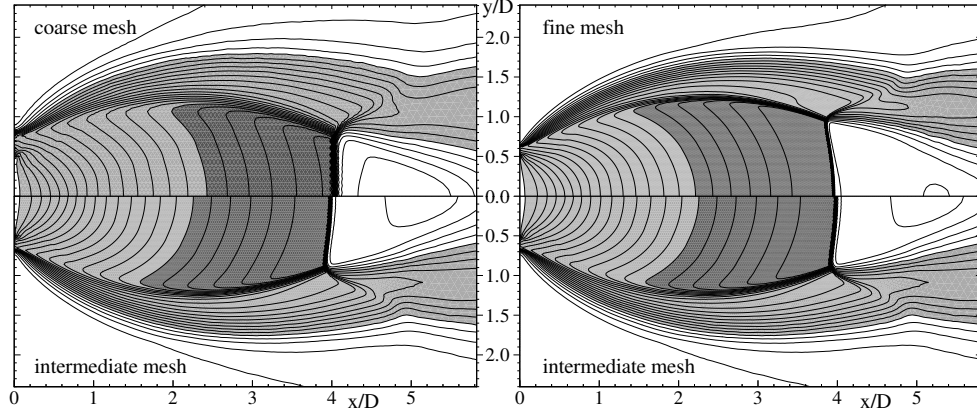


FIGURE 5.26: Underexpanded jet,  $p_r/p_a = 30$ . Mach number iso-contours for solutions on the coarse, intermediate and fine mesh. Light grey:  $M > 1$ ; dark grey:  $M > 4$ ;  $\Delta M = 0.2$

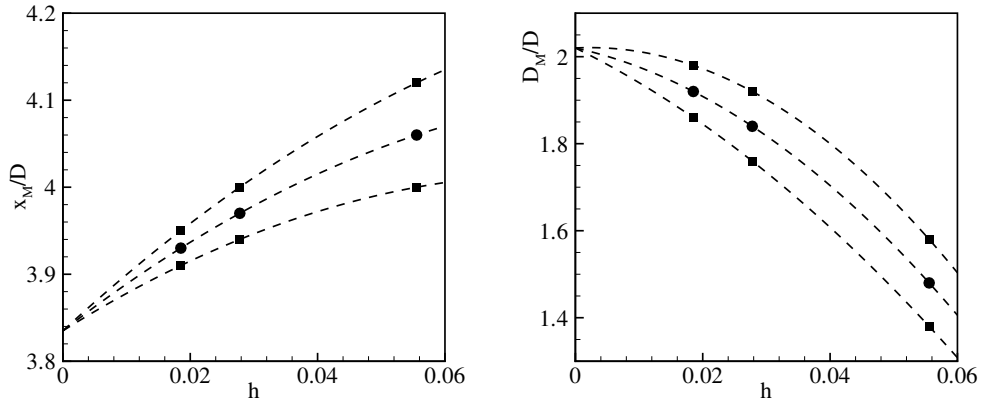


FIGURE 5.27: Underexpanded jet,  $p_r/p_a = 30$ . Mach-disk centerline location and Mach-disk diameter for the coarse, intermediate and fine mesh.

denote the lower and upper side of the barrel shock at the Mach disk, and the circle denotes the average of these two points. Using Taylor series expansion, we can write for the location of the Mach disk:

$$\hat{x}_M(h) = \hat{x}_M(0) + \hat{x}'_M(0)h + \frac{1}{2}\hat{x}''_M(0)h^2 + O(h^3) \quad (5.11)$$

where  $\hat{x} = x/D$ . Using the values found on the coarse, intermediate and fine mesh, we can write, using the Taylor series expansion:

$$\begin{pmatrix} 1 & h_1 & \frac{1}{2}h_1^2 \\ 1 & h_2 & \frac{1}{2}h_2^2 \\ 1 & h_3 & \frac{1}{2}h_3^2 \end{pmatrix} \begin{pmatrix} \hat{x}_M \\ \hat{x}'_M \\ \hat{x}''_M \end{pmatrix}_0 = \begin{pmatrix} \hat{x}_M(h_1) \\ \hat{x}_M(h_2) \\ \hat{x}_M(h_3) \end{pmatrix} + \begin{pmatrix} O(h_1^3) \\ O(h_2^3) \\ O(h_3^3) \end{pmatrix} \quad (5.12)$$

where  $h_1$ ,  $h_2$  and  $h_3$  denote the mesh-size in region I (see table 5.3) of the coarse, intermediate, and fine mesh, respectively. Omitting the truncation error  $O(h^3)$ , which is allowed for sufficiently small values of  $h$ , we can solve for the unknowns with  $\hat{x}_M(0)$ ,  $\hat{x}'_M(0)$ , and  $\hat{x}''_M(0)$ . In effect, we find parabolic functions for  $\hat{x}_M$ , and these parabola are drawn as dashed lines in Fig. 5.27. As can be seen from this figure, the parabola intersect at  $h = 0$ . This encourages the assumption that the solution which would be obtained on a mesh with an infinitely small mesh-size can be extrapolated from the solutions on the coarse, intermediate and fine mesh.

The extrapolated value of the location of the Mach disk at the centerline is  $x_M \approx 3.84D$ . This is in good agreement with the value that follows from the empirical formula, Eq. (5.9), which gives  $x_M = 3.67D$ , yielding a relative error of approximately 5%. The extrapolated value of the diameter of the Mach disk is  $D_M \approx 2.0D$ . This value agrees well with the empirical formula reported by Crist et al. [18],  $D_M/D \approx 0.35\sqrt{p_r/p_a}$ , which results for  $p_r/p_a = 30$  in a diameter of  $D_M = 1.9D$ , also yielding a relative error of approximately 5%. In Fig. 5.28, the data on which the empirical formula of Crist et al. [18] is based is shown.

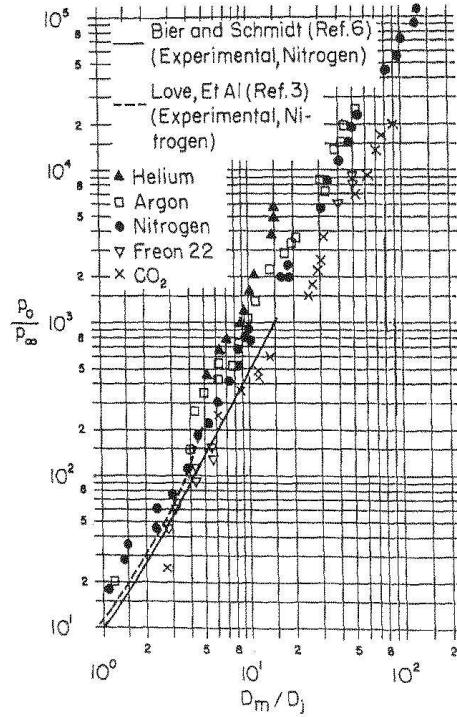


FIGURE 5.28: *Underexpanded jet. Mach-disk diameter versus pressure ratio, figure taken from Crist et al. [18].  $D_j$  is the diameter of the nozzle at the exit, i.e.  $D_j = D$ . The pressure ratio  $p_0/p_\infty$  corresponds to  $p_r/p_a$ .*

The scatter which is evident from this figure, is much larger than the difference between the present result and the value obtained from the empirical formula. Note that the plot includes data for underexpanded jets of different gases for pressure ratios ranging from approximately 20 up to 200,000.

In Fig. 5.29, the Mach-number along the centerline is plotted as a function of the distance from the nozzle orifice. Note that this plot does not extend up to the location of the Mach

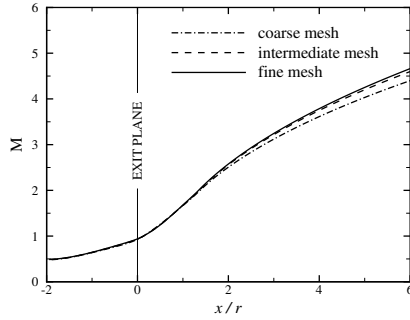


FIGURE 5.29: *Underexpanded jet,  $p_r/p_a = 30$ . Mach number along the centerline, present calculations.*

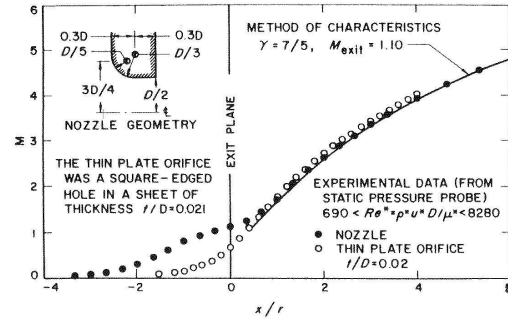


FIGURE 5.30: *Mach number along the centerline, figure taken from Ashkenas & Sherman [9].*

disk, and that we changed from  $x/D$  to  $x/r$ , with  $x/r = 2x/D$ . As was already evident from Fig. 5.26, the Mach-number at a certain location downstream of the nozzle orifice, increases with decreasing mesh-size. However, the difference between the intermediate and fine mesh result is small compared to the difference between the coarse and intermediate mesh result. In Fig. 5.30 the experimentally determined Mach-number distribution along the centerline is shown. The difference between the present results and the experimental data is approximately 3%. The small discrepancies between the computational results and the experimental data are probably caused by the artificial dissipation present in the computational method. The artificial dissipation has the effect of decreasing flow gradients, just like viscous effects would. The artificial dissipation will be different from the real viscous dissipation, causing the difference between the experiments and the computation. As the amount of artificial dissipation becomes smaller with decreasing mesh-size, flow gradients become larger, and the Mach-number increases.

### Recirculation behind the Mach disk

Looking in detail at the underexpanded flow, a recirculation zone is seen right behind the Mach disk in the coarse mesh solution, as depicted in Fig. 5.31. Such a recirculation zone is evidence of the presence of a vortical flow region. The vorticity required for this could have been produced by the Mach disk, which must then vary in strength from the centerline to the triple point. However, it follows from Fig. 5.31 that the Mach disk is almost a straight shock and that along the shock the variation of the Mach number just upstream of the shock is very small, suggesting that the Mach disk is almost constant in strength.

The recirculation behind the Mach disk was also found by Berzins et al. [11] for a pressure ratio of 31. Gribben et al. [26] also report the occurrence of a recirculation zone behind the Mach disk. However, they consider the underexpanded jet ejecting from a converging-diverging nozzle with an exit Mach-number of  $M = 3$ , for a pressure ratio of 342.9. Therefore it is difficult to compare their results with the present results.

As is evident from Fig. 5.31, the recirculation zone disappears as the mesh is refined, and on both the intermediate and the fine mesh, there is no recirculation present. To ensure that the solution obtained on the coarse mesh is unique (i.e. to exclude any possible bifurcation), the solution without recirculation obtained on the fine mesh is used as initial solution on the

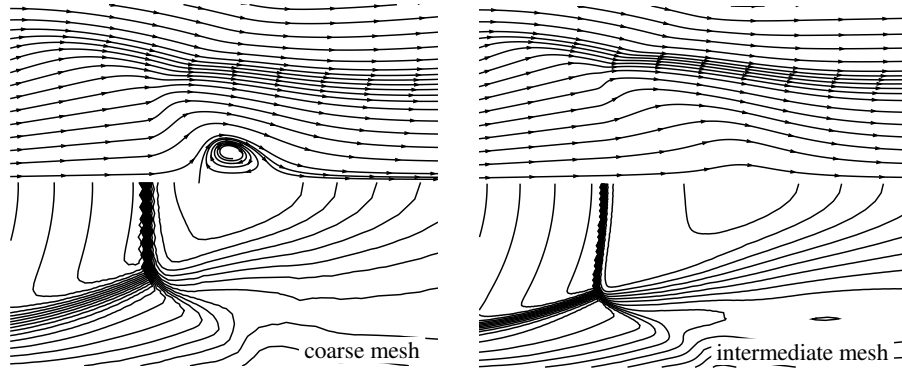


FIGURE 5.31: *Underexpanded jet,  $p_r/p_a = 30$ . Streamlines and Mach iso-contours for the solutions on the coarse mesh (left) and intermediate mesh (right).*

coarse mesh, thereby providing the computational method an initial solution without recirculation. The iterative process converges quickly, and the solution obtained is identical to the previous solution, i.e. there is no evidence to suggest that the solution on the coarse mesh is not unique and that another solution without recirculation is also possible on the coarse mesh. This clearly suggests that the vorticity seen in the solution on the coarse mesh has no physical meaning.

### 5.3.6 Results for varying pressure ratio

Underexpanded jets of air are calculated for a range of pressure ratios, and the results are compared with available experimental data. The flow is calculated with the axi-symmetric version of the computational method, using the AUSM<sup>+</sup> scheme with  $\alpha = 3/16$  and  $\beta = 1/8$ , and first-order accurate fluxes. Since the pressure in the reservoir is kept constant and equal to  $p_r = 1$  bar, the perfect gas equation of state is used.

#### Mach distribution for different pressure ratios

For pressure ratios ranging from 10 to 110 with an increment of 20, converged solutions are obtained on meshes with a mesh-spacing that is equal to that of the intermediate mesh. A new “optimal” mesh is created for each pressure ratio. For pressure ratios of 30, 50 and 70, the Mach iso-contours are shown in Fig. 5.32, and for pressure ratios of 70, 90 and 110, the Mach iso-contours are shown in Fig. 5.33. Note that for  $p_r/p_a = 110$  a slightly coarser mesh was used, since Delaundo was not able to create the intermediate mesh for this pressure ratio.

As is clearly visible from these figures, the topology of the flow remains very similar. The centerline Mach distribution, up to the Mach disk, is identical for the different pressure ratios, with the jet expanding further for higher values of the pressure ratio  $p_r/p_a$ . This illustrates the supersonic character of the flow. Note that in the expansion the Mach number reaches a maximum value of almost 7.1 for  $p_r/p_a = 110$ .

The diameter of the jet boundary, the barrel shock and the Mach disk all increase with increasing pressure ratio. These observations are all in line with the experimental observations

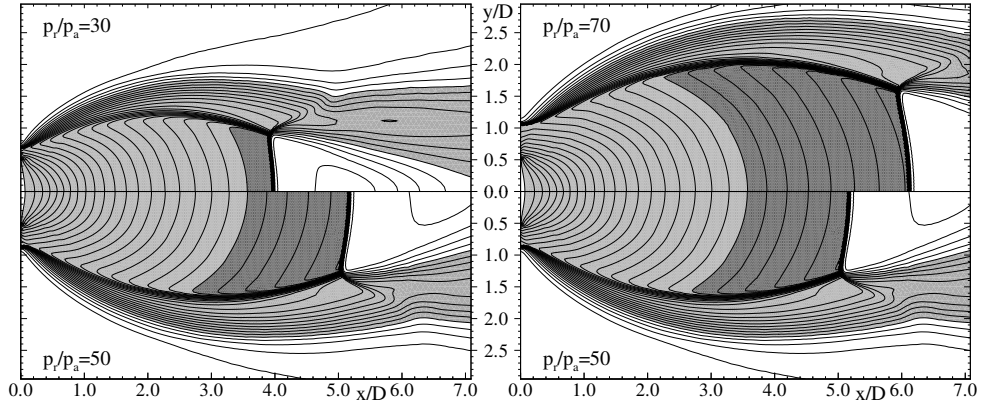


FIGURE 5.32: *Mach iso-contours for pressure ratios 30, 50 and 70. Light grey:  $M > 1$  ; dark grey:  $M > 5$  ;  $\Delta M = 0.2$ .*

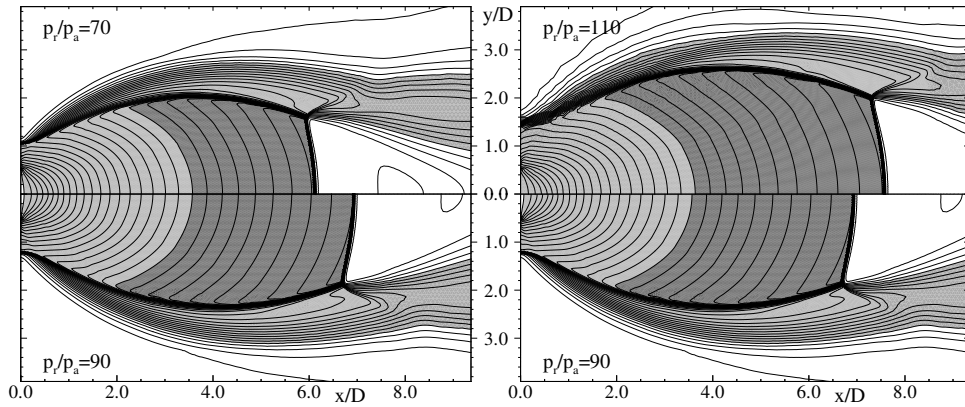


FIGURE 5.33: *Mach iso-contours for pressure ratios 70, 90 and 110. Light grey:  $M > 1$  ; dark grey:  $M > 5$  ;  $\Delta M = 0.2$ .*

made by Crist et al. [18]. Also note that with increasing pressure ratio the expansion of the flow about the nozzle lip becomes deeper and the “barrel shock” starts higher up along the wall. This effect contributes to the plume becoming wider with increasing pressure ratio.

#### Characteristics jet for different pressure ratios

For the range of pressure ratios, several characteristics of the jet are plotted in Fig. 5.34. The location of the Mach disk at the centerline  $x_M$  increases with increasing pressure ratio, as does the diameter of the Mach disk  $D_M$ . From Fig. 5.34 we also see that the maximum Mach-number  $M_{max}$ , the Mach number just upstream of the Mach disk, increases with increasing pressure ratio. We can also observe that the barrel-shock stand-off distance  $y_b$  increases with



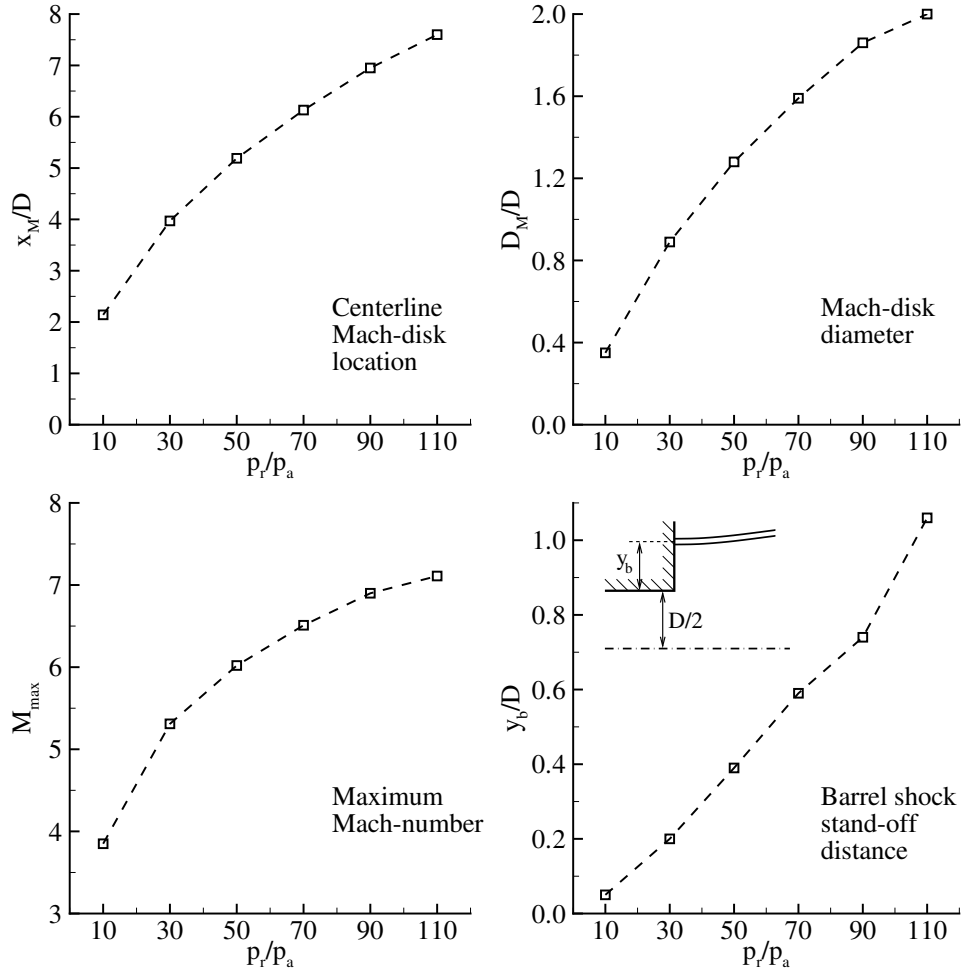


FIGURE 5.34: Characteristics of the jet for different pressure ratios.

increasing pressure ratio. The increase seems to be more or less proportional to  $p_r/p_a$ , in contrast to  $x_M$  and  $D_M$ , which are, according to Ashkenas & Sherman [9] and Crist et al. [18], proportional to  $\sqrt{p_r/p_a}$ .

In Fig. 5.35, the pressure distribution along the centerline for pressure ratios of 10, 30, 50, 70 and 90 is shown. The upper plot shows the static pressure relative to the ambient pressure. From this plot we observe that the static pressure downstream of the Mach disk is about equal to the ambient pressure, and nearly independent of the pressure ratio  $p_r/p_a$ . This is in agreement with the experimental observations made by Ashkenas & Sherman [9]. In the lower plot of Fig. 5.35, the static pressure relative to the reservoir pressure is shown. The distributions coincide up to the Mach disk, emphasizing the supersonic character of the jet. In both plots in Fig. 5.35 we observe that the pressure exhibits oscillations which decay in amplitude downstream and decrease in amplitude with increasing pressure ratio. The increase

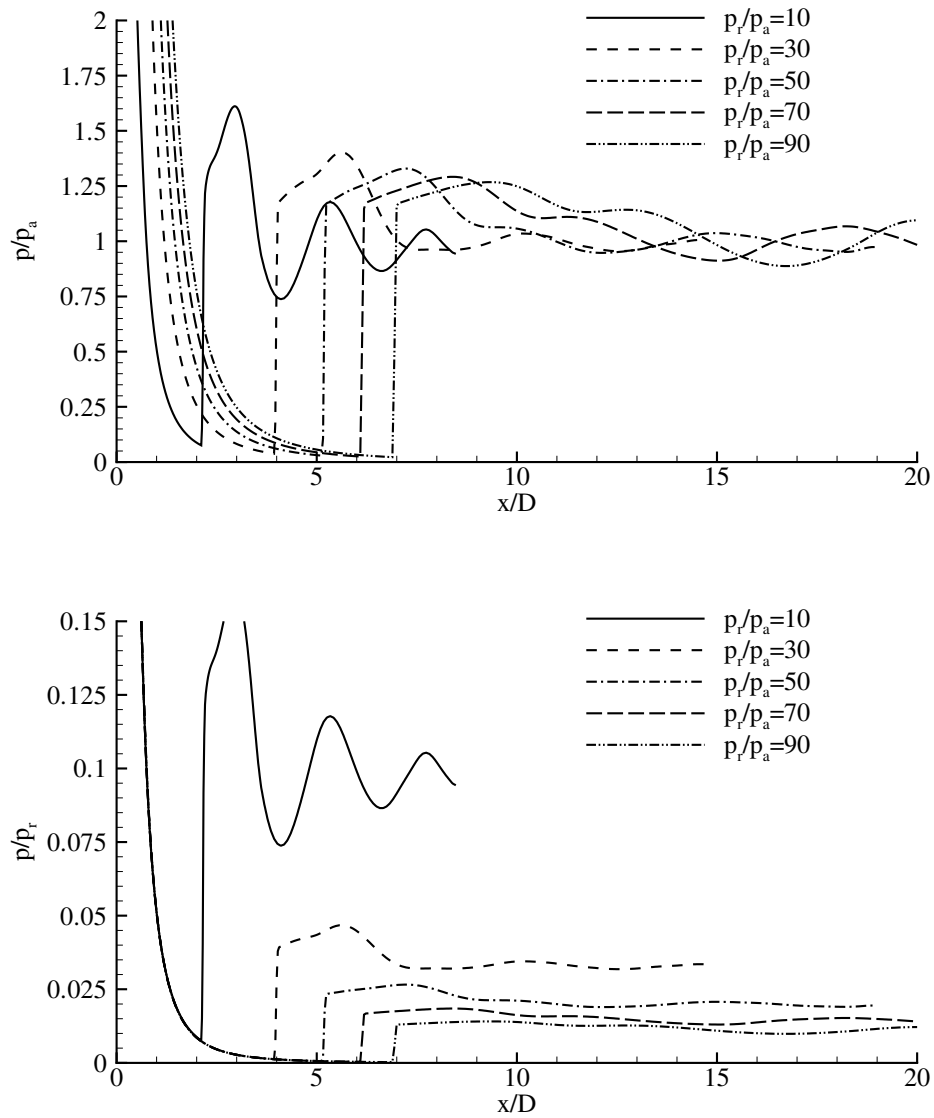


FIGURE 5.35: *Underexpanded jet: pressure distribution along the centerline for different pressure ratios.*

in pressure on the centerline just downstream of the Mach disk is caused by the slip surface emanating from the triple point (see Fig. 5.21), which decreases the effective area through which the air “processed” by the Mach disk flows. The subsonic flow downstream of the Mach disk is accelerated up to supersonic speed, indicating that the slip surface creates a virtual throat. Downstream of this virtual throat, the flow remains supersonic.

**Validation: Mach-disk location for different pressure ratios**

Shown in Fig. 5.36 are the locations of the Mach disk for the range of pressure ratios, and the empirical formula from Ashkenas & Sherman [9].

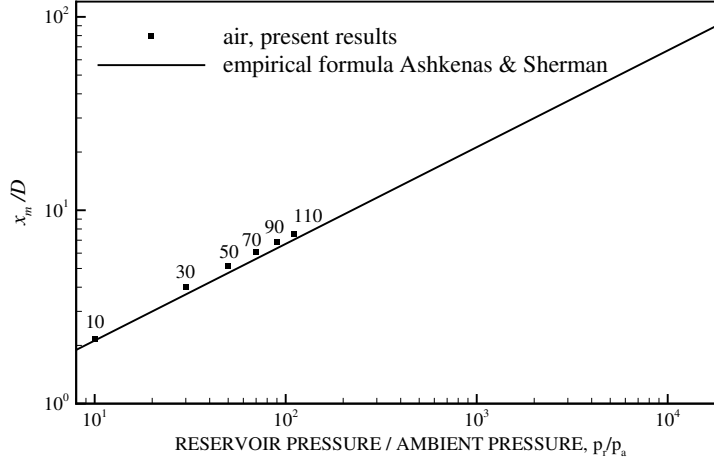


FIGURE 5.36: *Underexpanded jet. Mach-disk location, present calculations for different pressure-ratios on intermediate mesh; comparison with empirical formula Eq. (5.9).*

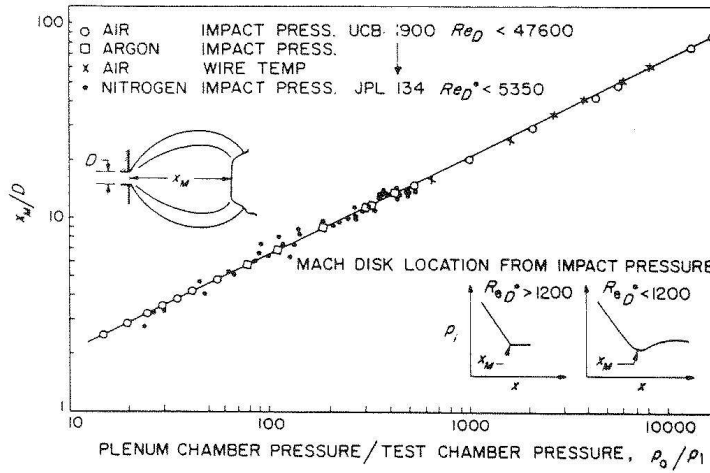


FIGURE 5.37: *Underexpanded jet. Mach-disk location, figure taken from Ashkenas & Sherman [9]. Plenum chamber pressure  $p_0$  corresponds to the reservoir pressure  $p_r$ , test chamber pressure  $p_1$  corresponds to ambient pressure  $p_a$ .*

The location of the Mach disk is somewhat over-predicted by the present computational method, but the results are well within the scatter in the experimental data, as is evident from Fig. 5.37. As we have seen from the grid convergence study, the Mach disk tends to move upstream as the mesh is refined (see Fig. 5.27), from which it can be concluded that agreement between experiment and the present results would be better still for meshes with smaller mesh-size.



---

# CONDENSATION OF XENON IN AN UNDEREXPANDED JET

---



## 6.1 Introduction

Laser produced plasmas provide a source of extreme ultraviolet (EUV) light rendering them well suited for use in next generation lithography tools, see Kanouff et al. [34] and De Bruijn et al. [14] [15]. The plasma is generated by directing a (pulsed) laser at the supersonic plume of an underexpanded free xenon jet, as is illustrated in Fig. 6.1. The expansion in the jet

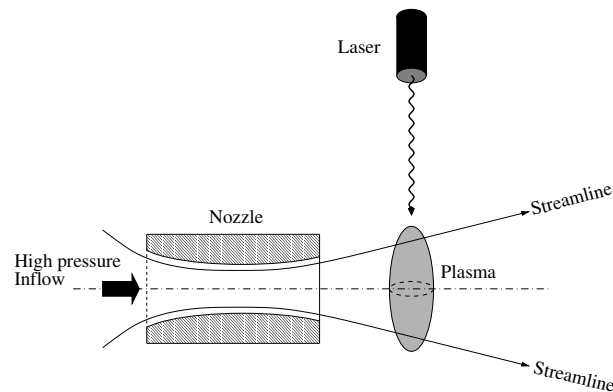


FIGURE 6.1: *Schematic representation of plasma formation in a supersonic jet*

causes the xenon to become super-saturated such that the gas partially condenses forming a non-equilibrium mixture of gas and small droplets. The gas-liquid mixture absorbs the laser energy leading to the formation of the desired laser produced plasma. The plasma is usually produced at a safe working distance downstream of the nozzle exit in order to minimize interaction between the hot plasma and the nozzle orifice, effectively minimizing debris production at the nozzle orifice.

The amount of EUV that is produced and is readily available depends on the laser power, the EUV absorption by the gas surrounding the plasma, and on the amount of matter that the laser beam encounters as it travels through the jet (the laser focal region). Absorption losses can be decreased by the use of a coaxial nozzle, in which the target gas (producing the plasma) flows through an inner nozzle, and a buffer gas (ideally not absorbing any laser

---

power) flows through an outer annular nozzle. The buffer gas confines the jet, effectively decreasing the jet width and its expansion-rate, increasing the amount of target gas (xenon) inside the laser focal region.

At the FOM-Institute for Plasma Physics Rijnhuizen, there is ongoing research in laser produced plasmas. The main focus is on ways to increase the EUV yield. Since the liquid droplets play an important role in the production of the EUV-light, a clear understanding of the condensation process taking place in the jet plume would be of great value. Towards this end, the flow with condensation in an axi-symmetric underexpanded xenon jet is computed with the present numerical method. A difference between the ongoing experiments at FOM Rijnhuizen and our numerical simulations is the shape of the nozzle. In the experiments, a converging-diverging nozzle is used, while in the computations a converging nozzle is used. In a converging-diverging nozzle, especially for a nozzle with a relatively long diverging part, most of the condensation would take place in the nozzle itself. If a nozzle is used with a convergent part only, the condensation will take place in the supersonic jet itself, so that the effect of condensation on the shape and structure of the jet plume becomes more pronounced than for a converging-diverging nozzle.

Since the main aim of the present investigation is merely to study the condensation process in an underexpanded xenon jet, the pressure ratio is chosen smaller than the pressure ratios of more than 1,000 used in the experiments carried out at FOM Rijnhuizen. Partly this accounts for the pressure drop in the diverging part of the nozzle. Furthermore, the reduced pressure ratio limits the axial and lateral size of the jet plume and therewith the computational domain, hereby keeping computation times within acceptable bounds. The absolute level of the pressure in the reservoir is set to  $p_r = 20$  bar, and the pressure in the chamber in which the jet exits, i.e. the ambient environment, is equal to  $p_a = 1$  bar, resulting in a pressure ratio of 20. The temperature in the reservoir is chosen such that the saturation in the reservoir is  $\Phi_0 = 30.0\%$ , corresponding to a temperature  $T_r = 296.9$  K. Since the condensation is taking place in the ambient, we can assume that the assumption of xenon behaving as a *perfect gas* is valid. Furthermore, a pressure of 20 bar is still moderate enough for the perfect gas law to be valid. The nozzle exit diameter is chosen as 1.0 mm, a value which is of the same order as the exit diameter of the nozzles used at FOM Rijnhuizen and the nozzles used in the experiments by Crist et al. [18], for underexpanded jets of, amongst others, nitrogen and argon.

In the light of the discussion in section 5.2.5 on the results of the wet flow in the A1 nozzle, it is noted here that the application of the present method to the condensation in the under-expanded flow of xenon, serves as a demonstration of the capability of the present method to numerically simulate such a flow. This because the amount of experimentally obtained material properties of xenon available in literature is very limited, while also recommendations like Lamanna [38] for air/water regarding the combination of nucleation model, droplet growth model, and surface tension are not available for the condensing flow of xenon.

## 6.2 Xenon jet without condensation

The computational domain is defined in the same way as for the computations without condensation, see Fig. 5.22. The mesh used is the fine mesh as described in table 5.3. The fine mesh is chosen since the solution on the fine mesh will exhibit the most detail. The mesh consists of 28,260 nodes and 55,875 triangles. Before computing the flow-field with con-

---

denensation, first a flow-field is computed without condensation. This is achieved by setting the maximum liquid mass fraction to zero,  $g_{max} = 0$ . In this way an underexpanded jet is obtained of a gas that has the thermodynamical properties of xenon, but which does not condensate.

The flow is calculated with the axi-symmetric version of the computational method, using the AUSM<sup>+</sup> scheme with  $\alpha = 3/16$  and  $\beta = 1/8$ , and first-order accurate fluxes. The perfect gas equation of state is used. The converged solution for the flow field without condensation is shown in Fig. 6.2. For comparison, the solution on the same mesh for the flow of air, for the

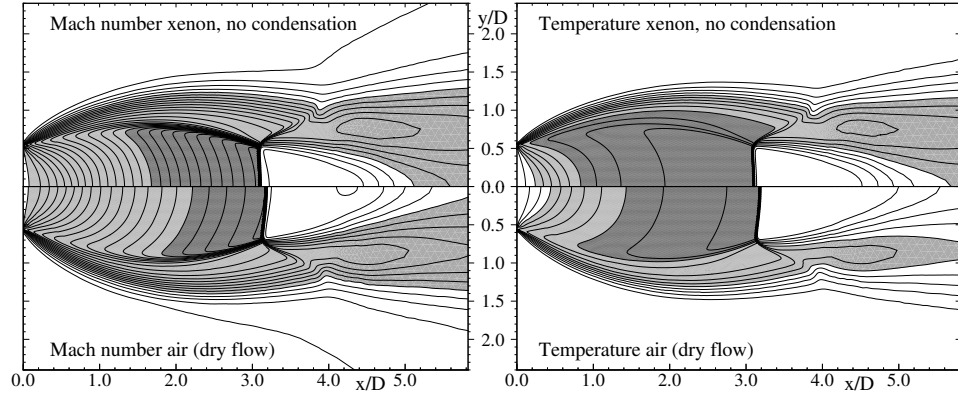


FIGURE 6.2: *Underexpanded jets of xenon without condensation and of dry air;  $p_r/p_a = 20$ ,  $T_r = 296.9$  K, 28,260 nodes.*

quantity	symbol	light grey	dark grey	increment
Mach-number	$M$	$> 1$	$> 4$	0.2
Temperature [K]	$T$	$< 200$	$< 100$	20

same pressure ratio and the same reservoir conditions, is also shown in this figure. The two solutions are very similar in topology. The expansion of xenon is deeper,  $M_{max,Xe} \approx 6.1$  and  $M_{max,air} \approx 4.9$ , and also the temperature is lower for xenon. The location of the Mach disk is approximately the same for xenon without condensation and for air. The diameter of the Mach disk, however, is clearly larger for air. These results are both in line with the conclusions drawn by Crist et al. [18], who state that the Mach-disk location is insensitive for the ratio of specific heats ( $\gamma = 1.40$  for air and  $\gamma = 1.67$  for xenon), and that the diameter of the Mach disk increases with decreasing ratio of specific heats  $\gamma$ . In the right plot of Fig. 6.2 it can be seen that the temperature decreases to  $T \approx 25$  K in the expansion upstream of the Mach disk. Creasy et al. [17] studied the underexpanded jet of hydroxyl radical (OH) at a pressure ratio of  $p_r/p_a = 1288.14$ . At this relatively large pressure ratio, Creasy et al. [17] compare numerical results with experimental data, and find that their numerical method predicts a minimum temperature as low as 10 K, while experimental data reveals that the temperature does not drop below a certain threshold ( $\sim 25$  K). For the present pressure ratio,  $p_r/p_a = 20$ , the temperature does not drop below 25 K either. Furthermore, condensation will add heat to the flow so that the temperature decrease in the supersonic expanding flow

is smaller, as we will see, for the xenon flow with condensation the minimum temperature is  $\sim 120$  K.

### 6.3 Xenon jet with condensation

With the underexpanded flow solution of xenon for  $g_{max} = 0$  available, we can now compute the flow solution with condensation, by setting the liquid mass fraction to  $g_{max} = 1$ . The computational method is then run for another 6,000 iterations. The convergence history is shown in Fig. 6.3. As can be seen from this figure, the residual of  $\rho$  reduces almost four

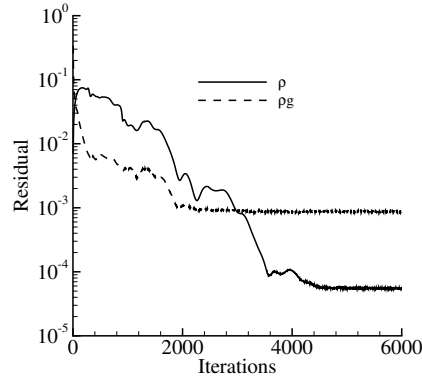


FIGURE 6.3: *Underexpanded wet xenon jet,  $p_r/p_a=20$ ,  $T_r = 296.6$  K,  $\Phi_0 = 0.30$ . Convergence history, 28,260 nodes.*

orders of magnitude, but the residual of  $\rho g$ , representing the amount of liquid per unit volume of vapour/liquid mixture (or liquid volume fraction), reduces just two orders of magnitude. This illustrates the sensitivity of the flow to the condensation process; after approximately 2,000 iterations, the liquid volume fraction residual remains at the same level, but the density residual still decreases. Eventually, after approximately 5,000 iterations, the density residual reaches a minimum as well. The largest residuals are found in the vicinity of the nozzle lip, where the flow is deflected supersonically over an angle of 90 degrees and large flow gradients are present. However, the solution is stable and does not change noticeably after the minimum level of the residuals is reached. The solution after 6,000 iterations is shown in Fig. 6.4. Globally speaking, the topology of the flow remains similar to the one in the xenon jet without condensation. In Fig. 6.4a we see that the flow expands to a supersonic speed of approximately  $M_f = 3.8$  right upstream of the Mach disk. In comparison with the flow without condensation, shown in Fig. 6.2, in which  $M = 6.1$ , the Mach-number is much lower, clearly indicating that the heat addition due to the condensation process reduces the Mach-number. We also see that the Mach disk moves slightly downstream, but that the diameter of the Mach disk has increased considerably, i.e. from  $0.55D$  to  $0.8D$ . This is due to the condensation process, which causes the stagnation pressure to decrease and the static pressure to increase. To accommodate the static pressure increase, the jet boundary moves to a larger diameter. Since the barrel shock, which is now weaker, is formed by expansion waves



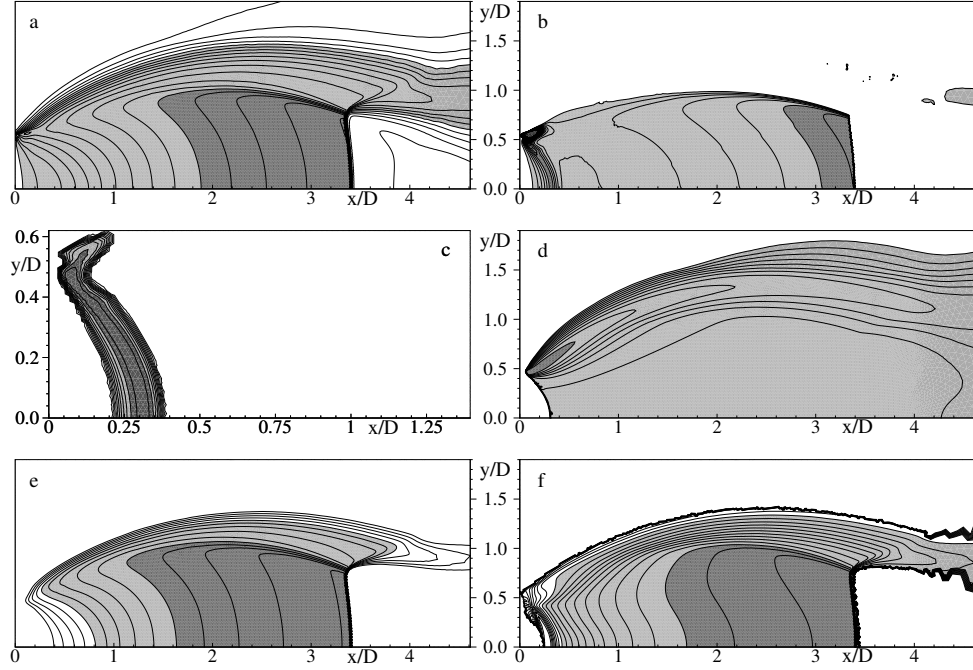


FIGURE 6.4: *Underexpanded wet xenon jet,  $p_r/p_a=20$ ,  $T_r = 296.6$  K,  $\Phi_0 = 0.30$ , 28,260 nodes;*

	quantity	symbol	light grey	dark grey	increment
a	Mach-number	$M_f$	$> 1$	$> 3$	0.2
b	super-saturation	$\Phi$	$> 1$	$> 2$	0.2
c	nucleation rate	$\log_{10} J$ [ $\text{m}^{-3}\text{s}^{-1}$ ]	$> 10$	$> 20$	2
d	number of droplets	$\log_{10} Q_0$ [ $\text{kg}^{-1}$ ]	$> 14$	$> 15$	0.1
e	liquid mass fraction	$g$	$> 0.1$	$> 0.2$	0.02
f	Hill droplet radius	$r_H$ [ $\mu\text{m}$ ]	$> 0.2$	$> 0.4$	0.02

that reflect as compression waves from the constant pressure boundary, the barrel shock will move to a greater diameter. Since the Mach disk terminates at the barrel shock, its diameter is also increased, provided that the location of the Mach disk does not change too much as a result of the condensation. This observation is in line with the experimental observations by Crist et al. [18], who find that the diameter of the Mach disk, the diameter of the jet boundary, and the diameter of the barrel shock increase with condensation.

In Fig. 6.4a we also observe that the Mach disk has moved downstream compared to the location in the flow without condensation. For the dry flow, the Mach disk is located at  $x_M \approx 3.1D$ , while for the wet flow  $x_M \approx 3.4D$ . Crist et al. [18] conclude from their experimental observations, that the location of the Mach disk is insensitive to condensation. Their conclusion is based on the fact that the Mach-disk location for the flow of argon, for which they clearly observed condensation, is approximately the same as that for other gases, such as helium and nitrogen, which do not condensate. To appreciate this conclusion, we consider the data on which Crist et al. drew this conclusion, reproduced in Fig. 6.5. From

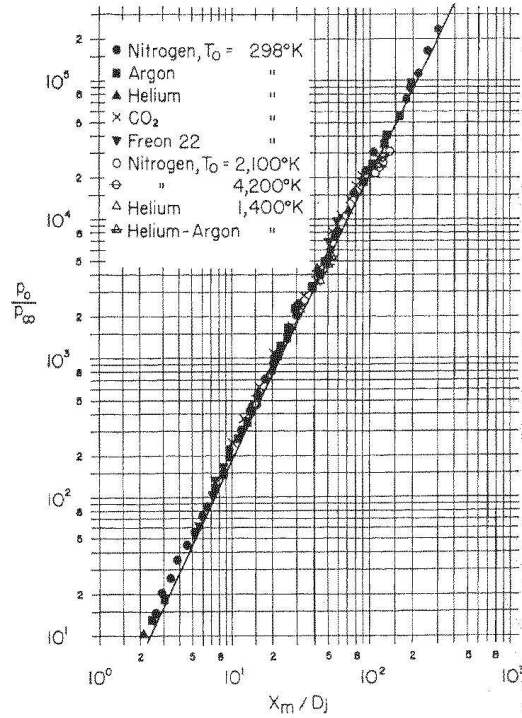


FIGURE 6.5: *Underexpanded jet. Mach-disk location from experiments, figure taken from Crist et al. [18].  $D_j$  is the diameter of the nozzle exit and corresponds to  $D$ , while  $p_0/p_\infty$  corresponds to the pressure ratio  $p_r/p_a$ . — fit:  $x_m/D_j = 0.65(p_0/p_\infty)^{1/2}$ .*

this figure, however, we see that the Mach-disk location for the different gases has a scatter of approximately 10%. This not fully justifies the conclusion that the Mach-disk location is insensitive to condensation. From Fig. 6.5 we find that Crist's results indicate that for  $p_r/p_a = 20$  the Mach disk is at about 3 to 3.5 $D$ .

Returning to the present results, we see in Fig. 6.4b that the super-saturation is relatively low throughout the jet. After the nucleation peak around  $x = 0.25D$ , the flow initially recovers to near equilibrium ( $\Phi \approx 1.1$ ) at  $x/D = 0.6$ , caused by the formation of liquid. Due to the relatively high expansion rate of the flow, the super-saturation increases again up to  $\Phi \approx 2.4$  just upstream of the Mach disk, which abruptly terminates the super-saturated state of the flow. As we can see, the saturation outside the barrel shock is indeed smaller than one, and remains so, indicating that outside the region enclosed by the Mach disk and the barrel shock, the liquid will evaporate. Considering Fig. 6.4c, which is on a larger scale than the other plots, we see that nucleation takes place just downstream of the nozzle exit, in a crescent-shaped region extending from the centerline to the nozzle lip. The nucleation rate reaches its maximum of almost  $10^{24}$  nuclei per  $\text{m}^3$  per second in the expansion fan around the nozzle lip. As we can see from Fig. 6.4d, the largest number of droplets of up to  $10^{15}$  nuclei per kg mixture are also formed in the expansion fan at the nozzle lip, where the nucleation is stretched out over a relatively large part of the flow.

The liquid mass fraction  $g$ , shown in Fig. 6.4e, increases in downstream direction, and the largest amount of liquid is found just upstream of the triple-point, where  $g/g_{max} \approx 0.28$ . The flow outside the barrel shock contains considerably less liquid than the flow inside the barrel shock. Downstream of the Mach disk most liquid has evaporated,  $g/g_{max} < 0.04$ . The liquid that passes through the reflected shock does not completely evaporate, but the amount of liquid decreases rapidly downstream of the reflected shock. In Fig. 6.4f which presents the (average, Hill) droplet size, we see that downstream of the nucleation zone the droplets increase gradually, first rapidly, further downstream at a lower rate.

The largest droplets are situated just upstream of the triple point, where they have a diameter of approximately  $0.9 \mu\text{m}$ . At radial locations larger than that of the barrel shock, the droplets rapidly decrease in size to values smaller than  $0.4 \mu\text{m}$  in diameter. The wiggles in the droplet-radius iso-contours downstream of the reflected shock are caused by the circumstance that the liquid mass fraction is very small here, but the number of droplets is still large. The average droplet radius here is then not well-defined. This is a drawback of the present method; the model does not include complete evaporation of the droplets. Once droplets have been created, they can only grow or shrink, but they cannot completely evaporate and disappear from the flow. This is not a problem, as long as the size of the droplets is larger than the critical droplet-size (droplets with a size smaller than the critical size are unstable and should evaporate completely). Upstream of the Mach disk and inside the boundary of the jet, the droplets are larger than the critical size, so that the model is valid here. Downstream of the Mach disk, however, the droplets become smaller than the critical droplet size and droplets should evaporate completely. Since de-nucleation (the rate at which droplets are “destroyed”) is not modeled in the present numerical method, the very small droplets do not evaporate and therefore the average radius of the droplets is not well-defined in regions where droplets become smaller than the critical droplet-size.

## 6.4 Influence of maximum liquid fraction on the underexpanded jet

Since the gas in the reservoir consists solely of vapour, the maximum liquid mass fraction is by definition equal to one,  $g_{max} = 1.0$ . However, from a numerical point of view, we can limit the maximum liquid mass fraction to values smaller than one. In this way we obtain a mixture consisting of xenon vapour, and a hypothetical inert gas having the same thermodynamical properties as xenon, but which does not condensate. By varying the maximum liquid mass fraction at the inlet of the nozzle, we can study the influence of a varying liquid mass fraction on the flow in the underexpanded jet.

Starting from the dry solution at  $g_{max} = 0.0$  (note that the pressure and the temperature in the reservoir are not altered:  $p_r = 20 \text{ bar}$ ,  $T_r = 296.9 \text{ K}$ ), a series of solutions is created, increasing  $g_{max}$  with 0.2 for each successive numerical simulation. The liquid mass fraction distribution for  $g_{max} = 0.2$  and  $g_{max} = 0.4$  is shown in Fig. 6.6, and for  $g_{max} = 0.6$  and  $g_{max} = 0.8$  in Fig. 6.7. The influence of  $g_{max}$  on the flow-field topology is small, with a gradual increase in Mach-disk diameter and barrel-shock diameter, and a downstream motion of the Mach disk. For  $g_{max} = 0.2$  and  $g_{max} = 0.4$ , almost no liquid is formed in the region bounded by the Mach disk and the barrel shock,  $g/g_{max} < 10^{-6}$  for  $g_{max} = 0.2$  and  $g/g_{max} < 3 \times 10^{-6}$  for  $g_{max} = 0.4$ . The little amount of liquid present is located in a

---

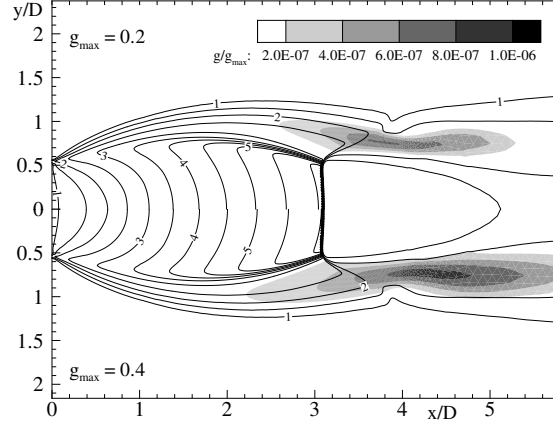


FIGURE 6.6: *Underexpanded xenon jet. Liquid mass fraction for  $g_{max} = 0.2$  and  $g_{max} = 0.4$  shown in grey-scale, labeled lines are Mach iso-contours.  $p_r/p_a=20$ ,  $T_r = 296.6$  K, 28,260 nodes.*

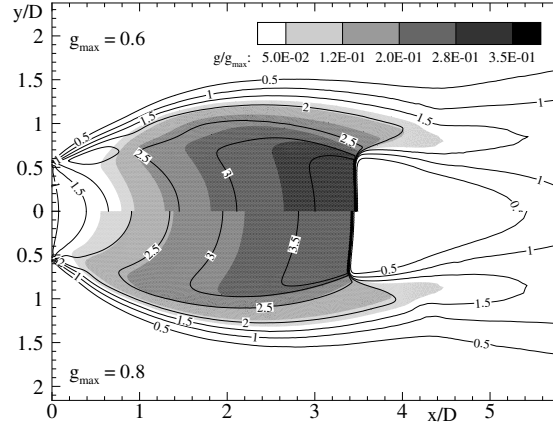


FIGURE 6.7: *Underexpanded xenon jet. Liquid mass fraction for  $g_{max} = 0.6$  and  $g_{max} = 0.8$  shown in grey-scale, labeled lines are Mach iso-contours.  $p_r/p_a=20$ ,  $T_r = 296.6$  K, 28,260 nodes.*

small region upstream and downstream of the reflected shock. As can be seen from the Mach iso-contours, the influence of the condensation on the flow is negligible. As for the dry flow case  $g_{max} = 0$ , see Fig. 6.2, the gas expands up to  $M_f = 6.1$  just upstream of the Mach disk, both for  $g_{max} = 0.2$  and  $g_{max} = 0.4$ .

For larger liquid mass fraction, however, condensation occurs inside the region bounded by the barrel shock and the Mach disk. The expansion is not as deep, only to  $M_f \approx 3.7$  for  $g_{max} = 0.6$  and  $M_f \approx 3.8$  for  $g_{max} = 0.8$ . The Mach disk now shifts to a location further downstream. We also observe that the diameter of the Mach disk increases as the liquid mass fraction is increased.

The Mach-disk location as a function of the maximum liquid mass fraction is shown in Fig. 6.8. Note that, in addition to the previous results, additional simulations were performed

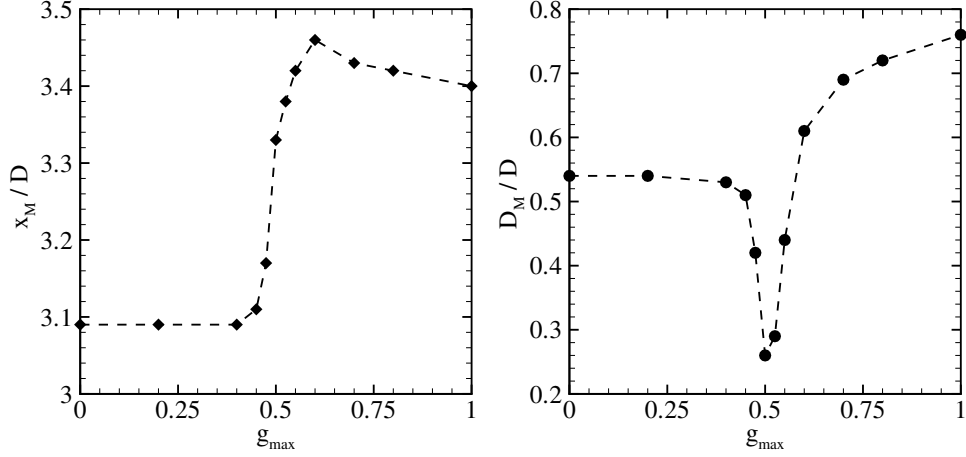


FIGURE 6.8: *Underexpanded xenon jet. Mach-disk location and diameter for various liquid mass fractions.  $p_r/p_a=20$ ,  $T_r = 296.6$  K.*

for  $g_{max} = 0.45, 0.475, 0.5, 0.525, 0.55$  and  $g_{max} = 0.7$ . As can be seen, there is a definite, relatively sharp increase in the distance of the Mach disk from the nozzle exit plane, obtaining a maximum at  $g_{max} \approx 0.6$ . Above this value of  $g_{max}$  the location is again more or less constant, as also seen in the left plot of Fig. 6.8. In case of  $g_{max} = 1.0$ , which corresponds to the real physical situation, the increase in the distance of the Mach disk from the nozzle exit plane is approximately 10%, within the scatter of the results of Crist et al. [18], see Fig. 6.5.

The diameter of the Mach disk, shown in the right plot of Fig. 6.8, varies more strongly with  $g_{max}$  than the Mach-disk location. Up to  $g_{max} = 0.4$ , the diameter is constant, but for  $g_{max} = 0.5$  the diameter becomes relatively small. For this value of  $g_{max}$ , there is a considerable amount of liquid (values up to  $g \approx 0.22$ ) present in the flow outside the barrel shock upstream of the reflected shock.

The heat released during the formation of the liquid increases the pressure outside the barrel shock and causes the barrel shock to be located closer to the centerline. This causes the sharp decrease of the diameter of the Mach disk at  $g_{max} = 0.5$ . For larger  $g_{max}$ , more liquid is formed inside the barrel shock and less outside the barrel shock, and the diameter of the Mach disk increases sharply with increasing  $g_{max}$ .

Attempts have been made to explore whether there exists a hysteresis in the flow pattern for the case of increasing or decreasing  $g_{max}$ . However, computing a sequence of solutions from low  $g_{max}$  to higher  $g_{max}$  or the other way around did not result in two different solutions, i.e. hysteresis was not found.

## 6.5 Influence of the saturation in the reservoir

As a further study of the influence of the condensation on the underexpanded jet, three additional simulations were performed. For these additional simulations, the temperature in the reservoir was set to  $T_r = 282.2$ ,  $T_r = 319.7$  and  $T_r = 364.3$ , corresponding to reservoir saturations of  $\Phi_0 = 0.40$ ,  $\Phi_0 = 0.20$  and  $\Phi_0 = 0.10$ , respectively. The results (for  $g_{max} = 1$ ) are shown in Fig. 6.9, which includes the earlier results for  $\Phi_0 = 0.30$  ( $T_r = 296.6$  K). The

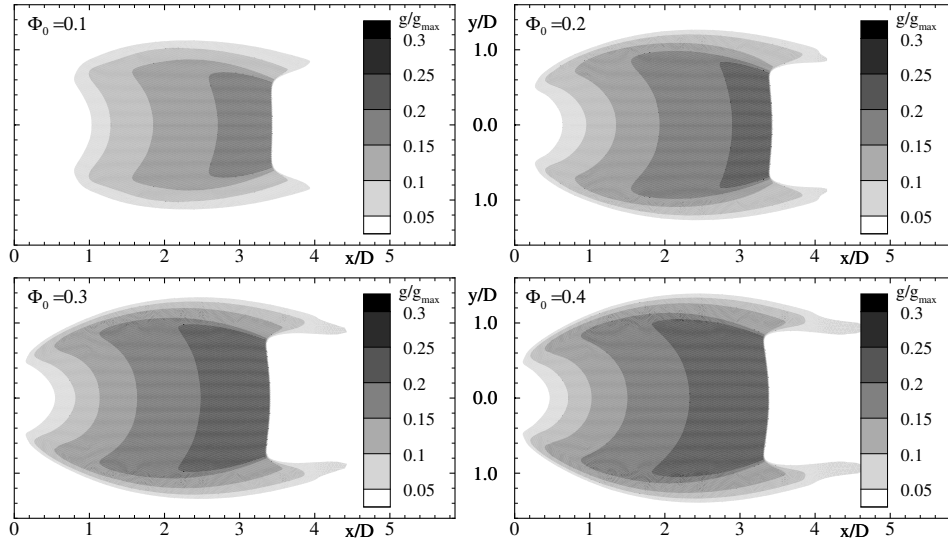


FIGURE 6.9: *Underexpanded xenon jet. Liquid mass fraction for varying reservoir saturation level.  $p_r/p_a=20$ .*

influence of the saturation ratio on the flow-field topology is small, with a gradual increase in Mach-disk diameter and barrel-shock diameter. As we can see, the location of the Mach disk is the same for all saturation ratios. The curvature of the Mach disk, on the other hand, becomes more pronounced as the saturation is increased. We can also see from Fig. 6.9 that the amount of liquid formed per kg mixture increases only slightly with increasing saturation, and if we consider the amount of liquid on the centerline, we see that there is even a small decrease in liquid mass fraction. This is caused by the increase in the diameter of the region where the liquid is located, i.e. the liquid mass fraction is high in a larger area.

## 6.6 Conclusion

The numerical results show that condensation has a considerable effect on the underexpanded jet of xenon. The condensation considerably reduces the maximum Mach number reached in the expansion, widens the plume and the Mach disk, and moves the Mach disk slightly aft. It is shown that for  $p_r/p_a = 20$ , most of the liquid appears inside the region enclosed by

the barrel shock and the Mach disk, in a cylindrical region of diameter of about two nozzle diameters and a length of about one nozzle diameter, immediately upstream of the Mach disk. This would form the best candidate region to focus the laser for producing EUV light. The amount of liquid that is encountered by the laser as it travels through the jet plume can be increased by lowering the reservoir temperature.

---



---

# CONDENSATION IN REAL-GAS FLOWS IN THREE DIMENSIONS

---



This chapter presents results that have been obtained with the 3D unstructured-grid numerical method based on the Euler equations and Hill's method of moments for multiple component mixtures. The 3D method requires a droplet-growth valid for all Knudsen numbers  $Kn$ , which is needed to describe droplet growth in a high-pressure background. The 3D method includes the real-gas model as described in chapter 3. The application concerns natural gas expanding in a Condi-Cyclone.

## 7.1 Hill's method of moments for a multiple component mixture

Hill's moment equations [31], for a mixture containing  $K$  components, of which  $N$  components nucleate, read (in integral conservation form):

$$\frac{\partial}{\partial t} \int_V \mathbf{U} \, dV + \int_{\partial V} \vec{\mathbf{F}} \cdot \vec{n} \, dS = \int_V \mathbf{W} \, dV, \quad (7.1)$$

with

$$\mathbf{U} = \begin{pmatrix} \rho Q_{0,n} \\ \rho Q_{1,n} \\ \rho Q_{2,n} \\ \rho g_{k,n} \end{pmatrix} \quad \text{and} \quad \vec{\mathbf{F}} = \begin{pmatrix} \rho \vec{u} Q_{0,n} \\ \rho \vec{u} Q_{1,n} \\ \rho \vec{u} Q_{2,n} \\ \rho \vec{u} g_{k,n} \end{pmatrix}, \quad (7.2)$$

where  $Q_{0,n}$ ,  $Q_{1,n}$  and  $Q_{2,n}$  are the zeroth, first and second moment of the droplet-radius distribution, respectively, of droplets that start as nucleus of component  $n$ , and  $g_{k,n}$  is the liquid mass fraction of component  $k$  in droplet nucleus of component  $n$ . The index  $n$  indicates the nucleating components ( $n = 1(1)N \leq K$ ). In a flow with multiple condensing components, more than one component can act as nucleus on which the other components then condense. In case of two nucleating components, for example, we have  $N = 2$  and we have to distinguish between two different droplet groups, one for nucleating component  $n = 1$ , and one for nucleating component  $n = 2$ . The liquid mass fraction of component  $k$  in droplet group  $n = 1$  is then given by  $g_{k,1}$  and that of component  $k$  in droplet group  $n = 2$  is given by  $g_{k,2}$ .

---

The source term consists of two parts. One term represents the formation of nuclei, the other term the condensation of all vapour components of the mixture on the formed nuclei. We denote this as  $\mathbf{W} = \mathbf{W}_{nucl} + \mathbf{W}_{cond}$ , where

$$\mathbf{W}_{nucl} = \begin{pmatrix} J_n \\ r_n^* J_n \\ r_n^{*2} J_n \\ \delta_{kn} \frac{4}{3} \pi \varrho_{l,k} r_n^{*3} J_n \end{pmatrix} \quad \text{and} \quad \mathbf{W}_{cond} = \begin{pmatrix} 0 \\ \rho Q_{0,n} \sum_{k=1}^{K} \dot{r}_k \\ 2\rho Q_{1,n} \sum_{k=1}^{K} \dot{r}_k \\ 4\rho \pi Q_{2,n} \varrho_{l,k} \dot{r}_k \end{pmatrix}, \quad (7.3)$$

with  $r_n^*$  and  $J_n$  the critical radius and the nucleation rate, respectively. In Eqs. (7.1) - (7.3) the last equation denotes any of the  $K$  components. The set of equations is valid for any of the  $N$  nucleating components. So Hill's moment equations for a mixture of gases with  $K$  components of which  $N$  components nucleate constitute a system of  $N(K+3)$  equations.

### 7.1.1 Multi-component droplet growth

The expression for diffusion-controlled droplet-growth in a multi-component system, in the limit of dilute vapour components in a non-condensing background gas, can be written as (see Luijten et al. [43])

$$\dot{r}^2 = 2 \frac{\hat{\rho}_v}{\hat{\varrho}_l} \sum_{k=1}^K D_k (y_{v,k} - y_{v,k}^{eq}), \quad (7.4)$$

provided that the components are well miscible. In this expression,  $\hat{\rho}_v$  and  $\hat{\varrho}_l$  are the total molar densities of the vapour and the condensate (i.e.  $\hat{\rho}_v = \rho_v / \mathcal{M}$  and  $\hat{\varrho}_l = \varrho_l / \mathcal{M}$ ), respectively. The actual molar fraction of the vapour  $y_{v,k}$  and the equilibrium molar fraction of the vapour  $y_{v,k}^{eq}$  are defined as

$$y_{v,k} \equiv \frac{\mathcal{N}_{v,k}}{\mathcal{N}} \quad \text{and} \quad y_{v,k}^{eq} \equiv \frac{\mathcal{N}_{v,k}^{eq}}{\mathcal{N}}, \quad (7.5)$$

where  $\mathcal{N}$  is the number of moles of the vapour/liquid mixture, and  $\mathcal{N}_{v,k}$  and  $\mathcal{N}_{v,k}^{eq}$  are the actual and equilibrium number of moles of vapour component  $k$  in the mixture, respectively.

The molar mass  $\mathcal{M}$  of the mixture follows from

$$\mathcal{M} = \sum_{k=1}^K y_{0,k} \mathcal{M}_k, \quad (7.6)$$

with  $\mathcal{M}_k$  the molar mass of component  $k$ , and  $y_{0,k}$  the (constant) molar fraction of the vapour and liquid of component  $k$ ,

$$y_{0,k} = y_{v,k} + y_{l,k}. \quad (7.7)$$

The molar liquid fraction  $y_{l,k}$  is defined as

$$y_{l,k} \equiv \frac{\mathcal{N}_{l,k}}{\mathcal{N}}, \quad (7.8)$$

where  $\mathcal{N}_{l,k}$  is the number of moles of liquid of component  $k$ . In Eq. (7.4),  $D_k$  denotes the diffusion coefficient. To extend the droplet-growth model to the free-molecular regime and the transition regime in between (see also Peeters et al. [51]), the droplet-growth model is modified in the following way:

$$\dot{r}^2 = \hat{\rho}_v \sum_{k=1}^K \frac{Nu_k^t}{\hat{\rho}_{l,k}} D_k (X_v y_{v,k} - X_v^{eq} y_{v,k}^{eq}), \quad (7.9)$$

with  $X_v$  and  $X_v^{eq}$  the total molar vapour fraction and the total equilibrium molar vapour fraction:

$$X_v = \frac{\sum_{k=1}^K \mathcal{N}_{v,k}}{\mathcal{N}} \quad \text{and} \quad X_v^{eq} = \frac{\sum_{k=1}^K \mathcal{N}_{v,k}^{eq}}{\mathcal{N}}, \quad (7.10)$$

respectively. The Nusselt number  $Nu_k^t$  of the transition regime, is included to extend the droplet-growth model to higher Knudsen numbers. The transition regime is the regime which lies in between the continuum and free-molecular regime. The Nusselt number of the transition regime is given by

$$Nu_k^t = \frac{Nu_k^f Nu_k^c}{Nu_k^f + Nu_k^c}, \quad (7.11)$$

where the superscript  $f$  denotes the free-molecular regime and  $c$  the continuum regime. Since  $Nu^c$  is always close to 2 (see Luijten [42]),  $Nu^f$  largely determines the behavior of  $Nu^t$ . It becomes very small in the free-molecular limit, so that  $Nu^c$  drops out and we have  $Nu^t \rightarrow Nu^f$ . In the continuum limit the situation is reversed, and we get  $Nu^t \rightarrow Nu^c = 2$ , and consequently Eq. (7.9) reduces to the growth-law for the continuum regime.

The Nusselt number of the free-molecular regime is given by

$$Nu_k^f = \sqrt{\frac{2}{\pi}} \sqrt{\frac{\mathcal{M}}{\mathcal{M}_k} \frac{Sc_k}{Kn}}, \quad (7.12)$$

where  $Sc$  is the Schmidt number. The Schmidt number is defined as (see Bird et al. [12]):

$$Sc_k \equiv \frac{\mu}{\rho_v D_k}, \quad (7.13)$$

where  $\mu$  is the dynamic viscosity, and the Knudsen number  $Kn$ , see section 2.2.4, is defined as the ratio of the mean free path of a vapour molecule and the droplet diameter

$$Kn = \frac{l}{2r}. \quad (7.14)$$

The mean free path is given by

$$l = \frac{2\mu\sqrt{RT}}{p}. \quad (7.15)$$

This multi-component droplet-growth model can be used for either molecular growth ( $Kn > 10$ ), diffusion controlled growth ( $Kn < 0.01$ ) and the transition region in between.

### 7.1.2 Nucleation model

The expression for the nucleation rate  $J$  given in section 2.2.3 for the CNT and ICCT model can also be applied to the real gas vapour/liquid mixture. For the determination of the super-saturation ratio  $\Phi_n$  of a nucleating component, however, a different expression is used, namely

$$\Phi_n = \frac{y_{v,n}}{y_{v,n}^{eq}}. \quad (7.16)$$

This expression is valid for both low and high pressures, and reduces to Eq. (2.1) for low pressures.

### 7.1.3 Closure of Hill's equations

To solve the governing equations, consisting of the 5 Euler equations for 3D flow, and Hill's method of moments for multiple condensing components, several physical properties have to be known. For natural gas, the necessary physical properties are listed below.

$\mu$ : dynamic viscosity

$\sigma$ : surface tension

$X_v^{eq}$ : equilibrium total molar vapour fraction

$y_{v,k}^{eq}$ : mole fraction of component  $k$  of the vapour in the equilibrium mixture

$D_k$ : diffusion coefficient per component

$\varrho_{l,k}$ : condensate density per component

For the 3D numerical method, these properties are available in the form of a database, given at user specified combinations of  $p$  and  $T$ . The values for any pressure  $p$  and temperature  $T$  are obtained from the data base by linear interpolation.

## 7.2 Determination of the coefficients of the real-gas EOS

With the real-gas EOS derived in chapter 3 we want to describe the thermodynamic behavior of a gas mixture at high pressure, consisting of  $K$  components. We assume that for the gas mixture considered, some auxiliary procedure creates the data-base (see also table 3.1), for the gas mixture. The data base is generated for a given range and increment of the pressure and the temperature.

If we denote the minimum and maximum pressure by  $p_{min}$  and  $p_{max}$ , respectively, the minimum and maximum temperature by  $T_{min}$  and  $T_{max}$ , respectively, and the increments in pressure and temperature by  $p_{inc}$  and  $T_{inc}$ , respectively, the auxiliary procedure creates table 7.1.

---

pressure (Pa)	temperature (K)	compressibility factor (-)	specific enthalpy J/kg	equilibrium molar vapour fraction; $k = 1(1)K$
$p_{min}$	$T_{min}$	$z$	$h$	$y_{v,k}^{eq}$
$p_{min}$	$T_{min} + T_{inc}$	$z$	$h$	$y_{v,k}^{eq}$
$\cdot$	$\cdot$	$\cdot$	$\cdot$	$\cdot$
$p_{min}$	$T_{max} - T_{inc}$	$z$	$h$	$y_{v,k}^{eq}$
$p_{min}$	$T_{max}$	$z$	$h$	$y_{v,k}^{eq}$
$p_{min} + p_{inc}$	$T_{min}$	$z$	$h$	$y_{v,k}^{eq}$
$p_{min} + p_{inc}$	$T_{min} + T_{inc}$	$z$	$h$	$y_{v,k}^{eq}$
$\cdot$	$\cdot$	$\cdot$	$\cdot$	$\cdot$
$p_{max} - p_{inc}$	$T_{max}$	$z$	$h$	$y_{v,k}^{eq}$
$p_{max}$	$T_{min}$	$z$	$h$	$y_{v,k}^{eq}$
$\cdot$	$\cdot$	$\cdot$	$\cdot$	$\cdot$
$p_{max}$	$T_{max}$	$z$	$h$	$y_{v,k}^{eq}$

TABLE 7.1: Real-gas data-base produced by an auxiliary procedure.

In formula form, the temperature and pressure can be written as

$$p_i = p_{min} + (i - 1)p_{inc} ; \quad i = 1(1)I , \quad (7.17)$$

$$T_j = T_{min} + (j - 1)T_{inc} ; \quad j = 1(1)J , \quad (7.18)$$

where

$$I = 1 + \text{int}\left(\frac{p_{max} - p_{min}}{p_{inc}}\right) , \quad (7.19)$$

$$J = 1 + \text{int}\left(\frac{T_{max} - T_{min}}{T_{inc}}\right) . \quad (7.20)$$

Typical values for  $I$  and  $J$  are  $10^2$ . From table 7.1 we can derive the density and internal energy in the following way (note that the real gas EOS reads  $p = z\rho RT$ )

$$R = \frac{\mathcal{R}}{\sum_{k=1}^K y_{v,k}^{eq} \mathcal{M}_k} , \quad (7.21)$$

$$\rho = \frac{p}{zRT} , \quad (7.22)$$

$$e = h - p/\rho . \quad (7.23)$$

In this way, we have found the density and internal energy at every combination of pressure and temperature, so for every combination of  $i$  and  $j$  we now have the following functions

$$z_{i,j} = z(\rho_{i,j}, e_{i,j}) , \quad (7.24)$$

$$T_{i,j} = T(\rho_{i,j}, e_{i,j}) . \quad (7.25)$$

By introducing a unique index  $\iota$ , defined as  $\iota \equiv (j-1)I + i$ , we can replace any combination of indices  $i, j$  by  $\iota$ , so that

$$z_\iota = z(\rho_\iota, e_\iota), \quad (7.26)$$

$$T_\iota = T(\rho_\iota, e_\iota). \quad (7.27)$$

In the real-gas EOS, these functions are specified by Eqs. (3.42) and (3.46), respectively, which are repeated here for convenience:

$$z(\rho, e) = z_{00} + z_{10}\rho + z_{20}\rho^2 + z_{11}\rho e + z_{01}e + z_{02}e^2, \quad (7.28)$$

$$T(\rho, e) = \frac{1}{-R\{z_{11}\rho + (z_{01} + 2z_{02}e)\ln(\rho)\} + T_0e^{-1} + T_1 + T_2e}. \quad (7.29)$$

First, the coefficients  $z_{00}, z_{10}, \dots, z_{02}$  in the expression for the compressibility factor  $z$  are determined. These are determined from the real-gas data-base using a least-squares method, resulting in the minimalisation of the following expression

$$\psi(b) = \sum_\iota \phi_\iota [z(\rho_\iota, e_\iota) - z_\iota]^2, \quad (7.30)$$

where  $b = (z_{00}, z_{10}, z_{20}, z_{11}, z_{01}, z_{02})^T$ , and  $\phi$  is a weight function (this function is explained later on in section 7.2.1). To find the minimum of  $\psi$  we set  $\frac{d\psi}{db} = 0$ . Differentiation of Eq. (7.30) gives

$$\begin{aligned} \frac{d\psi}{db} &= \frac{d}{db} \left( \sum_\iota \phi_\iota [z(\rho_\iota, e_\iota) - z_\iota]^2 \right) \\ &= \sum_\iota \frac{d}{db} (\phi_\iota [z(\rho_\iota, e_\iota) - z_\iota]^2) \\ &= 2 \sum_\iota \phi_\iota [z(\rho_\iota, e_\iota) - z_\iota] \frac{d}{db} z(\rho_\iota, e_\iota). \end{aligned} \quad (7.31)$$

Setting Eq. (7.31) equal to zero results in the following system

$$A b = c. \quad (7.32)$$

Matrix  $A$  and column vector  $c$  are given below:

$$A = \begin{bmatrix} \sum_\iota \phi_\iota & \sum_\iota \phi_\iota \rho_\iota & \sum_\iota \phi_\iota \rho_\iota^2 & \sum_\iota \phi_\iota \rho_\iota e_\iota & \sum_\iota \phi_\iota e_\iota & \sum_\iota \phi_\iota e_\iota^2 \\ \sum_\iota \phi_\iota \rho_\iota & \sum_\iota \phi_\iota \rho_\iota^2 & \sum_\iota \phi_\iota \rho_\iota^3 & \sum_\iota \phi_\iota \rho_\iota^2 e_\iota & \sum_\iota \phi_\iota \rho_\iota e_\iota & \sum_\iota \phi_\iota \rho_\iota e_\iota^2 \\ \sum_\iota \phi_\iota \rho_\iota^2 & \sum_\iota \phi_\iota \rho_\iota^3 & \sum_\iota \phi_\iota \rho_\iota^4 & \sum_\iota \phi_\iota \rho_\iota^3 e_\iota & \sum_\iota \phi_\iota \rho_\iota^2 e_\iota & \sum_\iota \phi_\iota \rho_\iota^2 e_\iota^2 \\ \sum_\iota \phi_\iota \rho_\iota e_\iota & \sum_\iota \phi_\iota \rho_\iota^2 e_\iota & \sum_\iota \phi_\iota \rho_\iota^3 e_\iota & \sum_\iota \phi_\iota \rho_\iota^2 e_\iota^2 & \sum_\iota \phi_\iota \rho_\iota e_\iota^2 & \sum_\iota \phi_\iota \rho_\iota e_\iota^3 \\ \sum_\iota \phi_\iota e_\iota & \sum_\iota \phi_\iota \rho_\iota e_\iota & \sum_\iota \phi_\iota \rho_\iota^2 e_\iota & \sum_\iota \phi_\iota \rho_\iota e_\iota^2 & \sum_\iota \phi_\iota e_\iota^2 & \sum_\iota \phi_\iota e_\iota^3 \\ \sum_\iota \phi_\iota e_\iota^2 & \sum_\iota \phi_\iota \rho_\iota e_\iota^2 & \sum_\iota \phi_\iota \rho_\iota^2 e_\iota^2 & \sum_\iota \phi_\iota \rho_\iota e_\iota^3 & \sum_\iota \phi_\iota e_\iota^3 & \sum_\iota \phi_\iota e_\iota^4 \end{bmatrix} \quad (7.33)$$

$$c = \begin{pmatrix} \sum_l \phi_l z_l \\ \sum_l \phi_l z_l \rho_l \\ \sum_l \phi_l z_l \rho_l^2 \\ \sum_l \phi_l z_l \rho_l e_l \\ \sum_l \phi_l z_l e_l \\ \sum_l \phi_l z_l e_l^2 \end{pmatrix} \quad (7.34)$$

We can solve for  $b$  via the  $LU$  decomposition of matrix  $A$  (Gauss elimination followed by back-substitution).

With the constants of the compressibility factor known, the constants  $T_0$ ,  $T_1$  and  $T_2$  of the temperature fit, Eq. (7.29), are determined by minimalisation of the following expression

$$\psi(b) = \sum_l \phi_l \left[ \frac{1}{T(\rho_l, e_l)} - \frac{1}{T_l} \right]^2, \quad (7.35)$$

where  $b = (T_0, T_1, T_2)^T$ . In the same way as for the compressibility factor, this results in the following system

$$A b = c, \quad (7.36)$$

where matrix  $A$  and column vector  $c$  are now given by

$$A = \begin{bmatrix} \sum_l \phi_l / e_l^2 & \sum_l \phi_l / e_l & \sum_l \phi_l \\ \sum_l \phi_l / e_l & \sum_l \phi_l & \sum_l \phi_l e_l \\ \sum_l \phi_l & \sum_l \phi_l e_l & \sum_l \phi_l e_l^2 \end{bmatrix} \quad (7.37)$$

$$c = \begin{pmatrix} \sum_l \phi_l [1/T_l + R_l \{z_{11} \rho_l + (z_{01} + 2z_{02} e_l) \ln(\rho_l)\}] / e_l \\ \sum_l \phi_l [1/T_l + R_l \{z_{11} \rho_l + (z_{01} + 2z_{02} e_l) \ln(\rho_l)\}] \\ \sum_l \phi_l [1/T_l + R_l \{z_{11} \rho_l + (z_{01} + 2z_{02} e_l) \ln(\rho_l)\}] e_l \end{pmatrix} \quad (7.38)$$

As before,  $b$  is solved by Gauss elimination and back-substitution.

### 7.2.1 The weight function

If we consider a flow without entropy creation, then all  $(p, T)$  values throughout the domain would be situated on the isentropic curve. Since the entropy in a flow with condensation increases, not all  $(p, T)$  values in the flow domain are situated on the isentropic curve. When creating the 9 parameters of the real-gas EOS, it would be irrelevant to include the  $(p, T)$  combinations which are located far away from the isentropic curve. For this reason, the weight function  $\phi$  is included. It is equal to 1 on the isentropic curve, and decreases exponentially away from this curve.

---

To determine the weight function, the parameters of the real-gas EOS have to be known (since we want to determine the isentropic curve). However, to determine the parameters of the real-gas EOS, the weight function has to be known.

To solve this problem, an initial weight distribution of  $\phi_\ell = 1$  is chosen, but the weight is set to zero at the points which satisfy one of the following conditions

$$T \geq T_{min} + \frac{1}{3}(T_{max} - T_{min}) + \frac{T_{max} - T_{min}}{p_{max} - p_{min}}(p - p_{min}) , \quad (7.39-a)$$

$$T \leq T_{min} - \frac{1}{8}(T_{max} - T_{min}) + \frac{T_{max} - T_{min}}{p_{max} - p_{min}}(p - p_{min}) . \quad (7.39-b)$$

This is visualized in Fig. 7.1, where the grey areas represent the regions of the  $(p, T)$  domain

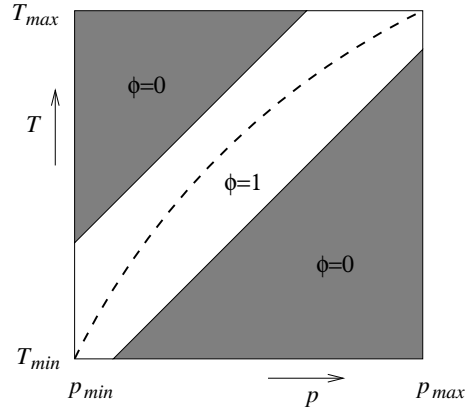


FIGURE 7.1: Fit region: weight factor of zero in grey areas. Dashed line denotes (estimated) isentropic curve.

where the weight  $\phi$  is set to zero. Note that the values for  $p_{min}$ ,  $p_{max}$ ,  $T_{min}$  and  $T_{max}$  should be chosen with care, i.e. such that the isentropic curve is located within the  $\phi = 1$  region in Fig. 7.1.

Next, table 7.1 is created with relatively high increments  $p_{inc}$  and  $T_{inc}$ . From this table, the 9 parameters of the real-gas equation of state are determined.

With the equation of state known, a reference entropy  $s_{ref}$  is calculated at a certain reference condition  $(p_{ref}, T_{ref})$ , for example the static pressure and temperature at an inflow boundary. This reference entropy is then used to isentropically calculate the temperature at  $p_{min}$ ,  $p_{med} = (p_{min} + p_{max})/2$  and  $p_{max}$ . This results in 3 different  $p, T$  combinations, which correspond to three different points in the  $(p, T)$  domain. These three points are used to determine a circle which passes through these three points. The equation of this circle is

$$(p - p_{cnt})^2 + (T - T_{cnt})^2 = r^2 , \quad (7.40)$$

where  $p_{cnt}$  and  $T_{cnt}$  represent the center of the circle, and  $r$  is the radius of the circle. With the circle known, the increments are set to, for example,  $p_{inc} = 1$  bar and  $T_{inc} = 1$  K, and



a new table is created, similar to table 7.1. However, for  $(p, T)$  combinations located in the grey domain in Fig. 7.1 no values are calculated, since these are not needed. With the new table the weights are then determined in the following way:

$$\phi_i = \begin{cases} \exp(-10\tilde{r}_i^2) & \tilde{r}_i > 0 \\ \exp(-200\tilde{r}_i^2) & \tilde{r}_i \leq 0 \end{cases}, \quad (7.41)$$

with

$$\tilde{r}_i = \sqrt{(p_i - p_{cnt})^2 + (T_i - T_{cnt})^2} - r, \quad (7.42)$$

and

$$\bar{r}_i = \frac{\tilde{r}_i}{\max_i(|\tilde{r}|)}. \quad (7.43)$$

For a practical situation the weights are given in Fig. 7.2 With the weights known, the 9

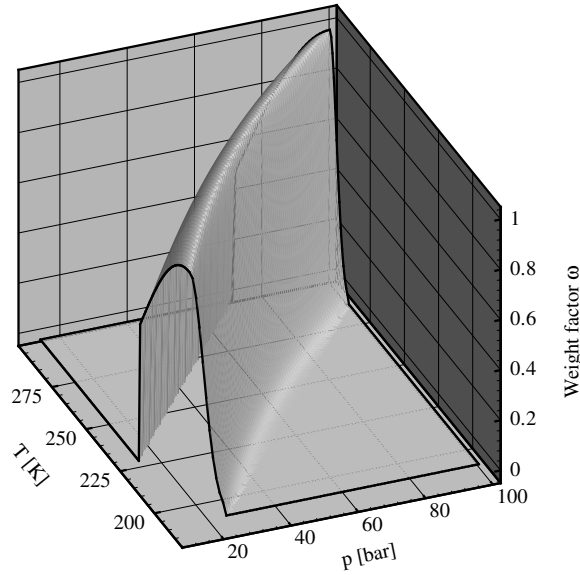


FIGURE 7.2: Weight distribution in  $(p, T)$  domain.

parameters of the real-gas EOS can be determined. The deviation of the pressure and the temperature obtained from the real-gas EOS from the values of  $p$  and  $T$  in the data-base is shown in Fig. 7.3. The deviation in both the temperature and the pressure is small and less than 2%.

---

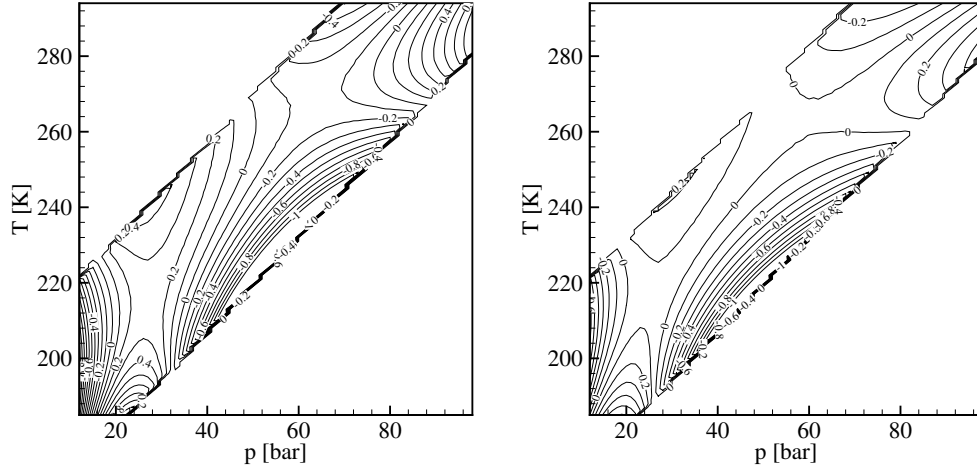


FIGURE 7.3: *Deviation between real-gas EOS and data-base. Left plot shows the deviation in pressure, right plot shows the deviation in temperature (both in %).*

### 7.3 3D test-case: The flow of natural gas through a Condi-Cyclone

A Condi-Cyclone is an apparatus consisting of a Laval nozzle, a vortex generator, and a deposition section, as sketched in Fig. 7.4.

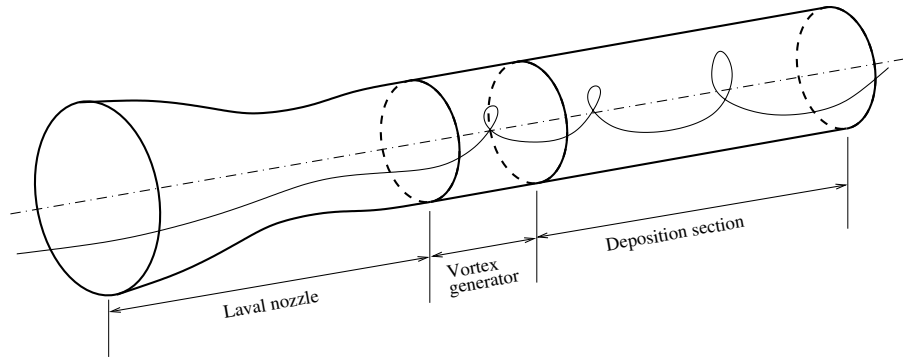


FIGURE 7.4: *Schematic representation of a Condi-Cyclone.*

The Laval nozzle expands the flow to supersonic velocity, such that most of the components in the natural gas become super-saturated. Nucleation of one or more of the components will take place, and the super-saturated components will condense on the existing nuclei. The droplets are then convected downstream with the flow towards the vortex generator. The vortex generator, in the present study consisting of a slender delta-wing attached to the tube wall, introduces swirl into the flow, and in the deposition section down-

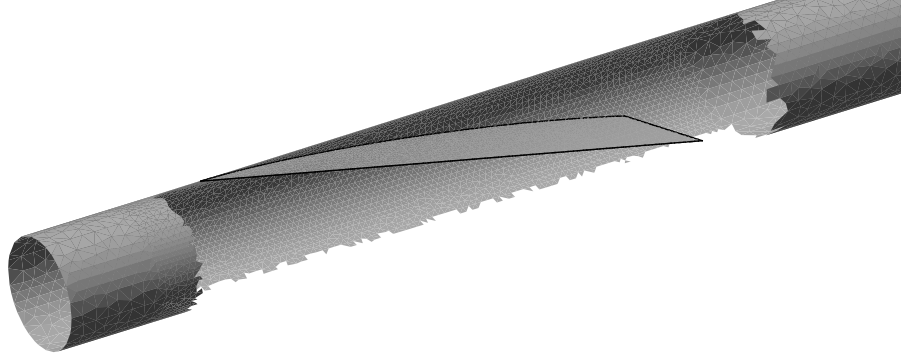


FIGURE 7.5: *Condi-Cyclone, close up of delta wing in the vortex generator.*

stream of the vortex generator, the droplets are centrifuged towards the tube wall under the influence of centrifugal forces. In the Condi-Cyclone, the droplets move relatively to the flow, i.e. there is slip between the gas and liquid phase. In the present 3D method, however, it was assumed that the droplets move with the flow, i.e. in the numerical method there is no slip between the gas and liquid phase. This implies that the present method includes the effect of the nucleation and condensation (specifically the heat addition) on the gas flow, but not the effect on the gas-dynamics of the slip between the liquid phase and the gas phase. With the gas-dynamics established in this way, a post-processing procedure is used, based on the Lagrangian equation of motion of the droplets in the given swirling flow, to compute the trajectories of a specified droplet distribution. This second step in the computational set-up provides information on the separation efficiency of the Condi-Cyclone. This procedure is not considered here further, since we merely want to demonstrate the capability of the 3D method to simulate the flow of multiple condensing components at high pressure in 3D geometries.

### 7.3.1 Generation of the real-gas EOS parameters

The multiple-component mixture flowing through the Condi-Cyclone is a natural gas, consisting of 20 components. The mixture consists of several light and heavy hydrocarbons, nitrogen, water, and carbon-dioxide. The minimum and maximum values of the temperature and the pressure, and the increments in pressure and temperature as listed below:

$$\begin{aligned}
 p_{min} &= 15 \text{ bar} \\
 p_{max} &= 100 \text{ bar} \\
 T_{min} &= 182 \text{ K} \\
 T_{max} &= 300 \text{ K} \\
 p_{inc} &= 1 \text{ bar} \\
 T_{inc} &= 1 \text{ K}
 \end{aligned}$$

The 9 parameters of the Maxwell-relations conforming real-gas EOS are obtained as described in section 7.2, resulting in the following values for the 9 parameters:

$$\begin{aligned}
z_{00} &= 0.64695 \\
z_{10} &= -0.72623 \times 10^{-2} \quad \text{m}^3/\text{kg} \\
z_{20} &= 0.19712 \times 10^{-4} \quad \text{m}^6/\text{kg}^2 \\
z_{11} &= 0.11780 \times 10^{-7} \quad \text{m}^3/\text{J} \\
z_{01} &= 0.20364 \times 10^{-5} \quad \text{kg}/\text{J} \\
z_{02} &= -0.28508 \times 10^{-11} \quad \text{kg}^2/\text{J}^2 \\
T_0 &= 0.97981 \times 10^3 \quad \text{J}/\text{kg} \cdot \text{K} \\
T_1 &= 0.41800 \times 10^{-2} \quad \text{K}^{-1} \\
T_2 &= -0.91526 \times 10^{-8} \quad \text{kg}/\text{J} \cdot \text{K}
\end{aligned}$$

### 7.3.2 Flow in the Laval nozzle

Since the flow leaving the Laval nozzle and entering the vortex generator is supersonic, it is possible to first obtain a flow solution in the Laval nozzle, and subsequently to solve the flow in the vortex generator and deposition section. The inflow conditions for the vortex generator are then taken equal to the outflow conditions of the Laval nozzle.

The method is, in principle, capable of considering all components as possible nuclei, but the number of Hill equations to be solved would then amount to  $20(20 + 3) = 460$ , which is not feasible in numerical simulations. Furthermore, the process of how precisely a certain component does or does not condense on a nucleus of another component or on a droplet covered with another component is not yet completely understood (Peeters [50]). Such knowledge should be added as model to the present method in order to make it an accurate tool. Therefore, the nucleating component is water, based on knowledge obtained from experiments, which appear to indicate that water nucleates first and that subsequently the other components condense on the water nuclei.

The Laval nozzle is rotational symmetric and has a smooth variation in diameter. Therefore, the flow in the nozzle can, in good approximation, be considered as quasi-one-dimensional (Q1D). In a Q1D flow we consider cross-sectional averaged flow field quantities and only the (cross-sectional averaged) axial component of the velocity. The flow in the nozzle is calculated with a Q1D method based on the Q1D Euler equations, augmented with Hill's method of moments for multiple-condensing components. The Q1D method is second-order accurate and contains the same droplet growth model and nucleation model as the 3D method and is based on the same numerical techniques. The benefit of a Q1D method, is that the generation of meshes is trivial and calculation times are very short.

For the Laval nozzle, a mesh with 200 nodes in  $x$ -direction was created. The convergence history of the numerical simulation for the present case is shown in Fig. 7.6. From this figure we see that the residual decreases linearly on a logarithmic scale, and that there are no bumps after 2,000 iterations, indicating that the solution is converging smoothly to machine-zero, which is reached after 8,000 iterations.

The results are shown in Fig. 7.7. The dashed lines represent the solution when the source term is set to zero, i.e. when no condensation takes place. The influence of the condensation can clearly be seen in the Mach number and in the thermodynamic properties. The Mach number increases in the nozzle from a low subsonic value to a low supersonic value of about 1.2. With the heat addition due to condensation, the Mach number should increase in the subsonic regime and decrease in the supersonic regime, as is observed in the numerical

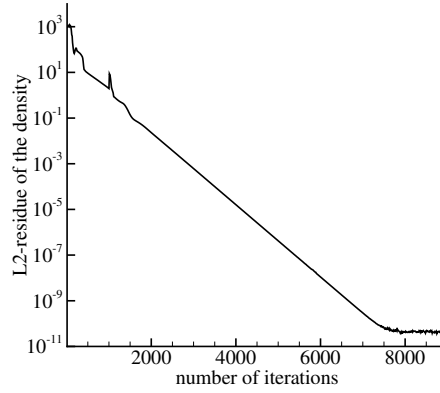


FIGURE 7.6: *Condi-Cyclone, convergence history of the flow in the Laval nozzle calculated with the Q1D method.*

results. The total temperature increases, while the total pressure decreases, both caused by the heat released during condensation. The compressibility factor  $z$  is also shown, and it can be seen that the condensation process tends to increase  $z$ , while the supersonic expansion decreases  $z$ . The plots of the nucleation rate and super-saturation ratio  $\Phi$  show the usual features. As soon as  $\Phi$  exceeds 1.0 nucleation starts, at an ever increasing rate, while in the rapidly expanding gas the super-saturation continues to increase. Then, as the number of nuclei is sufficiently large ( $10^{17}$  per  $\text{m}^3$  per s) the amount of liquid formed becomes significant and the super-saturation and the nucleation rate attain a maximum and subsequently decrease with increasing liquid mass fraction  $g$ . Note that in the present case most of the nucleation takes place in the subsonic part of the flow. This can be explained by the fact that the super-saturation in the reservoir is equal to 1.0, so that immediately upon entering the nozzle, the super-saturation exceeds 1.0 and the subsonic expansion will invoke nucleation.

The number of droplets per unit mass  $Q_0$  increases exponentially until the nucleation starts to decrease. After this, droplet-growth takes over the condensation process, leading to  $J = 0$  and to a constant number of droplets per unit mass. The droplet radius shown is the Hill-radius. Since the Hill-radius is an average property, it is ill-defined as long as the number of droplets is small. It is therefore common that the droplet radius exhibits some wiggles in regions where the number of droplets is relatively small. As can be seen in Fig. 7.7, the curve for the radius is smooth as soon as there are  $\sim 10^{13}$  particles per kg of mixture, i.e. for  $x > -0.06$ .

The last two plots in Fig. 7.7 show the liquid-mass fractions  $g_k$  and the normalized liquid mass fraction  $g_k/g_{max,k}$  of three components:  $\text{H}_2\text{O}$  (water),  $\text{C}_3\text{H}_8$  (propane) and  $\text{C}_9\text{H}_{20}$  (nonane). The liquid-mass fraction of water increases rapidly until the water vapour is nearly exhausted, while the other components shown grow on the existing water nuclei, and do not exhaust their vapour completely.

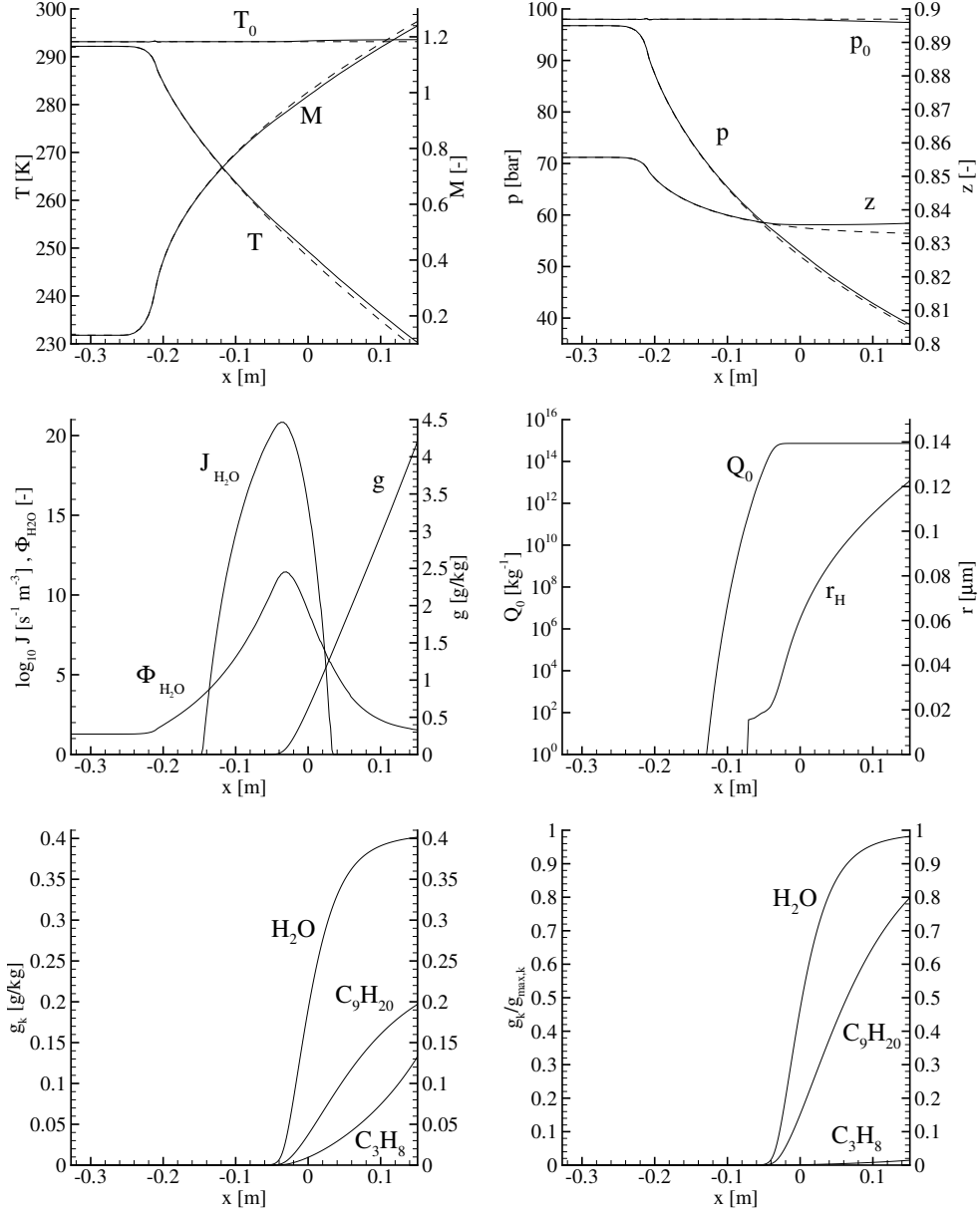


FIGURE 7.7: Condi-Cyclone, flow in the Laval nozzle calculated with the Q1D method. Dashed line denotes flow without condensation. Note that the nozzle throat is at  $x = 0$ .

### 7.3.3 Flow in the vortex generator and deposition section

The flow in the vortex generator and deposition section is solved with the 3D method, using the AUSM<sup>+</sup> scheme with  $\alpha = 3/16$  and  $\beta = 1/8$ , and second-order accurate fluxes with  $\kappa = 1/3$ . Nucleation is modeled with the ICCT model. The computational domain, consisting of the vortex generator and the deposition section, is discretized by a mesh consisting of tetrahedral elements. The mesh is generated with ICEM<sup>1</sup>. Two meshes have been created; a coarse mesh consisting of  $\sim 83\text{K}$  nodes and  $\sim 443\text{K}$  tetrahedra and a fine mesh consisting of  $\sim 154\text{K}$  nodes and  $\sim 840\text{K}$  tetrahedra.

The flow conditions at the outlet of the nozzle are used as inflow conditions for the Condi-Cyclone configuration. These conditions are:  $p = 38.78$  bar,  $T = 230.2$  K,  $u_x = 424.6$  m/s and  $u_y = u_z = 0$ , leading to a Mach-number of  $M = 1.24$ . At the inlet the liquid mass-fraction  $g$  is  $4.02$  g/kg and the Hill droplet radius  $r_H$  is  $0.12$   $\mu\text{m}$ . The conditions at the inflow boundary are used as initial conditions throughout the whole of the computational domain.

First, a solution on the coarse mesh is established, with 5,000 iterations. The solution obtained on the coarse mesh is then used to obtain an initial solution on the fine mesh, with the interpolation method described in appendix B. The numerical method is subsequently run for another 10,000 iterations. The convergence history of the simulations on the coarse and fine mesh are shown in Fig. 7.8.

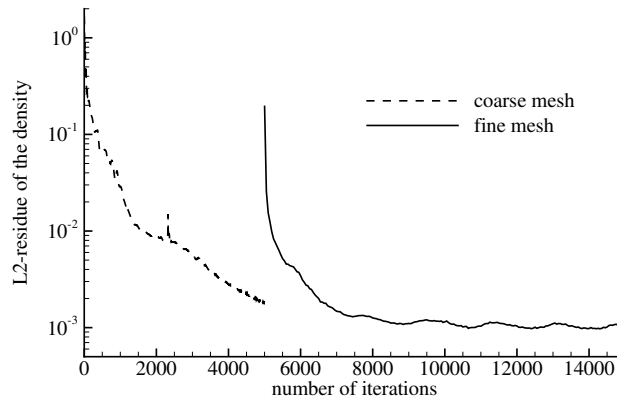


FIGURE 7.8: *Condi-Cyclone, convergence history for the flow in vortex generator and deposition section calculated with the 3D method.*

As we can see from the convergence history, the residual of the density decreases more than three orders in magnitude for the flow calculated on the coarse mesh. For the fine mesh, the residual decreases rapidly from the initial value and the decrease in the magnitude of the residual of the density for the flow on the fine mesh is around 3 orders in magnitude.

The results are presented in Figs. 7.9 and 7.10. All plots show the flow-field quantities on the upper-side of the delta wing and in a number of cross-flow planes normal to the tube-axis. As can be seen in Fig. 7.9a, the flow is supersonic everywhere in the tube. The supersonic flow

<sup>1</sup><http://www.icemcfd.com/>

around the sharp-edged slender delta-wing features a subsonic leading-edge, i.e. the Mach number normal to the leading edge is subsonic. This implies that the flow around the leading edge behaves as in subsonic flow, i.e. the edge is rounded by the flow, but since the edge is sharp it separates at the edge. In the present inviscid-flow method the numerical dissipation mimics the effects of the real viscosity in that the flow does separate at a sharp edge. This results in the formation of a shear layer that due to its self-induced velocity field rolls up into a vortex core, the so-called leading-edge vortex-core. From the apex of the delta wing to the trailing edge the vortex increases in strength to attain an appreciable strength. Downstream of the trailing edge the vortex is not fed by vorticity produced at the leading edge anymore and remains equal in strength. In this part of the tube, the deposition section, the vortex induces the swirling flow that causes the droplets formed in the condensation process to move towards the wall of the tube.

The vortex core can be detected in Fig. 7.9a, as the more or less circular region above the wing where the Mach number reaches a maximum. This region is also visible in the cross sections further downstream where the vortex follows a spiral-type of trajectory. In Fig. 7.9b we see that the temperature in the vortex core drops rapidly, to temperatures as low as 185 K. These extreme low temperatures induce a very high super-saturation of the nucleating component (water), even though here the water is already present as 97% liquid. This high super-saturation leads to nucleation above the upper side of the wing, and also downstream of the wing, see Fig. 7.9c, but has no significant effect on the number of nuclei. The total liquid mass fraction is shown in Fig. 7.10a. As can be seen, the highest liquid mass fractions occur in the vortex core.

The droplet diameter at the outlet of the tube is about  $0.4 \mu\text{m}$  and does not vary much over the outlet surface. Below the lower side of the wing however, which is not shown here, the droplet radius becomes very small, caused by the evaporation in the compression zone which is present there. In Figs. 7.10b and 7.10c the liquid mass fraction  $g_k$  of  $C_3H_8$  and  $C_9H_{20}$  is shown. Note that the liquid mass fractions of the individual components are shown as fraction of the maximum liquid mass fraction of that component, i.e.  $g_k/g_{max,k}$ . Components  $C_3H_8$  and  $C_9H_{20}$  represent the relatively light and heavy hydrocarbon components present in the mixture, respectively. As can be seen from these figures, the lighter hydrocarbons tend to condensate less than the heavier ones.

The results presented demonstrate, that the present method can be used to analyze the transonic flow of multi-component gas mixtures with condensation in complex geometries. However, features like multi-component nucleation and condensation (Peeters [50]), as well as de-nucleation need to be included in the physical model before detailed further analysis can be carried out.



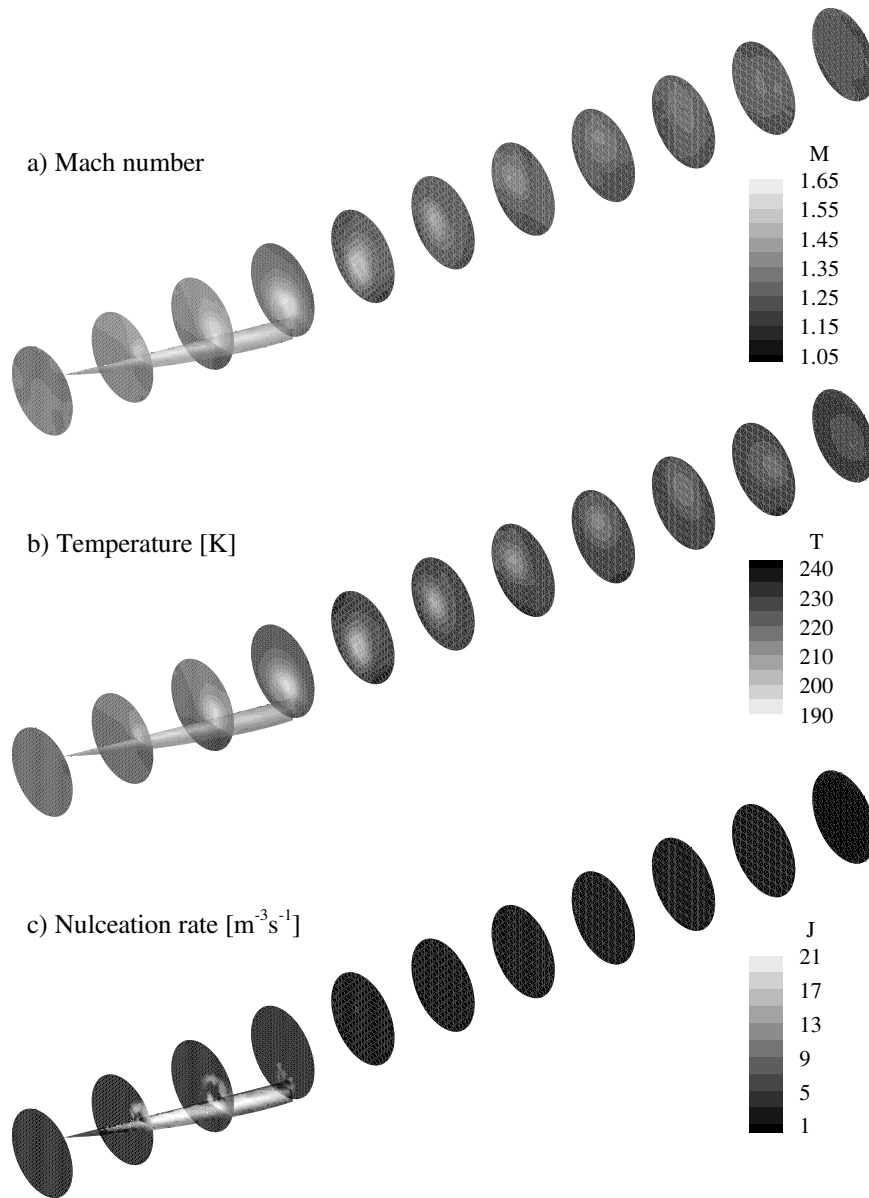
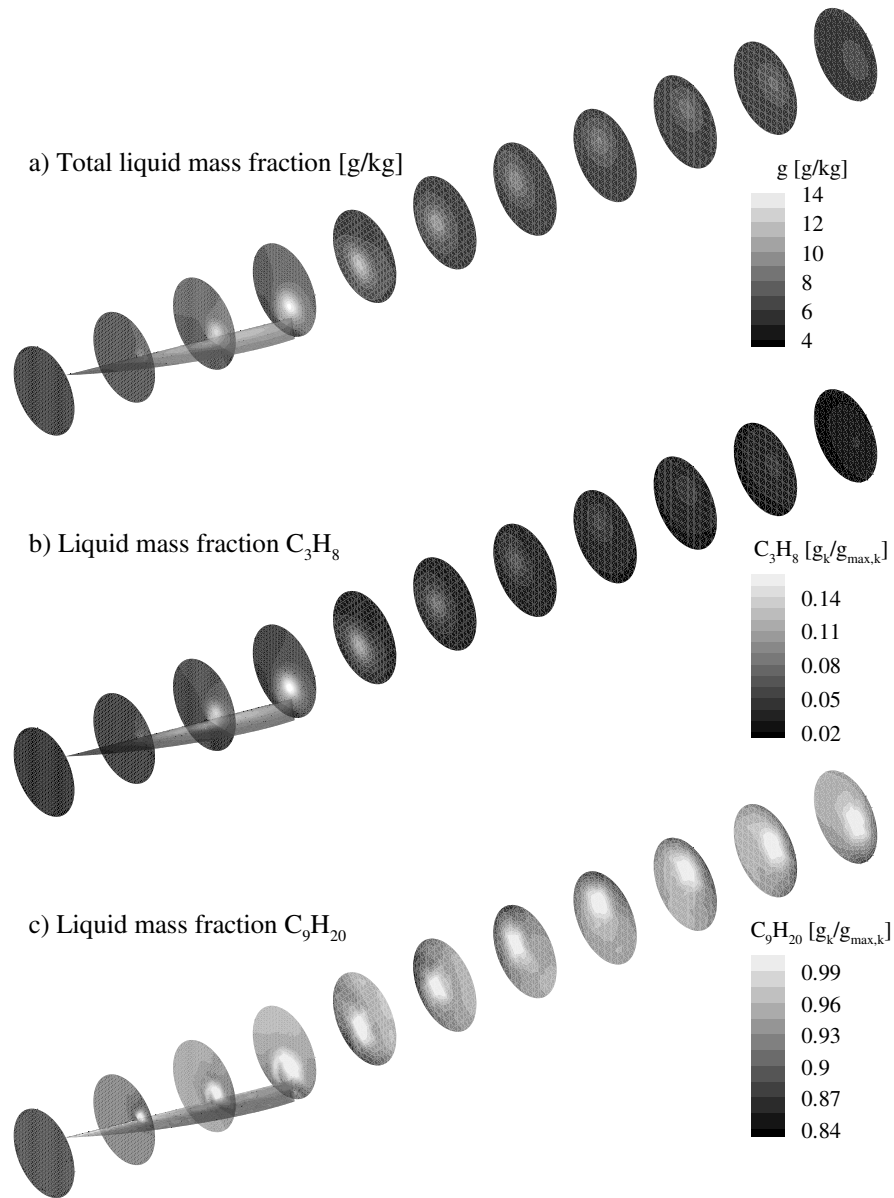


FIGURE 7.9: *Condi-Cyclone, results.*

FIGURE 7.10: *Condi-Cyclone, results.*

---

## CONCLUDING REMARKS

---



- For compressible flows of a (multi-component) gas with condensation, in the thesis a closed set of partial differential equations and algebraic relations is derived. It consists of the Euler equations of gas dynamics and Hill's Method of Moments describing the liquid phase, plus relations for material properties, such as surface tension, liquid density and equilibrium vapour pressure (the dew-curve). The most important assumptions underlying the model for the multi-phase dispersed flow are inviscid flow and zero slip between the gas and liquid phase.
  - It has been shown that Hill's Method of Moments can alternatively be derived from the General Dynamic Equation (which describes, in absence of coagulation and segregation, the conservation of droplets in phase-space).
  - For gases and mixtures of gases, utilizing Maxwell relations following from a combination of the first and second law of thermodynamics, equations of state and other thermodynamic relations have been derived for conditions ranging from (1) conditions of high pressure and moderate (room) temperature, to (2) low pressure and low temperature. The formulation contains only 9 free parameters that are determined from a weighted least-squares fit of data from a data-base. For a natural gas, it is shown that such real-gas equations of state are adequately accurate.
  - To achieve second-order spatial accuracy in the finite-volume discretization on unstructured grids, it is essential that the control-volume averaged solution is associated with the centroid of the control volume. In the second-order reconstruction algorithm this has to be considered carefully.
  - Validation of the computational method for two-dimensional and axi-symmetric flow problems has shown that the method produces results that agree well with other numerical results and with experimental data. For flows without condensation, this refers to the benchmark problem of the NACA 0012 airfoil compared to other numerical results and the axi-symmetric flow in an underexpanded supersonic jet compared to experimental data. For flow with condensation, results correlate well with other numerical results, which in its turn agree well with experimental data.
  - For the validation cases for which experimental data is available, the assumptions underlying the present method have proven to be valid. Convergence of the method for all validation cases is excellent; residuals can be reduced to machine accuracy and calculations generally require less than one day on an SGI O200.
  - The underexpanded xenon jet shows similar interesting flow features as the underexpanded jet of other gases, such as the Mach disk and the barrel shock. Condensation has a signif-
-

ificant effect on the diameter of the Mach disk and the diameter of the barrel shock. It is also demonstrated that there is a remarkably rapid shift in the location of the condensation when the saturation in the reservoir varies from lower values to higher values. For the underexpanded xenon jet flow, the method converges to adequate levels of accuracy but not to machine accuracy.

- It has been demonstrated that the computational method can be applied to the flow of a 20-component natural gas with condensation in a complex 3D geometry. The 3D flow features a strong expansion with a high cooling-rate and nucleation and droplet-growth followed by a strong swirling flow with additional nucleation, further droplet growth in regions with expansion and evaporation in regions with compression. However, features like multi-component nucleation and condensation, as well as de-nucleation need to be included in the physical model before detailed analysis can be carried out.

---

---

## REFERENCES

---

- [1] M. Abbett, *Mach Disk in Underexpanded Exhaust Plumes*, AIAA Journal, Vol. 9, No. 3, pp. 512-514 (1971).
  - [2] I.H. Abbott and A.E. Von Doenhoff, *Theory of Wing Sections*, Dover Publications (1958).
  - [3] S. Adam, *Numerische und experimentelle Untersuchung instationärer Düsenströmungen mit Energiezufuhr durch homogene Kondensation*, Ph.D. Thesis, Universität Karlsruhe, Karlsruhe, Germany (1996).
  - [4] AGARD Advisory Group For Aerospace Research & Development, *Test Cases For The Inviscid Flow Field Methods*, AGARD-AR-211 (1985).
  - [5] M. Aftosmis, D. Gaitonde and T.S. Tavares, *Behavior of Linear Reconstruction Techniques on Unstructured Meshes*, AIAA Journal, Vol. 33, No. 11 (1995).
  - [6] J.D. Anderson, *Modern Compressible Flow, With Historical Perspective*, Third Edition, McGraw-Hill (2003).
  - [7] J.D. Anderson, *Hypersonic and High Temperature Gas Dynamics*, McGraw-Hill (1989).
  - [8] W.K. Anderson, J.L. Thomas and B. van Leer, *Comparison of finite volume flux vector splittings for the Euler equations*, AIAA Journal, Vol. 24, pp. 1453-1460 (1986).
  - [9] H. Ashkenas and F.S. Sherman, *The Structure and Utilization of Supersonic Free Jets in Low Density Wind Tunnels*, In Fourth International Symposium on Rarefied Gas Dynamics, Academic Press, Vol. 2, pp. 84-105 (1966).
  - [10] G.K. Batchelor, *An Introduction to Fluid Dynamics*, Cambridge University Press (1970).
  - [11] M. Berzins, R. Fairlie, S.V. Pennington and J.M. Ware, *SPRINT2D: Adaptive Software for PDEs*, ACM Transactions on Mathematical Software, Vol. 24, No.4, pp. 475-499 (1998).
  - [12] R.B. Bird, W.E. Stewart and E.N. Lightfoot, *Transport Phenomena*, Second Edition, John Wiley & Sons, Inc. (2002).
-

- 
- [13] D.H. Bowman, R.A. Aziz and C.C. Lim, *Vapor pressure of liquid argon, krypton, and xenon*, Canadian Journal of Physics, Vol. 47, pp. 267-273 (1969).
- [14] R. de Bruijn, A. Bartnik, H. Fledderus, H. Fiedorowicz, P. Hegeman, R. Constantinescu and F. Bijkerk, *Characterization of a novel double-gas-jet laser-plasma EUV source*, SPIE 3997-17 (2001).
- [15] R. de Bruijn, K. Koshelev, G. Kooijman, E.S. Toma and F. Bijkerk, *Absorption of EUV in laser plasmas generated on xenon gas jets*, Journal of Quantitative Spectroscopy and Radiative Transfer, Vol. 81, pp. 97-105 (2003).
- [16] J.F. Campbell and J.R. Chambers, *Patterns in the Sky: Natural Visualization of Aircraft Flow Fields*, NASA SP-514 (1994).
- [17] D.J. Creasy, D.E. Heard, M.J. Pilling, B.J. Whitaker, M. Berzins, R. Fairlie, *Visualisation of a supersonic free-jet expansion using laser-induced fluorescence spectroscopy: Application to the measurement of rate constants at ultralow temperatures*, Applied Physics B, Vol. 65, pp. 375-391 (1997).
- [18] S. Crist, P.M. Sherman and D.R. Glass, *Study of the Highly Underexpanded Sonic Jet*, AIAA Journal, Vol. 4, No. 1, pp. 68-71 (1966).
- [19] C.A. Croxton, *Liquid State Physics - A Statistical Mechanical Introduction*, Cambridge University Press, pp. 140-189 (1974).
- [20] P.S. Cumber, M. Fairweather, S.A.E.G. Falle and J.R. Giddings, *Predictions of the Structure of Turbulent, Moderately Underexpanded Jets*, Journal of Fluids Engineering, Vol. 116, pp. 707-713 (1994).
- [21] P.S. Cumber, M. Fairweather, S.A.E.G. Falle and J.R. Giddings, *Predictions of the Structure of Turbulent, Highly Underexpanded Jets*, Journal of Fluids Engineering, Vol. 117, pp. 599-603 (1995).
- [22] H. Deconinck and R. Struys, *Consistent boundary conditions for cell centered upwind finite volume Euler solvers*, Numerical methods for fluid dynamics III, Clarendon Press (1988).
- [23] U. Dohrmann, *Ein numerisches Verfahren zur Berechnung stationärer transsonischer Strömungen mit Energiezufuhr durch homogene Kondensation*, Ph.D. Thesis, Universität Karlsruhe, Karlsruhe, Germany (1989).
- [24] M. van Dyke, *An Album of Fluid Motion*, The Parabolic Press, Stanford CA (1982).
- [25] N.T. Frink and S.Z. Pirzadeh, *Tetrahedral Finite-Volume Solutions to the Navier-Stokes Equations on Complex Configurations*, NASA/TM-1998-208961, December 1998.
- [26] B.J. Gribben, K.J. Badcock and B.E. Richards, *Numerical Study of Shock-Reflection Hysteresis in an Underexpanded Jet*, AIAA Journal, Vol. 38, No. 2, pp. 275-283 (2000).
- [27] R. Hagmeijer, *Equivalence of two different integral representations of droplet distribution moments in condensing flow*, submitted to Physics of Fluids (2002).
-

- [28] R. Hagmeijer, R.H.A. IJzermans and F. Put, *Local solution of the General Dynamic Equation along Fluid Paths generated by the Method of Moments*, to be submitted to Physics of Fluids.
  - [29] M. Heiler, *Instationäre Phänomene in homogen/heterogen kondensierenden Düsen- und Turbinenströmungen*, Ph.D. Thesis, Universität Karlsruhe, Karlsruhe, Germany (1999).
  - [30] C. Hirsch, *Second-Order Upwind and High-Resolution Schemes*, Numerical Computation of Internal and External Flows, Vol. 2, pp. 493-594 (1988).
  - [31] P.G. Hill, *Condensation of Water Vapour during Supersonic Expansion in Nozzles*, Journal of Fluid Mechanics, Vol. 25, part 3, pp. 593-620 (1966).
  - [32] H. Hornung, *Regular and Mach Reflection of Shock Waves*, Annual Review of Fluid Mechanics, Vol. 18, pp. 33-58 (1986).
  - [33] K. Ishizaka, T. Ikohagi and H. Daiguji, *A High-Resolution Numerical Method for Transonic Nonequilibrium Condensation Flows through a Steam Turbine Cascade*, Proc. of the 6th Int. Symp. on Comp. Fluid Dynamics (ISCFD), Lake Tahoe, USA, 4-8 Sept. (1995).
  - [34] Kanouff, H. Shields, L. Bernardez, D. Chenoweth and G. Kubiak, *Absorption of extreme ultraviolet light in a laser produced gas-jet plasma source*, Journal of Applied Physics, Vol. 90, No. 8, pp. 3726-3734 (2001).
  - [35] P.H. Kelleners, F. Put, H.W.M. Hoeijmakers and R. Hagmeijer, *A Three Dimensional Unstructured Grid Method For Flows With Condensation*, Presented at the ECCOMAS Computational Fluid Dynamics Conference 2001, Swansea, Wales, UK, September 4-7 (2001).
  - [36] P.H. Kelleners, F. Put, R. Hagmeijer and H.W.M. Hoeijmakers, *Development of a Numerical Method for the Simulation of Condensing Real Gas Flows*, Presented as paper 152 at the 4th International Conference On Multiphase Flow, New Orleans, Louisiana, May 27 - June 1 (2001).
  - [37] G.D.C. Kuiken, *Thermodynamics of Irreversible Processes, Applications to Diffusion and Rheology*, John Wiley & Sons (1994).
  - [38] G. Lamanna, *On Nucleation and Droplet Growth in Condensing Nozzle Flows*, Ph.D. Thesis, Eindhoven University of Technology, Eindhoven, The Netherlands (2000).
  - [39] A.J. Leadbetter and H.E. Thomas, Trans. Faraday Soc. **61**, 10 (1965).
  - [40] M.S. Liou and C.J. Steffen, *A New Flux Splitting Scheme*, Journal of Computational Physics, Vol. 107, pp. 23-39 (1993).
  - [41] M.S. Liou, *A Sequel to AUSM: AUSM<sup>+</sup>*, Journal of Computational Physics, Vol. 129, pp. 364-382 (1996).
  - [42] C.C.M. Luijten, *Nucleation and Droplet Growth at High Pressure*, Ph.D. Thesis, Eindhoven University of Technology, Eindhoven, The Netherlands (1998).
-

- 
- [43] C.C.M. Luijten, R.G.P. Van Hooy, J.W.F. Janssen and M.E.H. Van Dongen, *Multicomponent droplet growth in natural gas*, J. Chem. Phys., Vol. 109, pp. 3553-3557 (1998).
- [44] C.C.M. Luijten, P. Peeters and M.E.H. Van Dongen, *Nucleation at high pressure I: theoretical considerations*, J. Chem Phys., Vol. 111, pp. 8524-8534 (1999).
- [45] C.C.M. Luijten and M.E.H. Van Dongen, *Nucleation at high pressure II: Wave tube data and analysis*, J. Chem. Phys., Vol. 111, pp. 8535-8544 (1999).
- [46] G. Mundinger, *Numerische Simulation instationärer Lavalströmungen mit Energiezufuhr durch homogene Kondensation*, Ph.D. Thesis, Universität Karlsruhe, Karlsruhe, Germany (1994).
- [47] J.D. Müller, *On Triangles And Flow*, Ph.D. Thesis, University of Michigan (1996).
- [48] E.S. Oran and J.P. Boris, *Numerical Simulation of Reactive Flow*, Elsevier (1987).
- [49] K. Oswatitsch, *Kondensationserscheinungen in Überschallströmungen*, Z. angew. Math. Mech., Vol. 22, no. 1, pp. 1-14 (1942).
- [50] P. Peeters, *Nucleation and Condensation in Gas-Vapor Mixtures of Alkanes and Water*, Ph.D. Thesis, Eindhoven University of Technology, Eindhoven, The Netherlands (2002).
- [51] P. Peeters, C.C.M. Luijten, and M.E.H. van Dongen, *Transitional droplet growth and diffusion coefficients*, Int. J. Heat and Mass Transfer, Vol. 44, pp. 181-193 (2001).
- [52] B. Prast, *Condensation in Supersonic Expansion Flow*, Theory and Numerical Evaluation, Technische Universiteit Eindhoven, Stan Ackermans Instituut, 111 (1997).
- [53] S.M. Prudhomme and H. Haj-Hariri, *Investigation of supersonic underexpanded jets using adaptive unstructured finite elements*, Finite Elements in Analysis and Design, Vol. 17, pp. 21-40 (1994).
- [54] H.R. Pruppacher and J.D. Klett, *Microphysics of Clouds and Precipitation*, D. Reidel Publishing Company (1980).
- [55] F. Put, P.H. Kelleners, R. Hagmeijer and H.W.M. Hoeijmakers, *Numerical simulation of condensing real gas flows*, Presented as paper E20 at the 3rd International Symposium on Computational Technologies for Fluid/Thermal/Chemical Systems with Industrial Applications, July 22-26, Atlanta, Georgia, USA (2001).
- [56] F. Put, P.H. Kelleners, and H.W.M. Hoeijmakers, *Development of a numerical method for simulating transonic multi-phase flows*, Presented at the IUTAM Symposium Transsonicum IV, Göttingen, Germany, September 2-6 (2002).
- [57] R.C. Reid, B.E. Poling, J.M. Prausnitz, J.P. O'Connell, *The properties of gases and liquids*, New York, McGraw-Hill, 5th ed. (2000).
- [58] M.B. Rivers and R.A. Wahls, *Comparison of Computational and Experimental Results for a Supercritical Airfoil*, NASA TM-4601, November (1994).
-



- [59] J.H. Seinfeld, *Atmospheric chemistry and physics of air pollution*, Wiley, New York (1986).
  - [60] B.L. Smith, P.R. Gardner and E.H.C. Parker, *Surface Tension and Energy of Liquid Xenon*, The Journal of Chemical Physics, Vol. 47, No. 3, pp. 1148-1152 (1967).
  - [61] O. Šifner and J. Klomfar, *Thermodynamic Properties of Xenon from the Triple Point to 800 K with Pressures up to 350 MPa*, J. Phys. Chem. Ref. Data, Vol. 23, No. 1 (1994).
  - [62] D. Sonntag and D. Heinze, *Sättigungsdampfdruck- und Sättigungsdampfdichtetafeln für Wasser und Eis*, VEB Deutscher Verlag für Grundstoffindustrie (1982).
  - [63] Tannehill, Anderson and Pletcher, *Computational Fluid Mechanics and Heat Transfer, Second Edition*, Taylor and Francis (1997).
  - [64] F. Theeuwes and R.J. Bearman, *The  $p$ ,  $V$ ,  $T$  behavior of dense fluids V. The vapor pressure and saturated liquid density of xenon*, J. Chem. Thermodynamics, Vol. 2, pp. 507-512 (1970).
  - [65] B. Van Leer, *Flux-vector splitting for the Euler equations*, Lecture Notes in Physics, Vol. 170, pp. 507-512 (1982).
  - [66] B. van Leer, *Towards the ultimate conservative difference scheme. V. A second order sequel to Godunov's method*, Journal of Computational Physics, Vol. 32, pp. 101-136 (1979).
  - [67] Peter P. Wegener, *Nonequilibrium Flows*, Marcel Dekker (1969).
  - [68] M.M.R. Williams and S.K. Loyalka, *Aerosol science theory and practice*, Pergamon Press, Oxford (1991).
  - [69] G. Winkler, *Lauftrad-Leitrad-Wechselwirkung in homogen-heterogen kondensierenden Turbinenströmungen*, Ph.D. Thesis, Universität Karlsruhe, Karlsruhe, Germany (2000).
  - [70] W.H. Wisman, *Inleiding Thermodynamica*, Delftse Uitgevers Maatschappij (1991).
-

---

---

# COORDINATE TRANSFORMATION

---



## A.1 Governing equations in cylindrical coordinates

In this appendix, the governing equations are transformed from a Cartesian coordinate system to a cylindrical coordinate system. In cylindrical coordinates, instead of designating the coordinates of a point  $P$  by  $x, y, z$ , we locate the point by giving the values of  $r, \theta, z$  as is illustrated in Fig. A.1.

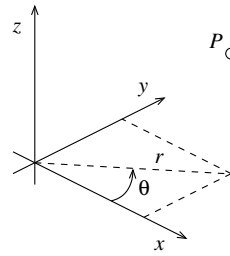


FIGURE A.1: *Definition of cylindrical coordinate system*

The cylindrical coordinates are related to the Cartesian coordinates by:

$$\begin{cases} x = r \cos \theta, & \text{(A.1-a)} \\ y = r \sin \theta, & \text{(A.1-b)} \\ z = z, & \text{(A.1-c)} \end{cases} \quad \begin{cases} r = \sqrt{x^2 + y^2}, & \text{(A.1-d)} \\ \theta = \arctan(y/x), & \text{(A.1-e)} \\ z = z. & \text{(A.1-f)} \end{cases}$$

The following notation will be used for the Cartesian and cylindrical coordinates, and for the velocities in the Cartesian and cylindrical coordinate system, respectively:

$$(x, y, z)^T = (x_1, x_2, x_3)^T, \quad \text{(A.2-a)}$$

$$(r, \theta, z)^T = (\xi_1, \xi_2, \xi_3)^T, \quad \text{(A.2-b)}$$

$$(u_x, u_y, u_z)^T = (u_1, u_2, u_3)^T, \quad \text{(A.2-c)}$$

$$(v_r, v_\theta, v_z)^T = (v_1, v_2, v_3)^T. \quad \text{(A.2-d)}$$

The coordinate transformation Jacobian matrix is defined by:

---

$$J \equiv \frac{\partial(x_1, x_2, x_3)}{\partial(\xi_1, \xi_2, \xi_3)} = \begin{bmatrix} x_r & x_\theta & x_z \\ y_r & y_\theta & y_z \\ z_r & z_\theta & z_z \end{bmatrix} = \begin{bmatrix} \cos \theta & -r \sin \theta & 0 \\ \sin \theta & r \cos \theta & 0 \\ 0 & 0 & 1 \end{bmatrix}, \quad (\text{A.3})$$

so that the determinant of  $J$  and inverse of  $J$  are

$$|J| = r \sin^2 \theta + r \cos^2 \theta = r, \quad (\text{A.4})$$

and

$$J^{-1} = \frac{\partial(\xi_1, \xi_2, \xi_3)}{\partial(x_1, x_2, x_3)} = \begin{bmatrix} r_x & r_y & r_z \\ \theta_x & \theta_y & \theta_z \\ z_x & z_y & z_z \end{bmatrix} = \begin{bmatrix} \cos \theta & \sin \theta & 0 \\ -\frac{1}{r} \sin \theta & \frac{1}{r} \cos \theta & 0 \\ 0 & 0 & 1 \end{bmatrix}, \quad (\text{A.5})$$

respectively. The governing equations (2.80), are repeated here for convenience:

$$\frac{\partial \mathbf{U}}{\partial t} + \frac{\partial}{\partial x_j} \{ \mathbf{F}_j(\mathbf{U}) \} = \mathbf{W}(\mathbf{U}). \quad (\text{A.6})$$

Applying the coordinate transformation to Eq. (2.80), the following transformed equation is obtained

$$\frac{\partial \mathbf{U}}{\partial t} + J_{mj}^{-1} \frac{\partial}{\partial \xi_m} \{ \mathbf{F}_j(\mathbf{U}) \} = \mathbf{W}(\mathbf{U}), \quad (\text{A.7})$$

where  $J_{mj}^{-1} = \{J^{-1}\}_{mj}$ , i.e. the element on the  $m$ -th row and the  $j$ -th column of the inverse of the Jacobian matrix. Note that the three components of the momentum equations are still the components in  $x, y$  and  $z$  direction. This equation can be cast in strong conservation form again by multiplying with  $|J|$  and by regrouping terms. This results in the following equation:

$$|J| \frac{\partial \mathbf{U}}{\partial t} + \frac{\partial}{\partial \xi_m} \{ |J| J_{mj}^{-1} \mathbf{F}_j(\mathbf{U}) \} - \mathbf{F}_j(\mathbf{U}) \frac{\partial}{\partial \xi_m} (|J| J_{mj}^{-1}) = |J| \mathbf{W}(\mathbf{U}). \quad (\text{A.8})$$

The last term is equal to zero and can be dropped, see Tannehill et al. [63]:

$$\frac{\partial}{\partial \xi_m} (|J| J_{mj}^{-1}) \equiv 0, \quad (\text{A.9})$$

leading to the following strong conservation form:

$$\frac{\partial \mathbf{V}}{\partial t} + \frac{\partial}{\partial \xi_m} \{ \mathbf{G}_j(\mathbf{V}) \} = |J| \mathbf{W}(\mathbf{U}). \quad (\text{A.10})$$

with

$$\mathbf{V} \equiv |J| \mathbf{U}, \quad \mathbf{G}_j(\mathbf{V}) = |J| J_{mj}^{-1} \mathbf{F}_j(\mathbf{V}/|J|). \quad (\text{A.11})$$

Note that the Jacobian matrix does not depend on time so that  $|J|$  can indeed be brought inside the time derivate in Eq. (A.8). Also note that the components of the momentum equation are still the components in  $x, y$  and  $z$  direction.

---

### A.1.1 Mass conservation equation

For the mass conservation equation the following relation is obtained

$$\frac{\partial |J| \rho}{\partial t} + \frac{\partial}{\partial \xi_m} \{ |J| J_{mj}^{-1} \rho u_j \} = 0. \quad (\text{A.12})$$

The velocity vector in the new coordinate system  $\vec{v}$  is found by multiplying the velocity vector in the old coordinate system  $\vec{u}$  with the inverse Jacobian matrix

$$v_m = J_{mj}^{-1} u_j, \quad (\text{A.13})$$

so that Eq. (A.12) becomes

$$\frac{\partial r \rho}{\partial t} + \frac{\partial r \rho v_m}{\partial \xi_m} = 0, \quad (\text{A.14})$$

or, expanded in terms of  $(r, \theta, z)$ :

$$\frac{\partial r \rho}{\partial t} + \frac{\partial r \rho v_r}{\partial r} + \frac{\partial r \rho v_\theta}{\partial \theta} + \frac{\partial r \rho v_z}{\partial z} = 0. \quad (\text{A.15})$$

### A.1.2 Momentum conservation equation

For the three momentum conservation equations ( $i = 1, 2, 3$ ) we get

$$\frac{\partial |J| \rho u_i}{\partial t} + \frac{\partial}{\partial \xi_m} \{ |J| J_{mj}^{-1} (\rho u_i u_j + \delta_{ij} p) \} = 0. \quad (\text{A.16})$$

Multiplying with the inverse Jacobian matrix gives

$$J_{ni}^{-1} \frac{\partial |J| \rho u_i}{\partial t} + J_{ni}^{-1} \frac{\partial}{\partial \xi_m} \{ |J| J_{mj}^{-1} (\rho u_i u_j + \delta_{ij} p) \} = 0. \quad (\text{A.17})$$

Since the Jacobian does not depend on time it can be brought inside the time derivative

$$J_{ni}^{-1} \frac{\partial |J| \rho u_i}{\partial t} = \frac{\partial}{\partial t} (|J| \rho J_{ni}^{-1} u_i) \stackrel{(\text{A.13})}{=} \frac{\partial |J| \rho v_n}{\partial t}. \quad (\text{A.18})$$

The second term in Eq. (A.17) can be worked out:

$$J_{ni}^{-1} \frac{\partial}{\partial \xi_m} \{ |J| J_{mj}^{-1} (\rho u_i u_j + \delta_{ij} p) \} = J_{ni}^{-1} \frac{\partial}{\partial \xi_m} (|J| \rho u_i J_{mj}^{-1} u_j + |J| J_{mj}^{-1} \delta_{ij} p) \quad (\text{A.19-a})$$

$$\stackrel{(\text{A.13})}{=} J_{ni}^{-1} \frac{\partial}{\partial \xi_m} (|J| \rho u_i v_m + |J| J_{mi}^{-1} p). \quad (\text{A.19-b})$$

The inverse Jacobian in the first term of Eq. (A.19-b) can be brought inside the brackets in the following way:

$$J_{ni}^{-1} \frac{\partial}{\partial \xi_m} (|J| \rho u_i v_m) = \frac{\partial}{\partial \xi_m} (|J| \rho J_{ni}^{-1} u_i v_m) - |J| \rho u_i v_m \frac{\partial}{\partial \xi_m} J_{ni}^{-1} \quad (\text{A.20-a})$$

$$\stackrel{(\text{A.13})}{=} \frac{\partial}{\partial \xi_m} (|J| \rho v_n v_m) - |J| \rho u_i v_m \frac{\partial}{\partial \xi_m} J_{ni}^{-1}. \quad (\text{A.20-b})$$

The velocities in the old coordinate system can be transformed to the new system by using the inverse of Eq. (A.13), i.e.  $u_i = J_{ij}v_j$  so that the last term of Eq. (A.20-b) becomes

$$|J|\rho u_i v_m \frac{\partial}{\partial \xi_m} J_{ni}^{-1} = |J|\rho J_{ij} v_j v_m \frac{\partial}{\partial \xi_m} J_{ni}^{-1}. \quad (\text{A.21})$$

The second term of Eq. (A.19-b) can be written as

$$J_{ni}^{-1} \frac{\partial}{\partial \xi_m} (|J| J_{mi}^{-1} p) = J_{ni}^{-1} |J| J_{mi}^{-1} \frac{\partial p}{\partial \xi_m}. \quad (\text{A.22})$$

Carrying out the index summations for each index this yields for the components of the momentum equation in  $r$ ,  $\theta$  and  $z$  direction

$$r(n=1) : \frac{\partial r v_r}{\partial t} + \frac{\partial r \rho v_r^2}{\partial r} + \frac{\partial r \rho v_r v_\theta}{\partial \theta} + \frac{\partial r \rho v_r v_z}{\partial z} + r \frac{\partial p}{\partial r} - r^2 \rho v_\theta^2 = 0, \quad (\text{A.23-a})$$

$$\theta(n=2) : \frac{\partial r v_\theta}{\partial t} + \frac{\partial r \rho v_\theta v_r}{\partial r} + \frac{\partial r \rho v_\theta^2}{\partial \theta} + \frac{\partial r \rho v_\theta v_z}{\partial z} + \frac{1}{r} \frac{\partial p}{\partial \theta} + 2 \rho v_r v_\theta = 0, \quad (\text{A.23-b})$$

$$z(n=3) : \frac{\partial r v_z}{\partial t} + \frac{\partial r \rho v_z v_r}{\partial r} + \frac{\partial r \rho v_z v_\theta}{\partial \theta} + \frac{\partial r \rho v_z^2}{\partial z} + r \frac{\partial p}{\partial z} = 0. \quad (\text{A.23-c})$$

### A.1.3 Energy conservation equation

In analogy with the mass conservation equation, the energy conservation equation in cylindrical coordinates is given by

$$\frac{\partial r \rho e_t}{\partial t} + \frac{\partial r \rho v_r h_t}{\partial r} + \frac{\partial r \rho v_\theta h_t}{\partial \theta} + \frac{\partial r \rho v_z h_t}{\partial z} = 0. \quad (\text{A.24})$$

### A.1.4 Hill's method of moments

For Hill's method of moments, consisting of four equations, we get ( $i = 0, 1, 2, 3$ ):

$$\frac{\partial |J| \rho q_i}{\partial t} + \frac{\partial}{\partial \xi_m} \{ |J| J_{mj}^{-1} (\rho q_i u_j) \} = r W^{(i+6)}. \quad (\text{A.25})$$

with  $\mathbf{q} = (Q_0, Q_1, Q_2, g)^T$ . Carrying out the index summations, we get

$$\frac{\partial r \rho q_i}{\partial t} + \frac{\partial r \rho v_r q_i}{\partial r} + \frac{\partial r \rho v_\theta q_i}{\partial \theta} + \frac{\partial r \rho v_z q_i}{\partial z} = r W^{(i+6)}. \quad (\text{A.26})$$

### A.1.5 Axi-symmetric flow without swirl

In the case of axi-symmetric flow without swirl the  $\frac{\partial}{\partial \theta}$  terms are zero, and in addition also the velocity in  $\theta$  direction,  $v_\theta$  is zero. As a result, the momentum equation in  $\theta$  direction can be dropped and the resulting set of governing equations in case of axi-symmetric flow without swirl is

$$\frac{\partial r \mathbf{U}}{\partial t} + \frac{\partial r \mathbf{F}}{\partial z} + \frac{\partial r \mathbf{G}}{\partial r} = \mathbf{H} + r \mathbf{W}. \quad (\text{A.27})$$

Column vectors  $\mathbf{U}$ ,  $\mathbf{F}$ ,  $\mathbf{G}$ ,  $\mathbf{H}$  and  $\mathbf{W}$  are given by:

---

$$\mathbf{U} = \begin{pmatrix} \rho \\ \rho v_z \\ \rho v_r \\ \rho e_t \\ \rho Q_0 \\ \rho Q_1 \\ \rho Q_2 \\ \rho g \end{pmatrix} \quad \mathbf{F} = \begin{pmatrix} \rho v_z \\ \rho v_z^2 + p \\ \rho v_z v_r \\ \rho v_z h_t \\ \rho v_z Q_0 \\ \rho v_z Q_1 \\ \rho v_z Q_2 \\ \rho v_z g \end{pmatrix} \quad \mathbf{G} = \begin{pmatrix} \rho v_r \\ \rho v_r v_z \\ \rho v_r^2 + p \\ \rho v_r h_t \\ \rho v_r Q_0 \\ \rho v_r Q_1 \\ \rho v_r Q_2 \\ \rho v_r g \end{pmatrix} \quad (\text{A.28})$$

$$\mathbf{H} = \begin{pmatrix} 0 \\ 0 \\ p \\ 0 \\ 0 \\ 0 \\ 0 \\ 0 \end{pmatrix} \quad \mathbf{W} = \begin{pmatrix} 0 \\ 0 \\ 0 \\ 0 \\ J \\ r^* J + \dot{r} \rho Q_0 \\ r^{*2} J + 2\dot{r} \rho Q_1 \\ \frac{4}{3} \pi \varrho_l (r^{*3} J + 3\dot{r} \rho Q_2) \end{pmatrix} \quad (\text{A.29})$$





---

# MESH-TO-MESH INTERPOLATION

---



In this appendix, an efficient method is presented to interpolate the solution from one (source) mesh to another (target) mesh. A structured equidistant background mesh is used as a means of reducing the computational effort required to obtain an initial solution on the target mesh from  $O(N^2)$  to  $O(N \log(N))$ . The method was originally developed for solution continuation on 3D unstructured tetrahedral meshes, but for clarity, it is presented here for solution continuation on 2D triangular meshes. Extension of the method to 3D tetrahedral meshes is straightforward.

In general, the information which is needed to describe a triangular or tetrahedral mesh, is the geometric location of every node, and for every triangle the index of the nodes which form the triangle. The file in which the geometric location of the nodes is stored will be referred to as the node file, and the file which stores the indices of the nodes spanning the element (triangle or tetrahedron) will be referred to as the element file. An example of a mesh consisting of only three triangles, and its corresponding node and element file, is given in Fig. B.1.

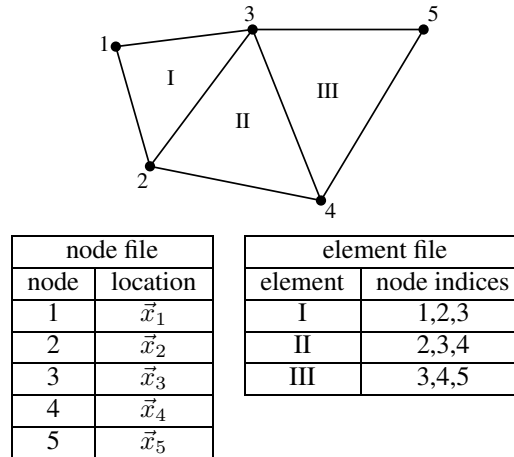


FIGURE B.1: *Example mesh consisting of three triangles with corresponding node and element file, black dots represent the nodes, elements are denoted in Roman.*

---

With the node and element file available, the mesh is fully described. Since the source mesh and the target mesh discretize the same geometry, every node of the target mesh will be located inside or on the edge of a triangle of the source mesh, except for some nodes on a curved boundary, as is illustrated in Fig. B.2. The solution in these target boundary nodes is

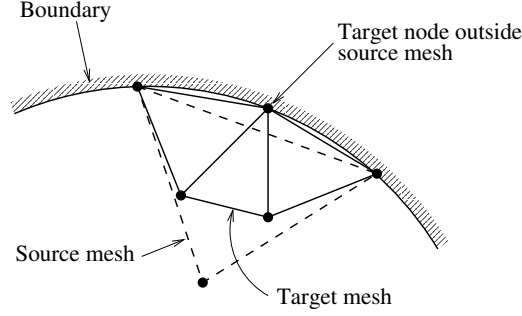


FIGURE B.2: *Target mesh and source mesh discretization of a curved boundary*

copied from the nearest source node, which is found by looping over all nodes of the source mesh. The amount of computational effort needed for this is limited, since the amount of boundary nodes for 2D meshes and especially for 3D meshes is very small compared to the number of interior nodes.

To prevent looping over all source mesh triangles when attempting to find the element number in which the target node lies, the aim is to loop only over a limited part of the domain. For this purpose, a structured mesh consisting of rectangles of a certain size is “superposed” over the coarse mesh, which completely overlaps the unstructured mesh, as is depicted in Fig. B.3 for the mesh of Fig. B.1. The structured mesh consists of  $N_x$  rectangles in  $x$ -

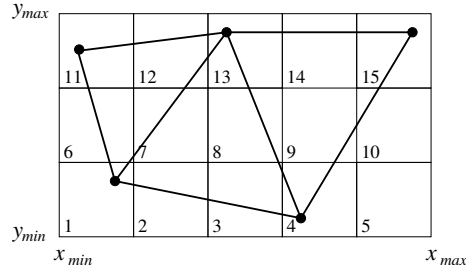


FIGURE B.3: *Structured mesh overlaying the unstructured mesh*

direction and  $N_y$  rectangles in  $y$ -direction, so that the total number of rectangles  $N_{\square}$  is equal to  $N_x N_y$ . The minimum and maximum value of  $x$  and  $y$  are denoted by  $x_{min}$  and  $y_{min}$ , and  $x_{max}$  and  $y_{max}$ , respectively. If we number the rectangular elements from 1 to  $N_{\square}$ , the rectangle number  $n$  in which an arbitrary point  $(x, y)$  is located is given by

$$n(x, y) = 1 + n_x(x) + n_y(y)N_x, \quad (\text{B.1})$$

where

$$n_x(x) = \text{int} \left( \frac{x - x_{min}}{\Delta x} \right), \quad (\text{B.2-a})$$

$$n_y(y) = \text{int} \left( \frac{y - y_{min}}{\Delta y} \right), \quad (\text{B.2-b})$$

with

$$\Delta x = \frac{x_{max} - x_{min}}{N_x}, \quad (\text{B.3-a})$$

$$\Delta y = \frac{y_{max} - y_{min}}{N_y}. \quad (\text{B.3-b})$$

The integer function “int” truncates its argument to an integer. With the number (index) of the rectangle known, we now need to know which triangles are partly or completely in the rectangle. However, this information is not available. The inverse problem on the other hand, i.e. determining which rectangles completely overlap a certain triangle is straightforward. The indices of these rectangles can easily be found by determining the minimum and maximum  $x$  and  $y$  coordinates of the triangle, denoted by  $x_{\Delta,min}$  and  $y_{\Delta,min}$ , and  $x_{\Delta,max}$  and  $y_{\Delta,max}$ , respectively. For the above mentioned example, see Figs. B.1 and B.3, the rectangles overlapping triangle I are 1-3,6-8 and 11-13. Note that rectangles 2,3 and 8 do not overlap triangle I, but, for simplicity, they are not omitted.

The procedure of determining which rectangles overlap a certain triangle is repeated for every triangle. During this procedure, a compact-storage array  $a_t$  of dimension  $[0 : N_{\square}]$  is created which counts how many times the index of a certain rectangle is encountered. For our example mesh, the contents of  $a_t$  is given in table B.1. Note that  $a_t[0] \equiv 1$ . Subsequently,

index	0	1	2	3	4	5	6	7	8	9	10	11	12	13	14	15
value	1	2	2	3	2	1	2	2	3	2	1	2	2	3	2	1

TABLE B.1: Contents of compact-storage array  $a_t$

the contents of  $a_t$  is modified in the following way:

$$a_t[i] + a_t[i - 1] \rightarrow a_t[i] \quad \text{for } i = [1, 2, \dots, N_{\square}]. \quad (\text{B.4})$$

The modified contents of compact-storage array  $a_t$ , for our example, is given in table B.2.

index	0	1	2	3	4	5	6	7	8	9	10	11	12	13	14	15
old	1	2	2	3	2	1	2	2	3	2	1	2	2	3	2	1
new	1	3	5	8	10	11	13	15	18	20	21	23	25	28	30	31

TABLE B.2: Contents of compact-storage array  $a_t$  after modification

After this is done, another compact-storage array  $b$  is created with dimension  $[1:n_a]$ , where  $n_a = a_t[N_\square] - 1$ . Array  $b$  will store the inverse information of which triangle belongs to which rectangle. This is done by looping over all triangles, and for each triangle looping over all overlapping rectangles, by using the information stored in array  $a_t$ . This procedure is best explained by explaining it in pseudo-programming language:

```

 $b[\ ] := 0$ 
For  $e = 1$  to  $N_\Delta$ 
  For  $i = n_x(x_{\Delta,min})$  to  $n_x(x_{\Delta,max})$ 
    For  $j = n_y(y_{\Delta,min})$  to  $n_y(y_{\Delta,max})$ 
       $k := 1 + i + jN_x$ 
       $n := 0$ 
      Do
        If  $b[a_t[k - 1] + n] == 0$  Then
           $b[a_t[k - 1] + n] := e$ 
          Exit
        Else
           $n := n + 1$ 
        End If
      End Do
    Next  $j$ 
  Next  $i$ 
Next  $e$ 

```

The statement "Exit" terminates the "Do - End Do" loop and jumps to the next statement, i.e. "Next  $j$ ". For the example mesh,  $b$  is given in table B.3.

index	1	2	3	4	5	6	7	8	9	10	11	12	13	14	15
value	I	II	I	II	I	II	III	II	III	III	I	II	I	II	I

16	17	18	19	20	21	22	23	24	25	26	27	28	29	30
II	III	II	III	III	I	II	I	II	I	II	III	II	III	III

TABLE B.3: Contents of compact-storage array  $b$

To determine whether a certain point  $P_0$  is inside, on, or outside of a given triangle  $P_1P_2P_3$ , we determine  $\alpha_1, \alpha_2, \alpha_3$  according to Eq. (4.35)

- (1) If  $0 < \alpha_1 < 1, 0 < \alpha_2 < 1, 0 < \alpha_3 < 1$ , then  $P_0$  is properly inside the triangle.
- (2) If  $0 \leq \alpha_1 \leq 1, 0 \leq \alpha_2 \leq 1, 0 \leq \alpha_3 \leq 1$ , and one or two of  $\alpha_1, \alpha_2$  and  $\alpha_3$  is zero, then  $P_0$  is on the triangle's boundary (one zero means edge, two zeroes means node).
- (3) If any of the inequalities in (2) above is false,  $P_0$  is outside the triangle.

The value in point  $P_0$  is then found from Eq. (4.34).

Now that the contents of the compact-storage arrays  $a_t$  and  $b$  have been established, and a method is available to test if a certain point is located inside a given triangle, finding the

---

triangle in which an arbitrary node of the target triangular mesh is located is straightforward. First, the number of the rectangle  $n(x_0, y_0)$  in which the node is located is determined using Eq. (B.1). Second, we test if  $P_0$  is located inside triangle  $j$ , for  $b[a_t[n(x_0, y_0) - 1]] \leq j \leq b[a_t[n(x_0, y_0)] - 1]$ . In this way, we can find the triangle of the source mesh in which the node of the target mesh is located by looping only over a restricted number of triangles. The initial solution in the node is also directly determined from Eq. (4.34). The computational effort to obtain the interpolated solution is in the order of  $N \log(N)$ , compared to  $O(N^2)$  for an interpolation method which runs over each triangle for every new node. To appreciate this, consider the effort it would require to interpolate a solution from a mesh with 10,000 nodes to a mesh with 40,000 nodes, which would be at least  $O(10^8)$  by running over each triangle, while for the present interpolation method, the effort would be at most  $O(10^5)$ . So, for example, the current interpolation method would reduce the computation time from one hour to 4 seconds.

---



---

# SUMMARY

---

Condensation in flows at high speed occurs in many practical situations and industrial applications, for example in the transonic flow of humid air around an aircraft, the expansion flow in steam turbines, phase-separation devices such as a Condi-Cyclone, or in the high-speed flow of an underexpanded jet. The subject of this thesis is the modeling and numerical simulation of high-speed (transonic) flows with condensation.

In the present study we consider flows that are rapidly expanding. Due to the rapid expansion, the onset of condensation is described by homogeneous nucleation, involving the spontaneous formation of vapour clusters in the flow. Under thermodynamic non-equilibrium conditions, the vapour clusters then grow into droplets. The condensation process releases heat to the flow, leading to a complex interaction of the condensation process with the flow itself.

In case of high-pressure flows, the perfect-gas equation of state can no longer be used. A novel real-gas equation of state is therefore developed, satisfying Maxwell's thermodynamic relations, which can be used to accurately describe the behavior of the gas in a specified range of pressure and temperature. The formulation contains only 9 free parameters that are determined from a weighted least-squares fit of data from a data-base. For a natural gas, it is shown that the present formulation of the real-gas equation of state is adequately accurate.

The numerical method developed is based on the Euler equations of gas dynamics and Hill's Method of Moments describing the liquid phase, plus relations for material properties, such as surface tension, liquid density and equilibrium vapour pressure. The governing equations are solved with an explicit finite-volume method. The computational domain is discretized using triangular (2D, axi-symmetric) or tetrahedral (3D) elements. This allows for relatively easy meshing of complex geometries and local clustering of control volumes. The fluxes are calculated with Liou's AUSM<sup>+</sup> scheme, and second order spatial accuracy is achieved by applying van Leer's MUSCL-scheme, with the control-volume-averaged solution assigned to the centroid of the median-dual mesh control-volume. The solution is iterated to a steady state using Heun's predictor-corrector method, while the condensation source term is treated by a fractional time-stepping method.

The method can be used to simulate compressible, high-speed, high-pressure flows of a (multi-component) gas with condensation. Two-dimensional and axi-symmetric flow problems have been utilized to validate the computational method. These are the dry flow of air around the NACA 0012 airfoil at a transonic flow condition, the flow of wet air through the A1 nozzle, and the axi-symmetric flow of dry air in an underexpanded supersonic jet. The validation cases show that the method produces results that agree well with other numeri-

---

cal results and with experimental data. Therefore, the assumptions underlying the present method have proven to be valid for the validation cases considered. Calculations for two-dimensional and axi-symmetric flows generally require less than one day turn-around time on an SGI O200.

As an application the underexpanded jet of xenon is considered. The underexpanded xenon jet shows that condensation has a significant effect on the diameter of the Mach disk and on the diameter of the barrel shock. When the reservoir conditions change such that the saturation varies from lower values to higher values, there is a remarkably rapid shift in the location of the condensation from outside of the barrel shock to inside of the barrel shock. This shows again the complex interaction of the condensation process with the flow that may occur in industrially relevant jet flows. For the underexpanded xenon jet flow with condensation, the method converges to adequate levels of accuracy but not to machine accuracy. Specifically in the vicinity of the nozzle lip, where the supersonic flow is deflected over an angle of 90 degrees, the exponential dependency of the nucleation rate on the flow prevents convergence to machine accuracy.

When the computational method is applied to the flow of a multi-component natural gas with condensation in a complex 3D geometry, the 3D flow features a strong expansion with a high cooling-rate and nucleation and droplet-growth followed by a strong swirling flow with additional nucleation, further droplet growth in regions with expansion and evaporation in regions with compression. However, features like multi-component nucleation and condensation, as well as de-nucleation need to be included in the mathematical model before detailed analysis can be carried out.

---



---

# SAMENVATTING

---

Condensatie in hogesnelheidsstromingen komt in veel praktische situaties en industriële toepassingen voor, bijvoorbeeld in de transsonische stroming van vochtige lucht rond een vliegtuig, de expansiestroming in stoomturbines, fasescheidingsapparaten zoals een Condi-Cyclone, of in de hogesnelheidsstroming van een ondergeëxpandeerde straal. Het onderwerp van dit proefschrift is de modellering en numerieke simulatie van hogesnelheids- (transsonische) stromingen met condensatie.

In het huidige onderzoek beschouwen we stromingen die snel expanderen. Als gevolg van de snelle expansie, wordt het begin van condensatie beschreven door homogene nucleatie, de spontane vorming van dampclusters in de stroming. Onder thermisch niet-evenwicht condities groeien de dampclusters vervolgens tot druppels. Tijdens het condensatieproces komt er warmte vrij in de stroming, wat leidt tot een complexe interactie van het condensatieproces met de stroming.

In het geval van hogedrukstromingen, kan de perfect-gas toestandsvergelijking niet langer worden gebruikt. Daarom is een nieuwe reëel-gas toestandsvergelijking ontwikkeld, die voldoet aan Maxwell's thermodynamische relaties, welke kan worden gebruikt om nauwkeurig het gedrag van het gas te beschrijven in een voorgeschreven bereik van druk en temperatuur. De formulering bevat slechts 9 vrije parameters die worden bepaald uit een gewogen kleinste-kwadraten fit van data uit een databank. Voor aardgas wordt aangetoond dat de huidige formulering van de reëel-gas toestandsvergelijking voldoende nauwkeurig is.

De ontwikkelde numerieke methode is gebaseerd op de Euler vergelijkingen voor de gasdynamica en Hill's Methode van Momenten welke de vloeistoffase beschrijft, plus betrekkingen voor stoffeigenschaften, zoals oppervlaktespanning, vloeistofdichtheid en evenwichtsdrostdruk. De beschrijvende vergelijkingen worden opgelost met een expliciete eindige volume methode. Het rekengebied wordt gediskretiseerd met driehoekige (2D, axiaalsymmetrisch) of tetraëdervormige (3D) elementen. Dit maakt het relatief eenvoudig om complexe geometriën te voorzien van een rekenrooster en om lokaal controlevolumes te clusteren. De fluxen worden berekend met Liou's AUSM<sup>+</sup> schema, waarbij tweede-orde nauwkeurigheid in de ruimte wordt bereikt door het toepassen van Van Leer's MUSCL schema, met de controlevolume-gemiddelde oplossing toegewezen aan het zwaartepunt van het mediaan-duale-rooster controlevolume. De oplossing wordt geïtereerd tot een stationaire toestand, gebruikmakend van Heun's predictie-correctie methode, terwijl de condensatie bronterm wordt behandeld met een fractionele tijdstap methode.

De methode kan worden gebruikt om samendrukbare, hogesnelheids-, hogedrukstromingen van een (multicomponenten) gas met condensatie te simuleren. Twee-dimensionale en axiaal-

---

symmetrische stromingsproblemen zijn gebruikt om de berekeningsmethode te valideren. Dit zijn de stroming van droge lucht rond het NACA 0012 profiel voor een transsone stromingsconditie, de stroming van vochtige lucht door de A1 nozzle, en de axiaalsymmetrische stroming van droge lucht in een ondergeëxpandeerde straal. De validatiegevallen laten zien dat de methode resultaten produceert die goed overeenkomen met andere numerieke resultaten en met experimentele data. De aannames die ten grondslag liggen aan de huidige methode hebben hierdoor bewezen geldig te zijn voor de beschouwde validatiegevallen. Berekeningen aan twee-dimensionale en axiaalsymmetrische stromingen kosten over het algemeen minder dan een dag tijd op een SGI O200.

Als toepassing wordt de ondergeëxpandeerde straal van xenon beschouwd. Deze laat zien dat condensatie een significante invloed heeft op de diameter van de Machschijf en op de diameter van de vatschok. Als de reservoircondities zo veranderen dat de verzadiging van lagere waarden tot hogere waarden varieert, vindt er een opmerkelijk snelle verschuiving plaats van de locatie van de condensatie van buiten de vatschok tot binnen de vatschok. Dit illustreert nogmaals de complexe interactie van het condensatieproces met de stroming zoals die plaats kan vinden in industrieel relevante straalstromingen. Voor de ondergeëxpandeerde xenon straalstroming met condensatie, convergeert de methode tot een toereikend nauwkeurighedsniveau, maar niet tot machinenauwkeurigheid. Met name in de nabijheid van de nozzlerand, waar de supersone stroming over een hoek van 90 graden wordt afgebogen, verhindert de exponentiële afhankelijkheid van de nucleatie met de stroming de convergentie tot machinenauwkeurigheid.

Als de berekeningsmethode wordt toegepast op de stroming van een multicomponenten aardgas met condensatie in een complexe 3D geometrie, vertoont de 3D stroming een sterke expansie met een hoge koelsnelheid en nucleatie en druppelgroei gevolgd door een sterk wervelende stroming met additionele nucleatie, verdere druppelgroei in gebieden met expansie en verdamping in gebieden met compressie. Het is echter nodig om verschijnselen als multicomponenten nucleatie en condensatie, als ook de-nucleatie, op te nemen in het wiskundige model voordat gedetailleerde analyse uitgevoerd kan worden.

---

---

# ACKNOWLEDGMENT

---

This thesis is the result of research work carried out in the past four and a half years. During this period, many people have made a contribution to this work. I owe thanks to them for their involvement. A number of people have been particularly important in the completion of this work. I would like to thank them here.

First, I would like to express my gratitude to Harry Hoeijmakers for the support, guidance and advice over the past period. Your enthusiasm for the field of fluid dynamics and your continuing support have been essential for the completion of this thesis. The enjoyable discussions and your sincere interest in many things outside the scope of my research work are greatly appreciated. Furthermore, I would like to express my gratitude to Rob Hagmeijer, for pursuing the contacts with the FOM-Institute for Plasma Physics. As brought to our attention by prof. Rini van Dongen, René de Bruijn's study at FOM Rijnhuizen provided me with an interesting application for my CFD method. Your enthusiasm about my obtained results and your good eye for detail have been of great value to me. Also I would like to thank my fellow PhD candidate Philip Kelleners, for the many fruitful discussions about CFD and for putting the inevitable frustrations that arise during the development of a CFD method into perspective. Your knowledge about unstructured meshes has been essential for the successful development of my own unstructured mesh CFD method.

The work presented in this thesis could not have been achieved without the financial support from Stork Product Engineering B.V. through grant ABOF 0096 "SPE/Shell Condi-Cyclone Research and Study into Vortices". This support is gratefully acknowledged.

I would like to thank prof. G.H. Schnerr of the group of Fluid Mechanics of the University of München for the opportunity to work in his former group Fachgebiet Strömungsmaschinen at the University of Karlsruhe for one week. Prof. Schnerr has conducted a vast amount of experiments in internal condensing flows, and is one of the pioneers in the field of numerical simulation of condensing flows. He provided an important validation case for my CFD method.

I would like to thank the staff, fellow PhD candidates and students of the Engineering Fluid Dynamics group at the University of Twente for providing an enjoyable working environment and for their direct or indirect contribution to this thesis. Special thanks go to Wouter den Breeijen for his efforts in keeping the computer network running and to the (former) secretaries of the group.

Finally, I would like to thank my parents and my brother for their invaluable support and understanding.

---



---

# CURRICULUM VITAE

---

- 2 december 1973 : geboren in Alblasterdam
- september 1986 - juni 1992 : Voorbereidend Wetenschappelijk Onderwijs,  
De Lage Waard,  
Papendrecht
- september 1992 - augustus 1998 : Luchtvaart- en Ruimtevaarttechniek,  
Technische Universiteit Delft
- april 1999 - september 2003 : Promovendus in dienst van UTwente,  
sub-faculteit Werktuigbouwkunde,  
vakgroep Technische Stromingsleer
-